*Acoustical Physics, Vol. 46, No. 6, 2000, pp. 635–640. Translated from Akusticheskiĭ Zhurnal, Vol. 46, No. 6, 2000, pp. 725–731.*


# The Two-Mode Waveguide Formed by a Rigid Plane and an Elastic Plate

**A. V. Akol'zin and M. A. Mironov**

*Andreev Acoustics Institute, Russian Academy of Sciences ul. Shvernika 4, Moscow, 117036 Russia*

*e-mail: bvp@akin.ru*

Received March 22, 2000

**Abstract**—The structure of the acoustic field formed in the gap between a rigid plane and an elastic plate excited by a point force is considered. Special attention is given to the frequency range near the coincidence frequency in the case of the small values of the load parameter characterizing the plate loading with the medium. Expressions for the energy fluxes in the plate and in the gap are obtained, and the characteristic length of the energy transfer into the gap, as well as the degree of completeness of such a transfer, is determined. © *2000 MAIK "Nauka/Interperiodica".*

In previous studies [1–3], two-mode acoustic waveguides with a pronounced spatial modulation of the acoustic energy flux along their axes were considered. It was found [1] that, in the case of an axial excitation of a liquid-filled elastic shell, the shell and liquid modes have approximately equal amplitudes of pressure in a liquid. Because of the different phase velocities of these modes, the total pressure field in a liquid has pronounced maximums and minimums. A waveguide formed by two narrow, acoustically coupled pipes was considered in [2]. The existence of coupling leads to periodic pumping of acoustic energy from one pipe to the other and back. In [3], a waveguide formed by a water-filled pipe with the insertion made of an elastic water-like material (rubber) was studied. Two modes (one symmetric and one antisymmetric) interfere in such way that the sound pressure in the water part of the waveguide vanishes in certain cross-sections of the pipe. Utilization of an insert made of an elastic material in a waveguide with rigid walls for designing acoustic silencers was considered in [4].

The purpose of this work is the investigation of acoustic energy fluxes in a two-mode waveguide formed by a flexurally oscillating plate and the gap between it and a rigid plane.

Let us consider an infinite homogeneous thin plate, which can perform flexural oscillations under the effect of the force $f$ applied normally to it (Fig. 1). A vacuum is on one side of this plate ($z > 0$), and a gap filled with a compressible liquid and bounded by a perfectly rigid plane is on the other side ($z < 0$). The thicknesses of the plate $h$ and the gap $H$ are assumed to be small as compared to the wavelengths of the waves propagating in such a waveguide. We assume a harmonic (with the circular frequency $\omega$) time dependence of all parameters of the problem.

Let us write down a system of equations for the normal displacement of the plate $\zeta$ and the pressure in the gap $p$:

$$\begin{aligned}\left(-\frac{\omega^2}{c_0^2}-\frac{\partial^2}{\partial x^2}\right)p-\frac{\rho_0}{H}\omega^2\zeta &= 0,\\ \left(\rho h\omega^2+D\frac{\partial^2}{\partial x^4}\right)\zeta-p &= f,\end{aligned} \tag{1}$$

where $\rho_0$ and $c_0$ are the density and the sound velocity in a liquid, $\rho$ and $D$ are the density and the flexural rigidity of the plate, and $f$ is the distributed external force applied to the plate. The term $-\frac{\rho_0}{H}\omega^2\zeta$ in the first equation describes the source of the volume velocity in the gap which is formed by the plate oscillations. The term $p$ in the second equation describes the force acting upon the plate from the side of the liquid in the gap.

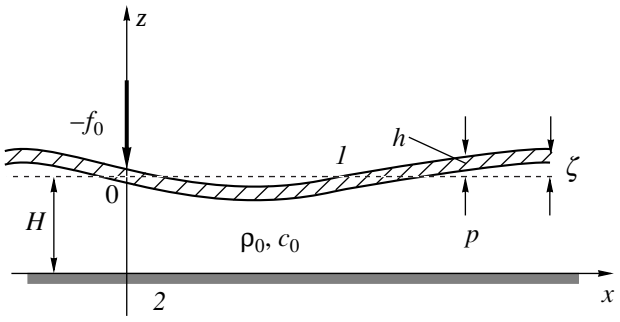


**Fig. 1.** Schematic diagram of the waveguide formed by (*1*) a plate and (*2*) a rigid plane.

1063-7710/00/4606-0635$20.00 © 2000 MAIK "Nauka/Interperiodica"

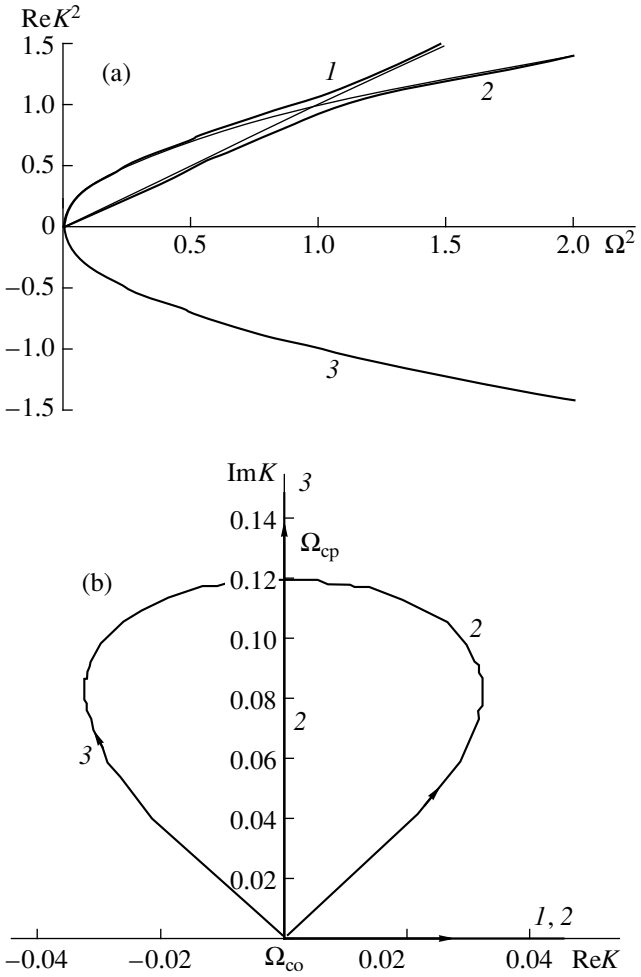


**Fig. 2.** (a) Frequency dependence of the real part of the squared wave number at $q = 10^{-2}$. The numbers *1–3* indicate the corresponding roots. (b) Positions of the roots of the dispersion equation in the complex plane depending on frequency at $q = 10^{-2}$. The arrows indicate the direction of the root motion with increasing frequency.

Using the Fourier transform with respect to the longitudinal coordinate $x$, the solution of the system of Eqs. (1) can be presented in an integral form

$$p(x) = \int_\Gamma \frac{\rho_0}{H}\frac{\omega^2}{\Delta}\hat{f}e^{ikx}dk,$$
$$\varsigma(x) = \int_\Gamma \frac{k^2-\omega^2}{\Delta}\hat{f}e^{ikx}dk, \quad (2)$$

where

$$\Delta = \left(k^2 - \frac{\omega^2}{c_0^2}\right)(Dk^4 - \rho h\omega^2) - \frac{\rho_0}{H} \quad (3)$$

and $\Delta = 0$ is the dispersion equation of the system of Eqs. (1). The contour of integration $\Gamma$ is drawn in a standard way; i.e., the poles located at the positive real half-axis are bypassed from below and those at the negative half-axis, from above.

As in other problems on flexural oscillations of thin plates in contact with a liquid (e.g., see [5–7]), it is convenient to use wave numbers and frequencies normalized to the wave number and frequency of coincidence, for which the phase velocity of the flexural wave in an unloaded plate coincides with the sound velocity in a liquid:

$$k_c = c_0\sqrt{\frac{\rho h}{D}}, \quad \omega_c = c_0^2\sqrt{\frac{\rho h}{D}}. \quad (4)$$

In terms of the dimensionless quantities $K = k/k_c$ and $\Omega = \omega/\omega_c$, the dispersion equation $\Delta = 0$ takes the form

$$(K^2 - \Omega^2)(K^4 - \Omega^2) - q\Omega^2 = 0. \quad (5)$$

The solutions $K(\Omega)$ to Eq. (5) depend on a single parameter

$$q = \frac{\rho_0}{\rho}\frac{1}{k_c h}\frac{1}{k_c H}, \quad (6)$$

which characterizes the degree of loading of the plate with the liquid layer. In the case of sound radiation by a thin plate into a halfspace, an analogous parameter is $\kappa = \rho_0/\rho k_c h$ [5–7], which is be a factor of $(k_c H)^{-1}$ less than the parameter $q$. In the problem formulation under study, we have $k_c H \ll 1$. This means that in the case of constant parameters of both the liquid and the plate, the loading of the plate with the liquid in the gap is greater than the loading with the liquid in the halfspace, i.e., $q \gg \kappa$.

The roots of the dispersion equation [Eqs. (3) and (5)] are simultaneously the poles of the integrands of solution (2) and determine the discrete spectrum of the eigenfunctions of system (1). The solution to Eq. (5), which is bicubic with respect to $K$, consists of three pairs of roots $\pm K_1$, $\pm K_2$, and $\pm K_3$. In the case of small load parameters, they can be associated with the corresponding roots of the dispersion equation of an unloaded plate and the roots of the dispersion equation of plane waves in an unbounded liquid medium.

Analysis shows that the pair of roots $\pm K_1$ is real in the entire frequency range. If the frequency tends to infinity for small load parameters $q$, the dispersion curve of these roots asymptotically tends to the dispersion curve of plane waves in an unbounded medium $K_1 \longrightarrow \Omega$, and the phase velocity tends to $c_0$ remaining slightly less than this asymptotic value (see Fig. 2a). At high frequencies, this provides an opportunity to formally attribute this wave to the class of the so-called "creeping" waves, which arise, for example, in the problems on sound radiation by a plate into a halfspace [6]. In the case of low frequencies $\Omega < 1$ for small $q$, this wave is close to the propagating flexural mode of an unloaded plate $K_1 \longrightarrow \sqrt{\Omega}$.

The frequency range for the pair of roots $\pm K_2$ can be split into three regions determined by two characteristic

frequencies $\Omega_{cp}$ and $\Omega_{co}$, $\Omega_{cp} < \Omega_{co}$. The frequency $\Omega_{co} = \sqrt{q}$ is the critical frequency of this waveguide for which $\pm K_2 = 0$. At frequencies higher than this, $\Omega > \Omega_{co}$, the roots $\pm K_2$ acquire purely real values. For $\Omega \longrightarrow \infty$, they asymptotically tend to the corresponding roots of the propagating flexural mode of the unloaded plate $K_2 \longrightarrow \sqrt{\Omega}$. Note that $\Omega_{cp}$ and $\Omega_{co}$ can be both higher and lower than the coincidence frequency $\Omega = 1$. In the case of a small load parameter $q$, when $\Omega_{co} \ll 1$, the curve $K_2(\Omega)$ is close to the dispersion curve of sound waves in an unbounded liquid $K_2 \approx \Omega$. Thus, with the transition through the coincidence frequency, the normal modes corresponding to the pairs of roots $\pm K_1$ and $\pm K_2$ exchange places. If, below the coincidence frequency, e.g., a propagating flexural wave of an unloaded plate corresponds to some of these normal modes, then, above the coincidence frequency, a plane wave in an unbounded liquid corresponds to it, and vice versa (Fig. 2a).

If the frequency becomes lower than the critical one $\Omega_{co}$, the roots $\pm K_2$ appear in the complex plane (Fig. 2b), and their normal modes become attenuating along the longitudinal *ox* axis. If the frequency decreases further, these roots stay at the imaginary axis, and, at the frequency $\Omega_{cp} \approx \frac{3\sqrt{3}}{2} q$ of the double root of Eq. (5) $K_{cp} \approx \sqrt{-\frac{3}{2}q}$, they merge with the corresponding roots of the pair $\pm K_3$. In the case of lower frequencies $0 < \Omega < \Omega_{cp}$, the roots of the pairs $\pm K_2$ and $\pm K_3$ are essentially complex and conjugate to each other, while their normal modes form a standing wave with the amplitude decreasing along the *ox* axis and with the total energy flux being equal to zero.

The roots of the pair $\pm K_3$ higher than the frequency of the double root $\Omega_{cp}$ lie on the imaginary axis. As the frequency increases, their magnitude also increases. At high frequencies, the asymptotic behavior of these roots corresponds to the attenuating modes of an unloaded plate $K_3 \longrightarrow i\sqrt{\Omega}$. For a wide waveguide with elastic boundaries, the root motion was considered in [8].

Let the force acting on the plate be a point force: $f = f_0\delta(x)$. According to the residue theorem, solution (2) can be represented in the form of the sum of normal modes propagating along the *ox* axis:

$$p(x) = q\Omega^2 \frac{f_0 k_c}{2\pi} \sum_i e^{iK_i X} R_i,$$
$$\zeta(x) = \frac{1}{\rho h \omega_c^2} \frac{f_0 k_c}{2\pi} \sum_i e^{iK_i X} (K_1^2 - \Omega^2) R_i, \quad (7)$$

where $X = k_c x$ is the dimensionless coordinate and $R_i$ are the factors related to the contribution of the residues of the integrand $(\rho h)^2 c_0^4 k_c^2 / D\Delta$ in the poles $K_i$:

$$R_i = 2\pi i \frac{1}{2K_i} \prod_{i \neq j} \frac{1}{K_i^2 - K_j^2}. \quad (8)$$

By virtue of the symmetry of the problem, we can restrict our consideration to the region of negative values of the $x$ coordinate. Here, Eqs. (7) and (8) involve only the roots $K_i$ of the dispersion equation (5) that have a positive imaginary part or lie on the positive real half-axis.

Using the representation of the field in the form of a sum of normal modes, i.e., Eq. (7), we write down the time-average total energy fluxes passing through the gap and plate cross-sections that are normal to the *ox* axis. According to the known expressions for the energy flux in a liquid and in a flexurally oscillating thin plate [9], we have

$$W_p = \frac{1}{2} \frac{f_0^2}{4\pi^2 \rho h c_0} q\Omega^3 \mathrm{Re} \sum_{i,j} R_i^* R_j K_j e^{i(K_j - K_i^*)X},$$
$$W_\zeta = \frac{1}{2} \frac{f_0^2}{4\pi^2 \rho h c_0} \Omega \mathrm{Re} \sum_{i,j} R_i^* R_j \quad (9)$$
$$\times (K_i^{*2} - \Omega^2)(K_j^2 - \Omega^2)(K_i^* + K_j) K_j^2 e^{i(K_j - K_i^*)X},$$

where $W_p$ is the energy flux in the gap and $W_\zeta$ is that in the plate. The sum of two these fluxes gives the total energy flux going out through the plate and the gap in the positive direction of the *ox* axis and equal to half of the total power emitted into the plate by the force applied to it:

$$W_f = 2W_f^{(1/2)}$$
$$= \frac{1}{2} \frac{f_0^2}{4\pi^2 \rho h c_0} 2\pi\Omega \mathrm{Im} \sum_i (K_i^2 - \Omega^2) R_i. \quad (10)$$

Let us consider the frequencies above the critical frequency of the waveguide $\Omega_{co}$. Apart from the normal mode of the invariably real root $K_1$, the wave corresponding to the root $K_2$ is also a propagating wave. The contribution of the attenuating wave $K_3$ to the total field (7) at large distances along the *ox* axis from the region of application of the point force, $|K_3|X \gg 1$, can be ignored, since the energy flux associated with it is equal to zero.

In the case of a small load parameter $q \ll 1$, the dispersion curves of the roots $K_1$ and $K_2$ are close to the corresponding dispersion curves of sound waves in an unbounded liquid and of flexural waves in the plate. Near the coincidence frequency $\Omega = 1$, the roots expe-

rience a small splitting, which depends on the parameter $q$. At the coincidence frequency, we have

$$K_{1,2} = 1 \pm \Delta K = 1 \pm \frac{1}{2}\sqrt{\frac{q}{2}}. \quad (11)$$

The values of the amplitudes of normal modes for a fixed frequency are completely determined by the position of the corresponding roots of the dispersion equation in the complex plane. Therefore, if $K_1$ and $K_2$ are located close to each other in the complex plane, e.g., at frequencies in the vicinity of the coincidence frequency (Fig. 2), the difference in the values of the amplitudes of their normal modes will also be small. The field given by Eqs. (7) and also the distribution of the energy fluxes (9) along the *ox*-axis have a pronounced periodic structure and represent contrast interference bands formed by two waves propagating with close velocities and having almost equal amplitudes.

In the general case, for an arbitrary frequency (above the critical one), the total energy flux of the waves $K_1$ and $K_2$ can be written in the form

$$W_{p,\zeta}(X, \Omega) = W^{(0)}_{p,\zeta}(\Omega) \mp \Delta W(\Omega)\cos 2\Delta K(\Omega) X. \quad (12)$$

Expanding it with respect to the small parameter $q$ at the frequency $\Omega = 1$, we obtain approximate expressions for the energy fluxes in the gap and in the plate

$$W_p \underset{\Omega=1}{=} \frac{1}{2}\frac{f_0^2}{16\rho h c_0}\left[1 + \frac{35}{32}q - \left(1 + \frac{19}{32}q\right)\cos\sqrt{\frac{q}{2}}X\right],$$
$$W_\zeta \underset{\Omega=1}{=} \frac{1}{2}\frac{f_0^2}{16\rho h c_0}\left[1 + \frac{17}{32}q + \left(1 + \frac{19}{32}q\right)\cos\sqrt{\frac{q}{2}}X\right]. \quad (13)$$

From these expressions and the more general expressions (12), it follows that the energy fluxes in the gap and in the plate consist of constant (with respect to the longitudinal $x$ coordinate) terms $W^{(0)}_p$ and $W^{(0)}_\xi$ and an interference term with the amplitude $\Delta W$ oscillating around them. The spatial period of these oscillations is equal to the doubled distance $d$ at which the energy flux in the plate or in the gap changes to its opposite value. At the coincidence frequency, we have

$$d = \frac{\pi}{2\Delta K} = \frac{\pi}{\sqrt{q/2}}. \quad (14)$$

The phase relations in Eq. (13) show that the spatial scale of "pumping" given by Eq. (14) is just the minimal length at which an efficient flow of power from the plate to the gap occurs with the increase in the distance along the longitudinal $x$ coordinate from the place of the point force application. Below, the quantity $d$ will be called the pumping length.

The amplitudes of the constant and the interference terms of the fluxes (13) in the zeroth order of smallness with respect to the load parameter $q$ are equal. This means that, under this approximation, the whole energy flux at the pumping length is transferred from the plate into the gap and back; i.e., in this sense, the energy emission from the plate into the gap is complete. However, the inclusion of the terms of the first order of smallness shows that, in reality, part of the flux can remain uninvolved in the process of pumping and, correspondingly, remain in the plate or in the gap. Although this part is proportional to $q$ and small, it is still nonzero. The quantity characterizing the degree of incompleteness of the energy transfer from the plate into the gap may be, for example, the ratio of the minimal (in the $X$ coordinate) flux in the gap given by Eqs. (13) to its maximal value:

$$V_p = \frac{W_p^{\min}}{W_p^{\max}} = \frac{W_p^{(0)} - \Delta W}{W_p^{(0)} + \Delta W} \underset{\Omega=1}{=} \frac{q}{4}. \quad (15)$$

A similar parameter $V_\zeta$ expressed through $W^{(0)}_\zeta$ and $\Delta W$ can be introduced for the plate. In the general case of load parameters $q$ that are not small, its value does not coincide with Eq. (15).

There is a certain correlation between the pumping length (14) and the incompleteness (15). If one of these parameters grows, then the other decreases, and vice versa. Therefore, for example, if it is necessary to emit energy from the plate into the gap at a smaller length $d$, then the degree of completeness of such emission will also be smaller. In its turn, a more complete emission will lead to a greater length at which it will be attained.

It is necessary to note that the minimal energy flux in the plate can be negative (directed in the negative direction of the $x$-axis), and the maximal energy flux in the gap can exceed half of the total power emitted by the force into the plate:

$$W_f \underset{\Omega=1}{=} \frac{1}{8}\frac{f_0^2}{\rho h c_0}\left(1 + \frac{13}{16}q\right). \quad (16)$$

The regions along the $x$ coordinate where this can occur are located symmetrically about the points of the minimal energy flux in the plate, $X = d(1 + 2n)$, $n \in Z$. The linear dimension of each of these regions is equal to

$$\delta = \frac{d}{2\pi}\sqrt{\frac{q}{2}} = \frac{1}{2}, \quad (17)$$

which is just a small part of the pumping length, and, as we can see, it is equal to half of the reduced wavelength $1/k_c$.

It is convenient to represent the distribution of energy fluxes in these regions in the following way. A vortex flow with a small amplitude proportional to $q$ is superimposed on the constant (with respect to the coordinate) energy fluxes in the plate and in the gap, the

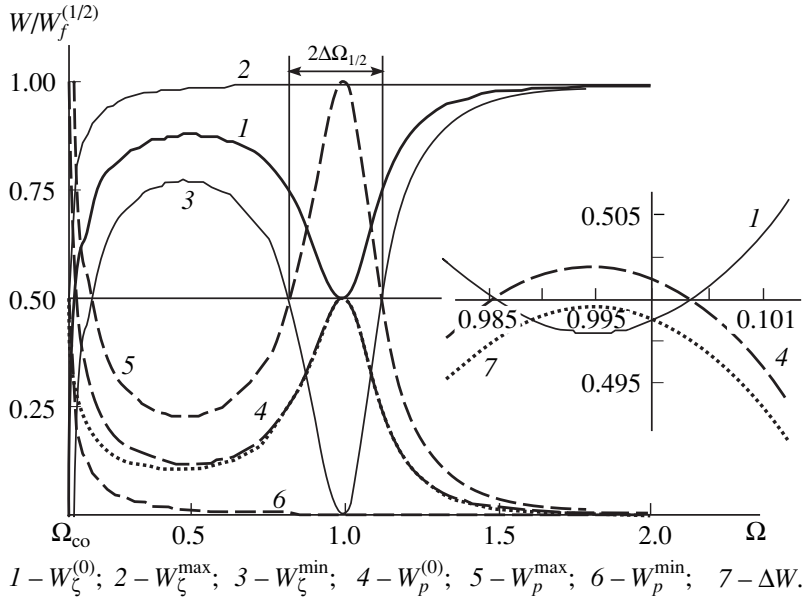


**Fig. 3.** Ratios of amplitudes of the constant and interference terms and the minimal and maximal total energy fluxes in the plate and in the gap to half of the total power as functions of frequency at $q = 10^{-2}$. The inset demonstrates the corresponding curves near the coincidence frequency $\Omega = 1$ and $W/W_f^{(1/2)} = 1/2$.

values of which are equal to zero and half of the total power $W_f$ given by Eq. (16), respectively:

$$W^g_{p,\varsigma} = \pm\frac{1}{2}\frac{f_0^2}{16\rho hc_0}\frac{q}{16}\left(1 - \frac{\Delta X^2}{\delta^2}\right),$$
$$W^g_{\perp p,\varsigma} = \frac{\partial W^g_{p,\varsigma}}{\partial x} = \mp\frac{1}{2}\frac{f_0^2}{16\rho hc_0}k_c\frac{q}{4}\frac{\Delta X}{\delta}, \qquad (18)$$

where $\Delta X = X - X_d$ ($-\delta < \Delta X < +\delta$) is the deviation of the longitudinal $X$ coordinate from the points $X_d$ corresponding to the minimal value of the flux in the plate, $W^g_p$ is the energy flux in the gap along the longitudinal *ox*-axis, $W^g_{\perp p}$ is the density of the energy flux directed along the transverse *oz*-axis from the plate into the gap through their interface, and $W^g_\zeta$ and $W^g_{\perp\zeta}$ are the corresponding values for the plate.

Let us investigate the distribution of the energy fluxes in the plate and in the gap for the case of frequency deviation from the coincidence frequency. It is possible to demonstrate that, at high frequencies $\Omega \gg 1$, almost the whole total energy flux carried in the positive direction of the *ox*-axis through the plate and the gap is concentrated in the plate itself (Fig. 3). By virtue of the smallness of the interference term at these frequencies, the difference of this flux from its average value is insignificant, and the degree of completeness of energy pumping from the plate to the gap is small.

As the frequency decreases and approaches the coincidence frequency $\Omega = 1$, the values of amplitudes of the interference and constant terms of the energy flux in the gap, $\Delta W$ and $W_p^{(0)}$, increase until they attain approximately half of the value of the total flux through the plate and the gap and become equal to the constant term $W_\zeta^{(0)}$ of the flux in the plate. Due to the approximate equality of these terms in the vicinity of these frequencies, the minimal fluxes in the plate $W_\zeta^{min}$ and the gap $W_p^{min}$ are close to zero, and the maximal fluxes $W_\zeta^{max}$ and $W_p^{max}$ are close to unity. Then, the energy pumping between the plate and the gap is almost complete. A further decrease in the frequency leads to a decrease in the degree of pumping completeness.

A detailed analysis of the frequency dependences of the terms of fluxes (12) divided by half of the total power (10) shows that their extremums near the coincidence frequency are attained not exactly at this frequency, but are somewhat shifted to lower frequencies (Fig. 3). In the general case, these frequencies, as well as the frequencies of extremums of the minimal and maximal fluxes in the plate and the gap, are different. However, to the first order of smallness with respect to $q$, all of them are equal and take the following value:

$$W_{ext} = 1 - q/2. \qquad (19)$$

The total energy fluxes (12) in the gap and the plate at this frequency are expressed as

$$W_{p\,\Omega=\Omega_{\text{ext}}} = \frac{1}{2}\frac{f_0^2}{16\rho h c_0}\left[1 + \frac{47}{32}q - \left(1 + \frac{31}{32}q\right)\cos\sqrt{\frac{q}{2}}X\right], \quad (20)$$

$$W_{\zeta\,\Omega=\Omega_{\text{ext}}} = \frac{1}{2}\frac{f_0^2}{16\rho h c_0}\left[1 + \frac{21}{32}q + \left(1 + \frac{31}{32}q\right)\cos\sqrt{\frac{q}{2}}X\right],$$

while the total power (10) emitted by the force into the plate is

$$W_{f\,\Omega=\Omega_{\text{ext}}} = \frac{1}{8}\frac{f_0^2}{\rho h c_0}\left(1 + \frac{17}{16}q\right). \quad (21)$$

The values of the roots $K_1$ and $K_2$ and their splitting $\Delta K$ at the frequency corresponding to the extremums differ from the analogous values at the coincidence frequency (11) only in higher orders of smallness with respect to $q$. The pumping length for $\Omega_{\text{ext}}$ can be considered equal to $d$ determined by Eq. (14) with the same accuracy. As one can see from expressions (20) for fluxes, the constant and interference terms, $W_p^{(0)}$ and $\Delta W$, experience equal increases relative to their values at the coincidence frequency, and, therefore, the incompleteness of pumping for the gap $V_p$ at the frequency of extremums coincides with its value for $\Omega = 1$, Eq. (15).

The appearance of a vortex energy flux near the points of minimal $W_\zeta$ occupies only a limited frequency band near $\Omega_{\text{ext}}$ (Fig. 3) with the half-width

$$\Delta\Omega_g = \sqrt{5}q/2. \quad (22)$$

Comparison of Eqs. (19) and (22) shows that, for small $q$, the coincidence frequency always falls into the considered frequency band $2\Delta\Omega_g$.

In conclusion, we consider a numerical example. Let us take an aluminum plate of thickness $h = 0.80$ mm positioned at the distance $H = 0.75$ mm from a rigid plane. The medium filling the gap is air. The coincidence frequency of such a combination is equal to 15 kHz, and the wavelength corresponding to it is 2.3 cm. The ratio of the wavelength to the plate thickness is approximately equal to 30. As was demonstrated in [10], already at the values of this ratio exceeding about 10, the classical equations (1) describe the frequency behavior of the zeroth mode of the flexural vibrations of a plate with an acceptable accuracy. Thus, in our case, at the coincidence frequency, as well as at lower and somewhat higher frequencies, the plate can be really considered as thin. The dimensionless load parameter $q$ takes a small value of $1.0 \times 10^{-2}$.

The pumping length $d$ of the waveguide is equal to 16 cm, and the half-bandwidth is $\Delta\Omega_{1/2} = 2.3$ kHz, which constitutes 0.15 of the coincidence frequency. The frequency shift of extremums $1 - \Omega_{\text{ext}}$ is equal to 79 Hz. One can ignore this shift in comparison with $\Delta\Omega_{1/2}$. The half-bandwidth of the vortex flow $\Delta\Omega_g$ is of the same order of magnitude.

## REFERENCES


1. S. D. Danilov and M. A. Mironov, Akust. Zh. **32**, 387 (1986) [Sov. Phys. Acoust. **32**, 240 (1986)].
2. M. A. Mironov and D. E. Orekhov, in *Proceedings of the Second International Symposium on Transport Noise and Vibration, St. Petersburg, 1994*, p. 97.
3. M. A. Mironov and D. E. Orekhov, Akust. Zh. **43**, 531 (1997) [Acoust. Phys. **43**, 455 (1997)].
4. L. Huang, J. Acoust. Soc. Am. **106**, 1801 (1999).
5. L. Ya. Gutin, Akust. Zh. **10**, 431 (1964) [Sov. Phys. Acoust. **10**, 369 (1964)].
6. A. D. Stuart, J. Acoust. Soc. Am. **59**, 1160 (1976).
7. D. G. Crighton, J. Sound Vib. **63**, 225 (1979).
8. Yu. A. Lavrov, Akust. Zh. **36**, 308 (1990) [Sov. Phys. Acoust. **36**, 167 (1990)].
9. V. N. Krasil'nikov, Akust. Zh. **6**, 220 (1960) [Sov. Phys. Acoust. **6**, 216 (1960)].
10. R. Mindlin, J. Appl. Mech. **18**, 31 (1951).


*Translated by M. Lyamshev*

*Acoustical Physics, Vol. 46, No. 6, 2000, pp. 641–647. Translated from Akusticheskiĭ Zhurnal, Vol. 46, No. 6, 2000, pp. 732–739.*


# The Role of the Wake in the Sound Scattering by a Moving Body

**V. N. Alekseev and A. G. Semenov**

*Andreev Acoustics Institute, Russian Academy of Sciences, ul. Shvernika 4, Moscow, 117036 Russia*

*e-mail: bvp@akin.ru*

Received October 18, 1999

**Abstract**—The propagation of sound is considered in the vicinity of an axially symmetric body moving in a viscous fluid so that a laminar wake is formed behind it. The sound scattering amplitude is determined as the function of the characteristic parameters of the fluid for an arbitrary ratio between the characteristic size of the body and the sound wavelength. The important role of the wake at high Reynolds numbers is demonstrated, and the specific features of the angular dependence of the scattering amplitude are analyzed. *© 2000 MAIK "Nauka/Interperiodica".*

The scattering of sound by moving bodies, suspended particles, and inhomogeneities is one of the topical, as well as complicated, problems in acoustics of moving media. Such problems arise in different fields of engineering. The solution of this problem is of fundamental value for calculating the laws of sound propagation and attenuation in the ocean and in the atmosphere, as well as for the assessment of the efficiency of some chemical and thermal processes in power or biological systems. Many recent publications were concerned with theoretical and experimental studies of this problem [1, 2]. The basic phenomenon considered in these publications is the scattering of sound by a body or a particle of a complex shape moving in a viscous fluid flow at different flow conditions. In our previous papers [3–8], we considered some reference problems concerned with the sound propagation near spherical bodies moving steadily in ideal and viscous fluids. We assumed that the velocity of the body motion $\mathbf{V}$ was well below the sound velocity in the fluid $c$ and that a moving body produced in the surrounding fluid a concurrent flow $\mathbf{U}(\mathbf{r}, t)$ whose velocity inhomogeneities formed the centers of additional sound scattering. Therefore, the sound propagation near a moving body was described not by the common classical wave equation, but by the more general Lighthill equation [9]:

$$\frac{\partial}{\partial t}\left(\Delta p - \frac{1}{c^2}\frac{\partial^2 p}{\partial t^2}\right) = 2\frac{\partial}{\partial x_\alpha}\left(U_\beta \frac{\partial^2 p}{\partial x_\alpha \partial x_\beta}\right). \qquad (1)$$

In studying the sound scattering by moving bodies [3–8], we showed that the total field $p(\mathbf{r}, t)$ can be represented as usual in the form of the sum of the incident and scattered fields, and the scattered field $p_s(\mathbf{r}, t)$, in its turn, can be separated into two components one of which is related to the sound scattering by the moving body, $p_{sp}(\mathbf{r}, t)$, and the other is related to the sound scattering by the inhomogeneities of the concurrent flow, $p_{sf}(\mathbf{r}, t)$. However, it was noted that such a separation is a matter of convention, and, to some extent, it is ambiguous. In fact, the presence of a scattering body always leads to the presence of waves reflected from it, and, when propagating in the medium, these waves may be additionally scattered by the inhomogeneities of the concurrent flow. Nevertheless, for computational purposes, it is convenient to separate the component $p_{sf}(\mathbf{r}, t)$ related to the scattering of the incident wave by the flow. In addition, in some cases, e.g., in the case of acoustically transparent bodies or localized vortices moving in an unbounded fluid, the scattering of sound by the bodies is basically absent and occurs exclusively by the inhomogeneities of the fluid flow.

A mathematically rigorous and detailed study was carried out for the scattering of low-frequency sound by a sphere of radius $a$ whose center $\mathbf{r}_0(t)$ was moving in an ideal fluid with a constant velocity $\dot{\mathbf{r}}_0(t) = \mathbf{V}$. On the condition that the flow about the body was a potential one, the velocity distribution $\mathbf{U}(\mathbf{r}, t)$ in the fluid was described by the widely known formula [10]

$$\mathbf{U}(\mathbf{r}, t) = a^3 \frac{3(\mathbf{V}\mathbf{n})\mathbf{n} - \mathbf{V}}{2|\mathbf{r} - \mathbf{r}_0|^3}; \quad (|\mathbf{r} - \mathbf{r}_0| \geq a), \qquad (2)$$

where the unit vector $\mathbf{n} = (\mathbf{r} - \mathbf{r}_0)/|\mathbf{r} - \mathbf{r}_0|$ was directed toward the observation point $\mathbf{r}$. The total scattering cross-section $\sigma$ calculated for the sound scattering by a perfectly rigid sphere had a rather simple form [4]:

$$\sigma = \frac{7}{9}\pi k_0^4 a^6 (1 - 6\mathbf{M}\mathbf{n}_0); \quad (ka \ll 1). \qquad (3)$$

Here, $\mathbf{M} = \mathbf{V}/c$ is the Mach vector, and $\mathbf{n}_0$ is the unit vector along the direction of the incident sound wave.

From the derivation of Eq. (3), it followed that the absolute corrections that should be introduced in the scattering amplitude obtained for a stationary sphere in order to allow for both the sphere motion and the sound scattering by the inhomogeneities of the concurrent flow are of the order of $k^2a^3M$. Hence, it follows that, when the Mach number $M$ and the parameter $ka$ are small, these corrections are very small, and their relative contribution to the total scattering amplitude and the total scattering cross-section of low-frequency sound is proportional to the Mach number $M$. On the other hand, in [6] we carried out similar calculations for a moving sphere whose radius was much greater than the incident sound wavelength ($ka \gg 1$). The solution of Eq. (1) with the same sound velocity distribution [given by Eq. (2)] yielded the following expression for the total scattering cross-section [8]:

$$\sigma = 2\pi a^2[1 + C_0 ka(\mathbf{M}\mathbf{n}_0)]; \quad (ka \gg 1), \qquad (4)$$

where $C_0$ is a dimensionless quantity of the order of unity and, to the zeroth approximation in $M$, this quantity is independent of the Mach number and the dimensionless parameter $ka$. We note the qualitative difference between Eqs. (3) and (4). In the case of the low-frequency sound scattering, the relative correction to the scattering cross-section given by Eq. (3) is proportional to the small Mach number and, hence, for $M \ll 1$, the correction is small. For a large-radius sphere ($ka \gg 1$), the corresponding correction in Eq. (4) is proportional to the product of the small Mach number $M$ by the large parameter $ka$. In the latter case, the correction may be comparable to unity and, hence, in the general diffraction problem, the flow should necessarily be taken into account.

An analysis of the results obtained earlier [4, 6, 11] showed that the features of the fluid flow both near the sphere and away from it strongly affect the character of the sound scattering by the flow. In this connection, we calculated the scattering amplitude for sound scattered by a rigid sphere moving in a viscous fluid at low Reynolds numbers [5]. It has been known [10] that, in the case of a Stokes flow about a sphere, the velocity of the concurrent flow decreases more slowly with distance from the body, as compared to the case of a potential flow. In contrast to the flow described by Eq. (2), the velocity of the fluid decreases with distance as $1/r$, and such a distribution of the flow velocity extends to distances of the order of $\sim a/\mathrm{Re}$, where $\mathrm{Re} = aV/\nu$ is the Reynolds number and $\nu$ is the kinematic viscosity of the fluid. The calculation of the sound scattering amplitude for such a flow [5] showed that the generation of vorticity in the medium and a formal increase in the scattering region could give rise to a considerable increase in the scattering amplitude and the scattering cross-section. This paper is an attempt to take into account the real character of the fluid flow about a moving body with less strict limitations on the shape of the body and the type of its motion.

We assume that an axially symmetric body with a characteristic size $a$ moves in a viscous fluid at a constant velocity $\mathbf{V} = \dot{\mathbf{r}}_0(t)$. At large distances behind the body, the motion of the fluid has certain specific features [10, 12]. In the case of moderate Reynolds numbers, the velocity of the fluid far behind the body is nonzero only within a relatively narrow region. This region is called the wake, and the fluid flow in the wake is commonly considered to be laminar for the Reynolds numbers up to $\mathrm{Re} \sim 10^4$. The fluid particles falling in this region are those moving along the streamlines passing the body at relatively small distances from its surface. The streamlines separated from the body surface form a boundary surface that divides the whole region of the fluid flow into two parts. In the outer region, the flow past the body can be considered as a potential one, as in the case of an ideal fluid flow about the body. In the region within the wake, the flow is characterized by vorticity. For simplicity, we assume that the axially symmetric body moves along its symmetry axis, which will serve as the $x$ axis of our coordinate system. In this case, the forces that act on the body in the transverse direction are absent, and the body experiences only the drag force $F_x$. In the coordinate system fixed to the body, we select the $x$ axis along the direction of the velocity $\mathbf{V}$ of the fluid flowing toward the body from infinity. When the characteristic size of the body is small relative to the distance $x$, the velocity distribution $U_x = V + v_x$ formed within the wake sufficiently far from the body is expressed as [10]

$$v_x = -\frac{F_x}{4\pi\rho\nu x}\exp\left\{-\frac{V(y^2 + z^2)}{4\nu x}\right\}. \qquad (5)$$

Here, $\rho$ is the fluid density and $F_x$ is the drag force acting on the body in the direction of the flow around it. According to [10], the drag force can be expressed through the velocity $v_x$:

$$F_x = -\rho V\int v_x dydz. \qquad (6)$$

As long as the boundary layer remains laminar, the flow pattern observed near the body at large Reynolds numbers is practically independent of the viscosity. From the dimensional considerations, one can obtain the following expression for the drag force [10]:

$$F_x = C_x\frac{\rho V^2}{2}S. \qquad (7)$$

Here, $S$ is the cross-sectional area of the body with respect to the direction of its motion and $C_x$ is the drag coefficient, which depends on the body shape. In the general case, the dimensionless coefficient $C_x$ also depends on the Reynolds number Re. Recall that for $\mathrm{Re} \ll 1$, i.e., for a Stokes flow, the drag coefficient is inversely proportional to the Reynolds number. With increasing Re, the decrease in $C_x$ becomes slower and corresponds to a weaker dependence than 1/Re. The

decrease occurs up to the Reynolds numbers $\mathrm{Re} \approx 5 \times 10^3$, and, somewhere in this region, the coefficient $C_x$ reaches its minimal value, after which the function $C_x(\mathrm{Re})$ exhibits some growth. In the region of Reynolds numbers $10^4$–$10^5$, the drag coefficient is practically constant and approximately equal to 0.5. At $\mathrm{Re} \approx (2\text{–}3) \times 10^5$, a drag crisis occurs, and $C_x$ suffers a four- to fivefold drop [10].

We note that, strictly speaking, Eq. (5) is valid only far away from the body when $r \gg a$. In the vicinity of the body, Eq. (5) does not hold. This specifically follows from the fact that the direct application of Eq. (5) leads to the violation of the boundary condition set at the body surface, $\mathbf{vn} = \mathbf{Vn}$. However, as will be seen from the following calculations, the maximal contribution to the integrals that determine the scattering amplitude caused by the flow inhomogeneities is made by the regions lying far away from the body. Therefore, below we will assume that, to the first approximation, Eq. (5) can be used for estimating the desired scattering amplitude in the whole range of distances $r$ up to the body boundary.

As for the velocity distribution in the fluid outside the wake, it can be considered as a potential one. However, unlike an ideal fluid flow, which occurs in the vicinity of the body without the separation of the streamlines from the body surface, the distribution of the velocity outside the wake contains a monopole component in addition to the dipole one corresponding to Eq. (2). Restricting our consideration to the monopole and dipole terms that are characterized by the slowest decrease at large distances, we can write the expression for the velocity outside the wake produced by an axially symmetric body in the form

$$\mathbf{v} = A_0 \frac{\mathbf{n}}{|\mathbf{r} - \mathbf{r}_0(t)|^2} + A_1 \frac{3(\mathbf{Vn})\mathbf{n} - \mathbf{V}}{|\mathbf{r} - \mathbf{r}_0(t)|^3} + \ldots, \quad \text{where } \mathbf{n} = \frac{\mathbf{r} - \mathbf{r}_0(t)}{|\mathbf{r} - \mathbf{r}_0(t)|}. \tag{8}$$

Here, the unknown coefficients $A_0$ and $A_1$ are determined as usual from the boundary conditions. The first coefficient $A_0$ is determined from the condition that the total flow through a large-radius sphere, as well as through any closed surface, must be equal to zero. The corresponding calculations with the use of Eqs. (5) and (8) yield $A_0 = F_x/(4\pi\rho V)$ [10]. Away from the axially symmetric body, the potential component of the fluid flow is of a radial character and has the most simple form:

$$\mathbf{v} = \frac{F_x}{4\pi\rho V r^2}\mathbf{n}. \tag{9}$$

We note that the velocity distribution Eq. (9), as well as formula (5), is not valid in the immediate vicinity of the body surface. However, if we assume that the axially symmetric body is a solid sphere of radius $a$ with the boundary condition $\mathbf{vn} = \mathbf{nV}$ being fulfilled at its surface, we can determine the unknown coefficient $A_1$. The calculations show that, in this case, we have $A_1 = a^3/2$, and the dipole component in the general Eq. (8) has a form similar to Eq. (2), which is valid in the case of an ideal fluid. It should be noted that solutions (8) and (9) are valid in the angular region $\theta \gg \theta_0 = \sqrt{\nu/(rV)}$, and expression (5) refers to the region $\theta \ll 1$; in the general case, when the inequalities $\sqrt{\nu/(rV)} \ll \theta \ll 1$ are valid, these regions can overlap.

Going back to the problem on the sound scattering by the flow generated in the vicinity of an axially symmetric moving body, we note that now the process will be formally described in terms of the Lighthill equation (1). We assume that the velocity distribution $\mathbf{U}(\mathbf{r}, t) = \mathbf{V} + \mathbf{v}$ is approximately described by Eqs. (5) and (8) and that a plane monochromatic wave of the type $p_i(\mathbf{r}, t) = p_0 \exp(i\mathbf{k}_0\mathbf{r} - i\omega_0 t)$ is incident on the body from infinity in the direction $\mathbf{n}_0$. The wave vector $\mathbf{k}_0$ is directed along the unit vector $\mathbf{n}_0$, and its magnitude is related to the sound frequency $\omega_0$ and the sound velocity in the fluid by the common formula $k_0 = \omega_0/c$. Since the body under consideration moves in the fluid with a constant velocity, it is convenient to solve the problem in the moving coordinate system in which the center of gravity of the body is at rest: $\mathbf{r}' = \mathbf{r} - \mathbf{r}_0(t)$. In this coordinate system, the coefficients of the transformed Eq. (1) become constant, i.e., time-independent, and the time dependence is retained only in the formulation of the boundary condition at infinity for the incident wave. As we change to the moving coordinate system, the field of the plane monochromatic wave is transformed to a sound wave of a similar form, $p_i(\mathbf{r}', t) = p_0 \exp(i\mathbf{k}_0\mathbf{r}' - i\omega t)$, but with another frequency. The new sound frequency $\omega$ is shifted relative to the initial frequency $\omega_0$ by a small value proportional to the Mach number: $\omega_0(1 - \mathbf{Mn}_0)$. The time dependence of the sought-for sound pressure in the moving coordinate system is determined by the temporal factor of the type $\exp(-i\omega t)$, and it will be omitted in the following calculations (as usual).

Using the relation between the sound pressure and the velocity and performing simple transformations, we represent Eq. (1) in the moving coordinate system:

$$\Delta' p + k^2 p = \frac{2i}{\omega}\frac{\partial}{\partial x'_\alpha}\left[(U_\beta - V_\beta)\frac{\partial^2 p}{\partial x'_\alpha \partial x'_\beta}\right]. \tag{10}$$

For simplification, in what follows, we omit the primes marking the coordinate $\mathbf{r}'$. However, it should be remembered that all results obtained below will be valid only in the moving coordinate system, and, in the final formulas, it will be necessary to formally replace the coordinate $\mathbf{r}$ by $\mathbf{r} - \mathbf{r}_0(t)$.

We consider Eq. (10) in combination with the condition at infinity and seek the solution to it in the form of the sum of the incident and scattered waves:

$$p(\mathbf{r}) = p_0(e^{ik_0\mathbf{n}_0\mathbf{r}} + P_s e^{ik\mathbf{r}\mathbf{M}}). \quad (11)$$

Here, $k$ is the new wave number related to the Doppler frequency $\omega$ by the formula $k = \omega/c$, and $P_s$ is the so-called gauge pressure (by analogy with the gauge potential in the theory of scattering). Assuming that $P_s$ is proportional to the hydrodynamic Mach number $M = V/c$ and substituting solution (11) into Eq. (10), we obtain that, correct to the terms linear in $M$, the field $P_s$ satisfies the following equation [8]:

$$\Delta P_s + k^2 P_s = -\frac{2ik_0^2}{\omega} n_{0\alpha} n_{0\beta} \frac{\partial}{\partial x_\alpha}(v_\beta e^{ik\mathbf{n}_0\mathbf{r}}) + \frac{2i}{\omega}\frac{\partial}{\partial x_\alpha}\left(v_\beta \frac{\partial^2 P_s}{\partial x_\alpha \partial x_\beta}\right). \quad (12)$$

In the general case, the scattered field $P_s$ is a sum of the field $P_{sp}$ scattered by the moving body and the field $P_{sf}$ scattered by the concurrent flow. Above, we already mentioned that such a separation is a matter of convention. The scattering by the surface of the moving body, $P_{sp}$, was studied in detail in our previous papers [4, 6, 7], and here we will not consider the characteristics of this component. Below, we will concentrate on the field $P_{sf}$ scattered by the concurrent flow and reveal its specific features. In fact, by the field $P_{sf}$ we mean an imaginary field formed as a result of the scattering of incident sound by the flow as though the body generating the concurrent flow outside the sphere were absent.

Using Green's function for the free space, we represent the approximate solution to Eq. (12) in the form of the Born integral. The first term of the perturbation series expansion without regard for the wave reradiation by the moving body surface has the form

$$P_s \approx \frac{ik_0 n_{0\alpha} n_{0\beta}}{2\pi c}\int d^3 r_1 \frac{e^{ik|\mathbf{r}-\mathbf{r}_1|}}{|\mathbf{r}-\mathbf{r}_1|}\frac{\partial}{\partial x_{1\alpha}}(v_\beta e^{ik_0\mathbf{n}_0\mathbf{r}_1}). \quad (13)$$

The integration in this formula is performed over the whole region occupied by the flow. As usual, we consider the behavior of this integral in the far wave zone and perform the conventional transformation of Green's function. Then, we take the resulting integral by parts and use the known Gauss formula for converting the volume integrals into surface ones. Here, it should be noted that, because of the aforementioned weak velocity decrease with distance from the body, the integral over an infinitely distant surface is nonzero and in the general case it should be taken into account. After the described transformations, we express the field $P_s$ through the scattering amplitude $f_f$, which is the factor multiplying the divergent spherical wave in the expression $P_s = (f_f/r)\exp(ikr)$:

$$f_f(\mathbf{n}, \mathbf{n}_0) = -\frac{k_0^2(\mathbf{n}\mathbf{n}_0)}{2\pi c}\int_V d^3 r_1 (\mathbf{v}\mathbf{n}_0) e^{i\mathbf{q}\mathbf{r}_1} - \frac{ik_0}{2\pi c}\int_{S_1, S_2} (\mathbf{dS}_{1,2}\mathbf{n}_0)(\mathbf{v}\mathbf{n}_0) e^{i\mathbf{q}\mathbf{r}_1}. \quad (14)$$

Here, the unit vector $\mathbf{n} = \mathbf{r}/r$ characterizes the direction of the scattered wave, and the wave vector $\mathbf{q} = k(\mathbf{n}_0 - n)$ has the physical meaning of the "momentum" transferred from the wave to the medium. The magnitude of the vector $\mathbf{q}$ is $q = 2k\sin(\vartheta/2)$, where $\vartheta$ is the scattering angle determined from the equality $\cos\vartheta = \mathbf{n}\mathbf{n}_0$. To simplify the following calculations, we assume that the body has the form of a solid sphere of radius $a$. Then, the integration in the second integral on the right-hand side of Eq. (14) will be performed over two spherical surfaces: the surface of the solid sphere $S_1$ and the infinitely distant spherical surface $S_2$. The normals to the surface elements $\mathbf{dS}_1$ and $\mathbf{dS}_2$ are directed toward each other and toward the fluid volume enclosed between these two surfaces.

As was mentioned above, the integration in the first term on the right-hand side of Eq. (14) is performed over the whole region occupied by the flow. We first calculate the part of this integral that is determined by the fluid outside the wake. Since, in this region, the velocity distribution $\mathbf{v}$ is of a potential type and is determined by Eq. (9), the corresponding integral can be represented in the form

$$I_v^{(1)} = \frac{F_x}{4\pi\rho V}\int_a^\infty dr \int d\Omega (\mathbf{n}\mathbf{n}_0) e^{irq_\alpha n_\alpha}. \quad (15)$$

Here, the inner integral over the spherical angles is calculated as in [9] by differentiating with respect to the parameter $irq_\alpha$. Since the inner integral has no singularities and the angle $\theta_0 = \sqrt{a/(r\,\mathrm{Re})}$ is small, the integration over the solid angle $d\Omega$ can be extended to the integration over the whole region $4\pi$. In this case, the inner integral is easily calculated and proves to depend exclusively on the wave vector magnitude $\mathbf{q} = k(\mathbf{n}_0 - \mathbf{n})$. In differentiating the resulting expression with respect to the components of the vector $\mathbf{q}$, it is necessary to follow the rule $\partial f(q)/\partial q_\alpha = (q_\alpha/q)(df/dq)$. Simple calculations show that the integral sought in Eq. (15) is equal to

$$I_v^{(1)} = \frac{iF_x}{2k\rho V}\frac{\sin(qa)}{(qa)}. \quad (16)$$

According to the general formula (14), the resulting expression (16) contributes to the scattering amplitude

for the sound scattering by the fluid flow [Eq. (14)], and the corresponding term has the form

$$f_v^{(1)} = -i\frac{C_x}{4}ka^2M(\mathbf{nn}_0)\frac{\sin(qa)}{(qa)}. \quad (17)$$

If for the velocity distribution we use the more general Eq. (8), we take the expression for the velocity **v** in the form of Eq. (2) and, for the volume integral given by Eq. (16), we obtain an additional term, which was calculated in our previous paper [8] and was found to be equal to

$$I_v^{(2)} = \pi a^3[3(\mathbf{Vn}) - (\mathbf{Vn}_0)]\frac{J_1(qa)}{(qa)}. \quad (18)$$

Here, $j_1(z) = -d/dz(\sin z/z)$ is the first-order spherical Bessel function. The corresponding term in the scattering amplitude determined by Eq. (14) has the form [8]

$$f_v^{(2)} = \frac{1}{2}k^2a^3[(\mathbf{Mn}_0) - 3(\mathbf{Mn})](\mathbf{nn}_0)\frac{j_1(qa)}{(qa)}. \quad (19)$$

Now, we calculate the part of the volume integral corresponding to the flow region occupied by the laminar wake. For this purpose, we take the velocity distribution within the wake in the form of Eq. (5). Then, the integral sought will have the form

$$I_v^{(3)} = -\frac{F_x}{4\pi\rho V\nu}(\mathbf{n}_0\mathbf{V})\int_a^\infty \frac{dx}{x}I(x, q_y)I(x, q_z)e^{iq_xx}. \quad (20)$$

For an axially symmetric flow, the inner integrals with respect to the *y* and *z* coordinates are of the same type, and, because of the narrowness of the wake and the fast decay of the integrands, the integration regions for these integrals can be extended to infinity. The corresponding calculations show that the integrals $I(x, q_y)$ and $I(x, q_z)$ are expressed as

$$I(x, q_y) = \int_{-\infty}^{\infty} dy\exp\left(-\frac{y^2V}{4x\nu} + iyq_y\right) = \sqrt{\frac{4\pi x\nu}{V}}\exp\left(-\frac{x\nu q_y^2}{V}\right). \quad (21)$$

We substitute these integrals in Eq. (20) and, upon integrating with respect to the longitudinal *x* coordinate, we obtain

$$I_v^{(3)} = -\frac{F_x}{\rho V^2}(\mathbf{n}_0\mathbf{V})\int_a^\infty dxe^{x(iq_x - \nu q_\perp^2/V)} = \frac{aF_x}{\rho V^2}(\mathbf{n}_0\mathbf{V})\frac{\exp(iaq_x - a^2q_\perp^2/\mathrm{Re})}{iaq_x - a^2q_\perp^2/\mathrm{Re}}. \quad (22)$$

Here, $q_x$ and $q_\perp = \sqrt{q_y^2 + q_z^2}$ are the longitudinal and transverse components of the wave vector $\mathbf{q} = k(\mathbf{n}_0 - \mathbf{n})$ with reference to the direction of the body motion. The contribution of the volume integral given by Eq. (22) to the total scattering amplitude (14) is as follows:

$$f_v^{(3)} = -\frac{C_x}{4}k^2a^3(\mathbf{Mn}_0)(\mathbf{nn}_0) \times \frac{\exp(iaq_x - q_\perp^2a^2/\mathrm{Re})}{iaq_x - q_\perp^2a^2/\mathrm{Re}}. \quad (23)$$

Now, we proceed to calculating the surface integrals in Eq. (14). As above, we divide each of the spherical surfaces, $S_1$ and $S_2$, into two parts. One part of each surface will bound the region of the potential flow, and the other part will bound the region of the vorticity flow, i.e., the wake. First, we take the velocity distribution outside the wake in the form of Eq. (9) and, using the method of differentiation with respect to a parameter, calculate each of the surface integrals over the corresponding regions. As above, taking into account the narrowness of the wake and the absence of singularities in the integrand, we extend the integration over the solid angle to the integration over the whole region $4\pi$. In this case, one can easily show that, with the velocity distribution (9), the second integral involved in Eq. (14) and taken over the entire body surface $S_1$ is equal to

$$I_s^{(1)} = \frac{F_x}{\rho V}\left[\frac{j_1(qa)}{(qa)} - (\mathbf{n}_0\mathbf{q}a)^2\frac{j_2(qa)}{(qa)^2}\right]. \quad (24)$$

One can see that, when the radius of the surface grows infinitely, the latter expression tends to zero. This means that a similar integral taken over an infinitely distant surface $S_2$ is equal to zero. Thus, the contribution of the surface integrals (24) to the total scattering amplitude has the form

$$f_s^{(1)} = -i\frac{C_x}{4}ka^2M \times\left[\frac{j_1(qa)}{(qa)} - k^2a^2(1 - \mathbf{nn}_0)^2\frac{j_2(qa)}{(qa)^2}\right]. \quad (25)$$

Now, we determine the expression for the corresponding term in expression (14) in the case of the velocity distribution in the form of Eq. (2). The calculations performed in [8] for the corresponding surface integral show that, in this case, the new additional term $f_s^{(2)}$ that appears in the expression for the scattering amplitude has the form

$$f_s^{(2)} = k^2a^3\left\{3[\mathbf{Mn}_0 - (\mathbf{Mn})(\mathbf{nn}_0)]\frac{j_2(qa)}{(qa)^2} + \frac{1}{2}(1 - \mathbf{nn}_0)(\mathbf{Mn}_0 - 3\mathbf{Mn})\left[\frac{j_1(qa)}{(qa)} - 3\frac{j_2(qa)}{(qa)^2}\right]\right\}. \quad (26)$$

As for the surface integrals taken over the parts of the spherical surfaces $S_1$ and $S_2$ bounding the wake, one

can easily show that their total contribution is equal to zero. Formally, this result is related to the fact that, in the approximation used above, each of the integrals is virtually reduced to the flux of matter in the wake. Since the flux of the fluid in the wake is constant, the corresponding integrals must be equal. Since the normals to the selected surfaces $S_1$ and $S_2$ are directed toward each other, the desired sum of the integrals is equal to zero. Hence, the additional term $f_s^{(3)}$ in the scattering amplitude will also be zero.

Adding together the components of the scattering field that are determined by Eqs. (17), (19), (23), (25), and (26), from using Eq. (14) we can determine the sound scattering amplitude caused by the inhomogeneities of the fluid flow in the vicinity of the moving body. Formally, the expression for the amplitude $f_f$ can be written in the form

$$f_f = \sum_{k=1}^{3} (f_v^{(k)} + f_s^{(k)}). \tag{27}$$

However, because the resulting expressions are cumbersome, we will not specify here the form of Eq. (27). Below, we consider only some specific features of the derived scattering amplitude.

First, it should be noted that the expression obtained for the scattering amplitude $f_f$ is valid for any ratio between the sound wavelength and the characteristic size of the body. However, for small-size bodies, when the inequality $ka \ll 1$ is valid, the corrections to the total scattering amplitude $f_t = f_p + f_f$ that are related to the sound scattering by the flow prove to be small because of the smallness of the Mach number. Therefore, of most interest are the large-size bodies for which the inequality $ka \gg 1$ is valid. As one can see from Eqs. (19), (23), and (26), the corresponding components of the scattered field are proportional to the product of the small Mach number by the large parameter $(ka)^2$. In this case, the scattering amplitude $f_f$ can be comparable to, or even much greater than, the scattering amplitude corresponding to the sound scattering by the body itself, $f_p \sim a$.

Second, the derived scattering amplitude proves to be anisotropic. This anisotropy is most pronounced when the condition $ka \gg 1$ is satisfied. In this case, at finite scattering angles, the dimensionless parameter $qa = 2ka\sin(\vartheta/2)$ is fairly large, and, hence, from Eqs. (17), (19), (23), (25), and (26), it follows that the scattering of high-frequency sound occurs exclusively in the forward direction. We note that the scattering amplitude that was obtained for the sound scattering by the flow formed near a sphere in an ideal fluid was also found to be anisotropic in the case $ka \gg 1$ and reached its maximum at $\vartheta = 0$ [8]:

$$f_f(0) = -\frac{1}{3}k^2a^3(\mathbf{M}\mathbf{n}_0). \tag{28}$$

The analysis of Eq. (27) shows that, in the transmission-type scattering, the total scattering amplitude caused by the flow behaves as $f_f \propto 1/\vartheta^m$ when $\vartheta \longrightarrow 0$. Depending on the scattering direction relative to the body motion, the parameter $m$ can be equal to unity at $q_\perp = 0$ or to two at $q_x = 0$. In the latter case, as one can see from Eq. (23), the scattering amplitude is proportional to the Reynolds number.

The fact that the scattering amplitude due to the scattering from the wake tends to infinity for $\vartheta \longrightarrow 0$ is related to the linear divergence of the integral (22) at zero values of all components of the wave vector $\mathbf{q}$. However, this divergence is of a purely formal character and can be easily eliminated by changing the form of the integrand in Eq. (22), as well as by selecting a finite domain of integration. The required change in the form of the integrand is related to using a more rigorous expression for Green's function in passing from Eq. (13) to its approximate version (14). The choice of a finite domain of integration can be made by taking into account the finite length of the transmitter–receiver base or by selecting a finite length of the wake. We note that, formally, at $\mathbf{q} = 0$, integral (22) is proportional to the wake length, as well as to the momentum of the fluid in the wake. In its turn, the determination of the finite length of the wake presents a special problem of hydrodynamics and falls outside the scope of this paper. Taking into account the aforementioned circumstances, we simply introduce a finite wake length $L$ and, thus, eliminate the divergence in Eq. (22) at the zero scattering angle. Then, the scattering amplitude described by Eq. (27) will be finite for the scattering in the transmission direction, and, in order of magnitude, it will be by a factor of $(L/a)$ greater than the scattering amplitude (28), which corresponds to the scattering by the flow in an ideal fluid at $\vartheta = 0$. Estimates of Eq. (23) show that, in the presence of the wake, the total scattering amplitude $f$ at the zero scattering angle is approximately (in the order of magnitude) equal to the quantity

$$f_f(0) \propto k^2a^2LM. \tag{28}$$

The third feature of the scattering amplitude derived for the sound scattering by the flow with a wake is its possible nonmonotone dependence on the scattering angle $\vartheta$. Studying the behavior of Eq. (25), one can notice that, at finite angles $\vartheta$, this expression is proportional to $k^3a^4M$, and, depending on the ratios between the parameters $ka$, $L$, and $\vartheta$, the sought amplitude $f$ for finite scattering angles can exceed the value given by expression (28) for the zero angle. The same conclusion can be inferred from analyzing Eq. (23) at different ratios between the parameters $ka$, Re, and $\vartheta$. Thus, we can conclude that, in some cases, the curve $f(\vartheta)$ can have a two-peak shape.

The fourth feature of the sound scattering by a flow with a wake is the specific angular dependence of the scattering amplitude corresponding to the transmission direction on the direction of the body motion. The anal-

ysis of Eq. (23) shows that the maximal amplitude values occur when the sound rays are directed along the line of the body motion. This fact agrees well with intuitive physical concepts of ray acoustics. It is precisely in this case that the maximal flow anisotropy along the sound ray is observed, and this anisotropy leads to the maximal focusing or defocusing of the acoustic lens formed in the fluid [3].

In connection with the latter effect, we note the fifth feature of the result under consideration. It is known that for short-wave sound scattering by a stationary, elongated, axially symmetric body, the scattering cross-section is minimal when sound is incident along the body axis and maximal for the perpendicular direction of incidence. In the case of the sound scattering by a fluid flow with a wake produced by the motion of the body, the corresponding scattering cross-section is maximal already for the scattering along the body axis. In closing, we note that all the described characteristic features of sound scattering by moving bodies testify to a considerable contribution of the wake to the total scattering pattern, and these features are characteristic not only of axially symmetric bodies, but also of bodies with arbitrary shapes. They can facilitate the interpretation of the experimentally observed specific features of sound scattering by moving particles, e.g., in the crystallization of particles from solutions or in the filtration of particles in a sound field [1, 2]. Preliminary estimates show that, by taking into account the asymmetric shape of the body (particle) and the lifting and lateral drag forces that occur in this case, we obtain an additional increase in the scattering intensity and a more complex angular dependence of the total scattering amplitude.

## ACKNOWLEDGMENTS

This work was supported by the Russian Foundation for Basic Research, grant nos. 97-02-16087, 98-02-17097, and 99-02-16618.

## REFERENCES

1. E. Trinh and K. Ohsaka, Acust. Acta Acust. **85**, S148 (1999).
2. J. Hawkes, C. Cousins, and W. Coakley, Acust. Acta Acust. **85**, S151 (1999).
3. V. N. Alekseev, A. V. Rimskiĭ-Korsakov, and A. G. Semenov, Akust. Zh. **38**, 581 (1992) [Sov. Phys. Acoust. **38**, 321 (1992)].
4. V. N. Alekseev and A. G. Semenov, Akust. Zh. **38**, 789 (1992) [Sov. Phys. Acoust. **38**, 433 (1992)].
5. V. N. Alekseev and A. G. Semenov, Akust. Zh. **39**, 197 (1993) [Acoust. Phys. **39**, 105 (1993)].
6. V. N. Alekseev and A. G. Semenov, Akust. Zh. **40**, 189 (1994) [Acoust. Phys. **40**, 166 (1994)].
7. V. N. Alekseev, Akust. Zh. **41**, 381 (1995) [Acoust. Phys. **41**, 331 (1995)].
8. V. N. Alekseev, A. G. Semenov, and A. T. Skvortsov, Akust. Zh. **41**, 876 (1995) [Acoust. Phys. **41**, 774 (1995)].
9. M. J. Lighthill, Proc. R. Soc. London, No. 6 (1952).
10. L. D. Landau and E. M. Lifshitz, *Course of Theoretical Physics*, Vol. 6: *Fluid Mechanics* (Nauka, Moscow, 1986; Pergamon, New York, 1987).
11. V. N. Alekseev and A. G. Semenov, Akust. Zh. **42**, 315 (1996) [Acoust. Phys. **42**, 273 (1996)].
12. L. M. Milne-Thomson, *Theoretical Hydrodynamics* (Macmillan, London, 1960; Mir, Moscow, 1964).

*Translated by E. Golyamina*

*Acoustical Physics, Vol. 46, No. 6, 2000, pp. 648–654. Translated from Akusticheskiĭ Zhurnal, Vol. 46, No. 6, 2000, pp. 740–747.*


# Experimental Study of the Acoustic Navigation of a Helicopter by Its Noise Radiation

**V. P. Antonov, A. K. Kuz'menko, V. D. Svet, and E. I. Spitsyn**

*Andreev Acoustics Institute, Russian Academy of Sciences,*
*ul. Shvernika 4, Moscow, 117036 Russia*

*e-mail: bvp@akin.ru*

Received June 11, 1999

**Abstract**—Results of experimental measurements of the coordinates and trajectories of an MI-8 helicopter flight are presented for various types of maneuvers and the landing approach. The current coordinates are measured in real time by acoustic differential navigation methods using the noise radiation of a helicopter. It is shown that, when a measuring base with a microphone spacing of 2 m or less is used, the spatial correlation coefficient for the signals in the frequency band from 200 to 5000 Hz approaches unity. This makes it possible to estimate the position of the helicopter with rms errors less than 0.4 m at all stages of flight and at the landing approach. *© 2000 MAIK "Nauka/Interperiodica".*

The current instrument landing systems for helicopters are based on the use of radiolocation and pulse-phase (correlation) navigation methods. In acoustics, these methods are known as differential navigation methods [1]. Without going into specific details of various navigation systems, one can conclude that, in the general case, their potential accuracy of coordinate determination depends on the wave size of the measuring base and the accuracy of measurement of the phase differences or the time delays (the ray path differences) between separate receivers (antennas). In its turn, the potential accuracy of the time delay measurement is inversely proportional to the bandwidth of the measuring signal.

In radio navigation systems with active radiation of signals, the resolution $\Delta X$ in a space coordinate is determined as $\Delta X = C^{(el)}/\Delta F^{(el)}$, where $C^{(el)}$ is the velocity of the electromagnetic wave propagation and $\Delta F^{(el)}$ is the signal bandwidth. A similar relation is true for an acoustic system that uses the noise signals radiated by the helicopter as navigation data: $\Delta X = C^{(ac)}/\Delta F^{(ac)}$. Let the two systems, i.e., the acoustic and the radio, provide the same space resolution, for instance, 0.3 m. For realizing this resolution in a radio system, we need a signal (or an equivalent short pulse) with a bandwidth of about $\Delta F^{(el)} = 10^9$ Hz. Since the sound velocity is much less than the light velocity, the corresponding bandwidth for an acoustic system is only $10^3$ Hz. Taking into account that the real bandwidth of the helicopter noise exceeds 7 kHz, it is possible to evaluate the potential spatial resolution achievable in the acoustic frequency band: it proves to be about several centimeters. For electromagnetic waves, such an accuracy can be obtained only in the infrared and optical bands.

Obviously, an acoustic system will not efficiently operate if the velocity of the flying vehicle (FV) is commensurable with the velocity of the sound wave propagation. In this case, the measurement of current coordinates by a single-position acoustic system will always lag. However, for helicopters in the course of landing, this lag can be neglected, because the velocity of a landing helicopter is very small, which allows the acoustic system to operate in real time without any lags.

It should be noted that the interest in acoustical methods of detecting FV increased significantly since the mid-1980s, which was associated primarily with the problem of detecting low-altitude targets inaccessible for radar. Interesting references to acoustic systems of this kind can be found in papers [3, 4] and patents [5, 6]. The success achieved in the development and application of acoustic technologies in helicopter aviation is largely related to the fact that helicopters are powerful sources of wide-band noise and move with comparatively low velocities. In particular, at the stage of level-off (descent from a height of flight of about 150 m along a slanting trajectory), the vertical velocity of a helicopter decreases from 3–4 to 0.5–1 m/s and further to 0.2 m/s at the moment of touchdown.

It is also very important that helicopter noise is relatively low frequency, and the propagating sound waves undergo neither scattering nor noticeable attenuation in the presence of atmospheric inhomogeneities such as fog, smoke, snow, or heavy rain. Sound attenuation in the atmosphere is characterized by the values $\beta = 0.003$ dB/m for $f = 200$ Hz and $\beta = 0.4$ dB/m for $f = 10$ kHz, and it can be neglected, especially, taking into account that the reduced noise level of a helicopter at a frequency of 1 kHz is about 95–105 dB relative to $2 \times 10^{-5}$ Pa $\text{Hz}^{-1/2}$ [2]. Thus, a receiving acoustic system at

short distances will always work with high values of the signal-to-noise ratio and, hence, provide a high accuracy in the determination of coordinates.

Weather conditions are always decisive in helicopter aviation for the safety of the landing approach and the landing itself, because these most crucial stages of flight are controlled only visually.

All the factors mentioned allow us to expect that acoustical methods of helicopter navigation can provide a high accuracy of the determination of the current coordinates and remain effective in the most unfavorable weather conditions.

In support of this statement, we present and discuss below some results of experimental studies of acoustical methods for measuring the current coordinates of a helicopter by its noise radiation.

The measuring setup consisted of a remote microphone receiving base, connecting cables, and a hardware–software system for signal processing on the basis of a PC. The receiving base included VSSh-201 acoustic systems, which included VMK-201 capacitor microphones, preamplifiers, power supply units, and units of temperature stabilization (Fig. 1).

The VSSh-201 acoustic system is designed for operation in the frequency range from 2 Hz to 20 kHz with a maximal acoustic pressure level of 160 dB relative to $2^{-10}$ Pa in the temperature range from –30 to +50°C. Signals from microphones were fed through cables to a wide-band multichannel amplifier with a unit of stepwise adjustment of the amplification, an overload indicator, and a preliminary filtering of subsonic and low-frequency components of signals. Every VSSh-201 system could be rigidly fixed on the ground, so that various schemes of the receiving base could be arranged: in the form of a line, a cross, a square, a triangle, and so on.

The hardware–software system was assembled on the basis of a PC with a DT 2838 signal input board (a multiplexer and an A/D converter). The A/D converter provided a sampling rate of 160 kHz with eight input channels of 16-bit capacity and contained a simultaneous sample-and-hold circuit for all input channels. The measuring system also included an ONOSOCI panoramic spectral analyzer for proximate analysis of signals and noise conditions, as well as TEAC and 7005 B&K multichannel tape recorders.

Remote microphone units were installed on the airfield of the Gromov Flight Testing Center (in Zhukovskiĭ), between the runway and the taxiway, at a distance of about 100 m from each other. Two variants of the microphone arrangement were used: along a line with various spacings between them (six microphones) and in the form of an equilateral triangle with an additional microphone at the triangle center (four microphones). In the line variant, the microphones were spaced at the intervals 2.5, 5, 10, 12.5, and 15 m for

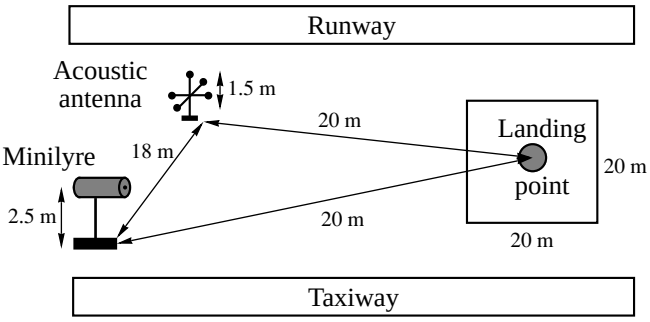


**Fig. 1.** Schematic diagram of the measurements.

measuring the functions and intervals of the space correlation of noise signals of the helicopter. In the triangle variant, the distance between the extreme microphones was 2 m with a height of 1 m above the ground. At a distance of 20 m from the center of the measuring base, a landing square 20 m on a side was marked on the ground, the center of this square being the landing point of the helicopter. The landing square was marked with signal flags. The measurements were made in daylight. For the tests, an MI-8 helicopter was used.

The monitoring of the helicopter maneuvers was carried out by using a TV camera, which could be rotated in the horizontal and vertical planes, and visually. The helicopter was controlled by using a standard ultrashortwave radio station and by the air-traffic control service.

Let us consider the following simplest scheme of the differential method of determining the coordinates. Let three microphones be located at equal distances on a circle of radius $a$, and the fourth, reference microphone be located at the center. The model of the signal $S_k(t)$ in the $k$th receiver can be written as

$$S_k(t) = 1/R_k S(t - R/C) + n(t),$$

where $S(t)$ is the desired signal generated by the helicopter, $n(t)$ is the independent additive noise, $R_k$ is the length of the $k$th ray determining the attenuation of the signal in a homogeneous medium due to the spherical divergence, and $R/C$ is the time of the signal propagation with the velocity $C$.

Let the position of the source be determined in a Cartesian coordinate system by the vector $\mathbf{r} = (x, y, z)$, and the position of the receivers by the vectors lying in the $X$–$Y$ plane

$$\mathbf{r} = (0, 0, 0), \quad \mathbf{r}_k = (a\cos\varphi_k, a\sin\varphi_k, 0), \quad k = 1, 2, 3, \tag{1}$$

where $\varphi_k$ is the angle between the vector $\mathbf{r}_k$ and the positive direction of the $OX$-axis. Let for definiteness the first receiver be located on the $OY$-axis, i.e.,

$$\varphi_k = \pi/2 + 2\pi/3(k - 1), \quad k = 1, 2, 3. \tag{2}$$

We introduce the following notation:

$$R = |\mathbf{r}| = (x^2 + y^2 + z^2)^{1/2},$$
$$R_k = |\mathbf{r} - \mathbf{r}_k| = (R^2 - 2\mathbf{r}\mathbf{r}_k + a^2)^{1/2}, \quad (3)$$
$$d_k = R_k - R,$$

where $R$ is the length of the reference ray, $R_k$ is the length of the ray arriving at the $k$th receiver, and $d_k$ is the ray path difference. After simple algebraic transformations, it is possible to derive from Eqs. (3) the following set of equations to solve for independent variables $R$, $X$, and $Y$, which fully determine the position of the noise source:

$$a^2 - d_k^2 = 2Rd_k + 2\mathbf{r}\mathbf{r}_k, \quad k = 1, 2, 3. \quad (4)$$

The determinant of this set has the form

$$\text{Det} = a^2[d_1 \sin(\varphi_3 - \varphi_2) + d_2(\varphi_1 - \varphi_3) + d_3(\varphi_2 - \varphi_1)] = a^2 D/2,$$

where $D = d_1 + d_2 + d_3$ is the sum of all path differences and is always positive, $0 < D \le 3a$, and the set of Eq. (4) always has a single-valued solution:

$$R = (3a^2 - d_1^2 - d_2^2 - d_3^2)/2D,$$
$$X = (d_2 - d_3)(2R + d_2 + d_3)/2a\sqrt{3}, \quad (5)$$
$$Y = (a^2 - d_1^2 - 2Rd_1)/2,$$
$$Z = (R^2 - X^2 - Y^2)^{1/2}.$$

Thus, the algorithm of the coordinate measurement includes the following sequence of operations:

(i) measurement of the time delays $\tau_k$ ($k = 1, 2, 3$) of the signals received by the peripheral receivers relative to the reference signal;

(ii) calculation of the ray path differences $d_k = C\tau_k$;

(iii) calculation of the coordinates by Eqs. (5).

For measuring the time delays, we used preliminary frequency filtering and a cross-correlation processing of signals for the corresponding pairs of microphones. All these operations of primary (time-domain) and secondary (space-domain) processing were realized as programs operating in real time. The flight trajectory in the $XY$ coordinates and the time dependence of the height estimate $Z(t)$ were displayed on a monitor screen.

Taking into consideration the limited flight time available for experimental investigations, we gave much attention to preliminary measurements with a simulator, which was a specially made point source of noise. The simulator could radiate a wide-band acoustic signal in the range 0.5–5 kHz and provide acoustic power of about 10 W. By using the simulator, we measured the current values of the sound speed (~336.6 m/s) and revealed certain systematic shift errors due to the low accuracy in determining the distance between the microphones, especially for large spacings, and errors in their height, since the ground surface at the test site was uneven. It should be noted that all distances could be measured accurately to 1 cm, which being converted to the speed of sound made it possible to evaluate the latter accurately to about 0.1%. Direct experimental measurements of the speed of sound gave a somewhat greater value of the error: 0.88 m/s, i.e., 0.25%. Apparently, some contribution to the error was made by possible fluctuations of the wind speed, which varied from 4 to 6 m/s. The mean temperature at the test site was about 4°C.

The flight assignment included 3 tasks. The first task consisted in the approach of the helicopter to the landing point and in landing. Then, the helicopter should rise vertically and hover successively at the heights 10, 20, 30, 40, and 50 m. At one of the heights, the helicopter should rotate through 360° if the wind speed was less than 6 m/s.

To fulfill the second task, the helicopter should fly around the vertexes of the landing square at a height of 30 m with hovering at certain points. Finally, the last task consisted in landing along a standard glide path. The accuracy of executing various tacks was monitored visually by the pilot, and the helicopter height was measured by an airborne radio altimeter. Periodically and at the moments of hovering, the pilot reported by ultrashortwave radio the values of height which were registered. Unfortunately, we failed to realize optical measurements of the current coordinates of the helicopter with the use of spaced theodolites and a miniature source of light attached to the helicopter. The lack of such independent measurements caused some difficulties in referencing the measured coordinates of the helicopter, i.e., in determining from which point of the helicopter the measured coordinates should be counted.

Since, in an acoustic navigation system, for determining current coordinates we used the correlation methods of measuring the time delays between various microphone pairs, the estimate of intervals of space correlation and the values of correlation was the main task. For this reason, we used various spacings between microphones in the linear scheme of measurement.

It is obvious that a helicopter with a diameter of the main rotor of about 20 m cannot be considered as an ideal point source of acoustic noise. In addition to the main rotor, the helicopter has other sources of noise: turbines, the tail rotor, and so on. So, the helicopter is a complex, spatially distributed source of noise, which should create certain problems in its navigation at short distances when the size of the measuring base, the size of the sound source, and the distance to the base are commensurable, and the measurements are performed in the Fresnel zone.

The detailed analysis of the space and time correlation functions of noise radiation of a helicopter, as well as of the accuracy of measuring the coordinates for var-

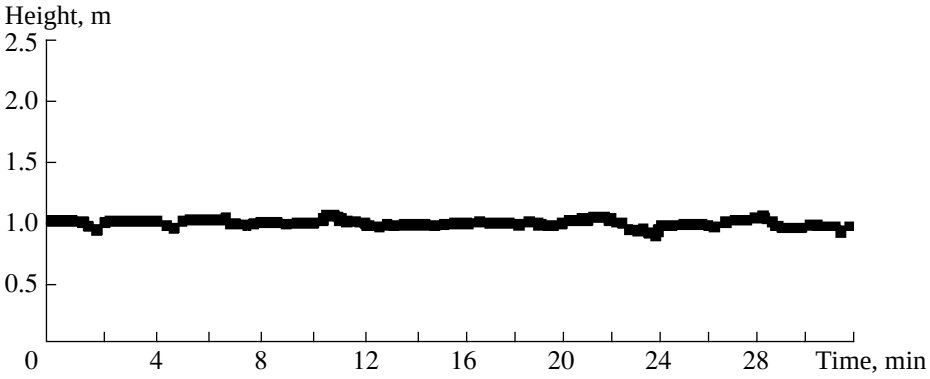


**Fig. 2.** Results of measuring the height of a stationary noise simulator.

ious microphone spacings, will be given in a special paper. Here, we mainly concentrate on the experimental results of the trajectory measurements. We note only that, for distances between the helicopter and the measuring base of 40 m and less, the space correlation of signals from microphones with spacings more than 2.5 m was unstable and had low values. Therefore, for coordinate measurements at the following stages of the experiment, we used the scheme of the measuring base in the form of a triangle with 2-m-long sides. For this spacing, the coefficient of space correlation was within 0.7–0.95, and the correlation function had one stable maximum, which made it possible to uniquely determine the time delays and the current coordinates of the helicopter. Subsequent measurements showed that even lesser spacings between the receivers (down to 1 m) are possible. It should be noted that the obtained estimates of microphone spacing correlate well with the data presented in [3, 4].

We now turn to the analysis of the experimental results.

First of all, it was necessary to investigate the long-term stability of the whole measuring system, to evaluate the optimal frequency range and the environmental noise conditions taking into account that the landing square was not far from the runway. For this purpose, at a distance of 10 m from the center of the measuring base, at a height of 1 m, a noise simulator was fixed. Figure 2 shows the results of measurement for the height of the fixed simulator within a long time interval. It is seen that the fluctuations of the height estimate are within ±10 cm, and they are most likely associated with the changes in the wind velocity, although the influence of powerful local noise from transport airplanes moving along the runway cannot be excluded from consideration.

Then an operator, holding the simulator at the same height of 1 m, moved with it along a straight line. The trajectory of its movement could be seen on a display (Fig. 3). On the basis of measurements with the noise simulator, we made the conclusion that the system can provide long-term stability and potential instrumental accuracy of measuring the coordinates within 10 cm in the frequency range 200–5000 Hz for the exponential averaging times used for the coordinate estimates 0.5–0.8 s. The real instrumental error turned out to be somewhat greater: about 15–20 cm (the rms error). Note that we could use a longer time of averaging, up to several seconds, since, at the initial distances of tracking (350–400 m), such small delays are of no significance.

The next figures present some of the results. Figures 4a, 4b, and 4c show the estimates of the helicopter trajectory during its landing along the glide path for the microphone base with a spacing of 5 m (Fig. 4a) and the results of the processing of the same tack for a 2-m (Fig. 4b) spacing. It is clearly seen that, for the large spacing between the microphones, large errors occur in the determination of the current coordinates due to the decorrelation of signals, especially at low heights. A quite different and stable trajectory is observed for the small spacing. In this case, the dispersion of the estimates is small, and the trajectory is reproduced with confidence. It is seen that, even at very low heights, 3 m and less, the system is able to obtain an accurate height estimate down to the moment of landing. Figure 4c presents the landing of the helicopter along a glide path, but with the approach from a different relative bearing.

Figure 5 shows the results of measurement of the trajectory of the helicopter flying above the landing point at a height of 50 m.

One should pay attention to the fact that the obtained trajectories have small but regular deviations from the mean curve along which the helicopter moves. These deviations do not exceed 2–3 m, i.e., the acoustic system makes it possible to evaluate the position of the helicopter to a high accuracy.

The performed experimental investigations show that the methods of correlation navigation of a helicopter by its noise radiation can be used as the basis for creating high-accuracy real-time instrument systems for helicopter landing.

For a 2-m spacing between the microphones, the spatial correlation of the noise signals was sufficiently high, which made it possible to estimate the current

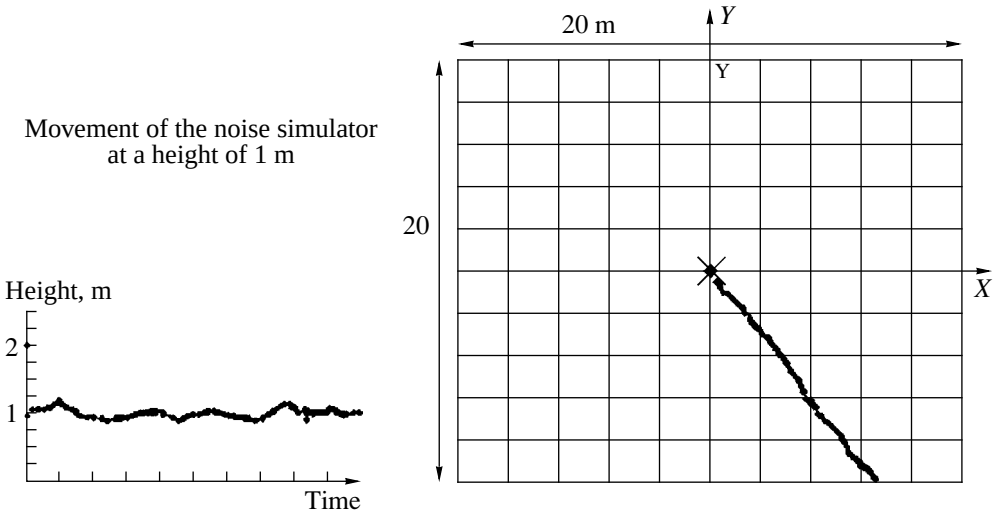


**Fig. 3.** Measured trajectory of the moving noise simulator.

coordinates of the helicopter with a high accuracy. The estimated rms errors of coordinate measurements did not exceed 0.4–0.5 m for this microphone spacing. A number of experiments were carried out with a smaller spacing (1 m). It was shown that, for this spacing, the accuracy in determining the horizontal coordinates was practically the same as for the 2-m spacing. However, the accuracy of the height measurements turned out to be somewhat lower. One of the possible reasons consists in the fact that the scheme of the measuring base did not use the vertical diversity of the receivers and, therefore, the initial instrumental accuracy of measuring the height at grazing angles was less than the accuracy of the estimates of the horizontal coordinates. The correctness of this statement is supported by the fact that, in practically all the experiments when the height of flight was 3 m and less, a somewhat greater dispersion of the estimates of the vertical coordinate was observed. Consequently, in the future, it is necessary to use additional vertical spacings between the microphones and, probably, greater heights of their positions above the ground. Since, for an approaching helicopter, the input signal-to-noise ratio of a single microphone is sufficiently high, the antenna array of the acoustic system may consist of the minimal number of receivers, which makes it compact and simple.

The small errors obtained for the estimates of the coordinates required us to choose a certain algorithm for relating the measured coordinates to a specific point of the helicopter. The reference of height was obtained by adding to the measured height the vertical size of the helicopter from the center of the main rotor to the ground. The reference of the horizontal coordinates was somewhat more complex, since the acoustic center of noise radiation migrated depending on the inclination of the main rotor. In this study, the acoustic center was also related to the center of the main rotor, and, for the performed experiments, the possible shift errors could be neglected. However, if for some applications of the acoustic navigation system, an accuracy higher than 0.4 m is needed, the problem of a correct referencing should be considered in greater detail.

If we compare the obtained data with the accuracy characteristics of the existing differential radio navigation landing systems, we can conclude that the acoustic systems are considerably superior to radio systems. Thus, in accordance with the ICAO standards, the accuracy (the rms error) required for the landing approach corresponding to the second and third (the highest) rating is 2–8.5 m, and, for carrying out special tasks (such as geological exploration or referencing), the accuracy should be within 0.25–4 m [7]. In civil aviation, there are no navigation systems with such a high accuracy. In particular, in paper [8], by using numerical modeling of a complex integrated system consisting of the GLONASS or GPS satellite system, an airborne system of inertial navigation, and an aneroid altimeter, it was shown that, theoretically, the conditions of landing according to the third rating could be provided, but with very long time of evaluation: 100 s with an accuracy of 2 m in the horizontal coordinates and 3–4 m in height. The accuracy of height measurements within 0.3–0.4 m is considered to be a far prospect of phase-differential radio navigation [9–11]. The existing radio navigation systems are described in the handbook [10]. However, not a single one of the 275 presented navigation systems provides the accuracy in determining the coordinates of flying vehicles according to the third rating of ICAO.

At the same time, it is the helicopters that most of all need precision instrument means of landing, especially for badly equipped landing sites, and the results of our experiments provide strong evidence for the promise of acoustical methods.

An acoustic navigation system, of course, cannot fully replace a radio navigation system, but it can and

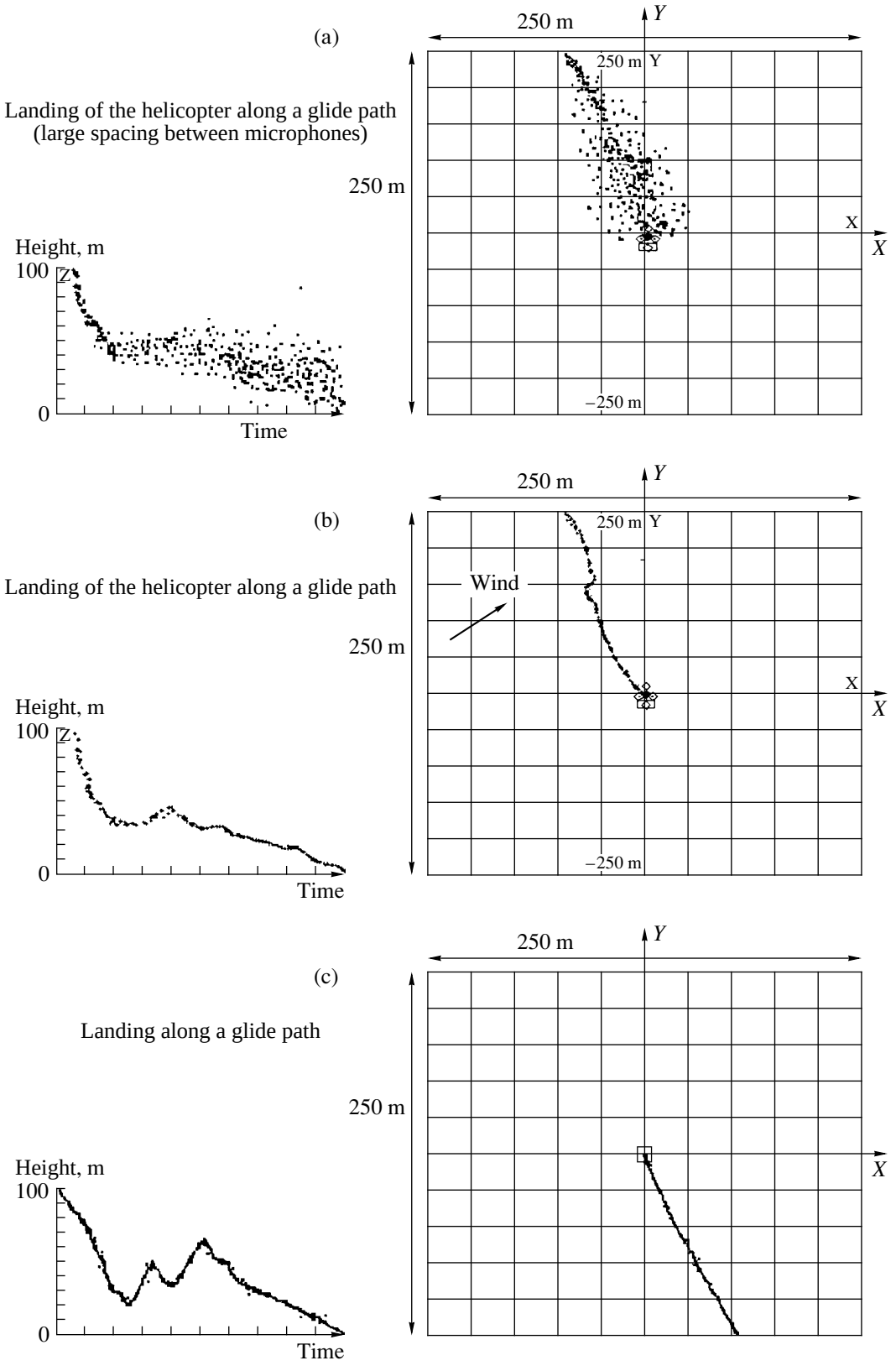


**Fig. 4.** (a) Landing of the helicopter along a glide path. Spacing between the microphones is 5 m. A wide scatter of the coordinate estimates is observed due to the decorrelation of signals. (b) Landing of the helicopter along a glide path. Spacing between the microphones is 2 m. (c) Landing of the helicopter along a glide path with the approach from a different relative bearing.

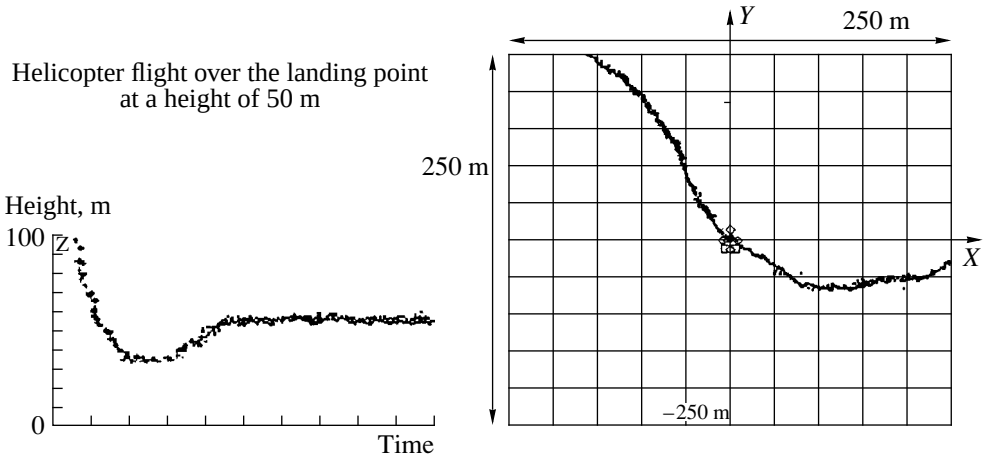


**Fig. 5.** Helicopter flight over the landing point at a height of 50 m with a subsequent turn.

must become an important component of a combined landing system for providing the safe approach and landing beginning from distances of about 1500–2000 m, depending of the type of the helicopter.

This system may also be designed as an independent system of instrument landing for small-size helicopter landing platforms (on high-rise buildings, offshore drilling platforms, or ship decks) or as a mobile navigation system that can be quickly put into operation, for example, for accurate guidance of helicopters to the source of a fire. The last application is especially topical taking into account that fires with a heavy smoke screen drastically reduce the optical visibility and hinder the orientation of a fire helicopter, whereas low-frequency acoustic signals propagate in this medium practically without interference.

## ACKNOWLEDGMENTS

We are grateful to V.I. Telyatnikov and D.A. Dement'ev, employees of the Aviatest company, and to the staff and pilots of the Gromov Flight Testing Center for assistance in organizing and executing the experiments.

## REFERENCES

1. P. H. Milne, *Underwater Acoustic Positioning Systems* (Gulf, Houston, 1983; Sudostroenie, Leningrad, 1989).
2. Yu. G. Matveev and V. N. Mel'nikov, Akust. Zh. **14**, 246 (1968) [Sov. Phys. Acoust. **14**, 199 (1968)].
3. V. J. Lubkin, Def. Sci. J. **7** (2), 13 (1988).
4. H. Broadbent, Jane's Defense Weekly, No. 34, 76 (1986).
5. Patent No. 2196119, GO1S3/80.20.04.1988, Plessey Co, GB.
6. Patent No. 2181547, GO1S/80.23.04.87 GEC, Avinonics Ltd., GB.
7. G. Dodel and I. Skoog, Radiotekhnika, No. 1, 74 (1996).
8. K. K. Veremeenko and V. A. Tikhonov, Radiotekhnika, No. 1, 94 (1996).
9. P. Klass, Aviat. Week Space Technol., May 10, 34 (1993).
10. *GPS World Receivers Survey* (GPS World, 1995, January).
11. H. Langer, Rotorblatt, No. 2, 38 (1999).

*Translated by A. Svechnikov*

*Acoustical Physics, Vol. 46, No. 6, 2000, pp. 655–662. Translated from Akusticheskiĭ Zhurnal, Vol. 46, No. 6, 2000, pp. 748–755.*


# Development and Experimental Testing of the Technique for Estimating the Energy Characteristics of a Vibrating Elastic Structure by Its Input Impedance

**Yu. I. Bobrovnitskiĭ and M. P. Korotkov**

*Blagonravov Institute of Machine Science, Russian Academy of Sciences, Malyĭ Khariton'evskiĭ per. 4, Moscow, 101830 Russia*

*e-mail: korotkov@imash.ac.ru*

Received February 17, 2000

**Abstract**—An effective technique proposed earlier (Acoustical Physics **45** (3) (1999)) for estimating the kinetic and potential energy, the loss coefficient, and other energy characteristics of a vibrating elastic structure is improved and tested experimentally. Refined formulas providing sufficiently accurate estimates of energy in a wide range of low and medium frequencies are derived. An experimental estimation method based on the Padé approximation is proposed. Results of a laboratory experiment demonstrating the efficiency of the proposed technique are presented. *© 2000 MAIK "Nauka/Interperiodica".*

For a linear elastic structure performing forced harmonic vibrations under the effect of one or several forces, an effective technique for estimating its energy oscillatory characteristics (potential and kinetic energy, loss coefficient, etc.) from the structure input impedances (conductivities) and their first derivatives with respect to frequency was proposed earlier [1, 2]. This technique requires neither the measurement of the parameters of the whole structure nor the use of its computational oscillatory model. One needs only to measure the forces and the velocities at the points of application of the external forces. In the simplest case when the structure vibrates under the effect of one point force, it is necessary to measure only two quantities, namely, the complex amplitude of the external force and the velocity at the point of force application, in order to calculate all the energy characteristics of the structure. With the help of computer simulations [1, 2], it was found that the technique provides fairly accurate estimates at all frequencies except for the vicinities of certain eigenfrequencies of the structure. This shortcoming was the main obstacle in the practical utilization of the method.

In this paper, which continues the studies described in [1, 2], the aforementioned shortcoming is eliminated. Refined formulas for estimating the energy characteristics, which are equally applicable at all frequencies, are derived. The corresponding experimental method for obtaining the energy characteristics of vibrations of real structures by this technique is proposed. The key feature of the method is the representation of the measured input impedances of the structure with the help of the so-called Padé approximation. The results of a laboratory experiment with a flexurally oscillating rod are also presented below. The estimates of the energy-related quantities, which are obtained using the proposed technique, agree well with the values obtained independently by other methods. The major result of this paper is the conclusion that the proposed effective technique for estimating the energy characteristics of a vibrating elastic structure is now modified to a form suitable for practical application.

Let us consider a linear elastic system with distributed parameters (a structure) that performs harmonic oscillations under the effect of a single force $f\exp(-i\omega t)$ concentrated at a point $x_0$. Let the complex amplitude $f$ of the force and the complex amplitude $v$ of the velocity of the structure vibrations at the point of force application be known (measured). The knowledge of the parameters and properties of the structure, except for its linearity, as well as the knowledge of other characteristics of the vibration field, is not presumed. Then, according to the proposed technique [1, 2], it is possible to calculate exactly the period-average loss power $\Phi$ and the difference between the kinetic and potential energies (the Lagrangian $L$) of the structure vibrations from the two known quantities $f$ and $v$:

$$\begin{aligned}\Phi &= (1/2)|v|^2\mathrm{Re}[z(\omega)] = (1/2)|f|^2\mathrm{Re}[y(\omega)],\\ L &= -(1/4)|v|^2\mathrm{Im}[z(\omega)/\omega] = (1/4)|f|^2\mathrm{Im}[y(\omega)/\omega],\end{aligned} \quad (1)$$

1063-7710/00/4606-0655$20.00 © 2000 MAIK "Nauka/Interperiodica"

and also estimate, i.e., determine approximately, the period-average total energy of vibrations $E$:

$$E \cong E_{\text{imp}} = -\frac{1}{4}|v|^2 \text{Im}\left[\frac{\partial z(\omega)}{\partial \omega}\right], \quad (2)$$

$$E \cong E_{\text{mob}} = -\frac{1}{4}|f|^2 \text{Im}\left[\frac{\partial y(\omega)}{\partial \omega}\right]. \quad (3)$$

Here the input impedance $z(\omega)$ and the input conductivity $y(\omega)$ are the functions of the measured quantities:

$$z(\omega) = f/v, \quad y(\omega) = v/f. \quad (4)$$

Combining Eqs. (1)–(3), it is easy to calculate separately the kinetic and potential energies and the loss factor of the structure. As it has been demonstrated in the previous papers [1, 2], estimate (2) of the total energy by the input impedance gives correct values of the energy at all frequencies except for the antiresonance ones and their small vicinities. On the contrary, estimate (3) by the input conductivity gives a good approximation at the antiresonance frequencies and in a wide frequency range, but leads to incorrect results at the resonance frequencies of the structure and in their vicinities. The estimate of the total energy derived below combines the advantages of the estimates given by Eqs. (2) and (3): at antiresonance frequencies, it coincides with the estimate by Eq. (3), and at all other frequencies including the resonance frequencies, it coincides with the estimate by the impedance, i.e., by Eq. (2).

Below, we use the following representation of the input impedance from Eqs. (4):

$$z(\omega) = z_0 \frac{\Delta_r(\omega)}{\Delta_a(\omega)} = z_0 \frac{\prod_n (\omega - \Omega_{rn})}{\prod_m (\omega - \Omega_{am})}. \quad (5)$$

The representation originates from the theory of electric circuits and is apparently correct for any linear continuous or discrete oscillating system [3, 4]. Here, $z_0$ is the frequency-independent dimensional factor, e.g., the characteristic impedance; $\Delta_r(\omega) = 0$ is an equation for complex eigenfrequencies $\Omega_{rn} = \omega_{rn} - i\delta_{rn}$, $n = 1, 2, \ldots$, of a structure in which the point $x_0$ is free from external action. In the vicinity of these frequencies, the input impedance is minimal and the structure response to a force acting at the point $x_0$ is maximal. The frequencies $\omega_{rn}$ and other quantities with the index $r$ will be called below the resonance frequencies. The roots of the equation $\Delta_a(\omega) = 0$, which correspond to zero values of the denominator in expression (5) for the impedance, are the complex eigenfrequencies $\Omega_{am} = \omega_{am} - i\delta_{am}$, $m = 1, 2, \ldots$, of the structure with the point $x_0$ being fixed. In the vicinities of these frequencies, which we will call below the antiresonance frequencies (the index $a$), the impedance (5) is maximal, and the response to a force acting on the structure is minimal. We should note that, in the case of a kinematic excitation of the structure, when the velocity amplitude is set at the point $x_0$, on the contrary, the maximal response of the structure occurs at antiresonance frequencies, while the minimal response occurs at resonance frequencies. Therefore, in the limiting case, when the structure is excited by a force source, the estimate (2) for the total energy by the input impedance can be used at all frequencies, because its errors correspond to the response minimums (antiresonances). For the same reason, a kinematic excitation is another limiting case of external action, when the estimate (3) by the input conductivity is applicable practically at all frequencies.

However, real sources of vibrations, in particular, electrodynamic vibrators (without special correcting devices), lead as a rule to mixed excitation: at some frequencies, it is close to force excitation and at other frequencies, to kinematic excitation. Therefore, practical utilization of the estimates given by Eqs. (2) and (3) is restricted by the necessity of a preliminary study of the type of the source at all frequencies. Although the improved estimate given below is somewhat more complicated than the estimates given by Eqs. (2) and (3), it is valid for external excitation of any type.

We derive the improved estimate by using the estimate (2) by the input impedance as the basis and introducing a suitable frequency-dependent correction coefficient for it. Since the estimate given by Eq. (2) does not work at antiresonance frequencies, we consider in more detail the input impedance (5) in the vicinity of one of such frequencies with the number $k$ and represent it in the form of a simple fraction

$$z(\omega) = \frac{\varphi_k}{\omega - \Omega_{ak}}, \quad (6)$$

where the complex constant $\varphi_k$ is calculated as

$$\varphi_k = (\omega - \Omega_{ak}) z(\omega)\big|_{\omega = \omega_{ak}} = i\delta_{ak} z(\omega_{ak}). \quad (7)$$

In this representation, we implicitly assume that the losses in the structure are sufficiently small and the distance between neighboring antiresonance frequencies exceeds the peak width $|\omega - \Omega_{ak}|^{-1}$. Under this assumption, the function $(\omega - \Omega_{ak})z(\omega)$ is a slowly varying function of frequency in the considered vicinity, and, for simplicity, this function in Eq. (6) can be replaced by a constant given by Eq. (7). Now, if we calculate the estimates according to Eqs. (2) and (3) using the input impedance (6) and its inverse value as the conductivity, then, after simple algebraic transformations, we obtain the relationship

$$E_{\text{imp}} = \alpha_k E_{\text{mob}}, \quad (8)$$

which shows that, in the vicinity of the $k$th antiresonance frequency, the energy estimate by the impedance,

$E_{\text{imp}}$, differs from the estimate by the conductivity, $E_{\text{mob}}$, by the following factor depending on the frequency $\omega$:

$$\alpha_k = \frac{\mathrm{Re}(\omega - \Omega_{ak})^2 - \mathrm{Im}(\omega - \Omega_{ak})^2 \mathrm{Re}\,\varphi_k/\mathrm{Im}\,\varphi_k}{|\omega - \Omega_{ak}|^2}. \quad (9)$$

However, since the estimate by the conductivity $E_{\text{mob}}$ coincides with the exact value of energy $E$ at the antiresonance frequency [1, 2], the factor given by Eq. (9) can be considered as a correction coefficient for the estimate by the impedance $E_{\text{imp}}$. Then, from Eq. (8), we obtain the estimate

$$E \cong E_{\text{imp}}/\alpha_k. \quad (10)$$

As it turned out, coefficient (9) has a remarkable property: it is equal to unity outside the vicinity of the frequency $\omega_{ak}$ (see Fig. 1). Therefore, it corrects the estimate $E_{\text{imp}}$ in the vicinity of the $k$th antiresonance frequency in Eq. (10) and does not affect it at other frequencies. Thus, estimate (10) has all advantages of the estimate by the impedance (2) and additionally gives true values of energy at the $k$th antiresonance frequency and in its vicinity.

If several antiresonance frequencies occur in the frequency range under consideration, we can take the product of the coefficients (9) as the correction coefficient to the estimate by the impedance (2) for all these frequencies:

$$E \cong E_{\text{imp}}/\alpha, \quad \alpha = \prod_k \alpha_k. \quad (11)$$

This is one of the desired refined estimates, which yields true values for the total energy of the structure at all frequencies, including resonance and antiresonance frequencies. Sometimes, it is more convenient to introduce correction coefficients $\alpha_k$ into the derivative of the input impedance (5) with respect to frequency for each antiresonance term separately,

$$\frac{\partial z(\omega)}{\partial \omega} = z(\omega)\left[\sum_n \frac{1}{\omega - \Omega_{rn}} - \sum_m \frac{(1/\alpha_m)}{\omega - \Omega_{am}}\right], \quad (12)$$

and then substitute Eq. (12) into Eq. (2). Analyzing simple model examples and the experimental results described below, we arrived at the conclusion that the difference between the improved estimates given by Eqs. (11) and (12) is small. It should be noted that the improved estimates for energy similar to Eqs. (11) and (12) are also obtained on the basis of the estimate by the conductivity (3). We do not present them here, because they have no advantages over the estimates given by Eqs. (11) and (12).

The domain of applicability of Eqs. (11) and (12) is the same as that of Eqs. (2) and (3). This is the frequency range where the mean distance between the neighboring eigenfrequencies of the structure is greater than the width of the resonance peaks [2]. In the case of real structures with the loss coefficient of material not exceeding 0.05, the domain of applicability of the proposed estimates is restricted to low and medium frequencies.

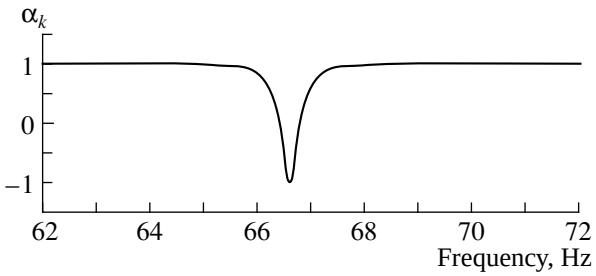


**Fig. 1.** Correction coefficient (9) for one of the experimental antiresonance frequencies.

Let us take as a numerical example a longitudinally vibrating thin homogeneous rod of length $l$; the rod is excited at its left end and free at the right end. Its input impedance is equal to [1, 2]

$$z(\omega) = -iz_0 \sin(k_c l)/\cos(k_c l), \quad (13)$$

where $k_c = \omega(\rho/E_c)^{1/2} = k(1 - i\eta)^{-1/2}$ is the complex wave number; $z_0 = (\rho E_c S^2)^{1/2}$ is the characteristic impedance of the rod; $E_c = E(1 - i\eta)$, $\rho$, and $\eta$ are the complex Young modulus, density, and loss coefficient of the material; and $S$ is the area of the rod cross-section. The correction coefficients for this structure, as well as for many others, are noticeably simplified: at the antiresonance frequencies $kl = \pi m + \pi/2$, the constants given by Eq. (7) are purely imaginary quantities ($\mathrm{Re}\,\varphi_m = 0$), and the product of the real parts $\Pi \mathrm{Re}(\omega - \Omega_{am})^2$ differs from the real part of the product $\mathrm{Re}\,\Pi(\omega - \Omega_{am})^2$ by the value of the order of $\eta$. Therefore, we can take here

$$\alpha = \frac{\mathrm{Re}[\cos^2(k_c l)]}{|\cos(k_c l)|^2} \quad (14)$$

as the general correction coefficient in Eq. (11). Solid lines in Fig. 2 present the exact values of the time-average total energy $E$ of the rod, and the dots show the improved estimate (11) with the correction coefficient (14). These results correspond to the case of kinematic excitation of the rod (the amplitude of the velocity $v_0$ is set at the left end, and this amplitude is the same at all frequencies), which is most unfavorable for utilization of the uncorrected estimate by the impedance (2): it gives erroneous results at antiresonance frequencies where the response is maximal (see Fig. 3a from [1]). As one can see from Fig. 2, the introduction of the correction coefficient (14) improves the estimate (2): at low frequencies ($kl < 9$), the approximate and exact values almost coincide, and, at medium frequencies ($kl < 20$), they differ by less than 10%; at higher frequencies, their difference increases (Fig. 2b), but this frequency range (as has been indicated above) falls outside the domain of applicability of the proposed technique.

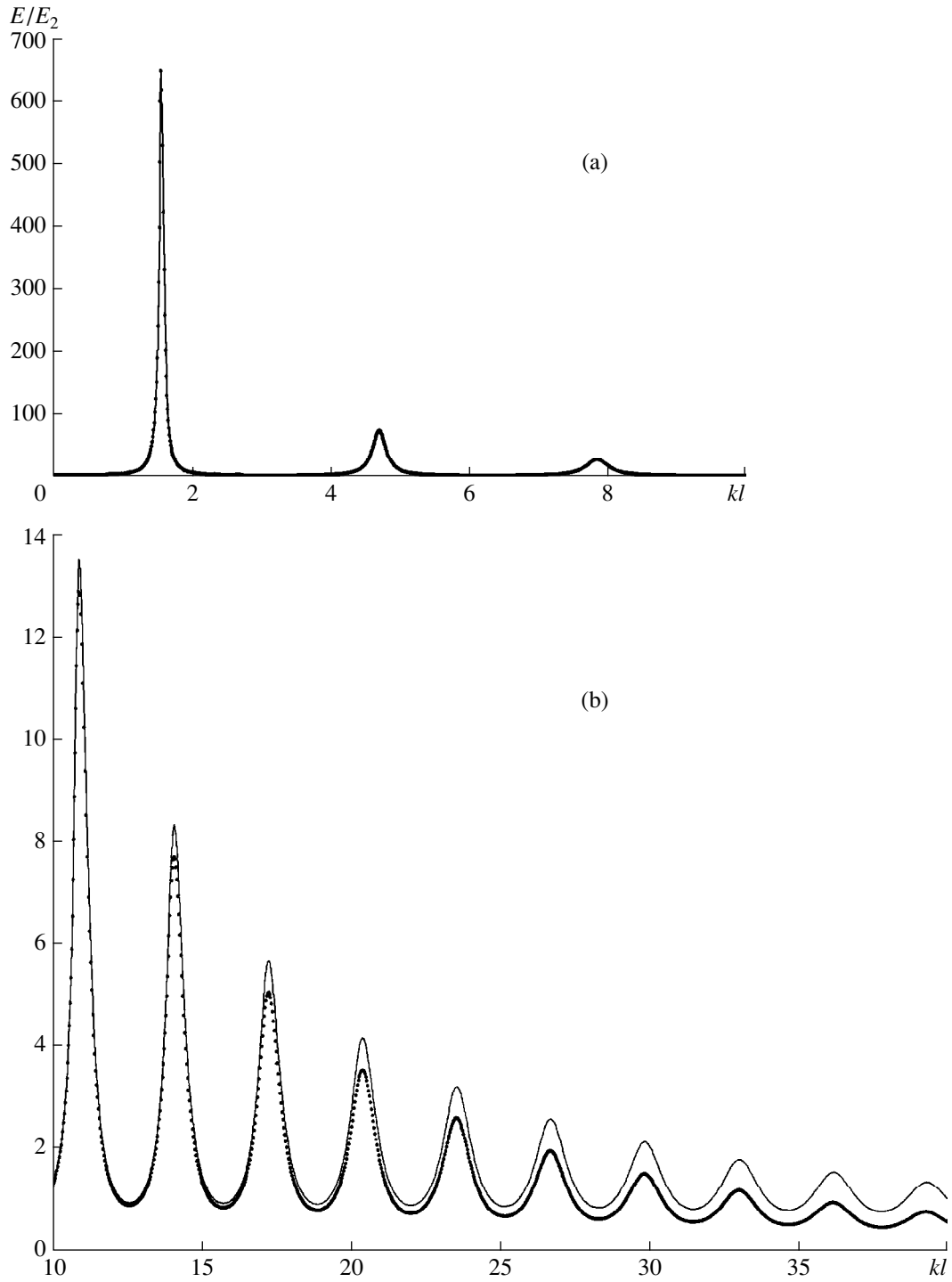


**Fig. 2.** Exact values of the total energy of a rod in the case of kinematic excitation (solid lines) and its approximate values (dots) obtained using the improved estimate (11) with the correction coefficient (14) for (a) small and (b) medium values of the wave size of the rod $kl$. Energy is normalized to the value $E_2 = \rho lS|v_0|^2/4$, and the loss coefficient of the rod material is equal to 0.05.

One of the problems of practical application of the proposed technique for estimating the energy characteristics is the differentiation of experimentally measured impedances or conductivities with respect to frequency. Differentiation is an ill-conditioned operation that is unstable with respect to variations of the input data [5]. If the differentiated function is set with a random error (as commonly happens in practice), the error of the direct calculation of the derivative can be arbitrarily large. In order to reduce these errors, the experi-

mental data are usually subjected to preliminary smoothing; i.e., they are approximated by smooth functions and, most frequently, by polynomials, or multipoint schemes are used [6]. In our opinion, from the point of view of the interference stability, the most stable procedure for calculating the derivatives with respect to frequency is the procedure based on the so-called Padé approximation of the experimental data with subsequent analytical differentiation of the approximating function. This procedure takes into account to the maximal extent the singularities of the impedance functions and provides more precise results as compared to other methods of differentiation.

The Padé approximation is the approximation of functions with the help of the ratio of two polynomials [7]. The grounds for its application in the problem under consideration are the representation of the input impedance on the whole frequency axis as a ratio of two integer functions $\Delta_r(\omega)$ and $\Delta_a(\omega)$ [see Eq. (5)]. In the finite part of the complex plane $|\omega| < a$, each of them contains a finite number of zeros [8]. Physically, this means that the system under consideration has a finite number of alternating resonances and antiresonances within the interval of real frequencies 0–$a$ (the Foster theorem [3]). Each of the integer functions within this frequency interval can be approximated by a polynomial of finite degree, and, therefore, the impedance (5) can be represented by a ratio of two polynomials, i.e., by the Padé approximation

$$z(\omega) \cong z_p(\omega) = z_0 \frac{(\omega - \Omega_{r1}) \ldots (\omega - \Omega_{rM})}{(\omega - \Omega_{a1}) \ldots (\omega - \Omega_{aN})}, \qquad (15)$$

where the complex parameters $z_0$, $\Omega_{rj}$, and $\Omega_{ak}$ are determined by the comparison of Eq. (15) with experimental data.

The procedure of identification of the parameters of the Padé model (15), which was used by us in the experiment described below and is adequate at low and medium frequencies, is as follows. First, the resonance and antiresonance frequencies (i.e., the real parts of the complex frequencies $\Omega_{rj}$ and $\Omega_{ak}$) are determined from the experimentally measured frequency dependences of the force $f(\omega)$ and of the acceleration $a(\omega)$. Then, the constant $z_0$ is determined from the function $z(\omega)$ at $\omega \longrightarrow 0$. And, finally, the imaginary parts of the complex frequencies are determined by the values of $z(\omega_{rj})$ and $y(\omega_{ak})$, which are proportional to the losses $\delta_{rj}$ and $\delta_{ak}$ at low and medium frequencies.

The proposed technique for estimating the energy characteristics was tested in a laboratory experiment with a flexurally vibrating rod. A steel rod with a rectangular cross-section and with the dimensions $40 \times 50 \times 1500$ mm was suspended on two strings and excited at one of its ends in the horizontal plane by an electrodynamic vibrator powered by a generator of harmonic signals of variable frequency. The amplitudes and phases of the force $f(\omega)$ and acceleration $a(\omega)$ were measured. These data were fed into a computer, which used them to calculate the speed $v(\omega) = ia(\omega)/\omega$, the impedance $z(\omega)$, the Padé approximant (15), and the desired estimates of the energy quantities.

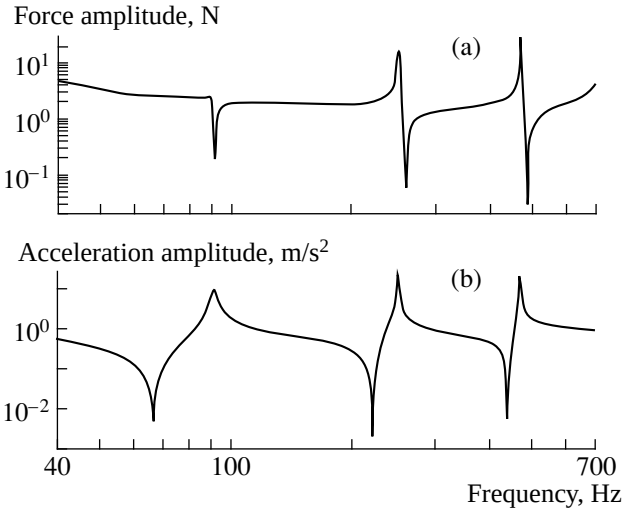


**Fig. 3.** Amplitudes of (a) force and (b) acceleration of the rod at the excitation point versus frequency.

Figure 3 presents the measured amplitudes of the force and the acceleration at the excitation point. As one can see from the plot, the vibrator is not a source of force or kinematic excitation: the force is constant only at separate parts of the spectrum, e.g., within the range 100–200 Hz. At other frequencies, the amplitudes of the force and acceleration vary within wide limits. In the studied frequency range 40–700 Hz, the rod has three resonances and three antiresonances. Their quality factor is high: $Q \cong 200$, which corresponds to the loss coefficient in the material $\eta \cong 0.005$.

Dots in Fig. 4 represent the imaginary part of the rod input impedance plotted according to the curves in Fig. 3, while the solid line shows the magnitude of the Padé approximant. In this case, the Padé approximant (15) contains $M = 5$ resonance factors in the numerator and $N = 4$ antiresonance factors in the denominator. According to the above consideration, the parameters of the model given by Eq. (15) were determined as follows. The first resonance frequency was assumed to be equal to zero, $\Omega_{r1} = 0$, since, at the lowest frequencies, the suspended rod behaves with respect to an external force as a mass $m_{eq}$, and the input impedance is proportional to frequency

$$z(\omega) \cong -i\omega m_{eq}. \qquad (16)$$

The next three resonance frequencies, 92, 254, and 487 Hz, were determined by the minimum of the force plot in Fig. 3a, and the fifth resonance was taken to be outside the operational frequency range. Analogously, the first three antiresonance frequencies, 66.5, 214, and 439 Hz, were determined by the minimums of the

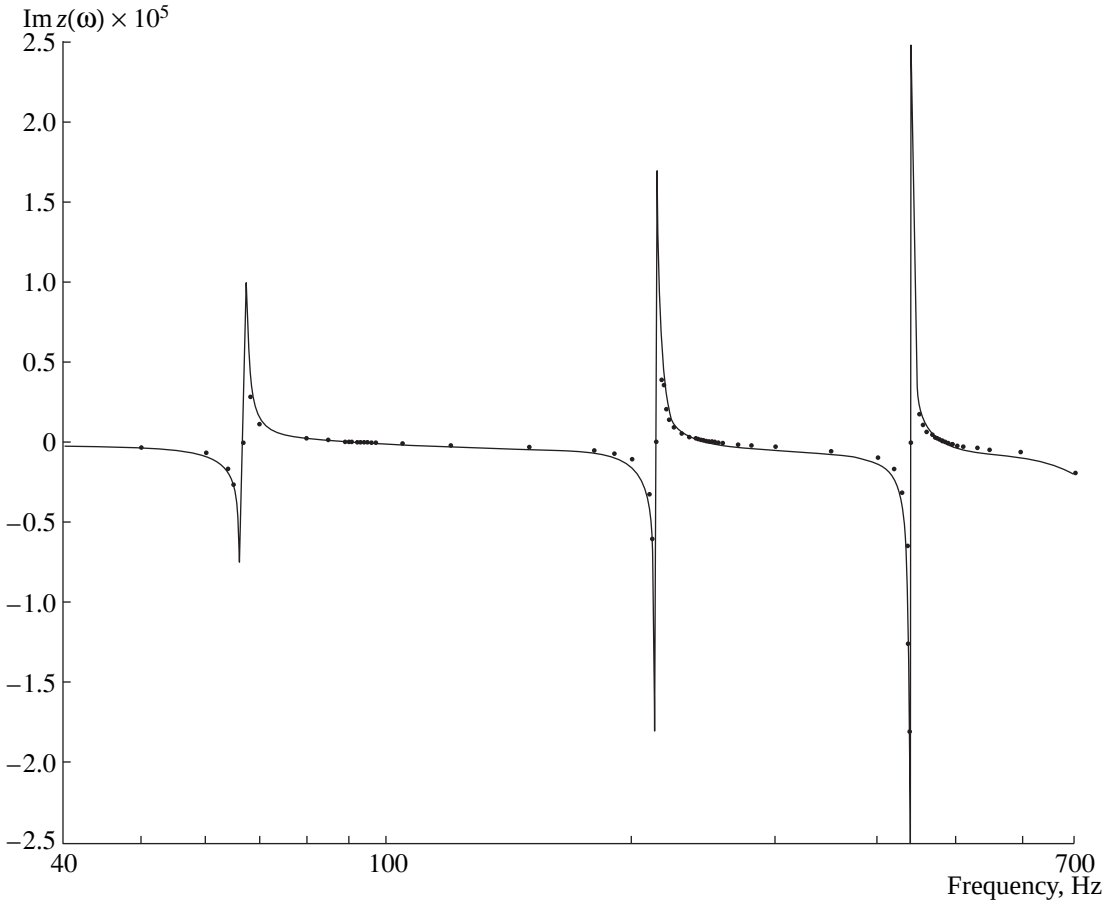


**Fig. 4.** Imaginary part of the experimental input impedance of the rod (dots) and its Padé approximant (the solid line).

acceleration curve in Fig. 3b, and the fourth one was above 700 Hz. The frequencies $\Omega_{r5}$ and $\Omega_{a4}$ lying beyond the operational range do not correspond to any real resonances and antiresonances of the rod. They were introduced into the Padé approximant (15) for correcting the impedance model in the upper part of the frequency range 500–700 Hz.

The constant $z_0$ in the framework of approximation (15) was determined from the condition $z(\omega) \cong -i\omega m_{eq}$ [see Eq. (16)]. In this case, a quarter of the rod total mass was taken as the equivalent mass: $m_{eq} = \rho Sl/4$. One can verify the correctness of this equality by considering the progressive and rotary motion of the rod as a solid under the effect of an external harmonic force of low frequency. The imaginary parts of the three complex resonance frequencies, 0.9, 0.32, and 0.28, and also the imaginary parts of the three antiresonance frequencies, 0.16, 0.09, and 0.19, of the operational range were determined from the condition of equality of the minimal and maximal values of the magnitudes of the experimental and model impedances. The Padé model (15) with the values of the basic parameters determined in such a way adequately describes the impedance measured experimentally (see Fig. 4).

Here, we have to note that, according to the Bernoulli–Euler theory of the vibration of thin rods [9], the input impedance of the rod under consideration is equal to

$$z_t(\omega) = iz_0 \frac{1 - \cosh(k_w l)\cos(k_w l)}{\cos(k_w l)\sinh(k_w l)/k_w l - \cosh(k_w l)\sin(k_w l)/k_w l}, \quad (17)$$

where, according to the general condition given by Eq. (5), the characteristic expression for the rod free at both ends stands in the numerator, while the characteristic expression for the rod free at one end and supported at the other end stands in the denominator; $z_0 = (MB/l^3)^{1/2}$ is the characteristic impedance; $M$, $B$, and $l$ are the mass, flexural rigidity, and length, respectively; and $k_w$ is the flexural wave number of the rod. Assuming that the Young modulus of the material is complex, $E = E_0(1 - i\eta)$, and varying the elastic and geometric parameters of the rod $E_0$, $\eta$, $\rho S$, $B$, and $l$ about their rated values, we tried to attain the maximal agreement between the impedance given by Eq. (17) and the experimental results. However, even in the best case it was impossible to achieve the coincidence of all resonance and antiresonance frequencies of the operational

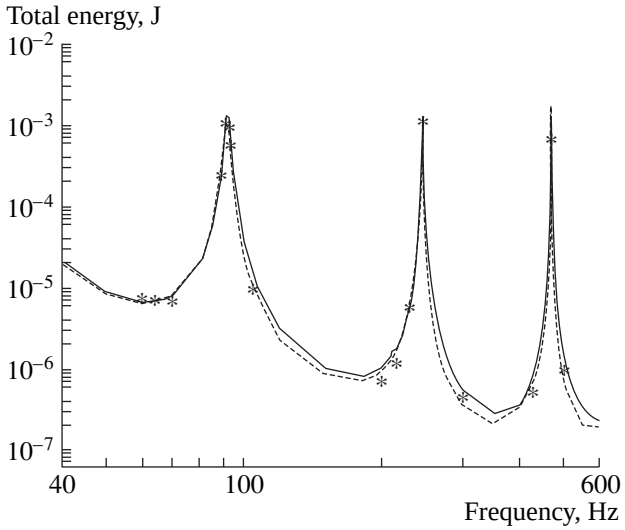


**Fig. 5.** Total energy of rod vibrations obtained experimentally by the improved technique (the solid line) and by two other methods (the dotted line and the stars).

range to better than 3%, which caused large errors in the impedance derivatives with respect to frequency and errors in the estimates of the energy quantities in the most important parts of the spectrum. Thus, the approximation of the experimentally measured input impedance by the functions given by Eq. (17), which are based on the classical theory of thin rods, proved to be not quite adequate in this problem apparently because of the influence of suspension and other factors that were not taken into account by the model. The commonly used methods of differentiation, which, as is known [6], are based on preliminary approximation by polynomials, proved to be even less accurate. With the method of the parameter identification described above, the Padé approximation provided the highest accuracy in estimating the energy characteristics of vibrations of the structure by the proposed method.

After the determination of the analytical Padé approximant for the experimental impedance, the total energy and other energy characteristics of the rod vibrations can be easily determined by the refined formulas (2), (12), and (9). The solid line in Fig. 5 shows the total energy of the rod vibrations calculated in this way. The dashed line shows the energy calculated according to the analytical solution of the problem on the basis of the Bernoulli–Euler theory with the substitution of the experimentally measured amplitudes of the external force and the experimental loss coefficient. The stars indicate the energy values obtained for certain characteristic frequencies by one more independent method based on a detailed measurement of the form of rod vibrations. As one can see from Fig. 5, the agreement of the results is fairly good.

We should note that the calculation by the unimproved Eq. (2) also provides adequate estimates of energy at all frequencies except for the narrow vicinities of three antiresonance frequencies of the operational range. Figure 6 demonstrates the vicinity of the third antiresonance frequency 439 Hz. The unimproved estimate (dots) gives erroneous results in this region, while the improved estimate by Eqs. (2), (12), and (9) (the solid line) coincides with the energy values obtained by other methods (stars).

Thus, the new effective technique for estimating the energy characteristics of a vibrating elastic structure, which was proposed in [1, 2], is improved and experimentally justified in this paper. The necessary refined formulas are derived, and the corresponding experimental technique using standard measuring equipment is presented. Now, the proposed technique is theoretically justified, tested by computer simulation and in a laboratory experiment, and can be used for studying the

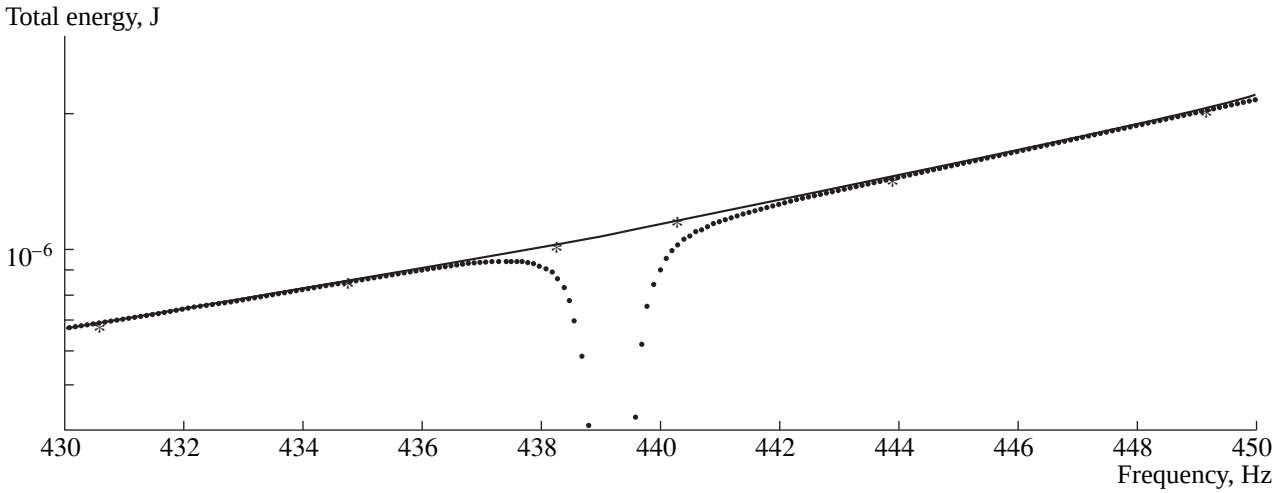


**Fig. 6.** Energy values in the vicinity of the antiresonance frequency: unimproved estimate by Eq. (2) (dots), improved estimate by Eq. (12) (the solid line), and the exact values (stars).

vibrations of practical engineering structures in the low and medium frequency ranges.

## ACKNOWLEDGMENTS

This work was supported in part by the Russian Foundation for Basic Research, project no. 98-01-00552a.

## REFERENCES

1. Yu. I. Bobrovnitskiĭ, Akust. Zh. **45**, 301 (1999) [Acoust. Phys. **45**, 260 (1999)].
2. Yu. I. Bobrovnitskiĭ, J. Sound Vibr. **217**, 351 (1998).
3. E. Skudrzyk, *Simple and Complex Vibratory Systems* (Pennsylvania State Univ. Press, Univ. Park, 1968; Mir, Moscow, 1971).
4. S. Karni, *Networks Theory: Analysis and Synthesis* (Allyn and Bacon, Boston, 1966; Svyaz', Moscow, 1973).
5. M. M. Lavrent'ev, *Some Ill-Posed Problems of Mathematical Physics* (Sib. Otd. Ross. Akad. Nauk, Novosibirsk, 1962).
6. I. S. Berezin and N. P. Zhidkov, *Computing Methods* (Fizmatgiz, Moscow, 1962; Pergamon, Oxford, 1965).
7. G. Baker and P. Graves-Morris, *Padé Approximations*, Part I: *Basic Theory* (Addison-Wesley, Reading, 1981; Mir, Moscow, 1986).
8. B. Ya. Levin, *Root Distribution of Integral Functions* (Gostekhizdat, Moscow, 1956).
9. *Vibration in Engineering: A Reference Book*, Ed. by V. V. Bolotin (Mashinostroenie, Moscow, 1978), Vol. 1.

*Translated by M. Lyamshev*

*Acoustical Physics, Vol. 46, No. 6, 2000, pp. 663–669. Translated from Akusticheskiĭ Zhurnal, Vol. 46, No. 6, 2000, pp. 756–763.*


# Experimental Studies of Low-Frequency Bistatic Reverberation in a Shallow Sea

**D. V. Guzhavina and É. P. Gulin**

*Andreev Acoustics Institute, Russian Academy of Sciences, ul. Shvernika 4, Moscow, 117036 Russia*

*e-mail: bvp@akin.ru*

Received November 12, 1999

**Abstract**—Experimental data are presented on time and frequency dependences of the reverberation level for bistatic transmission and reception at low acoustic frequencies. The data are obtained from the studies carried out in a coastal shallow-water region and in the central region of the Barents Sea with explosion-generated and pulsed cw signals. By using the simplest computational model, approximate estimates are obtained for the effective coefficient of spatial attenuation and the effective scattering coefficient in the frequency band 40–400 Hz.


In numerous publications on the sea reverberation (the information on these studies can be found, e.g., in monographs and reviews [1–7]), not much experimental data are available on the low-frequency (below 500 Hz) reverberation in shallow sea. Not long ago, these data were actually limited to those published in [4, 8–10], which dealt with power and correlation characteristics of reverberation generated by explosive sound sources. Also, there is insufficient information on the low-frequency reverberation for the case of a spatially separated source and receiver (the bistatic case) in a waveguide, when the distance between them is comparable with that to the scattering region, or even exceeds it [4, 11]. In recent years, a number of publications [12–19] appeared that present experimental data on the low-frequency reverberation for shallow-water regions, including the shelf zone of the ocean, for both monostatic and bistatic experimental layouts.

Here, we consider the data of the experiments carried out in the 1980s, in two regions of the Barents Sea, with the use of both pulsed cw signals and explosion-generated ones. The experiments were performed in the summer–autumn season, with a negatively refracting medium and a near-bottom sound channel. The wind speed was 4–5 m/s, the sea state was not higher than Beaufort 3. In the first region, the signal was received by hydrophones of a multielement linear array, which was bottom-moored in the coastal zone near Murmansk, at the depth about 135 m. At different distances (25 to 85 km) from the receiving system, at a depth of about 100 m, charges of 200 g in mass were exploded. On a path oriented from south to north, the sea depth increased from 135 m at the reception point to 200 m at a distance of 30 km, and then to 240 m at a distances of 80–90 km. On another path oriented from east to west, the sea depth varied from 130 to 145 m. According to the data of continuous echo-sounding along the path, the bottom microrelief at the experimental site can be characterized by distances between bottom rises and depressions 0.5 to 3 km, by depth differences 5 to 12 m, and by bottom slope angles 1°–1.5°. The bottom structure in this region is characterized by strong spatial inhomogeneity. On the background of a smooth bottom slope, features of a glacial nature (hills, billows, and knolls) are observed with outcrops of boulders, pebbles, and gravel onto the water–sediment interface. The studies showed a wide spread in the values of the acoustical parameters of the bottom even for a single sediment type. On average, the density of the upper sediment layer is 1.5–1.7 g/cm$^3$, the sound speed is 1550–1750 m/s, and both these quantities decrease as the distance from the coast and the sea depth increase.

Figure 1 presents examples of envelopes of the received explosion-generated signals after filtering in 1/3-octave bands at different frequencies from 40 to 400 Hz and integrating over 0.25-s time intervals. One can clearly distinguish the arrivals of the direct signal with the effective duration less than 1 s and the reverberation background whose level decreases as the time delay $t_d$ relative to the direct arrival increases. For rather high separation (25 km) of the source and receiver and for time delays lower than 10–20 s, the observed reverberation is formed by both backscattering and side-scattering, which sometimes can be accompanied by a considerable increase in the reverberation level. For the low frequencies at hand, the dominant factor is the boundary reverberation caused by scattering from inhomogeneities of the upper sediment layer, from the rough relief of its boundaries, and from the rough sea surface.

The analysis of the records showed that, as the frequency becomes lower, the reverberation level noticeably decreases relative to the levels of the direct signal and interfering noise, and the effective reverberation

1063-7710/00/4606-0663$20.00 © 2000 MAIK "Nauka/Interperiodica"

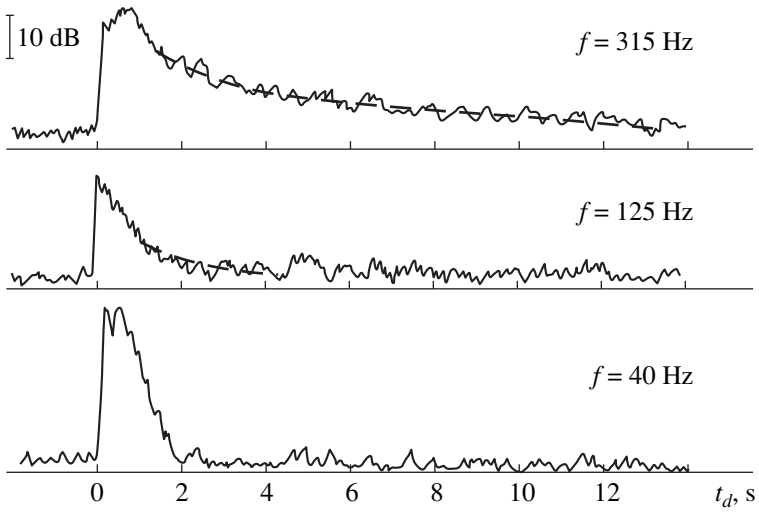


**Fig. 1.** Examples of envelopes of the direct signal and the reverberation in the 1/3-octave filter band at different frequencies for the source–receiver separation $r_{12}$ = 25 km. An explosive source, coastal region, path 1.

duration shortens. At the frequencies 400 and 315 Hz, traces of the reverberation can be found at times up to 15–20 s, at the frequencies 160–250 Hz, they extend up to 5–10 s, and, at 80–125 Hz, the reverberation is hidden under the interfering noise within 3–4 s after the direct arrival. Figure 2 presents the frequency dependences of the ratio $\delta = (I_r + I_n)/I_{ds}$, where $I_{ds}$ is the intensity of the direct signal, $I_r$ is the reverberation intensity at different delays $t_d$, and $I_n$ is the intensity of the interfering noise. At $t_d$ = 2–4 s, when the reverberation overrides the noise at all frequencies except for 40 Hz, the ratio $\delta$ decreases as the frequency increases. At $t_d$ = 6 s, the frequency dependence of $\delta(f)$ is affected by the frequency dependences of $I_n(t)$ and $I_{ds}(t)$, because the interfering noise becomes comparable with the reverberation in its level and begins to noticeably exceed it at frequencies lower than 250 Hz when $\Delta t_d \geq 10$ s. The increase in $\delta$ observed with decreasing frequency within the band 100–400 Hz is governed by the weak frequency dependence of the signal spectral density in this band and by the decrease in the spectral density of the interfering noise with frequency. According to the performed analysis, a sharp decrease in $\delta$ at the frequency 40 Hz is associated with the considerable decrease in the noise level rather than with interference effects in the field of the direct signal. Comparison of the ratios $\delta$ for different spatial separations of the source and receiver showed no pronounced dependence on the separation (Fig. 3) for sufficiently low delays ($t_d$ = 2–4 s), when $\delta$ is close to the relative reverberation level (RRL) measured with respect to the level of the direct signal. The spread of the values of $\delta$ is caused mainly by the interference in the field of the direct signal. On average, for the separation (distances) within 25–85 km, at frequencies 80–400 Hz, and for $t_d$ = 3–6 s, the RRL somewhat decreases as the separation increases.

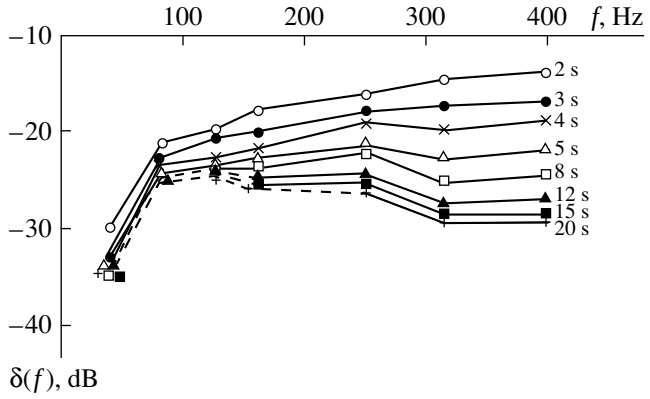


**Fig. 2.** Frequency dependences of the ratio $\delta$ of the total intensity of reverberation $I_r$ and interfering noise $I_n$ to the intensity $I_{ds}$ of the direct signal for different time delays $t_d$. Coastal region, path 1, $r_{12}$ = 25 km.

In Fig. 4, examples are presented of the signal envelopes for a source–receiver separation of 31 km along the path passing from east to west. On the background of the smoothly decaying average level of reverberation, an additional maximum can be seen within approximately 3 s from the beginning of the direct signal. This maximum is caused by the side reflection from the island coast (to be more precise, by refraction of the low-frequency sound field in the coastal wedge). This is confirmed by the calculation of the ellipses of scattering for different time delays $t_d$ and the relative source and receiver positions at hand. At the frequency 400 Hz, the level of the near-field reverberation ($t_d$ = 2–4 s) is so high that the coastal reflection is nearly invisible against it. As the frequency decreases, the level of the near-field reverberation noticeably decreases, and, therefore, the coastal signal is clearly seen. The highest level of the coast-reflected signal, which was observed

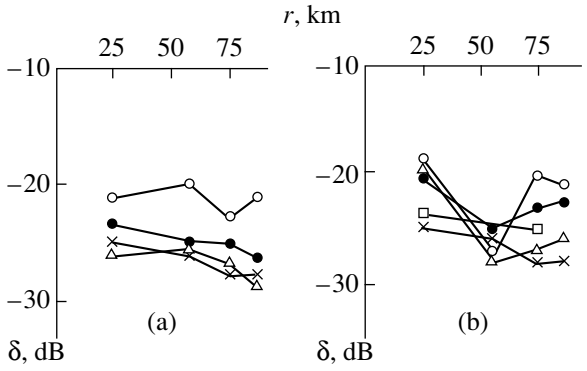


**Fig. 3.** Dependences of the ratio δ on the separation of the receiver and an explosive source (a) for different time delays $t_d$ at the frequency 100 Hz and (b) at different frequencies for the time delay $t_d$ = 4 s. (a) $t_d$ = (○) 2, (●) 3, (×) 4, and (△) 6 s; (b) $f$ = (○) 400, (●) 315, (△) 200, (×) 100, and (□) 80 Hz.

at the frequencies 100–315 Hz, is by as little as 5–7 dB lower than the level of the direct signal. The coast reflection leads to a considerable increase in the reverberation level for the time delays 3–4 s but, at $t_d > 5$ s, the difference between the reverberation levels observed on the two studied paths becomes insignificant. At $f$ = 40 Hz, both the coast-reflected signal and the reverberation background are masked by the interfering noise. Note that the envelopes shown in Fig. 4 were obtained without the 0.25-s integration, and, therefore, the fluctuations of the reverberation level and interfering noise are higher than in Fig. 1.

The reverberation levels were also compared at the separated hydrophones of the multielement linear array. The comparison showed that only for the shortest distance between the receivers (7.5 m) and for time delays lower than 3 s does a partial correlation remain in the space–time fluctuations of the envelopes at the frequencies of 80–200 Hz (the correlation coefficient was 0.5–0.6). At higher frequencies and with receiver separations of 15 m or more, the fluctuations become nearly uncorrelated. In the sequence of explosions that were performed each 30–60 s, the reverberation envelopes obtained at 80–400 Hz poorly replicate each other in detail, although the explosion depths were kept virtually constant and the distance to the receiving array varied by less that 10–20 m due to the vessel drift.

In the same coastal region, low-frequency narrowband sound sources deployed at the depth 50 m were used for sensing the sea medium with pulsed cw signals. These signals had carrier frequencies of 100 and 300 Hz, durations of 0.5 s, and a repetition rate of 15 s. In the experiments, the transmitting vessel drifted at a distance of 6.5 km, north from the bottom-moored receiving array. Figure 5 shows examples of the envelopes of the received signals filtered within the 3% band. When measured relative to the level of the direct signals, the 300-Hz reverberation level was signifi-

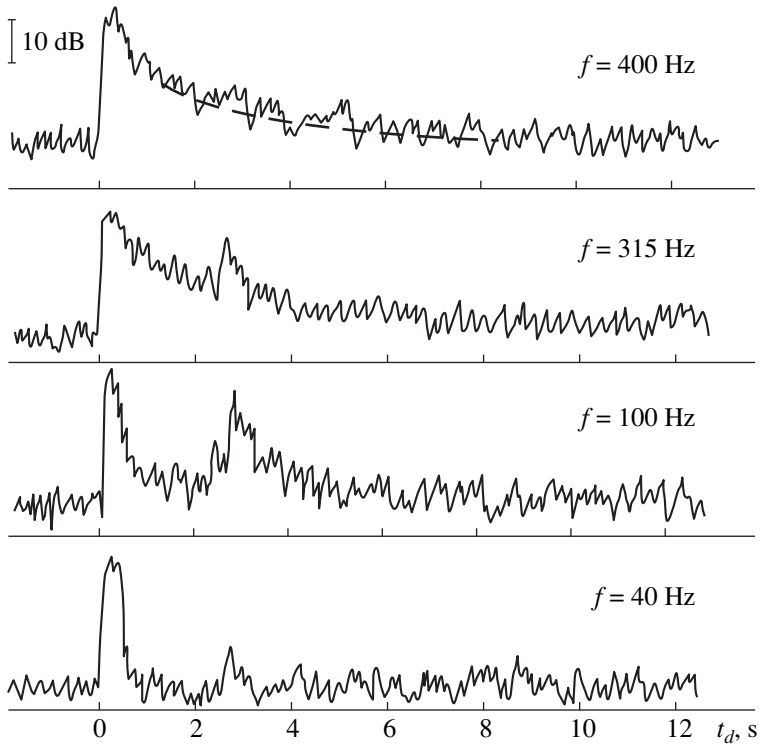


**Fig. 4.** Examples of envelopes of the direct signal and reverberation at different frequencies for the source–receiver separation 31 km. An explosive source, the coastal region, path 2.

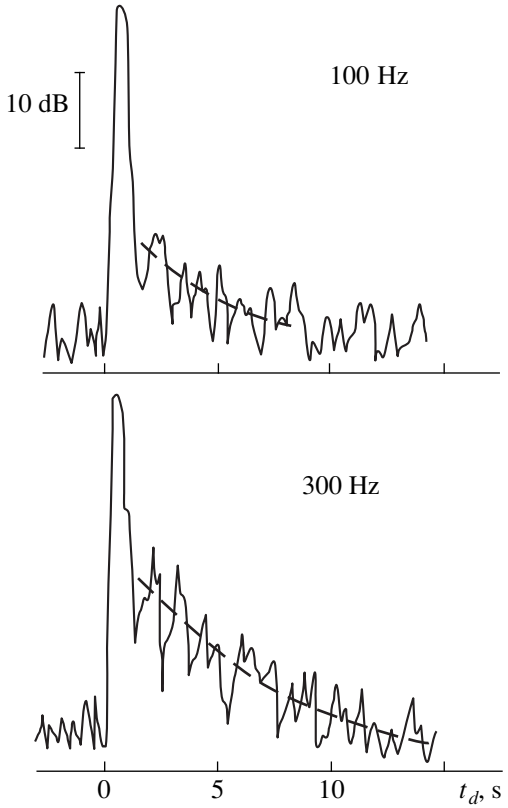


**Fig. 5.** Examples of envelopes of the direct signal and reverberation for the pulsed cw transmission at the frequencies 100 and 300 Hz in the coastal region. The source and receiver are separated by 6.5 km.

cantly higher than that at 100 Hz; it decays down to the level of the interfering noise in a time that is somewhat longer than the repetition period (15 s) of the pulses. At 100 Hz, the reverberation time (time of decay down to the noise level) is not higher than 3–4 s. On average, the RRL values insignificantly differ for the pulsed cw and explosion-generated signals at both frequencies.

From the periods of the beats in the reverberation envelope obtained with the pulsed cw signals of a long duration (2 min), approximate estimates were obtained for the effective width of the reverberation spectrum at the frequencies 100 and 320 Hz, with towing the sound sources at the speed about 3 k. For source–receiver separations of 9–12 km, the beat periods observed in different realizations after the direct arrivals were 5, 10, 3, 6, and 10 s at the frequency 100 Hz, and 2.5–3, 5, 2, 3, and 4 s at 320 Hz. These values correspond to the spectral components that are separated by 0.1–0.3 Hz at $f$ = 100 Hz and 0.2–0.5 Hz at $f$ = 320 Hz. The observed increase in the width of the reverberation spectrum (relative to the spectrum of the emitted signal) can be caused both by scattering from the rough sea surface and by bottom scattering that, with the moving source, leads to Doppler frequency shifts depending on the arrival direction of the scattered signals.

The second studied region was in the Central Hollow of the Barents Sea. According to the echo-sounding data, the sea depth here varied from 350 to 375 m. In geomorphologic terms, the sea bottom in the region is classified as "sub-horizontal accumulative surfaces of hollows." Within a rather thick (up to 50 m) layer of the bottom sediments (mainly clay and aleuritic-clay silts), the density and sound speed were 1.4–1.6 g/cm$^3$ and 1460–1500 m/s, respectively. At distances of 1.7–17.5 km from the drifting receiving vessel, 330-g charges were exploded at the depths 150 and 300 m. The signals were received by an omnidirectional hydrophone at a depth of 100 m. The data obtained in this relatively deep-water region of the Barents Sea are shown in Fig. 6. The shown reverberation envelopes decay more slowly than those obtained in the coastal region. At frequencies higher than 100 Hz, the reverberation time exceeds 20 s, and, at the frequencies 50–100 Hz, it decreases down to 5–10 s because of the increase in the noise level. Note that similar examples of the explosion-generated signals are reported in [20] to illustrate the shapes of low-frequency arrivals on a path in the central region of the Barents Sea. The noticeable difference between the shapes of the signals received at 20 km from the explosive source in [20] and our signals received at 25, 31, and 1.7 km (Figs. 1, 4, 6) testifies to a high spatial variability of the medium (in particular, the variability of the scattering properties of the bottom), which governs the low-frequency reverberation in the Barents Sea.

Figure 7 shows the frequency dependences of the reverberation level obtained in the central region for two distances between the source and receiver and three values of the time delay $t_d$. At 0 dB, we use the spectral level of the explosion-generated signal that is normalized to a 1-m distance for the field of a spherical wave and averaged over the filter band. This level was calculated for a given mass of the charge and a given explosion depth (see [4], p. 117). The values shown in Fig. 7 and taken with the opposite sign can be conditionally called losses due to propagation and scattering. This quantity, experimentally estimated for different distances and delays, weakly depends on the frequency within the band 60–500 Hz. When the source–receiver separation increases from 1.7 to 14.2 km, the losses increase up to 4–8 dB for the same time delays. For the band 60–500 Hz and the delays $t_d$ = 3–10 s, the propagation and scattering losses are within 85–98 dB (according to the data of Fig. 7).

To interpret the experimental data on bistatic low-frequency reverberation in the Barents Sea, consider the simplest semiphenomenological model for boundary reverberation in a shallow-water waveguide. Assuming incoherent scattering, for the time delay $t_d$ relative to the direct arrival, one can represent the bistatic reverberation intensity as follows:

$$I_r(t_d) = I_0 \int\int_S m_s \eta_1 \eta_2 ds, \qquad (1)$$

where $I_0$ is the intensity of the direct field at a unit distance in the zone of spherical spread of the wavefront (the normalized transmitting level); $m_s$ is the scattering coefficient; and $\eta_1$ and $\eta_2$ are the attenuation coefficients on the path from the source to the elementary scattering area and from the latter to the reception point, respectively. Integration is performed over scattering areas of the waveguide boundaries that form reverberation at the time delay $t_d$. If the distance from the sound source is long as compared to the thickness of the water layer, we have $\eta_1 = (A_{13}/r_{13}^2) \times 10^{-0.1\beta r_{13}}$ and $\eta_2 = (A_{23}/r_{23}^2) \times 10^{-0.1\beta r_{23}}$, where $r_{13}$ and $r_{23}$ are the horizontal distances from the elementary area to the source and receiver, respectively; $A_{13}$ and $A_{23}$ are the coefficients that determine the anomaly of the sound field at distances $r_{13}$ and $r_{23}$; and $\beta$ is the effective coefficient of spatial attenuation (in dB/km) ($r_{13}$ and $r_{23}$ should be expressed in km). Expression (1) can be considerably simplified if we assume that the coefficients $A_{13}$ and $A_{23}$ are determined by the relations $A_{13} = r_{13}/r_0$ and $A_{23} = r_{23}/r_0$, where the transition distance $r_0$ does not depend on the position of the scattering area relative to the source and the receiver. Then, we can introduce the effective scattering coefficient $\overline{m}_s$ that does not depend on the distance and the azimuth angle. Suppose also that, within the scattering area, the factor which governs the spatial attenuation can be factored out from under the integral sign. Then, Eq. (1) is reduced to

$$I_r(t_d) = (I_0/r_0) \times 10^{-0.1\beta(\bar{c}t_d + r_{12})} \overline{m}_s \iint ds/(r_{13}r_{23}), \quad (2)$$

where the substitution $r_{13} + r_{23} = \bar{c}\,t_d + r_{12}$ is made. Here, $r_{12}$ is the distance between the source and the receiver and $\bar{c}$ is the average horizontal velocity of sound propagation in the waveguide. For the duration $T$ of the emitted pulsed signal, the integration domain at the scattering surface (more precisely, at two scattering boundaries of the waveguide) is bounded by two ellipses with major semiaxes $a_1 = 0.5(r_{12} + \bar{c}\,t_d)$ and $a_2 = 0.5[r_{12} + \bar{c}\,(t_d + T)]$. Upon integration on the assumption that $\bar{c}\,T \ll \bar{c}\,t_d + r_{12}$, we obtain

$$I_r(t_d) \cong 2\pi\overline{m}_s[1 + 2r_{12}/(\bar{c}t_d)]^{-1/2} \times (I_0/r_0^2)(T/t_d) \times 10^{-0.1\beta(r_{12} + \bar{c}t_d)} \quad (3)$$

or, relative to the level of the direct signal, for $r_{12} \gg r_0$,

$$I_r(t_d)/I_{ds} \cong 2\pi\overline{m}_s(r_{12}/r_0)(T/t_d) \times [1 + 2r_{12}/(\bar{c}t_d)]^{-1/2} \times 10^{-0.1\beta\bar{c}t_d}. \quad (4)$$

The expressions obtained above can be used to estimate the effective coefficient of spatial attenuation and the effective scattering coefficient from the known parameters $I_0$, $T$, and $r_{12}$; the estimated values of $r_0$ and $\bar{c}$; and the experimentally determined values of the reverberation intensity $I_r$ or ratio $I_r(t_d)/I_{ds}$. Equations (3) and (4) can also be used in the case of explosion-generated signals. In this case, the duration $T$ of the emitted signal in Eq. (3) should be replaced by the effective duration $T_{\text{eff}}$ of the received signal, in view of its protraction in the conditions of multimode propagation in the waveguide. In Eq. (3), it is more convenient to change from the normalized transmission level to the total signal energy $E$ within the filter band. Then, expression (3) can be reduced to the form

$$I_r(t_d) = \pi E W^2 \bar{c}\overline{m}_s\tilde{r}[1 - (r_{12}/2\tilde{r})^2]^{-1/2}, \quad (5)$$

where $W^2$ means the attenuation coefficient

$$W^2 = \tilde{r}^{-2}r_0^{-2} \times 10^{-0.2\beta\tilde{r}} \quad (6)$$

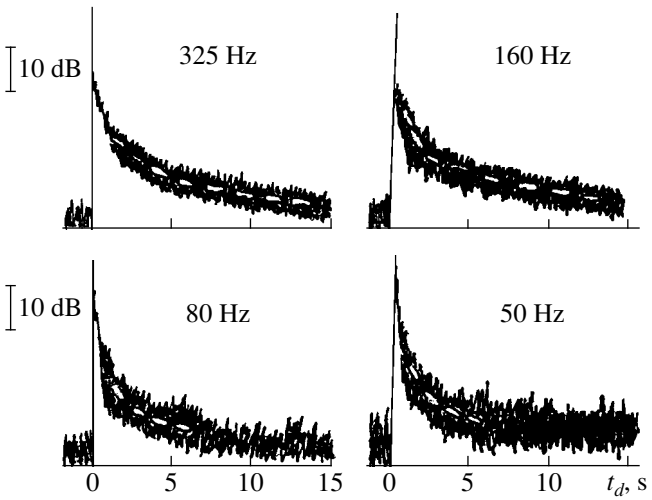


**Fig. 6.** Examples of envelopes of the direct signal and reverberation in the 1/3-octave filter band at different frequencies for the source–receiver separation 1.7 km. An explosive source, the central region.

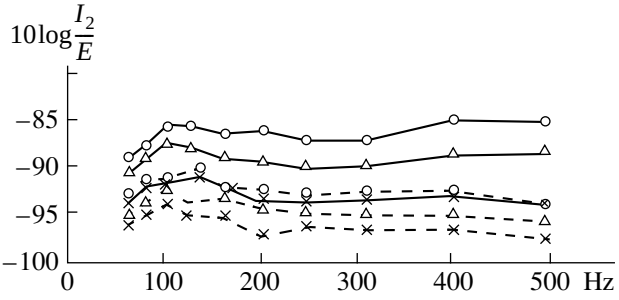


**Fig. 7.** Frequency dependences of the average reverberation level relative to the level of transmission for different time delays $t_d$ and separations $r_{12}$ of the receiver and an explosive source: the data obtained in the central region for $t_d$ = (○) 3, (△) 5, and (×) 10 s; $r_{12}$ = (—) 1.7 and (- - -) 14.2 km.

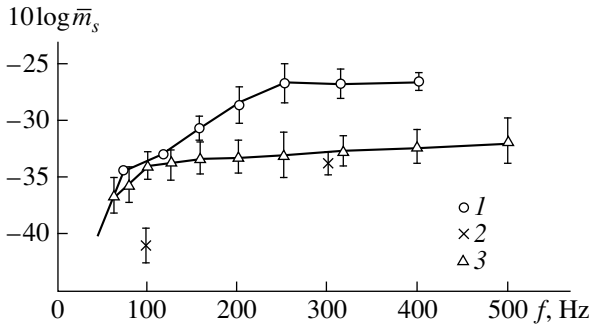


**Fig. 8.** Frequency dependences of the effective scattering coefficient calculated from the low-frequency reverberation data obtained in the (*1*, *2*) central and (*3*) coastal regions of the Barents Sea with the use of (*1*, *3*) explosion-generated and (*2*) pulsed cw signals.

and $\tilde{r} = 0.5\,(r_{12} + \bar{c}\,t_d)$. At $r_{12} = 0$, i.e., for the source and receiver being coincident in space, Eq. (5) coincides with the formula presented in [4].

With Eqs. (3)–(5), the values of $\beta$ and $m_s$ were estimated for the experiment in the Barents Sea at different frequencies. In accordance with the obtained data on the range dependences of the averaged sound intensity (the propagation loss), the value of $r_0$ was specified to be 250 m for the coastal region and 350 m for the central region. By applying the least squares method and using Eq. (3), it was shown that the values $\beta \cong 0.7$–$0.75$ dB/km yield the best approximation to the time dependences of the average reverberation intensities $I_r(t_d)$ for the coastal region in the case of a large separation ($r_{12}$ = 25 km) of the explosive source and the receiver (the corresponding approximating curves are shown in Figs. 1, 5, 6). These values weakly depend on frequency within the band 100–400 Hz. For the pulsed cw transmissions in the same region, $\beta \cong 0.7$ dB/km at the frequency 300 Hz and $\beta \cong 0.9$ dB/km at the frequency 100 Hz. According to the data of the studies with explosions in the central region, the attenuation coefficient decreases from 0.4 dB/km at the frequencies 300–500 Hz to 0.2–0.3 dB/km at the frequencies 100–160 Hz and to 0.1 dB/km at 60–80 Hz. For the two studied regions of the Barents Sea, the differences in the spatial attenuation coefficients and in their frequency dependences are mainly caused by the difference in sea depths and bottom structures in these regions. Note that the estimates of $\beta$ obtained by processing the dependences characterizing the reverberation decay with time agree well with the data on the spatial attenuation of the direct low-frequency signals on paths of several tens of kilometers in length. At the same time, on longer paths (100–200 km) in the Barents Sea (see [21]), the effective coefficient of spatial attenuation is lower than the aforementioned values. This is explained by the strong attenuation of rapidly decaying high-order modes, which significantly contribute to the field at short distances.

The obtained attenuation coefficients were used to estimate the effective scattering coefficient $\bar{m}_s$ at different frequencies. At the frequencies 40 and 80 Hz, for the coastal region, the values of $\beta$ were set to be equal to 1.5 and 1 dB/km, respectively, according to the measurements in the direct field. The frequency dependences of $\bar{m}_s$ are shown in Fig. 8. The observed decrease in the effective scattering coefficient agrees well with the data presented in [4]. The spread of the values of $\bar{m}_s$ is caused by both the inaccuracy of the method and the use of different values of $t_d$ and $r_{12}$ in estimating the scattering coefficient by Eqs. (3)–(6). Rather high values of the scattering coefficient $\bar{m}_s$ (from –25 to –40 dB) show that the bottom reverberation predominates, which is typical of negative refraction in a shallow sea. Noticeable differences exist in the values of $\bar{m}_s$ obtained for the coastal and central regions at frequencies higher than 150 Hz (at 200–400 Hz, the values of $\bar{m}_s$ are by 5–6 dB higher in the coastal region than in the central one). These differences presumably are caused by different characteristics of the bottom scattering and different effective grazing angles of the power-significant rays (modes) near the bottom in the two regions. At lower frequencies, the effect of the refraction phenomena becomes weaker. This fact can be a reason for the smaller differences in the values of $\bar{m}_s$ obtained in the studied regions at frequencies lower than 150 Hz. For pulsed cw signals, $\bar{m}_s$ was estimated according to Eq. (4). The underestimated values of $\bar{m}_s$ obtained at 100 and 300 Hz for the pulsed cw signals can be explained by the fact that, in the data processing, realizations were used with sufficiently high signal-to-noise ratios, which corresponded to the interference maximums of the sound field.

With formulas (5) and (6) in view of the estimated $\beta$, we also calculated the ratios of the reverberation intensities for the source–receiver distances $r_{12}$ = 1.7 and 14.2 km with equal time delays ($t_d$ = 3, 5, and 10 s). This calculation was performed for the conditions of the central region. The resulting values of 5–7 dB agree well with the experimental data (4–8 dB).

In the case of time delays that exceed the effective duration of the received signal, with sufficiently large source–receiver separations ($r_{12} \gg r_0$), the near-field reverberation produced by bottom and surface scattering is superimposed on multiple reflections from the bottom and surface. To estimate their contribution, we calculated the ray structure of the sound field for a waveguide whose parameters corresponded to the experimental conditions. In the calculations, the medium was modeled by an inhomogeneous liquid layer overlying an absorbing homogeneous liquid halfspace. For the specified values $h$ = 135 m (the sea depth), $r_{12}$ = 5–25 km, and $\beta$ = 0.7–1 dB/km (the bottom parameters were selected to provide the spatial attenuation with the given values

of β), the calculated level of the bottom-surface reflections rapidly decays in time, and, already at $t_d \cong 1.5$–2 s, it becomes 30–40 dB lower than the level of the direct field and, hence, lower than the observed level of the near-field reverberation. Similar calculations performed for the environment of the central region at $r_{12} = 20$ km showed that the observed reverberation levels exceed the level of the bottom reflections at delays $t_d \geq 2$–3 s.

In conclusion, it should be noted that the introduction of the effective scattering coefficient for predicting the average level of bistatic low-frequency reverberation in a shallow sea is expedient for at least two reasons. The first one consists in the small difference between the effective coefficients of spatial attenuation, which are determined from the decay of the level of the direct field with distance and from the decay of the reverberation level with time in the framework of the simplest model. The second reason is associated with the small spread of the values of $\overline{m}_s$ obtained for different time delays $t_d$ and source–receiver separations. For a more detailed analysis of the experimental data, more complicated reverberation models should be used that account for the refraction and multiray (multimode) nature of sound propagation in a shallow sea [22–24].

## ACKNOWLEDGMENTS

We are grateful to L.F. Bondar', G.A. Bakhtin, V.I. Moiseenkov, and A.V. Prudnikov for assistance in the experiments.

## REFERENCES

1. V. V. Ol'shevskiĭ, *Statistical Properties of Sea Reverberation* (Nauka, Moscow, 1966).
2. C. W. Horton, J. Acoust. Soc. Am. **51**, 1049 (1972).
3. *Ocean Acoustics*, Ed. by L. M. Brekhovskikh (Nauka, Moscow, 1974), pp. 371–394; pp. 451–490; pp. 493–558.
4. R. J. Urick, *Principles of Underwater Sound* (McGraw-Hill, New York, 1975; Sudostroenie, Leningrad, 1978).
5. V. V. Ol'shevskiĭ and T. A. Moroz, *Theoretical and Experimental Studies of Sea Reverberation* (TsNII Rumb, Leningrad, 1976).
6. A. V. Bunchuk and Yu. Yu. Zhitkovskiĭ, Akust. Zh. **26**, 641 (1980) [Sov. Phys. Acoust. **26**, 363 (1980)].
7. V. V. Ol'shevskiĭ, *Statistical Methods in Underwater Detection and Ranging* (Sudostroenie, Leningrad, 1983).
8. R. J. Urick, J. Acoust. Soc. Am. **48**, 392 (1970).
9. R. J. Urick and G. R. Lund, J. Acoust. Soc. Am. **47**, 342 (1970).
10. R. J. Urick and G. R. Lund, J. Acoust. Soc. Am. **47**, 909 (1970).
11. J. L. Stewart, J. Acoust. Soc. Am. **71**, 915 (1982).
12. V. S. Averbakh, L. F. Bondar', V. N. Golubev, *et al.*, Akust. Zh. **36**, 1119 (1990) [Sov. Phys. Acoust. **36**, 625 (1990)].
13. I. B. Andreeva and V. N. Lupovskiĭ, Akust. Zh. **39**, 564 (1993) [Acoust. Phys. **39**, 297 (1993)].
14. M. Yu. Andreev, Akust. Zh. **39**, 751 (1993) [Acoust. Phys. **39**, 395 (1993)].
15. D. I. Abrosimov, V. S. Averbakh, E. I. Bolonicheva, *et al.*, Akust. Zh. **41**, 364 (1995) [Acoust. Phys. **41**, 315 (1995)].
16. R. A. Vadov, D. V. Guzhavina, and S. I. Dvornikov, Akust. Zh. **43**, 409 (1997) [Acoust. Phys. **43**, 350 (1997)].
17. Shishido Masaaki, J. Acoust. Soc. Jpn. **53**, 552 (1997).
18. K. L. Williams and D. R. Jackson, J. Acoust. Soc. Am. **103**, 169 (1998).
19. D. H. Berman, J. Acoust. Soc. Am. **105**, Part 1, 672 (1999).
20. N. V. Studenichnik, Akust. Zh. **42**, 134 (1996) [Acoust. Phys. **42**, 119 (1996)].
21. N. K. Abakumova, in *Proceedings of the IX All-Russia Acoustical Conference* (Akust. Inst., Moscow, 1977), Sect. D, p. 5.
22. D. I. Abrosimov and L. S. Dolin, Akust. Zh. **27**, 808 (1981) [Sov. Phys. Acoust. **27**, 448 (1981)].
23. I. B. Andreeva and V. N. Goncharov, in *Problems of Ocean Acoustics* (Nauka, Moscow, 1984), pp. 69–77.
24. V. M. Kudryashov, Akust. Zh. **45**, 363 (1999) [Acoust. Phys. **45**, 320 (1999)].

*Translated by E. Kopyl*

*Acoustical Physics, Vol. 46, No. 6, 2000, pp. 670–675. Translated from Akusticheskiĭ Zhurnal, Vol. 46, No. 6, 2000, pp. 764–769.*


# Sound Scattering by a Karman Street Consisting of Large-Scale Vortices

**A. B. Ezerskiĭ, P. L. Soustov, and V. V. Chernov**

*Institute of Applied Physics, Russian Academy of Sciences, ul. Ul'yanova 46, Nizhni Novgorod, 603600 Russia*

*e-mail: ezer@appl.sci-nnov.ru*

Received December 30, 1999

**Abstract**—The scattering of acoustic waves by a vortex street formed behind a cylinder in an air flow is studied both theoretically and experimentally for the case of the sound wavelength being much less than the vortex size. The theoretical calculations show that, at flow velocities well below the sound velocity, the vortex street can be considered as a moving phase screen. The spectrum of scattered sound in the far zone is shown to consist of harmonics whose frequencies differ by a multiple of the vortex rate. The computational results agree well with the experimental data obtained for the diffraction of ultrasound of the wavelength $\lambda = 3$ mm by the Karman street formed behind a circular cylinder with an 8 mm diameter at a flow velocity of 7 m/s. © *2000 MAIK "Nauka/Interperiodica".*

## INTRODUCTION

Until now, the theoretical and experimental studies of sound scattering by a vortex wake behind a cylinder have been carried out for the case of the vortex core size being much less than the sound wavelength [1, 2]. In this case, the wake behind the cylinder can be approximated by a sequence of point vortices [1, 2]. Such an approximation made it possible to derive analytical expressions relating the flow parameters (the vortex rate, the spatial period, and the vortex circulation) to the spectrum of the scattered sound and to justify the method of remote acoustic sensing [3]. In practice, the point vortex approximation is often inappropriate. Even though it may be valid at short distances from the cylinder placed in a flow, it becomes incorrect at longer distances, because the size of vortices increases downstream due to the diffusion. A typical situation is that with the vortex core size being comparable to the sound wavelength or even much greater than it. The latter case is studied in this paper. We begin with describing the results of numerical calculations for the acoustic wave scattering by large-scale vortices. Then, relying on these results, we show that, in some cases, the scattering process can be analyzed by using a simple model that allows one to reduce the effect of vortices to phase distortions. In terms of this model, we calculate the spectrum of the scattered sound in the far zone. Finally, we present the results of the experiment performed in a wind tunnel and compare these results with our calculations.

## NUMERICAL ANALYSIS OF RAY PATHS

Let us consider the scattering of a plane sound wave by a two-dimensional Karman vortex street whose velocity field $\mathbf{U}(\mathbf{r}, t) = (U, V)$ is induced by vortices with a finite core size. We neglect the effects of viscosity and heat conduction and assume that the flow velocity is small as compared to the sound velocity $c$: $M = |\mathbf{U}|/c \ll 1$. From the linearized equations of motion of an ideal barotropic gas of density $\rho_0$, for the perturbations of density $\tilde{\rho}$ and the horizontal and vertical velocity components $\tilde{u}$ and $\tilde{v}$, we obtain:

$$\frac{\partial \tilde{u}}{\partial t} + U\frac{\partial \tilde{u}}{\partial x} + V\frac{\partial \tilde{u}}{\partial y} + \tilde{u}\frac{\partial U}{\partial x} + \tilde{v}\frac{\partial U}{\partial y} + \frac{c^2}{\rho_0}\frac{\partial \tilde{\rho}}{\partial x} = 0, \quad (1)$$

$$\frac{\partial \tilde{v}}{\partial t} + U\frac{\partial \tilde{v}}{\partial x} + V\frac{\partial \tilde{v}}{\partial y} + \tilde{u}\frac{\partial V}{\partial x} + \tilde{v}\frac{\partial V}{\partial y} + \frac{c^2}{\rho_0}\frac{\partial \tilde{\rho}}{\partial y} = 0, \quad (2)$$

$$\frac{\partial \tilde{\rho}}{\partial t} + U\frac{\partial \tilde{\rho}}{\partial x} + V\frac{\partial \tilde{\rho}}{\partial y} + \rho_0\left(\frac{\partial \tilde{u}}{\partial x} + \frac{\partial \tilde{v}}{\partial y}\right) = 0. \quad (3)$$

We assume that the characteristic length $L$ of the vortex field variation in the Karman street far exceeds the sound wavelength: $\lambda_a \ll L$. We represent the solution to Eqs. (1)–(3) in the form [4]

$$\begin{pmatrix} \tilde{u}(x, y, t) \\ \tilde{v}(x, y, t) \\ \tilde{\rho}(x, y, t) \end{pmatrix} = e^{-i\omega t}e^{i\omega\theta(x, y)}\begin{pmatrix} u(x, y) \\ v(x, y) \\ \rho(x, y) \end{pmatrix}, \quad (4)$$

where $\theta(x, y)$ is the eikonal.

1063-7710/00/4606-0670$20.00 © 2000 MAIK "Nauka/Interperiodica"

Assuming that the frequency $\omega$ is a large parameter, we retain only the terms of the highest order in $\omega$ in Eqs. (1)–(3); then, we obtain

$$\left(U\frac{\partial\theta}{\partial x} + V\frac{\partial\theta}{\partial y} - 1\right)u + \frac{c^2}{\rho_0}\rho\frac{\partial\theta}{\partial x} = 0, \quad (5)$$

$$\left(U\frac{\partial\theta}{\partial x} + V\frac{\partial\theta}{\partial y} - 1\right)v + \frac{c^2}{\rho_0}\rho\frac{\partial\theta}{\partial x} = 0, \quad (6)$$

$$\left(U\frac{\partial\theta}{\partial x} + V\frac{\partial\theta}{\partial y} - 1\right)\rho + \rho_0\frac{\partial\theta}{\partial x}u + \rho_0\frac{\partial\theta}{\partial y}v = 0. \quad (7)$$

For the system of Eqs. (5)–(7) to have a nonzero solution, its determinant must be equal to zero. The latter condition yields

$$(Uf + Vg - 1)((Uf + Vg - 1)^2 - c^2(f^2 + g^2)) = 0. \quad (8)$$

Here, $f = \partial\theta/\partial x$ and $g = \partial\theta/\partial y$. It can be readily seen that the solution to the equation $Uf + Vg - 1 = 0$ corresponds to disturbances carried by the flow rather than to an acoustic wave. We will seek the solution to Eq. (8) on the assumption that the first factor in Eq. (8) is nonzero.

To determine the solution, we used the method of characteristics (see, e.g., [5]). For this purpose, we introduced the ray parameter $z$. We determined the ray paths $(x(z), y(z))$ and the phase $\theta(z)$ correct to first-order terms in $M$ from the solution of a system of nonlinear first-order differential equations. In numerically calculating the acoustic ray paths, we used the model of a Karman street consisting of nonpoint vortices whose vorticity $\Omega$ was concentrated in a bounded region of radius $R_0$. We assumed that, for a single vortex with the circulation $\Gamma_0$, the vorticity had the form

$$\Omega = \begin{cases} \Gamma_0\dfrac{\cos\left(\pi\dfrac{R}{R_0}\right) + 1}{2}, & R < R_0 \\ \Omega = 0, & R > R_0. \end{cases} \quad (9)$$

The ray paths were calculated for fifty rays that were perpendicular to the mean line of the Karman street at $y = 10$ and were equidistant within the spatial period (Fig. 1). When the flow velocity is low (Fig. 1a), the ray paths are undistorted (compare with Fig. 1b showing the ray paths for higher velocities) and the wave amplitude remains constant. In this case, the effect of the vortex field on acoustic waves is reduced to an additional phase shift. From the eikonal $\theta(x, y)$, we eliminate the component that linearly grows with $y$, this component being the same for all fifty rays. Then, the quantity $\Psi(x) = \omega\theta(x, y) - ky$ will harmonically depend on the $x$ coordinate along the flow (see the solid line in Fig. 2). The period of the spatial modulation of the additional phase shift $\Psi$ coincides with the period of the vortex street, and the modulation amplitude can be of the order of $\pi$ even at low flow velocities. In terms of physics, this can be interpreted as follows. The vortex street consists of vortices rotating in opposite directions. When a ray passes through the vortex street (see Figs. 1a, 1b), the vortices from the upper and lower rows deflect the ray in opposite directions and their effects compensate

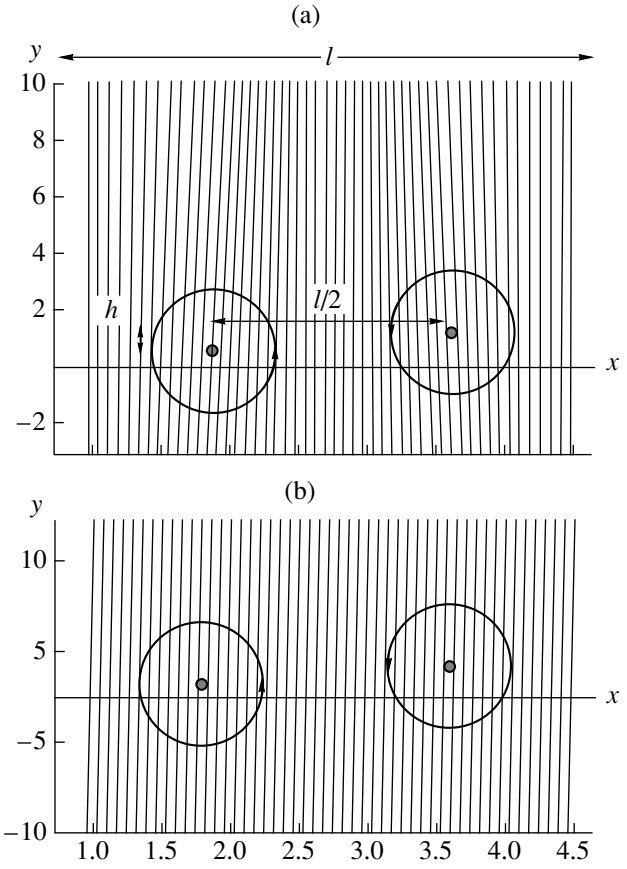


**Fig. 1.** Fifty ray paths uniformly distributed over the spatial period of the vortex street; the paths are calculated for $M$ = (a) 0.02 and (b) 0.1; all distances are normalized to the width of the vortex street $h$.

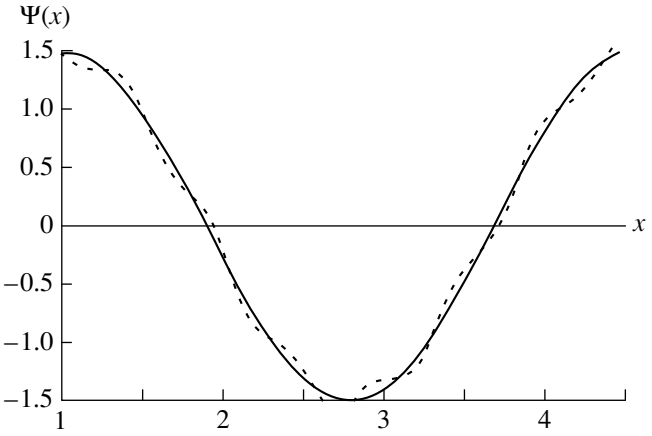


**Fig. 2.** Phase of the acoustic wave transmitted through the vortex street. The solid line corresponds to the numerical calculation by the ray theory, and the dotted line represents the calculation by the approximate formulas.

each other. For the additional phase shift, such a compensation does not occur and the effects of the vortices add up. Thus, in the case of low Mach numbers, the Karman street does not cause any curvature of rays and, for acoustic waves, it is equivalent to a phase plate. Using this result, we can analytically calculate the phase shifts for practically important cases.

## APPROXIMATE CALCULATION OF THE CHARACTERISTICS OF SOUND SCATTERED BY LARGE-SCALE VORTICES

The characteristics of the scattered sound were calculated as follows. In the geometric acoustics approximation, the Karman street is equivalent to a phase screen (as was shown above). Relying on this fact, we determined the phase modulation of the acoustic wave and, using the method of secondary sources (the Huygens–Fresnel principle), calculated the far field. Such a combination of the methods of geometric optics and secondary sources has been used in, e.g., studies of light scattering by large particles [6]. The necessity of applying the Huygens–Fresnel principle is related to the fact that we intend to consider the field at large distances from the vortex street. As was shown in the previous section, the ray curvature can be neglected only in the immediate vicinity of the vortex street. The accumulation of such a curvature will lead to the intersection of rays. The method used in our study allows one to correctly calculate the sound field at distances as long as one wishes.

For a plane acoustic wave propagating normally to the axis of the vortex street, the additional phase shift caused by the flow can be represented in the form

$$\partial\theta/\partial y \approx -V(x, y, t)/c\,. \tag{10}$$

In our calculations, we used the fact that the superposition principle is valid for Eq. (10) and represented the additional phase shift of the acoustic wave transmitted through the Karman street as a sum of the phase shifts caused by pairs of vortices with circulations of opposite signs. We calculated the phase shift caused by one pair of vortices and, then, performed the summation over an infinite number of pairs. When only point vortices are present and the rays are not curved, the additional phase shift that is caused by the vortices located at the points with the coordinates $x_+ = -l/4$, $y_+ = 2h$ and $x_- = +l/4$, $y_- = h$ has the form

$$\Psi(x, y) = \frac{\Gamma_0}{2\pi c}\left(\arctan\frac{x + \frac{l}{4}}{y - 2h} - \arctan\frac{x - \frac{l}{4}}{y - h}\right), \tag{11}$$

where $\Gamma_0$ is the vortex circulation.

For an infinite periodic vortex street consisting of vortices moving with the speed $U_0$, the additional phase shift is represented as the sum

$$\Psi(x, y, t) = \sum_n \frac{\Gamma_0}{2\pi c}\Phi_n(x, y, t),$$

$$\Phi_n(x, y, t) = \arctan\frac{x - U_0 t + nl + \frac{l}{4}}{y - 2} - \arctan\frac{x - U_0 t + nl - \frac{l}{4}}{y - 1}, \tag{12}$$

where $l$ is the period of the vortex street and $h = 1$ is the distance between the vortex rows (see Fig. 1).

To apply the Huygens–Fresnel principle, we place the plane of the secondary sources at a distance $y = y_\infty = 10$ from the vortex street axis. At large distances, the velocity fluctuations in the vortex street exponentially decrease and, at $y > 10$, the contribution of the eddy velocity field to the additional phase shift is small. To compare our theory with the experimental data, we used the following approach. We assumed that the vortex intensity depends on the $x$ coordinate along the flow in such a way that the vortex street is of finite length. This dependence can be represented by the empirical function

$$f(x) = \frac{\tanh(L - x) + \tanh(L + x)}{2}. \tag{13}$$

We assume that, for the vortex street, we have $L = 3l$, where $l$ is the spatial period of the vortex street. Such an approximation fits well the results of the direct measurements of velocity fluctuations behind the cylinder. With allowance for the variations in the vortex circulation, the phase can be represented in the form

$$\Psi(x, y, t) = f(x)\sum_n \frac{\Gamma_0}{2\pi c}\Phi_n(x, y, t). \tag{14}$$

This expression yields the additional phase shift, which, at $M = \frac{U_0}{c} = 0.02$, is close to that obtained from the exact calculation by the ray theory. Figure 2 presents the comparison between the additional phase shift calculated by the ray theory (the solid line) and that calculated by the approximate formula (12) (the dotted line). When a plane wave of amplitude $\rho_0$ is incident on the vortex street, the scattered sound field $\rho_{scat}$ formed at the distance $r$ from the vortex street can be

represented as an integral over the region of secondary sources:

$$\rho_{scat} = \frac{i\rho_0}{\lambda} e^{i\left(\frac{\pi}{4}+\omega t\right)} e^{-ik_0 r} \times \int_{-\infty}^{+\infty} \frac{1}{\sqrt{rk_0}} \left(1 - e^{\sum_n f(\zeta)\Phi_n(\zeta, y_0, t)}\right) e^{-ik_0 r} d\zeta, \quad (15)$$

where $r = \sqrt{\zeta^2 + r_0^2 - 2\zeta r_0 \sin\phi}$.

Our calculations showed that, in the case of the sound scattering by a vortex street having the form of a moving diffraction grating, the spectrum of scattered sound contains new harmonics with the frequencies $F = F_0 + nf_s$, where $F_0$ is the incident sound frequency, $f_s$ is the vortex separation frequency (the Strouhal frequency), and $n = \pm 1, \pm 2, \ldots$.

Figure 3 shows the calculated spectra of scattered sound for the incident wave of frequency $F = 120$ kHz when the length of the scattering region is $L = 12$ cm and the distance is $r = 120$ cm (the Fresnel parameter is $L/\sqrt{\lambda r} \approx 2$); the spectra were obtained for three different angles $\phi$. The choice of the parameters used for the calculations was determined by the conditions of the experiment, which will be described in detail in the following section. We note that, at greater distances, the spectra of scattered sound in the Fraunhofer diffraction region were similar to those shown in Fig. 3, but the difference in the amplitudes of the adjacent combination harmonics was 1–2 dB (compare with the spectra shown in Fig. 3).

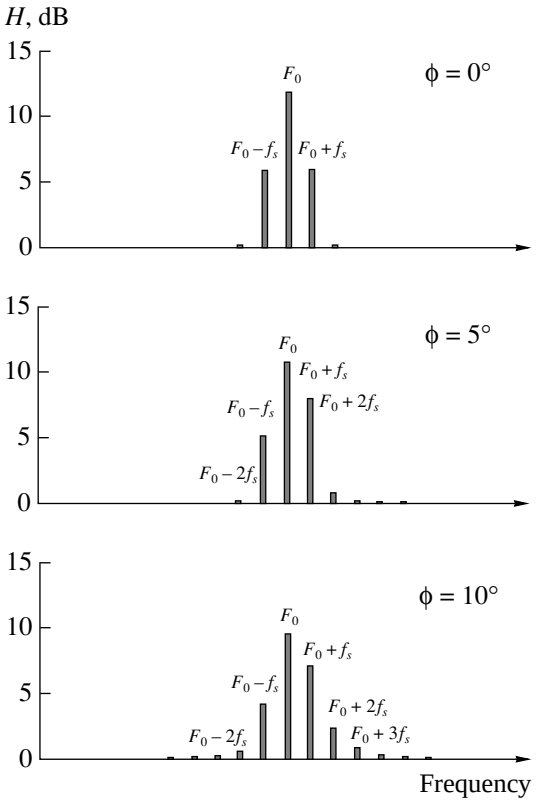


**Fig. 3.** Calculated spectra of scattered sound for different angles $\phi$.

## EXPERIMENT

The experiments on sound scattering by large-scale vortices were performed in a weak-turbulence wind tunnel belonging to the Institute of Applied Physics of the Russian Academy of Sciences. The schematic diagram of the experiment is shown in Fig. 4. We studied the scattering of ultrasound of frequency $F_0 = 120$ kHz by the vortex street behind a circular cylinder. The source of ultrasound (the radiator) was a piezoceramic transducer placed behind a screen with an opening of radius $r_{em} = 1$ cm. The screen was positioned at a distance $L_{em} = 65$ cm. The Fresnel parameter calculated for the radiator was $F_r = r_{em}/\sqrt{L_{em}\lambda} = 0.2$. The periodic vortex street was formed behind a cylinder of diameter $D = 8$ mm placed in the test section of the wind tunnel with the dimensions $30 \times 30$ cm$^2$; the flow velocity was $U = 7$ m/s. At this flow velocity, the Reynolds number was $\mathrm{Re} = UD/\nu \approx 3.7 \times 10^3$, where $\nu$ is the kinematic viscosity of air and $D$ is the diameter of the cylinder. The vortex separation frequency was $f_s = 190$ Hz, which corresponded to the Strouhal number $\mathrm{Sh} = f_s D/U \approx 0.21$. To measure the parameters of ultrasound, we used

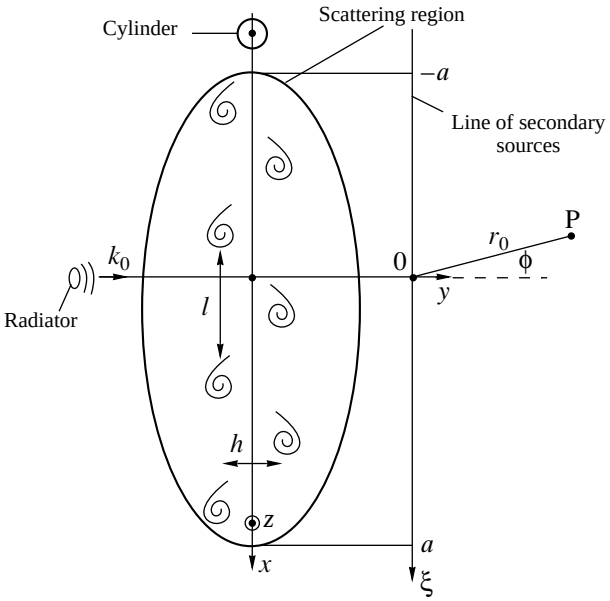


**Fig. 4.** Schematic diagram of the experiment.

a 4135 B&K high-frequency microphone; the electric signal from this microphone was transferred to the operating range of a 2034 B&K analyzer. The microphone facing the radiator was placed on the other side

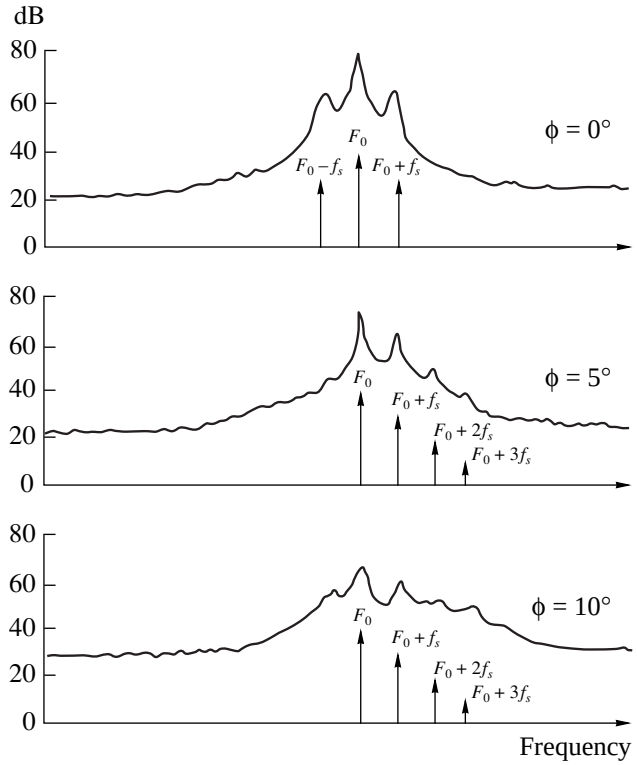


**Fig. 5.** Experimental spectra of scattered sound.

of the vortex street, at a distance $r_m \approx 1.5$ m from it. The Fresnel parameter calculated by the size of the scattering region, $L_{sc}$, was $F_r = L_{sc}/\sqrt{r_m\lambda} \approx 2$. Positioning the microphone at greater distances was hindered by two factors: an excessive amount of equipment in the room and an increase in noise masking the signal. In the course of the measurements, the microphone could be set at different angles to the direction of incident ultrasound to receive the acoustic radiation scattered by the vortices. Since the Fraunhofer diffraction condition was not fulfilled in the experiment, we recorded only the spectra of scattered ultrasound without determining the scattering patterns, as was done in our previous experiments [1, 2]. Figure 5 shows the scattering spectra for different scattering angles; each spectrum was obtained by averaging over ten independent realizations. In addition to the fundamental carrier frequency $F_0$, these spectra contain harmonics with the frequencies $F_0 \pm n190$ Hz. As one can see from Fig. 5, the ratio between the amplitudes of these harmonics depends on the angle $\phi$. As the scattering angle increases, the amplitudes of the higher combination harmonics increase, while the amplitude of the combination harmonic with $n = 1$ decreases.

## DISCUSSION

The theoretical (Fig. 3) and experimental (Fig. 5) spectra of acoustic waves prove to be qualitatively similar, if we compare the ratios between the amplitudes of harmonics as the functions of the scattering angle $\phi$. We note that the scattering spectra shown in Fig. 5 noticeably differ from those obtained in the previous experiments [1]. The main difference is that, earlier [1], only the scattering into the first combination harmonic ($n = 1$) was recorded; the amplitudes of all other harmonics were much smaller and virtually undetectable against the noise. The experiment described above provides the spectrum of scattered sound that contains a great number of harmonics (see Fig. 5). At first glance, this contradicts the fact (repeatedly mentioned in [1, 2]) that, in the Karman street, the fluctuation energy is mainly concentrated in the first harmonic. Nevertheless, this result correlates well with the calculations and can be interpreted in the following way. For acoustic waves, the vortex street represents a phase plate. In the case of the propagation of short-wave sound, the phase modulation index can be fairly large even at a low flow velocity (see the above theoretical consideration). In the case of a large index of the sinusoidal phase modulation, the signal should contain a great number of harmonics, which accounts for the type of experimental spectra shown in Fig. 5.

Although the experimental and theoretical data qualitatively agree, there is a quantitative difference between the amplitude ratios of higher harmonics and between the shapes of the spectra of scattered sound. In our opinion, these differences are related to the fact that, along with the scattering by regular fields for which the corresponding theoretical model is developed, some noise-induced effects take place. Firstly, the spectrum of scattered sound (Fig. 5) contains a pedestal, which is presumably caused by the eddy component of the air flow. Secondly, the experimental ratios between the amplitudes of the combination harmonics widely deviate from those calculated in the framework of the proposed model. For example, according to the calculations, the decrease in the amplitudes of harmonics with increasing number $n$ should be within 2–5 dB, while the experiment yields a value of 5–7 dB. Presumably, this occurs because, at Reynolds numbers about $\mathrm{Re} = 3.7 \times 10^3$, the separation of vortices occurs in a quasi-regular way. The effect of the quasi-regularity can be illustrated by a model example. Assume that we calculate the spectrum of the periodic signal

$$S(\omega) = \int \sum_n g(t - \tau_n) e^{i\omega t} dt,$$

$$\tau_n = T_0 n.$$

The spectrum of such a signal consists of the harmonics $m\Omega = m2\pi/T_0$. We assume that the sequence is a quasi-periodic one; i.e., $\tau_n = T_0 n + \xi_n$, where $\xi_n$ are independent random Gaussian quantities with the variance $\sigma$.

Then, if we calculate the spectrum $\langle S(\omega)\rangle$ averaged over the ensemble, we obtain (see, e.g., [7])

$$\langle S(\omega)\rangle = \langle \int \sum_n g(t-\tau_n) e^{i\omega t} dt\rangle$$

$$= \sum_n \int g(t)\langle e^{i\omega(t+T_0+\xi_n)}\rangle dt = e^{-\frac{\sigma^2}{2}\omega^2} S(\omega).$$

Thus, a random spread in the time of vortex separation most strongly affects the amplitudes of the high-frequency spectral components. Precisely this effect is observed in the experiment: the amplitudes of combination harmonics with large numbers are much less than those predicted by the model with a purely regular vortex separation.

In closing, we note that the proposed theoretical model makes it possible to efficiently combine the method of geometric acoustics with the Huygens–Fresnel method of secondary sources. This approach allowed us to obtain an analytical solution for the high-frequency sound field scattered by a vortex street consisting of large-scale vortices. The solution agrees well with the experimental data.

ACKNOWLEDGMENTS

We are grateful to I.N. Didenkulov, L.Ya. Lyubavin, and A.L. Virovlyanskiĭ for useful discussions and advice. The work was supported by the Russian Foundation for Basic Research, project no. 96-02-16834, and the program "Leading Scientific Schools," grant no. 96-15-96593.

REFERENCES

1. P. R. Gromov, A. B. Ezerskiĭ, and A. L. Fabrikant, Akust. Zh. **28**, 763 (1982) [Sov. Phys. Acoust. **28**, 452 (1982)].
2. A. B. Ezerskiĭ, A. B. Zobnin, and P. L. Soustov, Izv. Vyssh. Uchebn. Zaved., Radiofiz. **28**, 832 (1995).
3. A. B. Ezerskiĭ, M. I. Rabinovich, and A. L. Fabrikant, USSR Inventor's Certificate 1056042, 1983.
4. T. M. Georges, J. Acoust. Soc. Am. **51**, 206 (1972).
5. M. V. Vinogradova, O. V. Rudenko, and A. P. Sukhorukov, *The Theory of Waves* (Nauka, Moscow, 1979).
6. H. C. van de Hulst, *Light Scattering by Small Particles* (Wiley, New York, 1957).
7. V. I. Klyatskin, *Stochastic Equations and Waves in Randomly Inhomogeneous Media* (Nauka, Moscow, 1980).

*Translated by E. Golyamina*

*Acoustical Physics, Vol. 46, No. 6, 2000, pp. 676–683. Translated from Akusticheskiĭ Zhurnal, Vol. 46, No. 6, 2000, pp. 770–778.*


# Acoustic Imaging Based on a Mathematical Model

**V. A. Zverev**

*Institute of Applied Physics, Russian Academy of Sciences,*
*ul. Ul'yanova 46, Nizhni Novgorod, 603600 Russia*
*e-mail: zverev@hydro.appl.sci-nnov.ru*

Received March 19, 1998

**Abstract**—A technique for creating an acoustic image based on its mathematical model is proposed. The technique can be used when conventional methods are inapplicable because of the small aperture dimensions relative to the wavelength, the presence of fluctuations, or nonstationary conditions. The essence of the method and its features are illustrated by examples. The method is used to create an image of the angular distribution of scattered signals and of the angular spectrum of signals at the output of an array in a full-scale acoustic experiment. © *2000 MAIK "Nauka/Interperiodica".*

Acoustic images can be created similarly to the optical and radio images formed by wave fields. These methods are known and widely used. In acoustics, conditions may exist under which conventional imaging techniques encounter fundamental difficulties because of the small dimensions of the receiving aperture relative to the wavelength, the small data averaging time, the complex structure of the medium, and its nonstationary behavior. Below, we consider an alternate imaging method suitable for the conditions of a full-scale acoustic experiment.

The proposed imaging method is illustrated in Fig. 1. The diagram is organized in two rows, which is of principal significance. The upper row almost copies the conventional imaging scheme, but it does not include the final operation of creating the image. Traditionally, this final operation is performed through transforming the field received by an aperture [1] or transforming the complex correlation function (the coherence function) [2]. Instead, the row terminates by estimating a series of parameters, which still cannot be considered as an image of the input distribution. Based on these parameters, the conventional methods cannot produce an image. The corresponding inverse problem has no solution, because the aperture may be too small, and the fields may be irreversibly averaged. We will call this row of the diagram the natural row (NR). The image is created by the second row, which we will call the computer row (CR). At the beginning of the CR, the computer creates an initial image, which includes a series of parameters that change it. Subsequently, this image is transformed in the same way as the original image of the upper row. After that, the signal is processed as in the upper row producing the same parameters, which can take different values in the CR or have a different form (if they are functions) from those in the NR.

The desired image is created in the CR by changing the original input image so as to obtain the parameters or functions at the CR output that are close to those in the NR. These selection procedures include variations in the parameters of the computer-formed input image with the subsequent comparison between the results obtained in the CR and NR.

This is the general imaging scheme considered here. It is essential that no stage of the proposed procedure includes the process of solving the inverse wave problem. This feature allows us to obtain minor, but quite stable and reliable, data on the image and its parameters.

We will fill this general scheme with content in the course of considering particular examples. By now, the author has solved three problems that fit the above scheme. One of them has been published [3]. In this

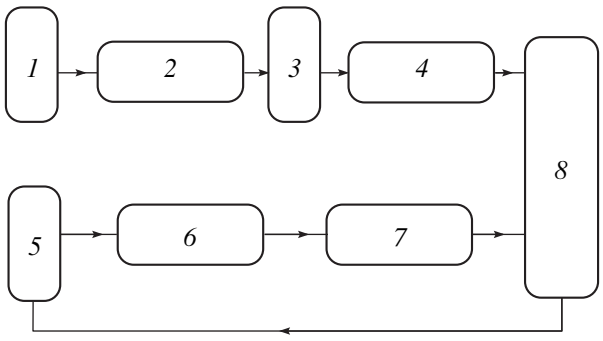


**Fig. 1.** Flowchart of the image formation on the basis of its numerical model: (*1*) original field (image); (*2*) field distortion due to the propagation; (*3*) field reception by the array aperture; (*4*) determination of a series of parameters of the received signal; (*5*) numerical model of the image; (*6*) mathematical model of unit *2*; (*7*) mathematical model of unit *4*; and (*8*) comparison of the results produced by units *4* and *6*.

1063-7710/00/4606-0676$20.00 © 2000 MAIK "Nauka/Interperiodica"

example, the coincidence between the parameters obtained by the NR and CR was not achieved. Here, we take into account and correct the drawbacks of that model.

The results of the field experiment that is used here as an example were reported in [4]. We will describe this experiment below, in the course of our consideration. The goal of the experiment was to find out the possibilities of the modern methods for array signal processing to suppress a strong signal in order to receive a weak signal. The study was carried out with acoustic signals propagating in the shallow sea (about 80-m deep with about 20-m variations) over a distance of about 10 km. A 237.5-Hz signal was received by a linear array consisting of 64 receiving elements spaced at half-wave intervals. The signal intensity was high enough to make the effect of additive noise negligibly small. In order to determine how high the intensity of a signal must be to be received in the presence of another intense signal, we used the second 235.0-Hz source, which was towed by a special ship. The difference in frequencies of the radiated signals was such that the signal of the second source could be filtered out, shifted in frequency, and mixed with the high-intensity signal in any proportion. Prior to being processed, the signals received by the array's hydrophones were transmitted through 0.2-Hz bandpass filters centered at the frequency of the intense radiation.

To characterize the conditions under which the experiment was carried out, we use the results of the preliminary processing of the high-intensity signal received by the array. These results will serve as the NR output signal. We use all the results presented in [4]. These are the instantaneous array responses and a number of particular correlation dependences. The cited paper [4] does not provide the total correlation function; therefore, we cannot use it. The main correlation dependence presented in [4] is

$$A(j) = 1 - |k(j, 31)|, \quad (1)$$

where $k(j, 31)$ is the complex correlation coefficient between the signals received by the $j$th and 31st hydrophone (all the hydrophones are numbered as they are ordered in the array). This pattern was averaged over 240 time realizations. The following dependence is also given in [4]

$$B(j) = 1 - |k(j, j + 1)|, \quad (2)$$

as is the ratio

$$C(j) = \frac{1 - |k(j, j + 1)|}{1 - |k(j, j + 2)|}. \quad (3)$$

Function (2) refines the behavior of dependence (1) in the neighborhood of its minimum. Ratio (3) is defined so as to be equal to 0.25 when the correlation interval of the wave field is much greater than the distance between the array hydrophones. Therefore, both the numerator and the denominator in Eq. (3) can be expanded in power series in the increment of the array element number. These series must begin with quadratic terms, which entails our statement. If this interval is shorter than the hydrophone spacing, the magnitudes of the correlation coefficients in the numerator and denominator of Eq. (3) become small; hence, ratio (3) becomes approximately equal to unity. Thus, ratio (3) characterizes the interval of field coherence along the array. In the figure presented in [4], this ratio averaged over the array is equal to 0.496, which indicates that the field coherence interval is smaller than the array length (200 m), but larger than the array receiver spacing (3 m).

The purpose of the experiment was to find the ratio between the signals of two radiators at which the signal of the weaker source can be observed against the background of the signal produced by the stronger source. This ratio was determined by the array signal extraction methods [4]. As a result of the experiment, this ratio was found to be less than 30 dB. Reception of the weaker signal is hindered by the noise produced by the stronger signal. This noise is caused by fluctuations of the stronger signal, which determine the above correlation dependences. The physical mechanism responsible for the fluctuation noise is not discussed in [4]. Its physical nature was addressed in [5]. Here, we will show how the computer method can be used to find the origin of this noise. Correlation dependences (1)–(3) given in [4] will serve as the final stage of the NR (Fig. 1).

According to our scheme, one should form a computer image. Let us define more specifically what we want to find out. We want to find out from which directions this noise, which shadows the weaker signal, arrives and how high its intensity is. In order to create the respective computer image, we use the physical model of the phenomenon [5]. In this case, the fluctuation phenomena are caused by scattering of acoustic waves by the rough sea surface. The shallow sea can be treated as an acoustic waveguide with an irregular boundary, which scatters the waves incident on it. As applied to this experiment, this phenomenon was considered in [6]. Through a number of simplifying assumptions, we succeeded in obtaining a smooth curve for the intensity of the scattered signals versus the angle of arrival. We will consider it as the initial computer image.

The main feature of a real wave field is that it contains the nonaveraged interference. In principle, such a field can be formed numerically using the results obtained in [7, 8]. However, in this technique, points should be placed on the surface with intervals shorter than $\lambda/2$, which involves an enormous amount of calculations, because the scattering surface is very large. Therefore, we will follow the approach used in [9] and will take into account the interference only at the final step of calculations ignoring the interference at all preceding steps (this requires a much smaller number of points).

Following paper [9], we form the complex random numbers

$$Q_{\vartheta, n} = A_{\vartheta + Ln} + iB_{\vartheta + Ln}. \quad (4)$$

Here, $A$ and $B$ are the sequences of random numbers generated by the computer. The sequences are taken to be sufficiently long so that, as can be seen from Eq. (4), they can be used to form sequences of complex numbers for $n$ realizations, each of which contains 360 numbers $\vartheta$, which can be connected with angular degrees. The computer image is represented by samples spaced by 1° apart.

We form the random spectral components

$$q(\vartheta, n) = \sqrt{S(\vartheta)}Q(\vartheta, n) + ZO\delta(\vartheta). \quad (5)$$

Here, $ZO$ is the constant number that must be determined through matching the parameters of the mathematical model with the experimental results. The function $\delta(\vartheta)$ is zero at all $\vartheta$ except for $\vartheta = 0$, where it is equal to unity. We associate each $\vartheta$ represented in degrees with a plane wave:

$$W(x, \vartheta) = \exp[iu(\vartheta)x], \quad (6)$$

where the wave vector $u(\vartheta)$ has the form

$$u(\vartheta) = \frac{2\pi}{\lambda}\sin\left(\frac{2\pi}{360}\vartheta\right) \quad (7)$$

and $x$ is the coordinate of a point in space in the $(x, y)$ rectangular coordinate system. The receiving array is aligned with the $x$ axis, and its edge is at the origin. The $y$-axis is directed towards the radiator placed on this axis. To form a wave field, we superimpose the plane waves (6) with the random amplitudes (5). As a result, we obtain the following wave field:

$$P(x, n) = \sum_{\vartheta} W(x, \vartheta)q(\vartheta, n). \quad (8)$$

Introducing plane waves with random amplitudes and phases in the form of Eq. (5), we obtain a field that simulates the plane wave interference. Into this field, we can place a linear array aligned with the $x$-axis.

Placing the array in this field, we obtain a set of instantaneous array responses, which can be calculated as the Fourier spectrum in the $x$ coordinate over all array elements. These responses can be compared with the experimental results.

The statistical characteristics of the wave field that are obtained in the experiment are represented as follows:

$$R(x) = 1 - \left|\frac{C(x)}{\sqrt{CE(x)CE(31)}}\right|, \quad (9)$$

where $C(x) = \frac{1}{N}\sum_n P(x, n)\overline{P(31, n)}$ and $CE(x) = \frac{1}{N}\sum_n [\,|P(x, n)|\,]^2$;

$$R1(x) = 1 - \left|\frac{C1(x)}{\sqrt{CE(x)CE(x+1)}}\right|, \quad (10)$$

where $C1(x) = \frac{1}{N}\sum_n P(x, n)\overline{P(x+1, n)}$; and

$$K(x) = \frac{R2(x)}{R1(x)}, \quad (11)$$

where $R2(x) = 1 - \left|\frac{C2(x)}{\sqrt{CE(x)CE(x+2)}}\right|$ and $C2(x) = \frac{1}{N}\sum_n P(x, n)\overline{P(x+2, n)}$.

The statistical characteristics defined by Eqs. (9)–(11) were measured in the experiment.

Thus, we can compare these characteristics and those obtained from the experiment and, therefrom, estimate the similarity and differences between the experimental and simulated images.

As the first step in creating the image of the scattering region, we took the image presented in [6]. The formulas presented above were used to calculate the necessary statistical characteristics and the instantaneous response of the array, which were compared with those obtained experimentally. The results were significantly different, which revealed the mismatch between the computer and desired images. The correlation between the values of the function $R(x)$ was noticeably lower than the correlation between the values of the function $A(j)$ for the NR, because the angular spectrum of the signal in the computer image was very wide (it covered the whole angular sector in which the signals arrive at the array). Variations in the medium parameters accepted for calculating the computer image (attenuation, waveguide depth, distance between the radiator and the receiver, decay characteristics of the scattered waves) did not bring the function $R(x)$ to a better agreement with $A(j)$. Therefore, we changed the computer image with the help of an external parameter that was not addressed in [6].

As we noted above, the NR signal was subjected to the narrow-band filtering before processing. This operation can eliminate or significantly reduce the scattering in the regions where the Doppler frequency shift exceeds the passband of the filter. The relative distribution of the Doppler frequency shift over the scattering surface is shown in Fig. 2. The frequency filtering limits the size and changes the shape of the region from which the scattered signals can arrive. The respective changes concerned with the filtering of the Doppler frequencies were introduced into the original computer

image. As a result, the shape of the region from which the scattered signals may arrive changed. Here, we took into account that the filter does not completely suppress the signals outside its passband. A –25-dB portion of the unfiltered signal was added to the filtered signal. The suppression level was selected so as to provide the best fit between the shapes of the instantaneous responses in the NR and CR rows.

The results of the comparison between the parameters of the NR and CR signals are presented separately for different scatterer velocities along the *x* and *y* axes. Figure 3 shows the correlation functions for the filter that suppresses the Doppler frequencies beyond a given portion of the maximal Doppler shift. For the sake of comparison, other parameters were averaged along the array and plotted in Fig. 4. Figure 5 shows the computer images corresponding to the filter bandwidths for which the comparison was made.

As is shown in Figs. 3 and 4, agreement between the parameters of the NR and CR is achieved when the filter cutoff frequency equals 0.075 of the maximal Doppler frequency shift. The computer image corresponding to this bandwidth is plotted in Fig. 5 with a heavy solid line. Images corresponding to other bandwidths are plotted by dotted lines, their width increasing with the bandwidth of the Doppler filter. These images illustrate the resolution of the method. For the Doppler filter cutoff frequency of about 0.1 of the maximal Doppler shift to coincide with the actual 0.2-Hz cutoff frequency of the filter specified in [4], the wave velocity at the surface must be about 5 m/s, which is a realistic value.

Figures 6–8 compare the characteristics of the NR and CR for the wind blowing along the *y* axis. They also provide a number of CR output parameters, which demonstrate an excellent agreement with the NR parameters. However, the cutoff frequencies of the Doppler filter are surely unfeasible, because they require that the wave velocity be greater by an order of magnitude. We note that, the shape of the surface image is in good agreement with the one obtained at a different direction of the scatterer velocity. This means that the simulations determine not the physical parameters of the experiment, but only the image of the region from which the scattered signals arrive. The NR and CR rows are formed in such a manner that this image does not distinguish directions that differ by 180°. With allowance for this property, we can consider that the image in Fig. 5 looks like the image in Fig. 8 obtained at a different direction of the scatterer motion.

The computer method that we consider allows one to create images in different planes. Above, we created an image in the plane of the input signals before the array where the scattering occurs. Now, we focus on another example and use the same method to create an image that refers to the array output. The number of

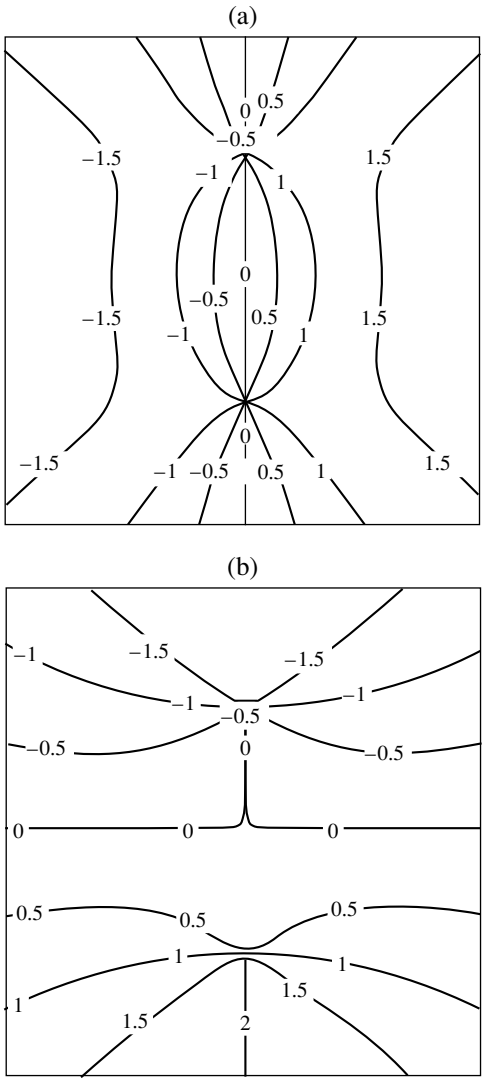


**Fig. 2.** Top view of the surface with the contour map of the Doppler frequency shifts: the scatterer moves (a) across the path (along the *x*-axis) and (b) along the path (along the *y*-axis).

points in this image equals the number of hydrophones in the array. Its coordinates are the spatial frequencies.

We represent the computer image by the following formula:

$$F(u) = \exp\left(-\frac{|u-32|}{D}\right) + PD + ZO\delta(u-32). \quad (12)$$

This formula contains three parameters, which should be selected so as to make the statistical characteristics of the NR and CR as close as possible.

First of all, we should form the necessary statistical characteristics of the CR. To this end, the sequence of random numbers (4) should be written with the number of values that are taken by the variable $\nu$, which is equal to the number of array elements (64). After that, the

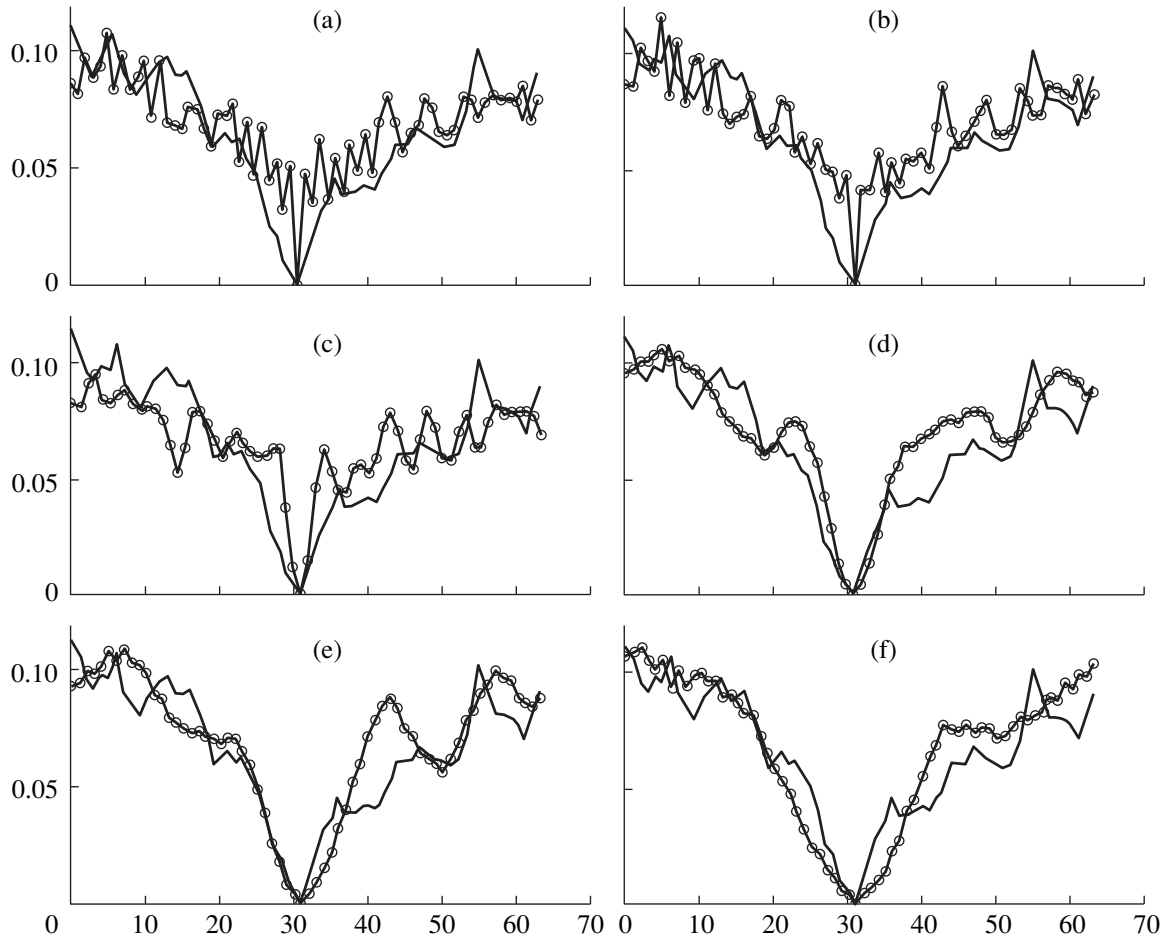


**Fig. 3.** Functions $A(j)$ (solid lines) and $R(j)$ (lines marked by circles) for the following cutoff frequencies of the Doppler frequency filter normalized by the maximal frequency shift: (a) 1, (b) 0.5, (c) 0.15, (d) 0.1, (e) 0.075, and (f) 0.05.

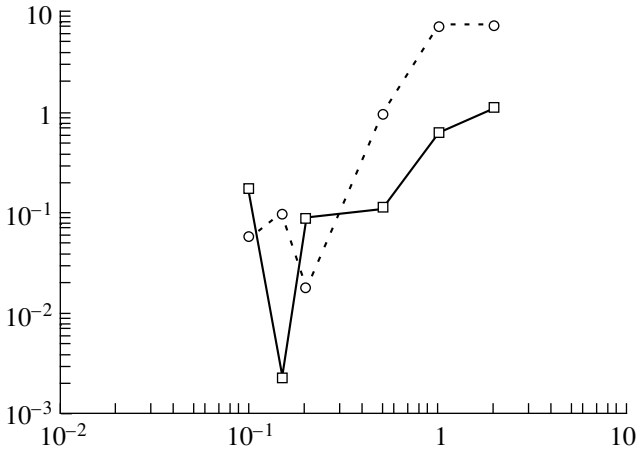


**Fig. 4.** Parameters of the NR and CR versus the cutoff frequency of the Doppler frequency filter: squared differences of the array-average values of $B(j)$ and $R1(j)$ (circles) and $C(j)$ and $K(j)$ (squares) divided by their products.

spectrum of this sequence with respect to variable ν should be multiplied by the computer image (12) (except for the last term, which is not random).

This series of values should be substituted into Eqs. (9)–(11) to form the statistical characteristics of the CR.

Next, we define the following relationships that can be used to compare the characteristics of the NR and CR:

$$W = \sqrt{\frac{A}{C}}, \tag{13}$$

where $A = \sum_j (A(j) - C(j))^2$, $C = \sum_j (A(j) + C(j))^2$,

$$W1 = \frac{\langle B(j)\rangle - \langle R1(j)\rangle}{\langle B(j)\rangle + \langle R1(j)\rangle}, \tag{14}$$

$$W2 = \frac{\langle C(j)\rangle - \langle K(j)\rangle}{\langle C(j)\rangle + \langle K(j)\rangle}. \tag{15}$$

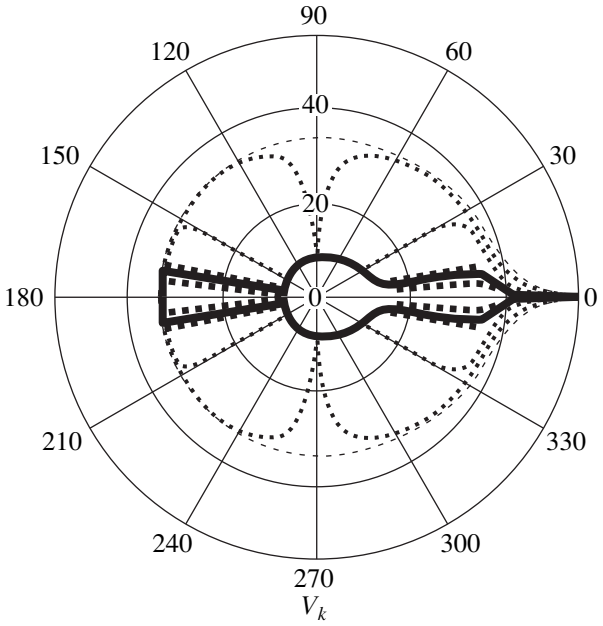


**Fig. 5.** Angular distribution of the scattered field intensity for the Doppler frequency filter bandwidths indicated in Fig. 3. The functions are plotted in decibels (with respect to their maximal values) plus 55 dB to make them positive everywhere.

The numbers *W*, *W*1, and *W*2 are considered as discrepancies between the CR and NR characteristics. The parameters of the computer image are selected so as to minimize the sum of magnitudes of these discrepancies.

An appropriate mathematical procedure can be employed for this purpose. For example, we proceeded as follows. We calculated all three numbers *W*, *W*1, and *W*2 in a certain domain of parameters *D*, *PD*, and *ZO*. Then, for each pair of values of *PD* and *ZO*, the minimal total discrepancy versus the parameter *D* was determined. The value of this minimum was represented as a function of two variables *PD* and *ZO*. A contour map of this surface is shown in Fig. 9. We seek the parameters for which the surface attains the absolute minimum. In Fig. 9, the point of the absolute minimum is clearly seen. This was achieved because, when the discrepancies were summarized, the parameters *W*, *W*1, and *W*2 were used with different weights. With smaller weights of the last two parameters, the point of the absolute minimum cannot be seen; when these weights are higher, local minimums appear, which do not change the coordinates of the absolute minimum. In the presence of the local minimums, the picture is not as clear, if the isolines are not indicated.

The computer image corresponding to the angular response of the array is displayed in Fig. 10. It also shows the image obtained from the formula in which a quadratic exponential function was used instead of the linear one given by Eq. (12). In this case, the minimal discrepancy is much greater.

Thus, we obtained an image of the angular array response that was observed in the experiment. This result is of interest in that it can be used to obtain all the results of paper [4] using only one radiator without employing a second one and without the intricate technique that was used for extracting the weak signal in the experimental work. Indeed, the spectral level of the

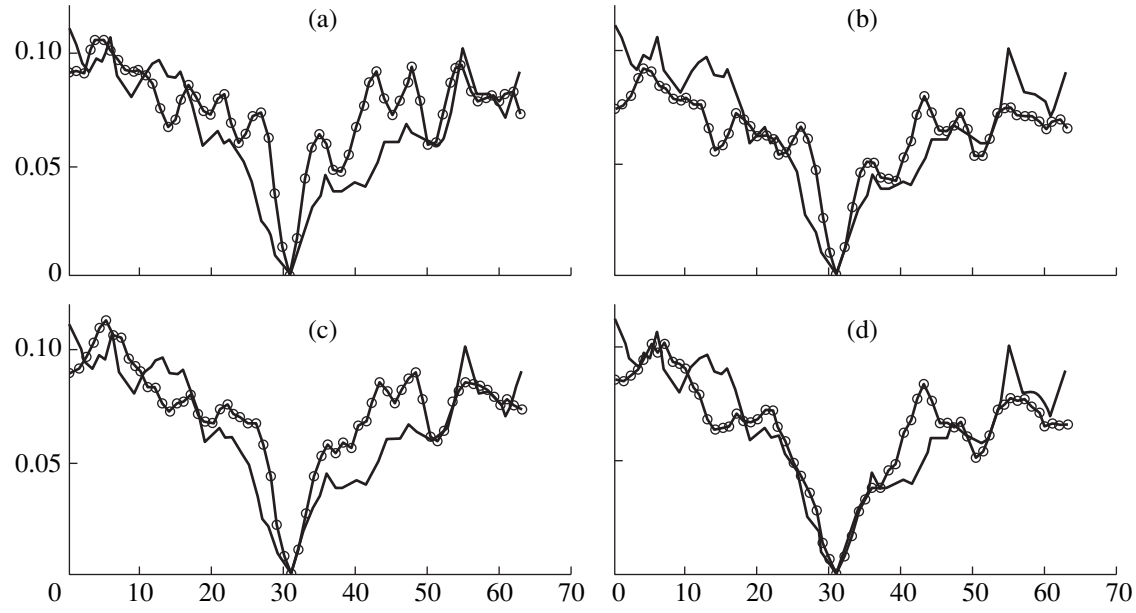


**Fig. 6.** Functions $A(j)$ (solid lines) and $R(j)$ (lines with circles) for the following cutoff frequencies of the Doppler frequency filter normalized by the maximal possible frequency shift: (a) 1, (b) 0.1, (c) 0.05, and (d) 0.01.

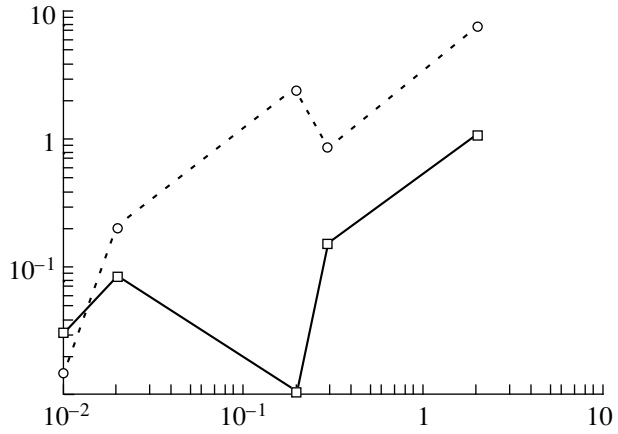


**Fig. 7.** Parameters of the NR and CR versus the cutoff frequency of the Doppler frequency filter: squared differences of the array-average values of $B(j)$ and $R1(j)$ (circles) and $C(j)$ and $K(j)$ (squares) divided by their products.

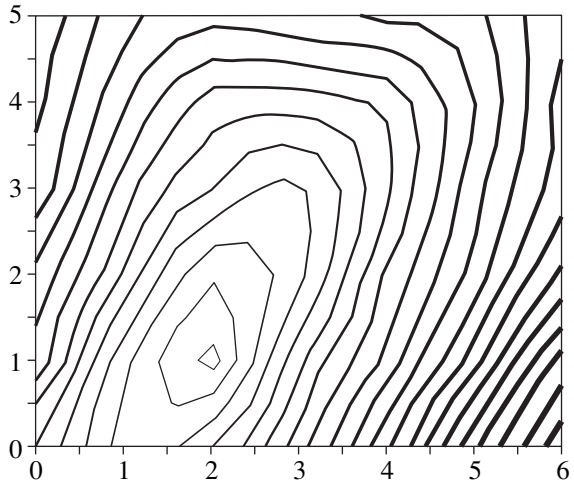


**Fig. 9.** Isolines of the minimum of the sum of discrepancies ($W + 0.1|W1| + 0.1|W2|$) for the parameter $D$ varying from 2 to 4.4. The parameter $PD$ is plotted on abscissa in $0.04 + 0.005x$ units. The parameter $ZO$ is plotted along the $y$ axis in $7 + 0.5y$ units.

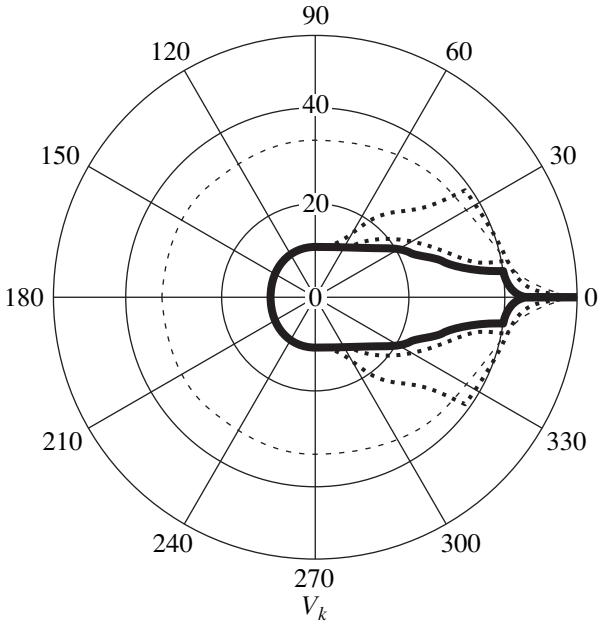


**Fig. 8.** Angular distribution of the scattered field intensity for the Doppler frequency filter bandwidths indicated in Fig. 6. The functions are plotted in decibels (with respect to their maximal values) plus 55 dB to make them positive everywhere.

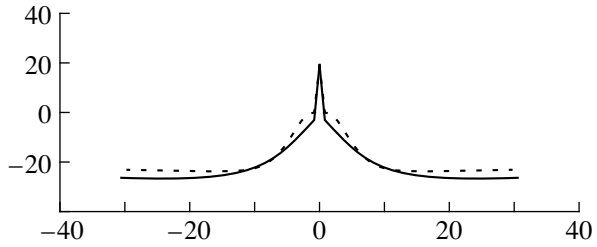


**Fig. 10.** Shape of the array response (in decibels) to the signal transmitted through the studied medium. The $x$ axis represents the spatial frequency in units of the array angular resolution. The solid line is calculated from Eq. (12) for $D = 2.9$, $PD = 0.05$, and $ZO = 8$. The minimal sum of the discrepancies is 0.1. The dotted line corresponds to Eq. (12) with the linear exponent replaced by the quadratic one for $D = 20$, $PD = 0.072$, and $ZO = 10$. The minimal sum of the discrepancies is 0.3.

image covers the entire acoustic horizon thus showing the noise level corresponding to the strong signal. The minimal level of the signal that can be extracted in the presence of the strong signal is determined from the computer image obtained at the array with the help of the usual statistical estimates. These calculations can be performed for all angles and not only for those at which the weak radiator is currently located.

Therefore, the constructed computer image, which shows the angular distribution of the scattered signals, gives a better insight into the physics of the phenomena under study. The practical value of this method is that it clearly shows the distribution of the interference produced by an intense signal in a waveguide with rough moving boundaries.

## ACKNOWLEDGMENTS

This work was supported by the Russian Foundation for Basic Research, project nos. 96-15-96603, 96-02-18621, and 97-02-17555.

## REFERENCES

1. V. A. Zverev, *Radio Optics* (Sov. Radio, Moscow, 1975).

2. V. A. Zverev, Akust. Zh. **41**, 790 (1995) [Acoust. Phys. **41**, 696 (1995)].
3. V. A. Zverev, Akust. Zh. **40**, 263 (1994) [Acoust. Phys. **40**, 229 (1994)].
4. A. B. Gershman, V. I. Turchin, and V. A. Zverev, IEEE Trans. Signal Process. **43**, 2249 (1995).
5. V. A. Zverev, Akust. Zh. **42**, 220 (1996) [Acoust. Phys. **42**, 192 (1996)].
6. V. A. Zverev, Akust. Zh. **44**, 456 (1998) [Acoust. Phys. **44**, 389 (1998)].
7. V. A. Zverev and M. M. Slavinskiĭ, Akust. Zh. **43**, 67 (1997) [Acoust. Phys. **43**, 56 (1997)].
8. V. A. Zverev, A. L. Matveyev, M. M. Slavinsky, and A. A. Stromkov, Proc. I.O.A. **18** (5), 85 (1996).
9. V. A. Zverev and N. V. Litvak, Akust. Zh. **45**, 807 (1999) [Acoust. Phys. **45**, 727 (1999)].

*Translated by A. Khzmalyan*

*Acoustical Physics, Vol. 46, No. 6, 2000, pp. 684–691. Translated from Akusticheskiĭ Zhurnal, Vol. 46, No. 6, 2000, pp. 779–788.*


# Low-Frequency Horizontal Acoustic Refraction Caused by Internal Wave Solitons in a Shallow Sea

**B. G. Katsnel'son and S. A. Pereselkov**

*Voronezh State University, Universitetskaya pl. 1, Voronezh, 394693 Russia*

*e-mail: katz@mph.vsu.ru*

Received December 20, 1999

**Abstract**—The effect of internal wave solitons on the sound field generated by a point source in a shallow sea is considered. In the framework of the theory of "horizontal rays and vertical modes," the sound field pattern governed by the aforementioned hydrodynamic effect is investigated. It is shown that solitons can induce time-periodic focusing and defocusing of horizontal rays propagating at shallow angles to the internal wave front. This may result in the formation of "dynamical" horizontal sound channels, which, in its turn, results in considerable temporal fluctuations of the field along the acoustic track oriented along the internal wave front. For the sound field calculations, an approach is developed on the basis of the parabolic approximation in the horizontal plane and the mode representation in the vertical direction. The results obtained can be used for remote monitoring of internal wave packets in a shallow sea. *© 2000 MAIK "Nauka/Interperiodica".*

Internal waves represent a hydrodynamic phenomenon that is widespread in an oceanic medium. They are one of the main factors responsible for the temporal fluctuations of acoustic signals that propagate in oceanic waveguides. That is why both experimental and theoretical investigations of the effect of internal waves on sound signals attract considerable interest. For a deep sea, the structure and the effect of internal waves on signals have been considered in the well-known monograph [1]. Here, in the ray approximation, the authors investigate in detail the fluctuations of the amplitude and phase of acoustic signals propagating in a deep sea with the canonical sound velocity profile that is perturbed by the internal waves described by the Garrett–Munk spectrum [2]. At the same time, it should be noted that acoustic fluctuations induced by internal waves in a shallow sea (at a shelf) essentially differ from those in the deep ocean. This difference is caused by a number of facts. First, in describing low-frequency sound fields that can propagate in a shallow sea for long distances (~ 10 km), one has to use the mode description of the field; second, the internal waves on the oceanic shelf essentially differ from those in a deep-water oceanic medium and cannot be described on the basis of the Garrett–Munk model. In particular, one of the features of the internal waves in a shallow sea is that their structure includes the packets (wave trains) of intense short-period oscillations, which stand out due to their large amplitudes against the background. By now, there are ample experimental data testifying to the permanent presence of such wave groups, which can be considered as soliton packets, in shallow oceanic regions [3].

It is precisely such internal waves packets and acoustic effects caused by these packets that attract the growing interest of researchers working in shallow water acoustics [5–10]. For example, Rubenstein and Brill [5] describe the results of an experiment carried out in July and August 1988 in the shelf zone near the Washington coast. The authors investigated the propagation of an acoustic signal of frequency 400 Hz along an acoustic track with a sea depth of ≈140 m and a length of 18.5 km. In the course of the experiment, the researchers noticed that temporal intervals where considerable fluctuations of sound intensity loss were observed alternate with the intervals within which the loss was almost invariable. It was also found that variations of the acoustic field pass over the horizontal train of hydrophones with a speed of ~0.75–1.00 m/s. Such a behavior of acoustic signals led the authors to the assumption that the main factor governing their behavior is the internal wave packets.

Zhou and Zhang [6] consider one of the possible interpretations of the results of an experiment carried out in the Yellow Sea. In the course of this experiment, anomalous absorption was recorded in the vicinity of one of the frequencies in the spectrum of a broadband signal. This selective absorption was interpreted as a result of the interaction of sound with the soliton packets. The calculation of possible selective absorption with allowance for the statistical properties of the soliton packets was carried out in our previous paper [7]. Apel *et al.* [8] obtained the theoretical expressions for the rms times of signal propagation in both the ray and mode description of the sound field in the presence of the internal wave solitons. The theoretical estimates are compared with the experimental results obtained in the region of the polar front in the Barents Sea. The modes and rays most sensitive to the effect of internal waves are determined.

1063-7710/00/4606-0684$20.00 

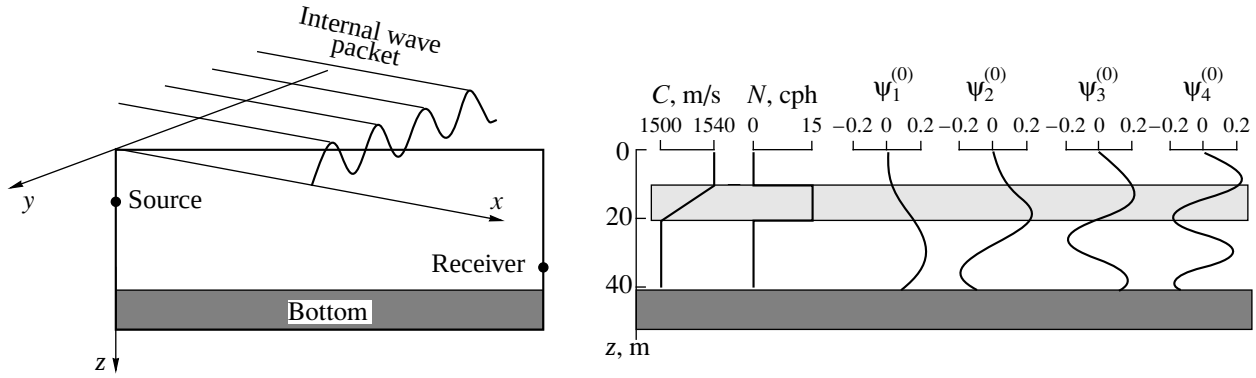


**Fig. 1.** Waveguide model. On the right: the sound velocity profile, the frequency of buoyancy, and the four first acoustic modes. The thermocline is shown by grey color at a depth of 20 m.

Borisov *et al.* [9] describe the results of an experiment carried out on stationary tracks of different lengths passing across the shelf of the Sea of Japan. In the experiment, signals in the frequency range of the order of several hundred hertz were used. The spectra of the fluctuations of the acoustic signal parameters are compared with the spectrum of the internal waves recorded in the same region. Borisov *et al.* [10] present the experimental data on the simultaneous observation of the acoustic signals received on a 34-km track in a coastal shelf and the sequence of the internal wave solitons recorded by a distributed sensor positioned near the hydrophone. Konyaev *et al.* [11], using the characteristics of the internal waves measured in the Yellow Sea and the Massachusetts Gulf as input data, carried out numerical modeling of acoustic fluctuations caused by a packet of the internal waves propagating across the acoustic track.

Briefly listing the main features of the internal waves at a shelf, we note that, according to experimental data (see, for example, [2–4]), the packets of internal waves in the shelf zone of the ocean have the form of trains ~1–3 km long, which are separated by calm intervals ~10 km in length and are quasi-sinusoidal in shape with a quasi-period of ~200–400 m and an amplitude of ~5–10 m. The packets propagate toward the beach with a speed of ~0.5–1.0 m/s. The packets are charaterized by

(i) anisotropy in the horizontal plane (i.e., they have an almost plane wave front with the radius of curvature ~10–20 km);

(ii) a quasi-sinusoidal shape in the direction of propagation (i.e., the spatial spectrum is rather narrow);

(iii) synchronous vertical displacements in depth (this testifies to the predominance of the first gravity mode).

These properties cause a considerable horizontal anisotropy of the sound velocity field in the presence of internal waves. The degree of this anisotropy can be estimated. For example, assuming that a jump in the sound velocity is ~20 m/s across the 10-m-thick thermocline (the vertical gradient is ~2 $s^{-1}$), the above-listed parameters of the soliton provide the same jump across the soliton front at a distance of ~200 m, which produces the horizontal gradient of the sound velocity ~0.1 $s^{-1}$, this value being comparable with the mean vertical gradient. Noting that this "transverse" gradient occurs along the long wave front (up to 20 km) of the soliton, we conclude that the effect of this anisotropy can be quite subatantial. This paper is devoted to studying the acoustic effects that can be caused by the internal wave solitons.

We represent a shallow-water oceanic medium as a three-dimensional hydroacoustic waveguide in the coordinate system $X$, $Y$, and $Z$ (Fig. 1). The waveguide is formed by a water layer with the density $\rho(z)$ and the squared refraction index $n^2(z) + \mu(x, y, z, t)$, where $n^2(z)$ corresponds to some mean equilibrium stratification of the layer (the respective sound velocity profile is denoted as $c(z)$) and $\mu(x, y, z, t)$ is its perturbation caused by the internal wave packet. The water layer is bounded in depth by the free surface at $z = 0$ and the homogeneous absorbing halfspace—the bottom—at $z = H$ with the density $\rho_1$ and the squared refractive index $n_1^2(1 + i\alpha)$, where $a$ is determined by the absorbing properties of the bottom.

According to [1], the expression for $\mu(\mathbf{r}, z, t)$ is determined by the parameters of the internal wave packet:

$$\mu(\mathbf{r}, z, t) = -\frac{2\delta c(\mathbf{r}, z, t)}{c(z)} = -2QN^2(z)\zeta(\mathbf{r}, z, t). \quad (1)$$

Here, $\delta c$ is the sound velocity variation caused by the displacement of the surface of constant density; $N(z) = \left(\frac{g}{\rho}\frac{d\rho}{dz}\right)^{1/2}$ is the frequency of buoyancy determined by the stratification of the water layer density; $g$ is the gravitational acceleration; $Q \approx 2.4$ $s^2/m$ is the constant determined by the physical properties of water; $\mathbf{r} = (x, y)$ is the radius-vector in the horizontal plane;

$\zeta$ describes the vertical displacements of the water layers, which can be written as [2, 3]

$$\zeta(\mathbf{r}, z, t) = \Phi(z)\zeta_S(\mathbf{r} - \mathbf{u}t), \tag{2}$$

where $\mathbf{u} = (u_x, u_y)$ is the horizontal speed of the soliton generally depending on the coordinates, which may cause a distortion of the wave front, and $\Phi$ is the first gravity mode normalized to its maximum value. The function $\Phi$ is determined by the boundary problem

$$\begin{gathered} d^2\Phi/dz^2 + (N^2(z)/\omega^2 - 1)\sigma^2\Phi = 0, \\ \Phi(0) = \Phi(H) = 0. \end{gathered} \tag{3}$$

Here, $\omega$ is the eigenvalue that determines the frequency of oscillations in the vertical plane.

According to the experimental data, the internal wave packets propagate rather slowly ($u \approx 0.5$–$1.0$ m/s). If the acoustic track length (between the transmitter and the receiver) does not exceed ~10–20 km, which is the distance travelled by the sound signal within ~10–20 s, the packet is displaced by no more than ~10–20 m in the course of its propagation. This displacement is at least an order of magnitude less than the typical quasi-period of the packet (the mean width of individual solitons in a packet is ~200–400 m). Therefore, we will consider the problem of sound propagation in the approximation of a frozen medium, i.e., the temporal variable $t$ will be considered as a parameter, and the factor $\exp(i2\pi ft)$ will be omitted ($f$ is the sound frequency).

For analyzing the sound field in the framework of the above-described three-dimensional model of the shallow sea, we use the known theory of "horizontal rays and vertical modes" [13], which was used, in particular, for calculating the horizontal refraction by internal waves [14] (see also [15]). According to this theory, the sound field $\Psi(\mathbf{r}, z)$ generated at the point of reception $(\mathbf{r}, z)$ by the source located at the point $(\mathbf{r}_0 = 0, z = z_0)$ satisfies the equation

$$\Delta\Psi + k^2n^2(\mathbf{R})\Psi = 0 \tag{4}$$

and the boundary conditions

$$\begin{gathered} [\Psi(\mathbf{r}, z)]_{z=0} = 0, \\ [\Psi(\mathbf{r}, z) - \Psi_1(\mathbf{r}, z)]_{z=0} = 0, \\ \left[\frac{1}{\rho}\frac{\partial\Psi(r, z)}{\partial z} - \frac{1}{\rho_1}\frac{\partial\Psi_1(r, z)}{\partial z}\right]_{z=H} = 0. \end{gathered} \tag{5}$$

We will seek the solution for $\Psi$ in the form

$$\Psi(\mathbf{r}, z) = \sum_n\sum_m A_{nm}(\mathbf{r})\psi_m(\mathbf{r}, z)\exp[i\theta_{nm}(\mathbf{r})]. \tag{6}$$

Here, $A_{nm}(x, y)$ is the amplitude and $\theta_{nm}(x, y)$ is the phase increment of the $m$th acoustic mode $\psi_m(x, y, z)$. Note that, in the general case, several horizontal rays corresponding to the given mode can arrive at the point of reception. These rays have different paths, and, therefore, they are characterized by different amplitudes and phase increments. Therefore, the summation in expression (1) is carried out over both the vertical modes (index $m$) and the horizontal rays (index $n$).

Assume that the hydroacoustic parameters of the medium vary rather slowly along the rays. This assumption is justified, because we consider the situation when the internal waves responsible for the spatial variability propagate across the acoustic track. In this case, we can deem that the modes $\psi_m(\mathbf{r}, z)$ and the corresponding wave numbers $\xi_m = q_m + i\gamma_m/2$ depend on the horizontal coordinate $\mathbf{r}$ as on a parameter; then, they are the solutions to the Sturm–Liouville problem

$$\begin{gathered} \frac{\partial^2\psi_m(\mathbf{r}, z)}{\partial z^2} + [k^2n^2(\mathbf{r}, z) - \xi_m^2(\mathbf{r})]\psi_m(\mathbf{r}, z) = 0, \\ \psi_m(\mathbf{r}, z)\big|_{z=0} = 0, \\ \left[\psi_m(\mathbf{r}, z) + g[\xi_m(\mathbf{r})]\frac{\partial\psi_m(\mathbf{r}, z)}{\partial z}\right]_{z=H} = 0. \end{gathered} \tag{7}$$

Here, $k = \dfrac{2\pi f}{c}$, where $c$ is the sound velocity at some fixed depth in the water layer, and the dependence $g(\xi_m)$ is determined by the bottom parameters. In particular, for a homogeneous absorbing bottom, this dependence has the form

$$g(\xi_m) = \frac{\rho_1}{\rho(H)}(\xi_m^2 - k^2n_1^2(1 + i\alpha))^{-1/2}. \tag{8}$$

The functions $\theta_{nm}(\mathbf{r})$ and $A_{nm}(\mathbf{r})$ are the phase increment and amplitude of the $n$th ray corresponding to the $m$th mode and arriving at the point of reception. These functions are determined by the eikonal equation and the transport equation

$$(\nabla_r\theta_{nm})^2 = q_m^2, \tag{9}$$

$$2\nabla_rA_{nm}\nabla_r\theta_{nm} + A_{nm}\nabla_r^2\theta_{nm} + q_m\gamma_mA_{nm} = 0, \tag{10}$$

where $\nabla_r = (\partial/\partial x, \partial/\partial y)$. From the eikonal equation, we can easily obtain differential equations determining the trajectory $\mathbf{r}_{nm}(s)$ for the $n$th horizontal ray that corresponds to the $m$th mode in the horizontal plane

$$\frac{d\mathbf{r}_{nm}}{ds} = \boldsymbol{\tau}_{nm}, \quad \frac{d\boldsymbol{\tau}_{nm}}{ds} = \frac{1}{q_m}\nabla_\perp q_m(\mathbf{r}), \tag{11}$$

where $ds = \sqrt{(dx)^2 + (dy)^2}$, $\boldsymbol{\tau}_{nm}$ is the unit vector tangential to the ray, and $\nabla_\perp$ is the gradient in the direction normal to the ray. Having solved differential equations (11) and determined the trajectories of rays $S_{nm}$ arriving at the point of reception and corresponding

to a given mode $\psi_m$, we can determine the eikonals and amplitudes for these rays with the use of the integrals over these trajectories:

$$\theta_{nm}(x, y) = \int_{S_{nm}} q_m(s)ds,$$
$$A_{nm}(x, y) = A_{nm}(0, 0)\exp\left(-\frac{1}{2}\int_{S_{nm}} \gamma_m(s)ds\right). \quad (12)$$

As seen from Eq. (9), the real part of the horizontal wave number $q_m(\mathbf{r})$ has the meaning of the wave number (proportional to the refractive index) for the horizontal rays corresponding to the $m$th mode. In the framework of our model of the shallow-water waveguide, the spatial dependence $q_m(\mathbf{r})$ is determined by the internal wave packet. We assume that the change in the water layer stratification due to the packets of the internal waves leads to fairly small changes in the horizontal wave number of the $m$th mode $q_m(\mathbf{r}) = q_m^{(0)} + \delta q_m(\mathbf{r})$, where $q_m^{(0)}$ is the eigenvalue of the Sturm–Liouville problem without internal waves. The value $\delta q_m(\mathbf{r})$ can be found from perturbation theory [16]

$$\delta q_m(\mathbf{r}) = \frac{1}{2q_m^{(0)}}\int_0^H [\psi_m^{(0)}(z)]^2 k^2 \mu(\mathbf{r}, z)dz. \quad (13)$$

Expressing $\mu(\mathbf{r}, z)$ in terms of the vertical displacements by using formulas (1, 2), we obtain

$$\delta q_m(\mathbf{r}) = -\left\{\frac{Qk^2}{q_m^{(0)}}\int_0^H [\psi_m^{(0)}(z)]^2 N^2(z)\Phi(z)dz\right\} \times \zeta_S(\mathbf{r} - \mathbf{u}t). \quad (14)$$

Expression (14) provides a correction that should be introduced in the effective refractive index in the horizontal plane because of the presence of the internal wave solitons. It is seen that the dependence on the horizontal coordinates is determined only by the form and speed of the solitons. It is also seen that the expression in the braces provides the dependence of the effective refractive index on the mode number. This dependence can be analyzed in the simplest cases. Let the thermocline region be rather narrow: $h < z < h + h_t$, where $h_t \ll H$. The frequency of buoyancy is assumed to be constant in this region, $N = N_0$, and equal to zero outside it. Because in a shallow sea the predominant contribution to the sound field is made by the lowest, i.e., relatively smooth, eigenfunctions, we can assume that the eigenfunction is invariant within the interval $h_t$. With allowance for these simplifying assumptions for $\delta q_m$, we obtain

$$\delta q_m(\mathbf{r}) = -\frac{Qk^2}{q_m^{(0)}}N_0^2\int_h^{h+h_t} [\psi_m^{(0)}(z)]^2 dz\zeta_S(\mathbf{r} - \mathbf{u}t)$$
$$\approx -\frac{Qk^2}{q_m^{(0)}}N_0^2[\psi_m^{(0)}(h)]^2 h_t\zeta_S(\mathbf{r} - \mathbf{u}t). \quad (15)$$

In order to estimate this quantity, we make further simplifications. Assume that the sound velocity jump in the thermocline is small, so that lower acoustic waveguide modes are reflected from the surface and can roughly be represented by the modes of the Pekeris waveguide: $\psi_m(z) \approx \sqrt{\frac{2}{H}}\sin\frac{m\pi}{H}z$. Then, for the correction on the right-hand side of Eq. (9), which determines the effect of the horizontal anisotropy, we obtain the estimate

$$2q_m^0\delta q_m(\mathbf{r}) \approx -4Qk^2N_0^2\frac{h_t}{H}\sin^2\frac{m\pi h}{H}\zeta_S(\mathbf{r} - \mathbf{u}t). \quad (16)$$

It is seen that the effective refractive index increases with the mode number for lower modes and oscillates for higher modes. In the general case, the pattern is certainly more complicated; however, from expression (14) we can conclude that a soliton mainly affects the mode that has the maximal intersection with the thermocline (the region where the frequency of buoyancy is the highest).

Consider the sound field pattern caused by a typical soliton. The specific feature of a shallow-water sound channel is that, because of the bottom loss in the course of the propagation over a long track (10–20 km), the modal composition of the sound signal arriving at the receiver is determined by a relatively small number of propagating modes. Therefore, in analyzing the effect of horizontal refraction, we will consider horizontal rays for separate modes, mainly, for the lower modes. First, we consider the case of a plane wave front of the solitons, i.e., we assume that the function of the vertical displacement depends only on the coordinate $y$; in addition, according to our assumption on the frozen medium, we have $\zeta = \zeta_S(y - ut) = \zeta_S(y - y_0)$, where the parameter $y_0$ determines the position of the source with respect to the soliton packets. In this case, the effective refractive index in expression (7) depends only on $y$, and the ray patterns for the horizontal rays in the $(x, y)$ plane are plotted similarly to the rays in a plane layered medium. For a brief analysis of such a situation, we assume that the source is positioned in the $(x, y)$ plane, at the point $(x = 0, y = 0)$, and the acoustic track coincides with the $x$-axis. According to the statement of the problem, we are interested in the ray pattern in a relatively narrow sector of horizontal launch angles of rays

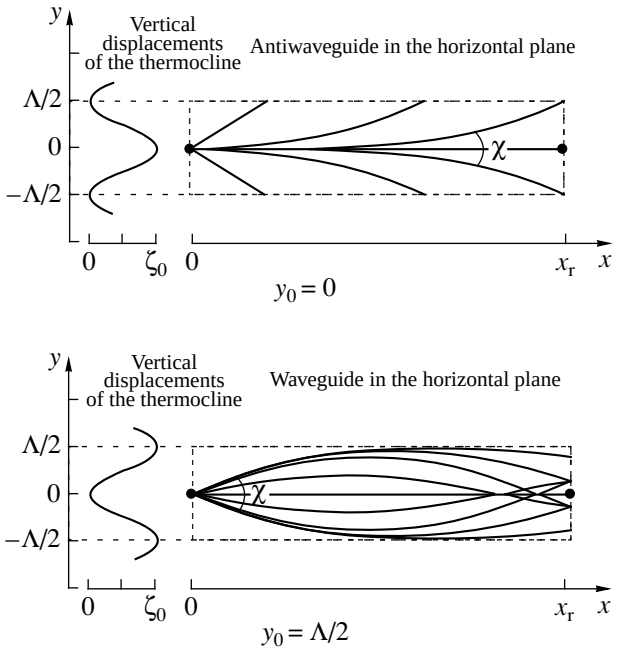


**Fig. 2.** Ray patterns in the horizontal plane for the case of a plane front of soliton packets. The dependence of the thermocline displacement on the transverse coordinate is shown on the left.

about the *x*-axis. If the position of the source is fixed, while the plane wave front of the soliton moves in the *y* direction, the refractive index varies in time and, therefore, the ray pattern in the horizontal plane also varies. For further analysis, we specify the form of the soliton. Assume that the soliton packet has the cosinusoidal form within a segment of width $L_y$ (this form is a fairly good approximation for model calculations):

$$\zeta_S(y - y_0) = \frac{\zeta_0}{2}\left\{\cos\left[\frac{2\pi}{\Lambda}(y - y_0)\right] + 1\right\}, \qquad (17)$$

where the parameter $\Lambda$ denotes the quasi-period of the packet (the relation $L_y \approx 4$–$5\Lambda$ usually takes place) and $\zeta_0$ is the amplitude of the soliton.

The character of the ray pattern in the horizontal plane depends on the position of the soliton packets relative to the source. If the packet is outside the source, the ray pattern in the horizontal plane corresponds to the conventional cylindrical divergence of linear horizontal rays. When the packet covers the source, the ray pattern depends on the source position inside the packet. Consider two limiting cases: the source is in the area of the maximal or minimal values of the soliton amplitude, $\zeta_S = 0$ or $\zeta_0$. The first case corresponds to the source position at a point with the minimal sound velocity value (with respect to the nearest vicinity in the *y* direction). In this case, the horizontal rays launched from the source are deflected toward the *x*-axis because of the refraction. In the second case, the source is at a point with the maximal sound velocity value, the rays launched from the source are deflected away from the *x*-axis. Both cases are presented in Fig. 2, which shows the results of the calculations for some model packet of solitons (the parameters are indicated in the figure caption). It is seen that the first case corresponds to the possible waveguide propagation (for a considerable horizontal refraction). The second case corresponds to the antiwaveguide propagation.

For the first case, we estimate the sector of horizontal launch angles of rays originating from the source and trapped by the horizontal channel. Assuming that the sound velocity variations at the channel boundary $\delta c$ are caused by the soliton concentrated in the narrow thermocline, we obtain the estimate

$$\chi \approx 2\sqrt{\frac{2\delta q}{q}} \approx 2\sqrt{\frac{2QN_0^2 h_t \zeta_0}{h}},$$

which for the parameters $N_0 = 15$ cph, $h_t/H \approx 0.2$, $\zeta_0 \approx 5$ m, and $\Lambda \approx 400$ m yields $\chi \approx 10°$.

For such a noticeable horizontal refraction, the formation of a waveguide in the horizontal plane is generally possible. In this case, we can obtain the corresponding phase condition for rays multiply crossing the *x* axis as the quantization condition. According to these conditions, the number of such rays (waveguide modes) can be estimated as $M \approx \frac{k\Lambda}{2\pi}\sqrt{\frac{\delta q}{q}}$. For a frequency of 300 Hz and the aforementioned parameters, we have $M \approx 4$. A more accurate estimate must take into account the dependence of all the pattern parameters on the mode number.

If the wave front of the soliton packet is not a plane, the ray pattern in the horizontal plane slightly changes. Consider, for example, the case when the wave fronts are circles with large curvature radii, which corresponds to the expression

$$\zeta_S(\mathbf{r} - \mathbf{u}t) = \frac{\zeta_0}{2}\left\{\cos\left[\frac{2\pi}{\Lambda}(r - r_0)\right] + 1\right\}, \qquad (18)$$

where the packet width satisfies the condition $L_r \ll r$ ($r$ is the polar radius that is equal to the current curvature radius of the wave front of the packet, and $r_0$ is the parameter determining the position of the soliton packet). In this case, the longitudinal coordinate along the track is proportional to the polar angle $\varphi$. Figure 3 shows the ray patterns corresponding to the first and third vertical modes for the cases of the waveguide and antiwaveguide formation in the horizontal plane. The parameters used for the calculations are shown in the figures. It is seen that, for the third mode, the refraction is considerably greater than for the first mode. This follows from formula (14) and Fig. 1: one can see that the

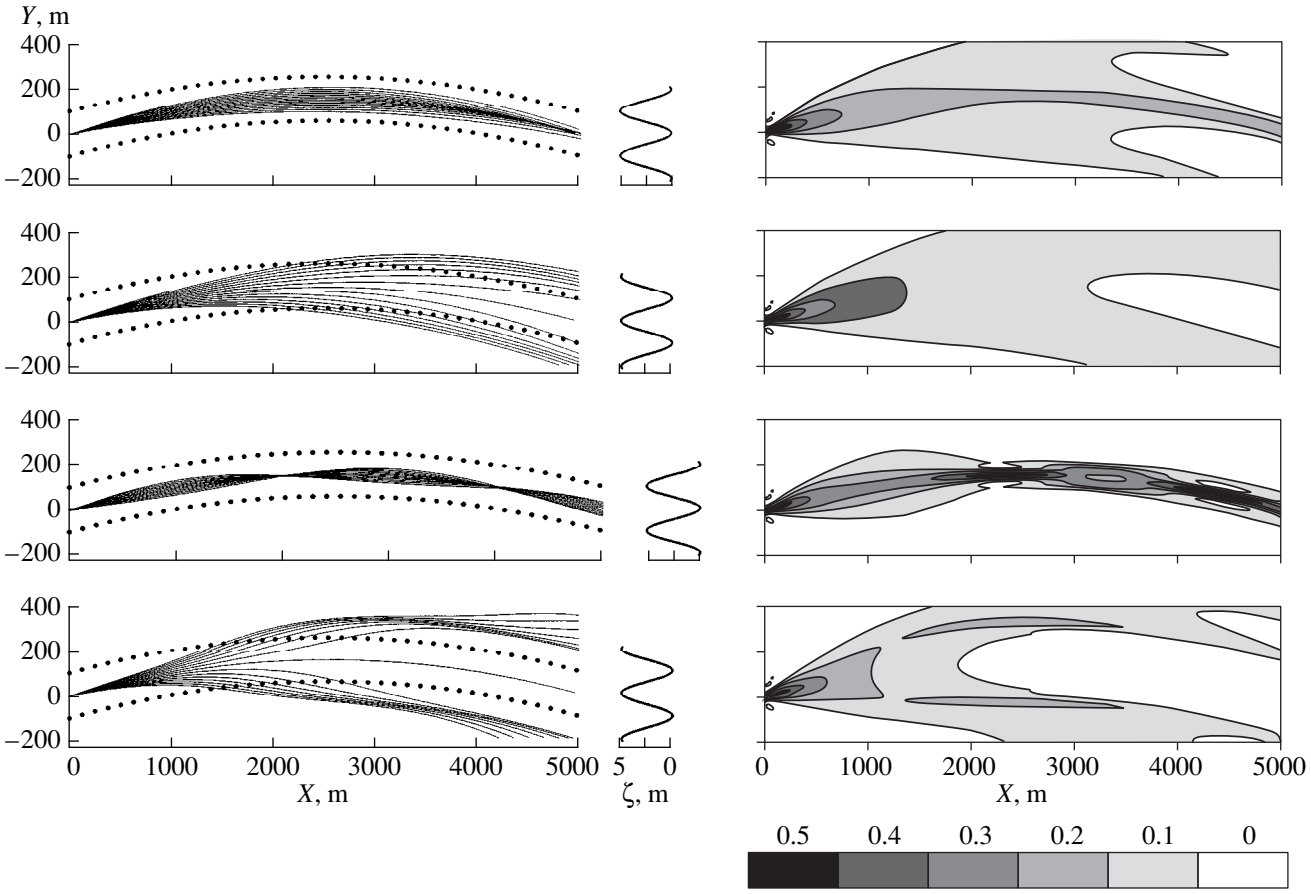


**Fig. 3.** Horizontal rays (on the left) and the distribution of the relative intensity in the horizontal plane, which was obtained by solving the parabolic equation (on the right) for the first (two upper diagrams) and the third (two lower diagrams) vertical modes in the case of a curvilinear (circular) wave front of the soliton packet. The vertical displacements of the thermocline as a function of the transverse coordinate are shown in the middle. The dotted lines on the left indicate the soliton wave fronts. The parameters of the internal wave packet are chosen according to formula (18): $\zeta_0 = 5$ m, $\Lambda = 200$ m, the front curvature radius $R_{iw} = 10^4$ m, and the sound frequency in the parabolic equation $f = 250$ Hz. The scale of intensities for the parabolic equation is shown at the bottom.

interaction between the soliton and the third mode is stronger than that between the soliton and the first mode. Moreover, we note that, although the degree of focusing and defocusing depends on the mode number, the presence of these effects does not depend on the mode number. It means that the sound field fluctuations (the effects of focusing and defocusing) caused by the propagation of the soliton packets through the acoustic track will take place for all acoustic modes synchronously, which enhances these effects in the case of a real multimode sound propagation.

We calculate the intensity field distribution in the horizontal plane in the presence of internal waves. This calculation can be performed with the ray theory described above by calculating the number of arriving rays and combining their amplitudes. However, it is more expedient to develop an approach based on the parabolic equation, which is largely free of the disadvantages of the geometric acoustics approximation. The method described below can be called the method of vertical modes and a parabolic equation in the horizontal plane.

We seek the solution to Eq. (4) as the expansion in the reference waveguide modes, $\psi_m(\mathbf{r}; z)$, which depend on the coordinates $\mathbf{r}$ in the horizontal plane as on the parameters:

$$\Psi(\mathbf{r}, z) = \sum_{m=0}^{M} P_m(\mathbf{r})\psi_m(\mathbf{r}; z), \tag{19}$$

where the functions $P_m(\mathbf{r})$ satisfy the equation

$$\Delta_{\mathbf{r}} P_m(\mathbf{r}) + \xi_m^2(\mathbf{r}) P_m(\mathbf{r}) = 0. \tag{20}$$

We first assume that the wave front of intense internal waves is plane. In this case, we introduce the Cartesian coordinates in the horizontal plane and direct the $OX$ axis along the front of the internal waves and the $OY$ axis along the normal to this front. In expression (20), the Laplace operator has the form

$$\Delta_{\mathbf{r}} = \partial^2/\partial x^2 + \partial^2/\partial y^2. \tag{21}$$

We seek the solution to Eq. (20) in the form

$$P_m(\mathbf{r}) = F_m(x, y)\exp[iq_m^{(0)}x], \quad (22)$$

where $F_m(x, y)$ is a slowly varying function of the $x$ coordinate. For the function $F_m(x, y)$ in the approximation of forward scattering ($\partial F_m/\partial x \ll q_m^{(0)} F_m$), we obtain the parabolic equation

$$\frac{\partial F_m}{\partial x} = \frac{i}{2q_m^{(0)}}\frac{\partial^2 F_m}{\partial y^2} + \frac{iq_m^{(0)}}{2}(n_q^2(x, y) - 1)F_m, \quad (23)$$

where $n_q(x, y) = q_m(x, y)/q_m^{(0)}$ plays the role of the refractive index corresponding to the $m$th mode.

For numerically solving Eq. (23), we used the conventional scheme known as the Split Step Fourier (SSF) algorithm [17, 18]

$$F_m(x + \Delta x, y) = \exp[-iq_m^{(0)}\Delta x U_m(x, y)] \times FFT\left\{\exp[iq_m^{(0)}\Delta x T_m(x, \xi)] \times FFT[F_m^*(x, y)]^*\right\}, \quad (24)$$

where $FFT$ is the operator of the fast Fourier transform, $T_m(q) = \frac{1}{2}\left(\frac{q}{q_m^{(0)}}\right)^2$ is the operator in the Fourier space $q$, and $U_m(x, y) = -\frac{1}{2}[n_q^2(x, y) - 1]$ is the operator in the space of the horizontal coordinates $x$, $y$.

To set the initial conditions for calculating by scheme (6), we assumed that the source located at the origin of coordinates $x = 0$, $y = 0$ generates a field that, in the Fourier space $q$, is described by the expression $a_m\exp(-q^2/2\Delta_m^2)$, where the parameter $a_m$ determines the mode amplitude, which depends on the mode value at the source depth, and the parameter $\Delta_m = q_m^{(0)}\sin\theta_{\max}$ characterizes the angular range of the source radiation taken into account in the calculation. The angle $\theta$ is counted from the $OX$-axis.

Considering now a more realistic model of the internal wave packet, we assume that the packets have a curved front rather than a plane front. In this case, it is more convenient to use curvilinear coordinates $(\tau, \eta)$ in the horizontal plane. The $\tau$ coordinate is counted along the internal wave front, and the $\eta$ coordinate is directed normally to the front. In this case, the Laplace operator in the horizontal plane takes the form

$$\Delta_{\mathbf{r}} = \frac{1}{h_\eta h_\tau}\left\{\frac{\partial}{\partial\eta}\left(\frac{h_\tau}{h_\eta}\frac{\partial}{\partial\eta}\right) + \frac{\partial}{\partial\tau}\left(\frac{h_\eta}{h_\tau}\frac{\partial}{\partial\tau}\right)\right\}, \quad (25)$$

where $h_\tau$ and $h_\eta$ are the Lame coefficients corresponding to the chosen curvilinear coordinates:

$$h_\tau = \sqrt{(\partial x/\partial\tau)^2 + (\partial y/\partial\tau)^2},$$
$$h_\eta = \sqrt{(\partial x/\partial\eta)^2 + (\partial y/\partial\eta)^2}.$$

We seek the solution to Eq. (2) in the form

$$P_m(\mathbf{r}) = F_m(\tau, \eta)\exp[iq_m^{(0)}\tau]. \quad (26)$$

As a result, we obtain the equation for the function $F_m(\eta, \tau)$ in the forward scattering approximation:

$$\frac{\partial F_m}{\partial\tau} = \frac{i}{2q_m^{(0)}}\frac{h_\tau}{h_\eta}\frac{\partial}{\partial\eta}\left(\frac{h_\tau}{h_\eta}\frac{\partial F_m}{\partial\eta}\right) + \frac{iq_m^{(0)}}{2}(h_\tau^2 n_q^2 - 1)F_m. \quad (27)$$

The numerical scheme for solving Eq. (27) differs from that considered above only in that we need to determine the Lame coefficients at every step:

$$F_m(\tau + \Delta\tau, \eta) = \exp[-iq_m^{(0)}\Delta\tau U_m(\tau, \eta)] \times FFT\left\{\exp[iq_m^{(0)}\Delta\tau T_m(\tau, \xi)] \times FFT[F_m^*(\tau, \eta)]^*\right\}, \quad (28)$$

where $T_m(\xi) = \frac{1}{2q_m^2}\left\{q_m^2(h_\tau/h_\eta)^2 + \frac{q_m}{2}\frac{\partial(h_\tau/h_\eta)^2}{\partial\eta}\right\}$ is the operator in the Fourier space $q$ and $U_m(\tau, \eta) = -\frac{1}{2}[h_\tau^2 n_q^2 - 1]$ is the operator in the space of horizontal coordinates $\tau$ and $\eta$.

Figure 3 shows the results of calculations by the above-mentioned approach for the distribution of the acoustic energy of the $m$th mode in the horizontal plane

$$\delta = |F_m(\tau, \eta)|^2/|F_m(0, 0)|^2. \quad (29)$$

The two upper figures correspond to the first mode of the sound field, and the two lower figures correspond to the third mode. In our calculations, we assumed that the sound channel stratification corresponds to that shown in Fig. 1; the packet of the internal waves has the sinusoidal form (18) with the parameters indicated in the figure caption; the sound frequency is $f = 250$ Hz; and the parameter $\theta_{\max}$ determining the field distribution at $x = 0$ equals $\theta_{\max} = \pi/18$, which corresponds to the inclusion of horizontal rays launched at angles not exceeding 10° in both directions with respect to the tangent to the internal wave front. The maximal value of the ratio (29) is unity (at the source), and other values are separated into five groups according to the degree of blackening; the scale is shown in Fig. 3.

From Fig. 3, it follows that the effect of the horizontal inhomogeneity on the third mode is much greater than on the first mode, which agrees well with the preceding inference about the fraction of the vertical mode

confined in the thermocline. These modal calculations allow one to estimate the amplitude of the field fluctuations caused by the soliton packets crossing the track. We will briefly analyze the distribution of the field intensity in the horizontal plane. For this purpose, we use the curvilinear coordinate system $(\tau, \eta)$, where the lines $\eta = \text{const}$ coincide with the wave fronts of the soliton packets (the values $\eta = \pm\Lambda/2$ are shown by the dotted lines in the part of Fig. 3 that corresponds to the ray approximation). Let the source position be determined by the coordinates $\tau_s = 0$ and $\eta_s = 0$ and the receiver position by the coordinates $\tau_r$ and $\eta_r$. In these coordinates, the soliton form is given by the formula $0.5\zeta_0\{\cos[2\pi(\eta - \eta_0)/\Lambda] + 1\}$, where the parameter $\eta_0$ determines the position of the soliton packet at a given time. For the first and third modes, Fig. 3 presents two source positions relative to the soliton fronts: the source is on the crest of the soliton ($\eta_0 = 0$), which corresponds to the antiwaveguide, and the source is in the hollow between two crests of the soliton ($\eta_0 = \Lambda/2$), which provides the possibility of the waveguide formation in the horizontal plane. The patterns of the field intensity distribution for these two source positions obtained by the parabolic equation (the eikonal equation) can be represented as two instantaneous patterns of the intensity distribution (or the ray patterns) at some instants of time for which the interval between them is determined by the speed of the packet motion (for the speed $u \sim 1$ m/s and $\Lambda \sim 200$ m, this interval is 200 s). In other words, for fixed $\tau_r$ and $\eta_r$, we will observe temporal intensity fluctuations. In particular, for $\tau_r \sim 4000$ m and $\eta_r \sim 0$, the intensity of both modes in Fig. 3 varies from the maximal value (in the case of focusing) to almost zero (for defocusing) within the aforementioned time interval. For this model example, the level of fluctuations is of the order of 6 dB. More precisely, the maximal fluctuations (whose level is determined by the specific conditions) will take place when $|\eta_r - \eta_s| < \Lambda$, which means that the source and the receiver may fall within one interval between two adjacent crests of the soliton. When $|\eta_r - \eta_s| > \Lambda$, the level of the fluctuations is lower, but they remain significant due to the redistribution of the sound intensity in the horizontal plane. In particular, for a distance of $\tau_r \sim 4000$ m and $\eta_r \sim \Lambda$, the level of fluctuations is ~3 dB for both modes. Thus, if we speak about the possibility of an experimental detection of the sound field intensity fluctuations caused by soliton packets, then, in order to record their maximal allowable level, we must set the source and the receiver so that they are crossed simultaneously by the same soliton crests. The fact that these fluctuations are precisely caused by the solitons is confirmed by the synchronism of the fluctuations in the depth (all modes are focused and defocused simultaneously) and by the temporal scale of the fluctuations that is determined by the speed and the quasi-period of the soliton packets: $\sim\Lambda/u$.

One can expect that the mentioned features of the received signals caused by the soliton packets in a shelf area can serve as the basis for recording intense internal waves crossing an acoustic track.

## ACKNOWLEDGMENTS

This work was supported by the Russian Foundation for Basic Research, project no. 97-05-64878.

## REFERENCES

1. *Sound Transmission through a Fluctuating Ocean*, Ed. by S. Flatte (Cambridge Univ. Press, Cambridge, 1979; Mir, Moscow, 1982).
2. C. J. R. Garrett and W. H. Munk, J. Geophys. Res. **80**, 291 (1975).
3. A. N. Serebryannyĭ, Izv. Akad. Nauk, Fiz. Atmos. Okeana **29**, 285 (1993).
4. S. I. Muyakshin, D. A. Selivanovskiĭ, and A. Yu. Sokolov, in *Problems of Ocean Acoustics*, Ed. by L. M. Brekhovskikh and I. B. Andreeva (Nauka, Moscow, 1984), pp. 164–175.
5. D. Rubenstein and M. N. Brill, in *Ocean Variability and Acoustic Propagation*, Ed. by J. Plotter and A. Warn-Varnas (Kluwer Academic, Dordrecht, 1991), pp. 215–228.
6. Ju-Xun Zhou and Xue-Zhen Zhang, J. Acoust. Soc. Am. **90**, 2042 (1991).
7. B. G. Katsnel'son and S. A. Pereselkov, Akust. Zh. **44**, 653 (1998) [Acoust. Phys. **44**, 684 (1998)].
8. J. R. Apel, M. Badiey, C. S. Chiu, *et al.*, IEEE J. Ocean. Eng. **22**, 465 (1997).
9. S. V. Borisov, A. V. Gritsenko, S. B. Kozitskiĭ, *et al.*, Akust. Zh. **40**, 749 (1994) [Acoust. Phys. **40**, 664 (1994)].
10. S. V. Borisov, R. A. Korotchenko, A. N. Rutenko, and M. Yu. Trofimov, Akust. Zh. **42**, 702 (1996) [Acoust. Phys. **42**, 618 (1996)].
11. K. D. Konyaev, D. E. Leĭkin, K. D. Sabinin, *et al.*, Akust. Zh. **44**, 470 (1998) [Acoust. Phys. **44**, 407 (1998)].
12. Zhou Ju-Xun, Xue-Zhen Zhang, and P. H. Rogers, in *Proceedings of IEEE Conference "Ocean'96," Fort Lauderdale, Florida, 1996*, Vol. 1, pp. 1–8.
13. *Wave Propagation and Underwater Acoustics*, Ed. by J. B. Keller and J. S. Papadakis (Springer, New York, 1979).
14. A. Yu. Shmelerv, A. A. Migulin, and V. G. Petnikov, J. Acoust. Soc. Am. **92**, 1003 (1992).
15. Yu. A. Kravtsov, V. M. Kuz'kin, and V. G. Petnikov, Akust. Zh. **30**, 79 (1984) [Sov. Phys. Acoust. **30**, 45 (1984)].
16. B. G. Katsnel'son and V. G. Petnikov, *Acoustics of a Shallow Sea* (Nauka, Moscow, 1997).
17. K. B. Smith and F. D. Tappert, *UMPE: The University of Miami Parabolic Equation Model, Version 1.1* "MPL Technical Memorandum 432," 1993.
18. F. D. Tappert, in *Wave Propagation and Underwater Acoustics: Lecture Notes in Physics*, Ed. by J. B. Keller and J. S. Papadakis (Springer, New York, 1977), Vol. 70, Chap. 5, pp. 224–287.

*Translated by Yu. Lysanov*

*Acoustical Physics, Vol. 46, No. 6, 2000, pp. 692–699. Translated from Akusticheskiĭ Zhurnal, Vol. 46, No. 6, 2000, pp. 789–797.*


# Scale Invariance of the Intensity Anomaly Induced by the Ice Cover in the Sound Field of a Tone Source in an Arctic Waveguide

**V. D. Krupin**

*Andreev Acoustics Institute, Russian Academy of Sciences, ul. Shvernika 4, Moscow, 117036 Russia*

*e-mail: bvp@akin.ru*

Received December 20, 1999

**Abstract**—On the basis of the normal mode method and the theory of sound scattering by a stochastically rough surface of an elastic layer, the specific features of the frequency dependence of the intensity anomaly induced by the ice cover in the sound field generated by a tone source in an arctic waveguide are studied. The anomaly is determined by the difference between the level (in dB) of the coherent component of the sound intensity that occurs in the waveguide with the ice cover and the intensity level in a waveguide with an ice-free surface. Using the WKB approach, it is shown that the intensity anomaly is invariant for all values of the frequency, the mean ice thickness, and the rms amplitude and correlation radius characterizing the rough undersurface of ice on the condition that the ratios of all the aforementioned geometric parameters to the sound wavelength in water remain constant. This property is confirmed by precise calculations of the anomaly by the mode program and explained by the specific features of the frequency dependence of attenuation coefficients and their distribution in the numbers of normal modes. Possible practical applications of the revealed property of the intensity anomaly are suggested. © *2000 MAIK "Nauka/Interperiodica".*

In the waters of the Arctic basin, the upper water layer underlying the ice cover and reaching several hundred meters in thickness is characterized by a constant temperature close to the freezing point. As a result, according to the known empirical equations, the depth dependence of the sound velocity is mainly determined by the hydrostatic pressure, because the effects of salinity prove to be of the second order of smallness. This leads to the formation of a fully-developed subsurface sound channel with a positive gradient of the sound velocity which almost linearly increases with depth in the upper water layer.

It is well known that, because of the presence of this channel in the waters of the Arctic basin, the sound attenuation there is governed by the ice cover, which by itself is a complex elastic system. The latter can be represented as an inhomogeneous absorbing elastic layer that has rough boundaries and is characterized by depth-dependent velocities of longitudinal and shear waves and by attenuation due to the internal friction between ice grains. The experimental data on the elastic wave attenuation in the bulk of ice show [1] that the attenuation of both longitudinal and shear waves is proportional to the imaginary parts of the corresponding complex wave numbers and linearly depends on frequency in the frequency range from several dozen hertz to 2 kHz; in addition, the attenuation of shear waves exceeds that of longitudinal waves by approximately a factor of six.

In theoretical and numerical studies of sound propagation under the ice cover, it is common practice to use a simplified model of the ice cover in the form of a set of homogeneous absorbing elastic layers. This model serves as the basis for the development of refined numerical models used for describing the sound scattering from the ice surface and the sound propagation under the ice cover with allowance for the spatial-statistical features of the ice undersurface [2–6].

The studies of the effects of various parameters of the arctic waveguide on the frequency characteristics of sound fields are of interest from the viewpoint of both the design and operation of hydroacoustic systems with optimal parameters and the development of methods for acoustical monitoring of waters in the Arctic basin [7]. The numerical modeling of these problems, which includes multiple calculations of the space-frequency characteristics of sound fields for the set of values of the parameters to be estimated, encounters certain difficulties related to the increase in the computational error at high frequencies, as well as to the long time required for such calculations.

In this paper, for a typical model of the arctic sound channel with the ice cover in the form of a homogeneous absorbing elastic layer with smooth boundaries, we derive some simple laws that govern the behavior of the frequency dependences of the waveguide characteristics. The laws represent the "scale invariance"—the property that allows one to increase the efficiency of

1063-7710/00/4606-0692$20.00 

numerical modeling of both direct and inverse problems of underice sound propagation. According to [1], the use of such a simplified model of the ice cover instead of the more realistic multilayer model does not noticeably affect the angular structure and the magnitude of the reflection coefficient for a plane harmonic sound wave incident on the water–ice boundary within the frequency range from several dozen hertz to 2 kHz and for ice thickness up to ~3 m. Therefore, the effects of the multilayer ice structure can be neglected in this study. With the use of new results [5, 6] on sound reflection and scattering from an elastic layer with stochastically rough boundaries, the aforementioned laws are generalized for the model of the arctic waveguide with a rough undersurface of the ice cover. Finally, some possible applications of the established laws are suggested.

At first, we assume that the arctic waveguide is a system consisting of an upper elastic layer with smooth boundaries, a water layer, and a layered absorbing bottom. If the water layer is excited by a concentrated harmonic source with the coordinates $(0, z_0)$ and with a cyclic frequency $\omega = 2\pi f$, the sound pressure $p$ observed at an arbitrary point $(r, z)$ is determined as a sum of normal modes [8]:

$$p(r, z, z_0, \omega) = -\omega\rho_0\frac{Q}{4}\sum_{n=1}^{\infty} w_n(z_0, \xi_n^2)w_n(z, \xi_n^2)H_0^{(1)}(\xi_n r), \quad (1)$$

where $\rho_0$ is the water density; $Q$ is the volume velocity of the source; $z_0$ and $z$ are the transmission and reception depths, respectively; and $r$ is the horizontal distance between the source and the receiver. The quantities $w_n(z)$ and $\lambda_n = \xi_n^2$ (the square of the horizontal complex wave number of the $n$th mode) involved in Eq. (1) are the $n$th normalized eigenfunction and the $n$th eigenvalue, respectively, of the spectral boundary-value problem

$$\frac{d^2w}{d^2z} + \left[\frac{\omega^2}{c^2(z)} - \xi^2\right]w = 0, \quad (2)$$

$$\left[\frac{dw}{dz} + G_s(\xi^2)w\right]_{z=0} = \left[\frac{dw}{dz} + G_b(\xi^2)w\right]_{z=H} = 0, \quad (3)$$

where $\xi$ is the spectral parameter (the horizontal wave number), $H$ is the thickness of the water layer, $c(z)$ is the sound velocity in it, $G_s$ is the input admittance of the homogeneous absorbing ice layer covering the water layer along the plane $z = 0$, and $G_b$ is the input admittance of the absorbing layered bottom ($z \geq H$).

Recasting the matrix expressions given in [1], which relate the displacement potentials of longitudinal and shear waves to their normal derivatives at the upper and lower boundaries of the ice cover, we obtain an expression for the admittance $G_s$:

$$G_s = m_i^{-1}\alpha G_1/G_2, \quad (4)$$

where

$$G_1 = k_s^4[(2\xi^2 - k_s^2)^2\coth(\alpha l) - 4\alpha\beta\xi^2\coth(\beta l)], \quad (5)$$

$$G_2 = \left[(2\xi^2 - k_s^2)^2 - 4\alpha\beta\xi^2\tanh\left(\frac{\alpha l}{2}\right)\coth\left(\frac{\beta l}{2}\right)\right] \times\left[(2\xi^2 - k_s^2)^2 - 4\alpha\beta\xi^2\coth\left(\frac{\alpha l}{2}\right)\tanh\left(\frac{\beta l}{2}\right)\right]^{-1}. \quad (6)$$

Here, $\alpha = \sqrt{\xi^2 - k_p^2}$, $\beta = \sqrt{\xi^2 - k_s^2}$, $k_p = (\omega/c_p)(1 + i\eta_p)$, $k_s = (\omega/c_s)(1 + i\eta_s)$, $c_p$ and $c_s$ are the velocities of the longitudinal and shear waves in the ice layer, $\eta_p$ and $\eta_s$ are the loss coefficients for these waves, $l$ is the ice cover thickness, $m_i = \rho_i/\rho_0$ is the ratio of ice and water densities, and $i = \sqrt{(-1)}$. We assume that a plane harmonic wave is incident from the homogeneous water halfspace characterized by the sound velocity $c_0 = c(0)$ on the water–ice boundary at a grazing angle $\chi$ and this wave has the horizontal wave number $\xi = k_0\cos\chi$, where $k = 2\pi f/c_0$ is the wave number in water near the ice surface. Then, it is easy to verify that the expression for the reflection coefficient $V_s$ that corresponds to the admittance $G_s$ coincides with the formula obtained by Brekhovskikh [9]. From Eqs. (4)–(6), it follows that the reflection coefficient characterizing the sound reflection from the ice surface depends on the grazing angle $\chi$, the physical parameters of ice, and one scale parameter $s = (kl) = 2\pi l/\lambda = s_0 = \text{const}$ ($k = 2\pi f/c_0$ is the wave number, $f$ is the frequency, and $\lambda$ is the wavelength in water) and does not explicitly depend on the frequency $f$. This property of the reflection coefficient will be used below in the analysis of the sound field intensity.

For definiteness, we consider the model of the bottom in the form of a set of $J$ homogeneous absorbing water-saturated layers (with constant thicknesses $h_j$, longitudinal wave velocities $c_j$, densities $\rho_j$, and loss coefficients $\eta_j$, where $j = 1, 2, \ldots, J$) lying on a liquid or elastic absorbing halfspace (substrate), which is characterized by the velocities $c_L$ and $c_T$ of longitudinal and shear waves, the loss coefficients $\eta_L$ and $\eta_T$ for these two types of elastic waves, and the density $\rho_b$. The admittance $G_b$ of such a bottom is determined by the equality [10]

$$G_b = G_0, \quad (7)$$

in which the function $G_0(\xi^2)$ is the zeroth term of the recurrence sequence $\{G_j\}$ of the input admittances at the boundaries between the sediment layers:

$$G_{j-1} = \frac{\rho_{j-1}}{\rho_j}\alpha_j\frac{G_j + \alpha_j\tanh(\alpha_j h_j)}{\alpha_j + G_j\tanh(\alpha_j h_j)}, \quad (8)$$

where $a_j = \sqrt{(\xi^2 - k_j^2)}$, $k_j = (\omega/c_j)(1 + i\eta_j)$, $j = 1, \ldots, J-1, J$). The initial term of this sequence is the admittance $G_J$ of the bottom substrate. For the liquid and elastic bottom models, this admittance is determined by the expressions

$$G_J = m_b^{-1}\sqrt{\xi^2 - k_L^2}, \tag{9}$$

$$G_J = k_T^4 m_b^{-1}\sqrt{\xi^2 - k_L^2}F(\xi^2), \tag{10}$$

respectively. Here, $m_b = \rho_b/\rho_J$ is the ratio of the substrate density to the density of the lowest sediment layer, $F(\xi^2)$ is the Rayleigh function $F(\xi^2) = (2\xi^2 - k_T^2)^2 - 4\xi^2\sqrt{(\xi^2 - k_L^2)(\xi^2 - k_T^2)}$, and $k_L = (\omega/c_L)(1 + i\eta_L)$ and $k_T = (\omega/c_T)(1 + i\eta_T)$ are the complex wave numbers of the longitudinal and shear waves in the substrate. From Eqs. (7)–(10), it follows that the bottom reflection coefficient $V_b$, which characterizes the reflection of a plane wave incident on the boundary $z = H$ at a grazing angle $\chi_H$ from the side of the liquid halfspace [with the density $\rho_0$ and the sound velocity $c_H = c(H)$], depends on the grazing angle, the acoustic parameters of the bottom, and the dimensionless scale parameters $s_{b,j} = k_j h_j = 2\pi h_j f/c_j$, ($j = 1, 2, \ldots, J$) and does not explicitly depend on frequency.

The normalized eigenfunctions $w_n$ of the boundary-value problem given by Eqs. (2) and (3) can be calculated by dividing its arbitrary eigenfunction $w(\xi_n^2, z)$ (determined within a constant factor) by the normalizing coefficient

$$N_n = w(\xi_n^2, 0)\frac{\partial}{\partial\xi} \times \left[\frac{d}{dz}w(\xi^2, z) + G_s(\xi^2)w(\xi^2, z)\right]_{\xi = \xi_n,\, z = 0}, \tag{11}$$

where the function $w(\xi^2, z)$ is the solution to Eq. (2) that satisfies the second boundary condition (3) at $z = H$. Assuming that $kr \gg 1$ and replacing $H_0^{(1)}$ in Eq. (1) by its asymptotic expression at large values of the argument, we obtain

$$p(r, z, z_0, \omega) = -\omega\rho_0\frac{Q}{\sqrt{8i\pi r}} \times \sum_{n=1}^{\infty}\xi_n^{-1/2}w_n(z_0, \xi_n^2)w_n(z, \xi_n^2)\exp(i\xi_n r). \tag{12}$$

This expression will be used below for analyzing the frequency dependences of the sound field intensity. It is convenient to represent the pressure

$$p = p_1 + p_2, \tag{13}$$

where $p_1$ is the sum of the sound pressures of the normal modes with the numbers $n = 1, 2, \ldots, N(f)$, which are characterized by the lowest attenuation and, at sufficiently high frequencies, correspond to rays refracted upwards and reflected from the ice surface without interacting with the bottom, and $p_2$ is the sum of the remaining modes, i.e., modes with the numbers from $N(f) + 1$ to infinity, which correspond to rays multiply reflected from the two absorbing boundaries of the water layer. The mode of number $N(f)$ corresponds to the boundary ray whose grazing angle at the ice surface is close or equal to the angle $\chi_N = \arccos[c(0)/c(H)]$. Therefore, we can assume that, at sufficiently long distances $r$ from the source, the dominant contribution to the sound field is made by the normal modes with the numbers $n = 1, 2, \ldots, N(f)$. According to the high-frequency asymptotic theory (the WKB approximation), the attenuation coefficients for these normal modes, $\beta_n$ (in dB/km), are determined by the expressions [11]

$$\beta_n = (20\log_{10}e)\,\mathrm{Im}\,\xi_n \times 10^3 = -20\log_{10}[|V_s(\chi_n, s)|] \times 10^3/(D_n + \Delta_n), \tag{14}$$

$$D_n = 2\cos(\chi_n)\int_0^{z_t}\left[\left(\frac{c_0}{c(z)}\right)^2 - \cos^2(\chi_n)\right]^{-1/2}dz, \tag{15}$$

$$\Delta_n = -\left(\frac{\partial\varphi_s}{\partial\xi}\right)_{\xi = \xi_n}, \tag{16}$$

where $D_n$ is the cycle length of a geometric ray with the grazing angle $\chi_n$ at the water–ice boundary (this length is equal to the distance between two successive reflections of the ray from the ice surface); $\Delta_n$ is the horizontal displacement of the bundle of rays due to the reflection from the ice surface; $|V_s|$ and $\varphi_s$ are the magnitude and phase of the reflection coefficient at the water–ice interface, respectively; and $z_t$ is the depth of the turning point of the ray with the given grazing angle, this depth being the unique root of the equation $c_0/c(z) - \cos\chi_n = 0$. The grazing angle $\chi_n$ of the ray incident on the ice cover and corresponding to the $n$th mode is determined from the relation $\mathrm{Re}\,\xi_n = k\cos\chi_n$, where $\xi_n$ is the horizontal complex wave number of the mode. It should be noted that, since the magnitude $|V_s|$ and phase $\varphi_s$ of the reflection coefficient at the water–ice boundary explicitly depend on the grazing angle $\chi_n$ and the scale parameter $s = kl$ and do not explicitly depend on the frequency $f$, the attenuation coefficients $\beta_n$ of the normal modes with the numbers $n = 1, 2, \ldots, N(f)$ also do not explicitly depend on frequency and are only functions of the parameter $s$ and of the physical parameters of ice.

For the arctic waveguide, which is characterized by the sound velocity linearly increasing with a depth $c(z) = c_0 + gz$ ($g > 0$, $g$ is the sound velocity the gradient), the

cycle length of a ray with a small grazing angle $\chi_n$ is equal to

$$D_n = 2\chi_n c_0/g \tag{17}$$

and the magnitude of the reflection coefficient $|V_s(\chi_n)|$ can approximately be represented in the form

$$|V_s(\chi_n)| \approx \exp[-\chi_n\gamma], \tag{18}$$

where $\gamma$ is the derivative of the magnitude of the reflection coefficient $|V_s|$ with respect to the grazing angle $\chi$ taken at the zero grazing angle. This quantity does not depend on $\chi_n$ and is a function of the scale parameter $s = kl = 2\pi l/\lambda$ and the physical parameters of ice. Using Eqs. (14)–(16) and taking into account the condition $\Delta_n \ll D_n$, we obtain a fairly accurate expression for the attenuation coefficients $\beta_n$ (in dB/km) of the normal modes captured by the underice sound channel:

$$\beta_n = \sigma\gamma(s)g/c_0 = \beta = \text{const}, \tag{19}$$

where $\sigma = (20\log_{10}e) \times 10^3$. From this expression, it follows that the values of $\beta_n$ are equal for all mode numbers $n = 1, 2, \ldots, N(f)$ and explicitly depend on the scale parameter $s = kl = 2\pi l/\lambda$ and the physical parameters of ice. Then, we note that, at sufficiently high frequencies, the eigenfunctions $w_n$ for these modes are exponentially small in a relatively large depth $z$ interval adjacent to the boundary $z = H$. Since $\mathrm{Im}\xi_n \ll \mathrm{Re}\xi_n$, the normalized eigenfunctions differ little from the corresponding eigenfunctions of a waveguide with an ideal nonabsorbing ice cover ($\eta_p = 0$, $\eta_s = 0$). The wave numbers $\xi_n$ and the eigenfunctions $w_n$ of these modes almost coincide with the corresponding characteristics, $\bar{\xi}_n$ and $\bar{w}_n$, of a waveguide with a nonabsorbing ice cover and an acoustically soft boundary $z = H$. Therefore, we can set $\xi_n = \bar{\xi}_n + i\beta\sigma^{-1}$, $n = 1, 2, \ldots, N(f)$. Thus, for sufficiently high frequencies, the total sound pressure $p_1(r, z, z_0, \omega)$ of the set of normal modes with the numbers $n = 1, 2, \ldots, N(f)$ can be closely approximated by the expressions

$$p_1(r, z, z_0, \omega) = \exp[-\beta(s)\sigma^{-1}r]\bar{p}_1, \tag{20}$$

$$\bar{p}_1(r, z, z_0, \omega) = -\omega\rho_0\frac{Q}{\sqrt{8i\pi r}} \times \sum_{n=1}^{\infty}\bar{\xi}_n^{-1/2}\bar{w}_n(z_0, \bar{\xi}_n^2)\bar{w}_n(z, \bar{\xi}_n^2)\exp(i\bar{\xi}_n r), \tag{21}$$

where the quantity $\beta$ is determined by Eq. (10) and represents the acoustic attenuation coefficient (in dB/km) related to the sound absorption in the bulk of the ice cover, and $p_0$ is the sound pressure in the waveguide with a nonabsorbing ice cover.

Following the theory developed in [12–14], we will obtain an approximate expression for $\bar{p}_1$. We replace the eigenfunctions $\bar{w}_n$ and the wave numbers $\bar{\xi}_n$ in the sum involved in Eq. (21) by the corresponding WKB expressions and transform it to a sum of Fourier integrals with the use of the Poisson summation formula; then, we perform calculations by the method of the stationary phase. As a result, we represent the sound pressure $p_0$ in the form of an infinite sum of fields of all possible rays that (i) leave the source in the upward and downward directions at the angles (with respect to the horizon) whose magnitudes are less than the angle of departure of the boundary ray, (ii) are reflected only from the surface of the nonabsorbing ice cover, and (iii) arrive from above and from below to the observation point $(r, z)$:

$$\bar{p}_1 = -\frac{\omega\rho_0 Q}{\sqrt{8i\pi}} \times \sum_{j=1} A_{s,j}\exp\left[2i\pi f T_{s,j} + i\left(N_{s,j}\varphi_{s,j} - N_{s,j}\frac{\pi}{2}\right)\right]. \tag{22}$$

Here, $A_{s,j}$, $T_{s,j}$, and $\varphi_{s,j}$ are the ray amplitude, the time of signal arrival to the observation point over the $j$th ray that experienced $N_{s,j}$ reflections from the nonabsorbing ice cover, and the phase of the reflection coefficient with a unit magnitude for the reflection of the $j$th ray from the nonabsorbing ice cover, respectively. The expression for the amplitude of the $j$th ray has the form

$$A_{s,j} = \left|r\left(\frac{\partial r}{\partial\mu_{s,j}(z_0)}\right)\tan\mu_{s,j}(z)\right|^{-1/2}, \tag{23}$$

where $\mu_{s,j}(z_0)$ is the departure angle at which the $j$th ray leaves the source (with respect to the horizon) and $\mu_{s,j}(z)$ is the grazing angle of this ray at the point of reception.

Similarly, following the theory [12–14] and using the same transformations, the component $p_2$, which is equal to the sum of the normal modes with the numbers $n > N(f)$, can be represented in the form of the sum of fields of all possible bundles of rays reflected from the bottom and the lower ice surface:

$$p_2 = -\frac{\omega\rho_0 Q}{\sqrt{8i\pi}} \times \sum_j A_{sb,j}\exp[2i\pi f T_{sb,j} + i(N_{s,j}\varphi_{s,j} + N_{b,j}\varphi_{b,j})], \tag{24}$$

where

$$A_{sb,j} = |V_s(\mu_{s,j}, s)|^{N_{s,j}} \times |V_b(\mu_{b,j}, s_{b,1}, s_{b,j})|^{N_{b,j}}\left|r\left(\frac{\partial r}{\partial\mu_{sb,j}(z_0)}\right)\tan\mu_{sb,j}(z)\right|^{-1/2}, \tag{25}$$

$A_{sb,j}$ and $T_{sb,j}$ are the ray amplitude and the time of signal arrival to the observation point for the $j$th ray, $\mu_{s,j}$ and $\mu_{b,j}$ are the grazing angles of the $j$th ray at the points of reflection from the ice surface and from the

bottom, $\mu_{sb,j}(z_0)$ and $\mu_{sb,j}(z)$ are the grazing angles of the $j$th ray at the transmission and reception depths, $N_{s,j}$ and $N_{b,j}$ are the corresponding numbers of reflections of the $j$th ray, and $\varphi_{s,j}$ and $\varphi_{b,j}$ are the phases of the reflection coefficients for the ice-surface and bottom reflections of the $j$th ray. From Eq. (24), it follows that the absorption of elastic waves in the ice layer and in the sediment layers may lead to fast attenuation of the component $p_2$ with increasing $r$, as compared to the component $p_1$.

Using Eqs. (20), (22), and (23) obtained above for $p_1$ and Eqs. (24) and (25) obtained for $p_2$, we select the main characteristic of the sound field in the form of the anomaly $A(r, z, z_0)$ of the sound field intensity and determine this quantity as the relative intensity level in decibels:

$$A = 10\log_{10}[I(r, z, z_0)/I_0(r, z, z_0)], \tag{26}$$

where $I(r, z_0, z)$ is the sound field intensity obtained as a result of an incoherent summation of the intensities of normal modes, and $I_0$ is the sound field intensity in the aforementioned sense in a waveguide without the ice cover ($l = 0$). Using the method of the stationary phase for calculating the sums of integrals of rapidly oscillating functions with the phase factors of types $\exp\{2\pi if[T_{s,j+1}(r) - T_{s,j}(r)]\}$ and $\exp\{2\pi if[T_{sb,j+1}(r) - T_{sb,j}(r)]\}$ over the interval of averaging, we arrive at the following expression correct to the small terms $O(\omega^{-1/2})$:

$$A = 10\log_{10}\left\{\left[\exp\left(-2\frac{\beta}{\sigma}r\right)\sum_{j=1}^{\infty}|A_{s,j}|^2 + \sum_{j=1}^{\infty}|A_{sb,j}|^2\right]\Big/\left[\sum_{j=1}^{\infty}|A_{s,j}|^2 + \sum_{j=1}^{\infty}|\bar{A}_{sb,j}|^2\right]\right\}, \tag{27}$$

where

$$\bar{A}_{sb,j} = |V_b(\mu_{b,j}, s_{b,1}, s_{b,2}, \ldots, s_{b,J})|^{N_{b,j}} \times \left|r\left(\frac{\partial r}{\partial \mu_{sb,j}(z_0)}\right)\tan\mu_{sb,j}(z)\right|^{-1/2} \tag{28}$$

are the amplitudes of rays in the waveguide in the absence of the ice cover.

Consider now the consequences of Eq. (27) for the anomaly $A$ and those of Eqs. (25) and (28) for the amplitudes $A_{sb,j}$ and $\bar{A}_{sb,j}$.

In the special case of a waveguide with the bottom in the form of a homogeneous liquid or elastic halfspace, when the reflection coefficient $V_b$ is a function of the grazing angle and does not depend on the frequency, the anomaly $A$ also does not explicitly depend on the frequency and is a function of the scale parameter $s$ and the parameters $r$, $z$, and $z_0$. This means that the anomaly $A$ is invariant for all frequencies $f$ and ice cover thicknesses $l$ that satisfy the condition of constancy for the scale parameter $s = 2\pi fl/c_0 = \text{const}$ or for the product $q = fl = \text{const}$, and it is invariant at any distances $r$. In the case of a layered bottom with an arbitrary number of sediment layers, the anomaly $A$ does not explicitly depend on the frequency and remains constant for all values of $f$, $l$, and the sediment layer thickness $h_j$ ($j = 1, 2, \ldots, J$), if two conditions are simultaneously satisfied: $s = \text{const}$ and $s_{b,j} = k_j h_j = s(h_j/l)(c_0/c_j) = \text{const}$ ($j = 1, 2, \ldots, J$). At sufficiently long distances from the source, the anomaly $A$ is approximately equal to

$$A = -\beta(s)r, \tag{29}$$

where the quantity $\beta$ (in dB/km) is determined by Eq. (19). From Eq. (29), it follows that, independently of the model of the layered bottom, the anomaly $A$ does not explicitly depend on frequency and is invariant for all values of $f$ and $l$ that satisfy the condition: $s = \text{const}$.

To test the scale invariance property of the sound field intensity, which was revealed theoretically with the use of the WKB approach, the dependences of the anomaly $A$ (in dB) on the horizontal distance $r$ were calculated for different pairs of values of the frequency $f$ and the ice cover thickness $l$ that satisfied the condition $s = \text{const}$ on the basis of the waveguide model typical of one of the shallow-water regions of the Arctic basin. The results of these calculations are presented in Fig. 1.

The depth dependence of the sound velocity in the water layer, whose thickness was $H = 204.47$ m, was set in the form of a linearly increasing function $c(z)$ with a positive hydrostatic gradient of $1.8 \times 10^{-2}$ s$^{-1}$ and with $c_0 = c(0) = 1461.45$ m/s and $c(H) = 1465.15$ m/s. The ice cover was modeled as a homogeneous absorbing elastic layer of density $\rho_i = 0.9$ g/cm$^3$ with the following typical parameters [1]: the longitudinal wave velocity $c_p = 3832.7$ m/s, the shear wave velocity $c_s = 1903.5$ m/s, and the damping factors for longitudinal and shear waves $\delta_p = 0.058$ (dB/m)kHz$^{-1}$ and $\delta_s = 0.348$ (dB/m)kHz$^{-1}$, which correspond to the loss coefficients $\eta_p = 4.068 \times 10^{-3}$ and $\eta_s = 1.212 \times 10^{-2}$. For the bottom of a shallow sea, the model was selected in the form of a single homogeneous water-saturated sediment layer overlying an elastic halfspace with the following acoustic parameters: the sediment layer thickness $h_1 = 40$ m, the longitudinal wave velocity in the sediment layer $c_1 = 1640$ m/s, the sediment density $\rho_1 = 1.8$ g/cm$^3$, and the loss coefficient for longitudinal waves in the sediment layer $\eta_1 = 0.005$. The corresponding parameters of the substrate were as follows: the density $\rho_b = 2.2$ g/cm$^3$, the longitudinal wave velocity $c_L = 2260$ m/s, the shear wave velocity $c_T = 400$ m/s, and the loss coefficients for the longitudinal and shear waves $\eta_L = 0.001$ and $\eta_T = 0.005$.

Figure 1 shows the dependences $A(r)$ calculated for the frequencies 300, 600, and 1000 Hz by the values of the incoherent sums $I_0$ and $I$ for the normal modes, the necessary number of which was 90, 180, and 260,

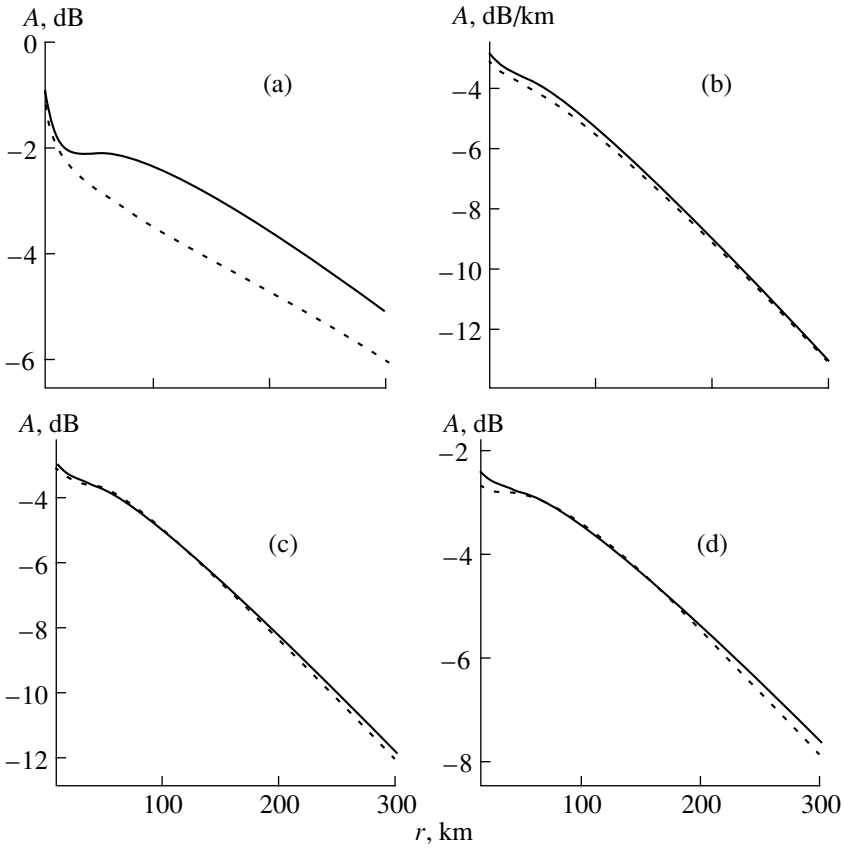


**Fig. 1.** Dependences of the anomaly $A$ on the horizontal distance $r$ for the transmission and reception depths $z_0 = 10$ m and $z = 50$ m, respectively, and for different values of the ice thickness $l$ and frequency $f$ the solid lines correspond to: $l$ = (a) 0.5, (b) 0.6, (c) 1.2, and (d) 1.8 m; $f$ = (a) 600 and (b), (c), (d) 1000 Hz; the dashed lines correspond to: $l$ = (a), (b) 1, (c) 2, and (d) 3 m; $f$ = (a) 300 and (b), (c) and (d) 600 Hz.

respectively. The characteristics of modes were calculated by the mode program that was a modified version of the program developed earlier [8] and took into account Eq. (4) for the admittance $G_s$. As one can see from Fig. 1, the curves $A(r)$ for pair frequency values virtually coincide, which confirms the property of the anomaly that was determined in the WKB approximation. In Fig. 1a, the difference between the curves $A(r)$ obtained for the frequencies 300 and 600 Hz does not exceed 1 dB, and, for the frequencies 600 and 1000 Hz, the difference is of the order of 0.1 dB. These small differences are explained by both the errors of the WKB approximation and the weak effect of the frequency-dependent two-layer model of the waveguide bottom. The scale invariance of the anomaly $A$ is explained by the existence of a set of least attenuating normal modes with equal attenuation coefficients $\beta_n$, which are the functions of the scale parameter $s$ and the parameters of the ice cover and do not explicitly depend on frequency. This property is confirmed by the frequency dependences of $\beta_n$ and the distributions of $\beta_n$ in the mode numbers that were obtained using the mode program and are presented in Figs. 2 and 3. As is seen from Fig. 2, at the frequencies 300, 600, and 1000 Hz, the groups of modes with the numbers $n$ = 1–3, 1–7, and 1–14, respectively, do have identical attenuation coefficients $\beta_n$, while, at a lower frequency of 100 Hz, the values of $\beta_n$ monotonically increase with the mode number. According to Fig. 3, the modal attenuation coefficients $\beta_n$ are nonmonotone functions of the frequency $f$. The curves $\beta_n(f)$ exhibit a characteristic feature, which manifests itself in the fact that all these curves asymptotically merge into one smooth curve with increasing frequency, and this curve can be seen as a lower thick line (envelope) in each of Figs. 3a–3d. At sufficiently high frequencies, every point of this envelope is truly characterized by the equality of the attenuation coefficients of normal modes for the lower mode numbers.

Now, we proceed to the generalization of the results for a more realistic model of the ice cover with a statistically rough lower boundary. For such a model, the most suitable characteristic of the sound field is the coherent component of the sound pressure averaged over the statistical ensemble of realizations of various types of roughness [15], $\langle p \rangle$. The corresponding anomaly of the coherent component of the sound field, $\langle A \rangle$, is

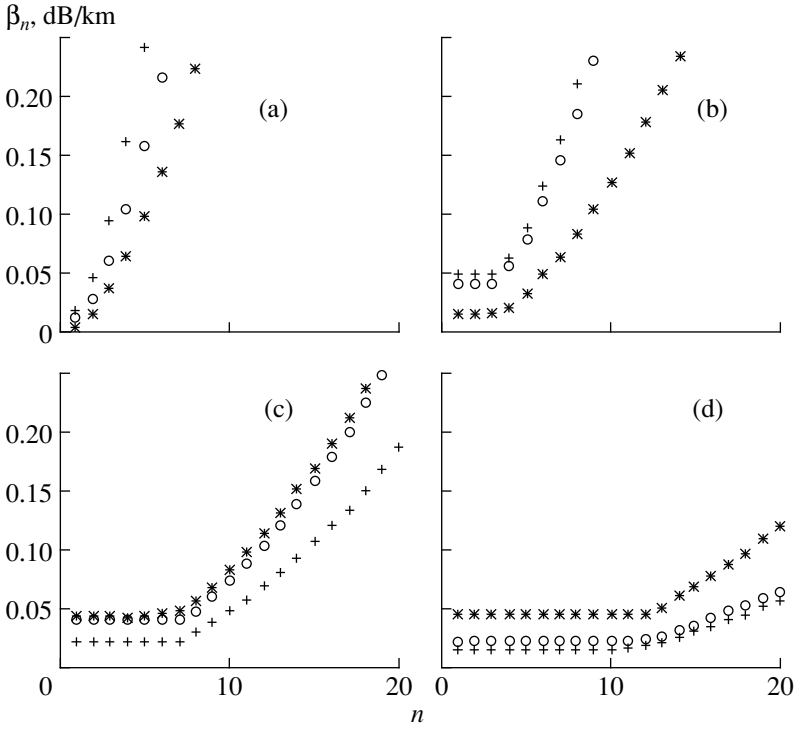


**Fig. 2.** Distributions of the attenuation coefficients of normal modes $\beta_n$ (in dB/km) in the numbers $n$ for three values of the ice thickness $l$ = (*) 1, (○) 2, and (+) 3 m and four frequencies $f$ = (a) 100, (b) 300, (c) 600, and (d) 1000 Hz.

determined by Eq. (26) in which the quantity $I$ is replaced by the quantity $\langle I\rangle$; the latter is equal to the incoherent sum of the intensities of normal modes of a waveguide with the statistical-mean plane ice–water boundary characterized by the coherent reflection coefficient $\langle V_s\rangle$ rather than by $V_s$. In this case, the corresponding components $\langle p_1\rangle$ and $\langle p_2\rangle$ are determined by Eqs. (20), (22), and (23) and Eqs. (24), (25) with the quantity $V_s$ being replaced by $\langle V_s\rangle$. The quantity $\langle V_s\rangle$ is determined as the statistical-mean amplitude of the mirror-reflected wave that occurs when a plane wave of a unit amplitude is incident on the ice surface from the side of the water. If the value of $\langle V_s\rangle$ is known, the coefficient $\tilde{\beta}$, which characterizes the decrease in the intensity $\langle I\rangle$ with distance due to both the attenuation of elastic waves in the bulk of the ice and the sound scattering from the lower boundary of the ice cover, and the anomaly $\langle A\rangle$ are determined by expressions similar to Eqs. (19) and (29):

$$\tilde{\beta} = \sigma\tilde{\gamma}g/c_0, \tag{30}$$

$$\langle A\rangle = -\tilde{\beta}(s)r, \tag{31}$$

where $\tilde{\gamma}$ is the derivative of the quantity $|\langle V_s\rangle|$ with respect to the grazing angle at the zero value of the latter.

For $\langle V_s\rangle$, we can use the expressions derived in [5, 6] for composite models of a rough lower boundary of the ice cover with one or several types of roughness whose amplitude distributions correspond to one or several statistical laws. From these expressions, it follows that the reflection coefficient $\langle V_s\rangle$ does not explicitly depend on frequency and is a function of the parameter $s$ and the statistical parameters $(k\delta_i)^2 = (s\delta_i/l)^2$ and $(k\delta_i)^2(ka_i)^{-1/2} = s^{3/2}(\delta_i/l)^2(a_i/l)^{-1/2}$, where $\delta_i$ are the rms roughness amplitudes with respect to the mean lower boundary of the ice cover, $a_i$ are the spatial correlation radii of the boundary roughness, $l$ is the mean ice thickness, and the subscript $i$ = 1, 2, … indicates the type of roughness of the composite model of the ice cover. Thus, the intensity anomaly $\langle A\rangle$ and the quantity $\tilde{\beta}$ also are functions of the parameter $s$ and of all statistical scale parameters $\zeta_i = \delta_i/l$ and $\nu_i = a_i/l$, which are equal to the ratios of the rms heights and correlation radii of roughness, respectively, to the mean ice cover thickness, and do not explicitly depend on frequency. Hence, for the anomaly $\langle A\rangle$, the scale invariance property remains valid, which means that the value of $\langle A\rangle$ remains constant for all frequencies of the sound field and for all values of the mean ice cover thickness, sediment layer thickness, and rms heights and correlation radii of roughness on the condition that the scale parameters $s$, $s_{b,j}$ ($j$ = 1, 2, …, $J$), $\zeta_i$, and $\nu_i$ are constant.

Eqs. (19) and (29) for $\beta$ and $A(r)$, Eqs. (30) and (31) for $\tilde{\beta}$ and $\langle A(r)\rangle$, and the described features of their frequency dependences can be used in practice to select the optimal frequencies of sound propagation in the arctic waveguide on the basis of the conditions

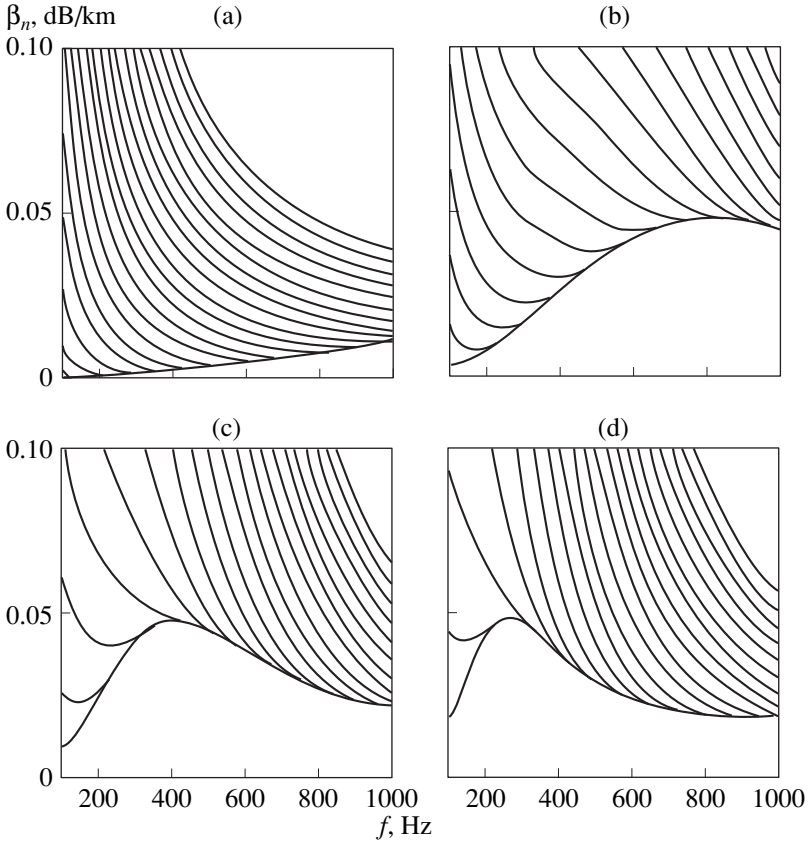


**Fig. 3.** Frequency dependences of the attenuation coefficients of normal modes with the numbers $n$ = 1–20 for the values of the ice thickness $l$ = (a) 0.25, (b) 1, (c) 2, and (d) 3 m. The curves representing $\beta_n$ (in dB/km) follow from left to right in order of increasing number $n$ (from 1 to 20).

$d\beta/df = 0$ or $d\tilde{\beta}/df = 0$, as well as to solve various problems of the acoustical monitoring of the Arctic waters (e.g., the reconstruction of the thermohaline structure of the water medium and the reconstruction of the parameters of the ice cover on the basis of acoustic tomography). They can also be used to increase the speed of operation of computer programs for solving direct and inverse problems of sound propagation under the ice cover, which can be achieved by replacing the calculation of intensity at high frequencies by the faster and more accurate equivalent calculations for lower frequencies that satisfy the condition of constancy for the scale parameter: $s = l/\lambda$ = const.

## ACKNOWLEDGMENTS

This work was supported by the Russian Foundation for Basic Research, project no. 99-02-18359.

## REFERENCES

1. D. F. McCommon and S. T. McDaniel, J. Acoust. Soc. Am. **77**, 499 (1985).
2. F. I. Kryazhev, V. M. Kudryashov, and N. A. Petrov, Morsk. Priborostr., Ser. Akust., No. 2, 56 (1972).
3. V. M. Kudryashov, Akust. Zh. **33**, 1075 (1987) [Sov. Phys. Acoust. **33**, 625 (1987)].
4. W. A. Kuperman and H. Schmidt, J. Acoust. Soc. Am. **86**, 1511 (1989).
5. V. M. Kudryashov, Akust. Zh. **42**, 247 (1996) [Acoust. Phys. **42**, 215 (1996)].
6. V. M. Kudryashov, Akust. Zh. **45**, 529 (1999) [Acoust. Phys. **45**, 472 (1999)].
7. A. B. Baggeroer, W. A. Kuperman, and P. N. Mikhalevsky, IEEE J. Ocean. Eng. **18**, 401 (1993).
8. V. D. Krupin, Sudostr. Prom., Ser. Akust., No. 2, 82 (1989).
9. L. M. Brekhovskikh, *Waves in Layered Media* (Akad. Nauk SSSR, Moscow, 1957; Academic, New York, 1960).
10. N. S. Ageeva and V. D. Krupin, Akust. Zh. **26**, 161 (1980) [Sov. Phys. Acoust. **26**, 89 (1980)].
11. C. T. Tindle, D. E. Weston, and S. G. Payne, J. Acoust. Soc. Am. **68**, 1489 (1980).
12. H. Weinberg, J. Acoust. Soc. Am. **58**, 97 (1975).
13. V. M. Kudryashov, Akust. Zh. **22**, 484 (1976) [Sov. Phys. Acoust. **22**, 406 (1976)].
14. L. B. Felsen and I. Ishihara, J. Acoust. Soc. Am. **65**, 595 (1979).
15. I. A. Aleksandrov, Akust. Zh. **40**, 738 (1994) [Acoust. Phys. **40**, 654 (1994)].

*Translated by E. Golyamina*

*Acoustical Physics, Vol. 46, No. 6, 2000, pp. 700–704. Translated from Akusticheskiĭ Zhurnal, Vol. 46, No. 6, 2000, pp. 798–802.*


# A Numerical Halynometry Experiment on an Acoustic Path in the Arctic Ocean

**V. M. Kudryashov**

*Andreev Acoustics Institute, Russian Academy of Sciences, ul. Shvernika 4, Moscow, 117036 Russia*

*e-mail: bvp@akin.ru*

Received November 10, 1999

**Abstract**—It is shown that, in the Arctic-type deep-water waveguide, the first water mode can be used for acoustic halynometry at frequencies of about 40 Hz and higher. For this task, the stochastic sound scattering by the ice cover and the frequency dispersion of modes are the interfering factors. The data of numerical modeling are presented for the levels of the regular and stochastic components of the pseudo-noise signal and for the impulse response of the waveguide to narrow-band and broadband transmissions. To suppress the stochastically scattered component of the sound field, one can use a horizontal extended array. However, choosing the experimental site in a region with a mainly smooth ice cover may be more advantageous. It is shown that the frequency band of the received signal can be broadened by introducing a frequency–time correction of the propagation time of the first mode as a function of the sound frequency. © *2000 MAIK "Nauka/Interperiodica".*

In the framework of the Arctic ATOC Program [1, 2], acoustic thermometry of Atlantic waters was implemented in the deep-water Arctic region. Sabinin [3] proposed using a similar technique for measuring the time–space variability of salinity within the desalinated water layer in the Arctic waveguide bounded by the ice cover and the layer of the Atlantic waters. He substantiated the scientific and practical-purpose value of such an experiment. He also initiated the studies [4, 5] on the preliminary mathematical validation of the experiment on acoustic halynometry of the desalinated near-ice water layer, which forms the near-ice waveguide. The sound speed profile within this waveguide has a high positive gradient that is sufficient to entirely capture the first water normal wave at sound frequencies about 40 Hz and higher. The salinity variations in the near-ice waveguide are supposed to be measured by estimating the propagation time for the pulse that corresponds to the first water mode. Similarly to the aforementioned experiments [1], the pulse response of the waveguide is to be formed by using a long pseudo-noise signal. The carrier frequency $f_0$ of the signal is modulated by a random function of time $F(t)$, whose parameters can be reproduced with high precision. From the receiving array, the signal of duration $T$ passes to one input of the correlator that includes a multiplier and an integrator. The reference signal is fed to the second correlator input; this signal is produced by a special-purpose oscillator with the same central frequency $f_0$, the frequency band $\Delta f$, and the modulating function $F(t - \tau)$. Then, at the output of the integrator, we have a signal that consists of deterministic and fluctuating components, the envelope of the deterministic one reproducing the shape of the pulse whose power frequency spectrum coincides with $F(t)$ except for the time $t$ being replaced by the delay $\tau$ [4, 5]. The fluctuating component (at the integrator output) has a variance that is by a factor of $1/(4\Delta f T)$ lower than at the integrator input, provided that the output signal of the array remains statistically stationary and ergodic within the time $T$. The antenna array also receives other signals: ambient and ship's noise, etc. However, if they are statistically independent of $F(t)$, the interfering noise has no effect on the deterministic component of the output voltage. The latter fact is very important, because the effects to be detected are weakly pronounced even on long Arctic paths, and relatively low errors in estimating the mode propagation time $t_m$ can lead to a high inaccuracy in the measured variations of the water salinity. The errors in $t_m$ can be caused by the frequency dispersion in the near-ice waveguide, and, hence, the pulse must have a narrow frequency band. On the other hand, in this case, the duration and width of the pulse top will be large, because they are proportional to $1/\Delta f$. That is why we propose to look for a modulating function that provides a sharp pulse top. For example, one can use the maximal length sequence for the phase modulation of the carrier signal, although other suitable functions may exist.

The theory of the normal wave method can be found in monograph [6]. The sound pressure is expanded into waveguide eigenfunctions $\Phi_m(z)$ that correspond to the longitudinal wave numbers $\zeta_m$, where $m$ is the mode ordinal number and $z$ is the vertical coordinate oriented across the waveguide. In a horizontally stratified waveguide, $\Phi_m(z)$ and $\zeta_m$ do not depend on the horizon-

1063-7710/00/4606-0700$20.00 

tal coordinate **r**. If the properties of the waveguide vary with **r**, the functions $\Phi_m(z)$ and $\zeta_m$ can also be functions of **r**. The dependence of $\Phi_m(z)$ on **r** leads to scattering of the modes, i.e., to their interchange. Then, the sound pressure can be calculated with the use of the method of coupled modes, a version of which can be found in papers [7, 8] for tonal and noise-type signals, respectively.

Sound scattering can be both regular and stochastic, depending on the nature of the inhomogeneities of the water bulk and waveguide boundaries. Scattering by the ice cover can be attributed to the stochastic type, though this determination is somewhat conditional. During the observation time for the sound field, the shapes and sizes of the scatterers formed by the ice cover remain nearly unchanged. In other words, one deals with a single realization rather than with an ensemble of realizations. If the ice profile is precisely known, the sound pressure can be calculated with the method of regular scattering. Most likely, this is what must be done when the distance between the corresponding points is comparable with the horizontal sizes of the inhomogeneities. On long paths, the ice roughness can be satisfactorily described by the histogram of the ice draught and the statistical approach is preferable, because the roughness of the ice boundaries are random in their shapes, sizes, and locations. If the mean horizontal scale $\rho$ of the ice roughness is much less than the lengths of the Brillouin mode cycles that contribute to the sound field and the roughness is statistically homogeneous on ranges that are much longer than these cycles (this property being an analog of stationary conditions for time processes) and spatially ergodic [9], one can replace the ensemble averaging by averaging over the ice surface. In doing so, the surface area must be much greater than the cycle lengths along the propagation direction and than the transverse cross-section of the scattering diagram. In the framework of the model of multicomponent ice floes [10], from the histograms one can find the mean thicknesses $h_j$, the variances $\sigma_j^2$, and the coefficients $\varepsilon_j$ that characterize the representability of the $j$th ice type. We attribute the ice fields to one type, if their distribution functions are Gaussian. The resulting distribution function of the ice draught is equal to the sum of the distribution functions of the components composing the ice cover, with the weighting factors $\varepsilon_j$. The mean ice thickness $h$ is [11]

$$h = \sum_{j=1}^{N} \varepsilon_j h_j,$$

where $N$ is the number of components. Being constructed from the same data of ice profiling as used for the histogram, the correlation function of ice also equals to the sum of the correlation functions of the ice-cover components, with the same weighting factors $\varepsilon_j$ [10].

It is worth mentioning that stochastic sound scattering acts to equalize the mean energy fluxes in the modes that form the stochastic component of the sound field, as well as the propagation times of the modes. In this process, the sound energy accumulates in the power component of the stochastic sound field, the fluctuating component being weakly pronounced, because the signals are summed with random phase differences that span the entire interval from 0 to $2\pi$.

The algorithm for computing the sound pressure of the coherent (statistically averaged over the roughness of the ice boundaries) field is based on calculating the following expression:

$$\langle p(\mathbf{r}, z, t)\rangle = \mathrm{Re}\sum_{m=1}^{M}\int_0^\infty G(\omega)P_m(\mathbf{r})\Phi_m(z)\exp(-i\omega t)d\omega, \quad (1)$$

where **r** and $z$ are the coordinates of the observation point, $t$ is time, $G(\omega)$ is the frequency spectrum of the transmitted signal, $\omega = 2\pi f$, and $f$ is the sound frequency. In a planar stratified waveguide, we have

$$P_m(\mathbf{r}) = i\pi\Phi_m(z_0)H_0^{(1)}(\zeta_m r),$$

where $z_0$ is the source depth. For a horizontally irregular waveguide, $P_m(\mathbf{c})$ are calculated according to the scheme given in [7, 8].

To construct the impulse response for the noise-like signal, $G(\omega)$ is considered to be equal to the power spectrum of the function $F(t)$, which is corrected for the passband of the receiving filter (whose frequency response is assumed to be rectangular) and is multiplied by the power $W$ of the sound source. In practice, for a broadband transmission, the sound field is calculated as a sum of narrow-band signals into which the broadband one is broken within the frequency band $\Delta f$. For a tonal signal, the variance of the stochastic component of the sound pressure is calculated according to [12], with corrections for the regular sound scattering. The variance of a broadband signal is also represented as a sum of variances of narrow-band signals. In turn, the variance of a stochastically scattered narrow-band signal is calculated as the variance of a tonal signal multiplied by the factor $W\Delta\tilde{f}/\Delta f$, where $\Delta\tilde{f}$ is the frequency band of the narrow-band component. One can do so, because the variance of the stochastic component includes no interference part. Note that the procedure of calculating the impulse response of a narrow-band noise signal is nearly the same as for a deterministic pulsed signal, if one replaces the modulating function $F(t)$ by its time correlation function $B(\tau)$, and the time $t$ by the time delay [4, 5]. In addition to our previous computations [4, 5], we carried out the calculations for

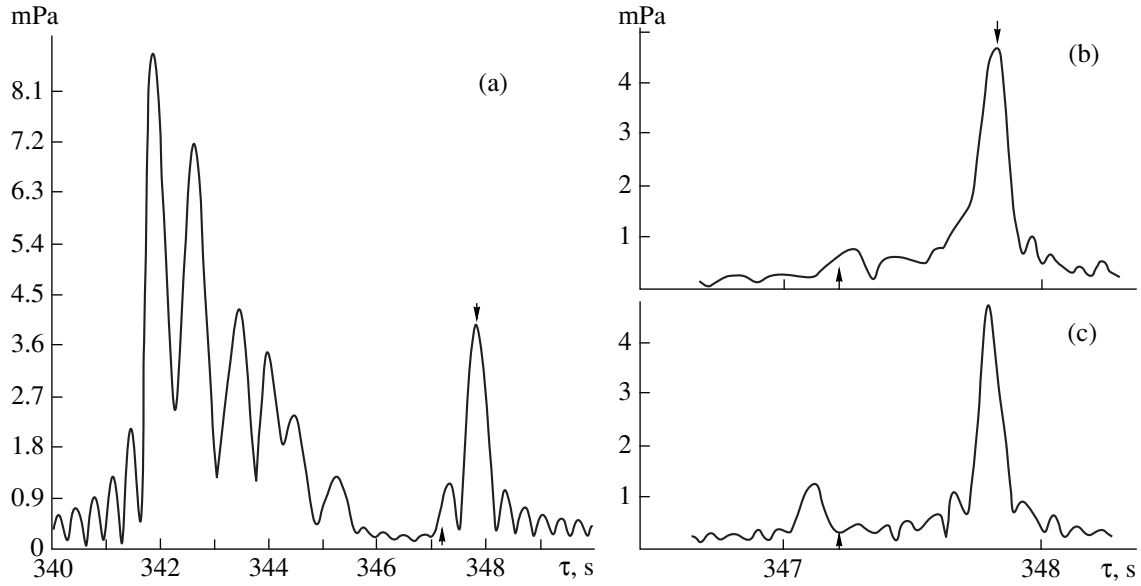


**Fig. 1.** Waveguide impulse response to the coherent noise field: $f_0$ = 60 Hz, $z = z_0$ = 60 m, $r$ = 500 km, $\Delta f$ = (a) 3, (b) 10 without correction, and (c) 10 Hz with correction for the waveguide dispersion of the first water mode.

the profiles of the velocity of sound for the path used in the experiment of 1976. The ice cover was described by the two-component model: a combination of a "smooth" and a hummock ice. The histogram used was that obtained in the central Arctic region. For smooth ice, $\varepsilon_1 = 0.65$. The mean thicknesses were specified as 2.6 and 6.6 m for the smooth and hummock ice types, respectively. The following values were accepted for the ice-water interface: $\sigma_1 = 1.6$ m, $\sigma_2 = 3.3$ m, $\rho_1 = 120$ m, and $\rho_2 = 44$ m. The mean ice thickness $h$, as a whole, was 4 m, and the corresponding value of the ice draught $\sigma$ was 2.91 m. The velocities of the longitudinal and shear waves in ice were specified as $3500(1 + i0.04)$ and $1800(1 + i0.04)$, respectively. The ice density was chosen to be 0.91 relative to the water density.

The sound source is at a depth of 60 m and emits the power $10 \log \hat{W} = 190$ dB, where $\hat{W}$ is normalized to the 1-Hz band and the distance $r$ = 1 m (relative to 1 μPa). The sound signal is received at a depth of 60 m. A central signal frequency of 60 Hz is specified. At this frequency, the first mode nearly does not reach the layer of the Atlantic waters, and the frequency dependence of the mode group velocity is weak. Figure 1a shows the envelope of the correlation convolution of the noise signal with the reference signal for the band $\Delta f$ = 3 Hz, on a path of 500 km in length. Within this frequency band, the signal can be treated as a "narrow-band" signal. According to the plot, the modes of the near-ice waveguide are separated from the others in time. The pulses corresponding to the near-ice modes are located at the end of the plot, because their group velocities are lower than those of other modes.

Figure 1b shows a similar plot for $\Delta f$ = 10 Hz. The broader frequency band of the signal leads to a shorter duration of the mode pulse, but the entire duration of the waveguide impulse response is retained. In Fig. 1b, the terminal part of the impulse response is shown on a stretched time scale. The frequency dispersion of the waveguide broadens the mode pulse and distorts the shape of its envelope. However, the frequency spectrum of the signal can be corrected at the correlator input in such a way that the group velocity $v_m$ of the first mode will remain unchanged. As a result, the impulse responses to modes of other numbers $m$ can be destroyed to a greater extent than is possible with only the frequency dispersion, but these modes are of no interest to us. The correction of the first water mode allows one to increase the frequency band $\Delta f$ in which the signal is analyzed. Hence, for the first water mode, the pulse duration is minimized and the fluctuating component is suppressed to a greater extent at the same duration $T$ of the realization. By doing so, one decreases the error in measuring the propagation time of the first water mode. To correct for the frequency dependence of the group velocity of the desired mode, one should know the law of the channel frequency dispersion. It can be calculated from the known sound speed profile in the water column and the mean thickness $h$ of the ice cover. If $h$ is much less than the sound wavelength, the ice cover weakly affects the phase of the reflected wave. Nevertheless, this effect may be worth accounting for, because high sound attenuation in the Arctic waveguide limits the acceptable length of the propagation path for higher $f_0$.

Figure 1b corresponds to $\Delta f = 10$ Hz with no correction. Figure 1c is similar to Fig. 1b but calculated with the correction of the signal with respect to the first water mode. One can see that the sharpness of the mode pulse is changed to the level corresponding to the narrow-band approximation for the frequency 10 Hz.

The impulse response of the waveguide is computed for the coherent (regular) component of the sound pressure. However, sound scattering by the ice cover creates the stochastically scattered component of the sound pressure, which has a zero mean value and a finite variance, the latter characterizing the mean intensity of the stochastic component. Even for tonal transmission, this component of the sound pressure has a random phase and amplitude. If a pseudo-noise signal is transmitted, the stochastic component correlates with the reference signal, and, hence, it distorts the impulse response of the waveguide (it is formed by mutual scattering of all propagating modes). Since the scattered energy accumulates, the variance of the stochastic component of the sound pressure increases as the frequency $f$ and distance increase and it can exceed the intensity of the coherent component.

For the same propagation path as in Fig. 1, Fig. 2 shows the range dependence of the mean squared sound pressure for $\Delta f = 3$ Hz and the source power $\hat{W}$ within the 1-Hz band, at 1 m from the acoustic center of the transmitting array. The zero level of the sound pressure is equal to 1 μPa, $10\log\hat{W} = 190$ dB. The coherent and total sound fields are labeled by numbers *1* and *2*, respectively. The difference between the plots illustrates the variance of the stochastically scattered component. At 60 Hz, this difference is not large, but corresponds to the sound energy summed over all modes. Figure 1 shows that the maximal level of the coherent field in the first mode is much lower than the maximal value of the total signal. Therefore, for the first water mode, the actual ratio between the coherent and total fields can differ from that shown in Fig. 2 (numbers *3* and *4* correspond to the coherent and total fields in this mode). At a distance of 600 km, the coherent field of the first mode is entirely masked by the stochastically scattered one, so that the stochastic component is an interfering noise in our case. The ratio of the mean intensities of the coherent and stochastic components does not depend on the source power, in contrast to the ratio of intensities for the valid signal and the interference produced by the medium and other sources. To improve the intensity ratio of the valid (i.e., coherent) signal and the interference (also including the stochastically scattered component), one can use a horizontal extended receiving array [13], which is compensated for the phase front of the coherent field of the first water mode with its longitudinal wave number used as that for the array compensator. In this case, at the array output, the ratio of the mean intensities of the coherent and stochastically scattered fields increases in comparison with the input ratio (i.e., in the medium). This increase is proportional to the ratio of the array length and the spatial correlation scale of the stochastic sound field component along the wave front of the coherent field [24]. Note that the presented calculations are performed for the least favorable conditions of sound propagation. The situation will be better if the experiment is carried out in a region where the hummock component of the ice cover does not exist or is weakly pronounced and the variance of the roughness draught is minimal.

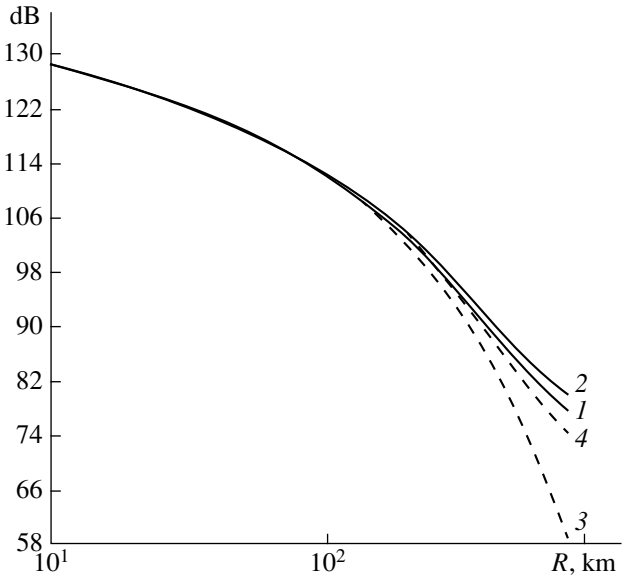


**Fig. 2.** Range dependence of the power component of the noise field: (*1*, *2*) for the coherent and total field of the entire signal and (*3*, *4*) for the signal concentrated in the first water mode; $f = 60$ Hz, $\Delta f = 3$ Hz, $z = z_0 = 60$ m, $10\log\hat{W} = 190$ dB.

## REFERENCES

1. P. N. Mikhalevsky, A. B. Baggeroer, A. Gavrilov, and M. Slavinsky, EOS Trans. Am. Geophys. Union **76**, 265 (1995).
2. P. N. Mikhalevsky, A. N. Gavrilov, and A. B. Baggeroer, IEEE J. Ocean. Eng. **24** (2), 183 (1999).
3. K. D. Sabinin, V. M. Kudryashov, and G. I. Kozoubskaia, in *Proceedings of the Conference IEEE/OES OCEANS'98, Nice, France, 1998*, Vol. 1, pp. 138–142.
4. V. M. Kudryashov, F. I. Kryazhev, and K. D. Sabinin, in *Acoustics of the Ocean* (GEOS, Moscow, 1998), pp. 297–301.
5. G. I. Kozubskaya, V. M. Kudryashov, and K. D. Sabinin, Akust. Zh. **45**, 250 (1999) [Acoust. Phys. **45**, 217 (1999)].
6. L. M. Brekhovskikh, *Waves in Layered Media* (Nauka, Moscow, 1973; Academic, New York, 1980).

7. V. M. Kudryashov, Akust. Zh. **33**, 55 (1987) [Sov. Phys. Acoust. **33**, 32 (1987)].
8. V. M. Kudryashov, Akust. Zh. **34**, 117 (1988) [Sov. Phys. Acoust. **34**, 63 (1988)].
9. V. M. Kudryashov, Metody Predstavl. Apparaturn. Analiz Sluchaĭn. Protsess. Poleĭ **3** (2), 53 (1970).
10. V. M. Kudryashov, Akust. Zh. **45**, 529 (1999) [Acoust. Phys. 45, 472 (1999)].
11. V. M. Kudryashov, Sudostr. Prom., Ser. Akust., No. 4, 99 (1989).
12. V. M. Kudryashov, Akust. Zh. **42**, 438 (1996) [Acoust. Phys. **42**, 386 (1996)].
13. F. I. Kryazhev and V. M. Kudryashov, Akust. Zh. **30**, 790 (1984) [Sov. Phys. Acoust. **30**, 469 (1984)].
14. F. I. Kryazhev and V. M. Kudryashov, Akust. Zh. **24**, 209 (1978) [Sov. Phys. Acoust. **24**, 118 (1978)].

*Translated by E. Kopyl*

*Acoustical Physics, Vol. 46, No. 6, 2000, pp. 705–709. Translated from Akusticheskiĭ Zhurnal, Vol. 46, No. 6, 2000, pp. 803–808.*


# Acoustic Nonlinearity of Cracks Partially Filled with a Viscous Liquid: A Quadratic Approximation

**V. E. Nazarov**

*Institute of Applied Physics, Russian Academy of Sciences,*
*ul. Ul'yanova 46, Nizhni Novgorod, 603600 Russia*
*e-mail: nazarov@hydro.appl.sci-nnov.ru*

Received February 25, 1999

**Abstract**—A mechanism that accounts for the acoustic nonlinearity of cracks partially filled with a viscous liquid is proposed. The mechanism is related to the nonlinear dependences of the capillary and viscous pressures in liquid on the distance between the crack surfaces and on the rate of change of this distance. The nonlinear equation of state is obtained for this type of cracks, and the parameters of this equation are determined. It is shown that the presence of a viscous liquid can lead to a considerable increase in the acoustic nonlinearity of such cracks, as compared to the cracks filled with an ideal liquid. © *2000 MAIK "Nauka/Interperiodica".*

## INTRODUCTION

One of the topical problems in acoustics is the development of physical models and the construction of the equations of state for highly nonlinear media. The origin of a strong acoustic nonlinearity of a medium is the presence of various microdefects (or inhomogeneities) in its structure, and, therefore, such media are called microinhomogeneous [1–4]. The interest expressed by researchers in studying nonlinear acoustic effects in these media is determined by the prospects for the application of nonlinear methods in diagnostics and nondestructive testing. The prospects are related to the fact that the nonlinear properties of a medium are more sensitive than the linear ones to the presence of defects [3, 5].

This paper, which continues our previous studies [5–7], presents a theoretical description of the acoustic nonlinearity of cracks partially filled with a viscous liquid. The nonlinearity is caused by the nonlinear dependences of the capillary and viscous pressures in a liquid on the distance between the crack surfaces and on the rate of change of this distance. The defects of this type are characteristic of rock masses in natural conditions [8, 9].

## CRACK MODEL AND ITS EQUILIBRIUM STATE

To construct the nonlinear equation of state of a crack filled with a viscous liquid, we use the following assumptions.

(1) A crack is a narrow cavity formed in a solid and occupying an area bounded by a circle of radius $R$.

(2) The crack is partially filled with an incompressible viscous liquid that connects the two crack surfaces within a circle of radius $R_0 < R$ centered at the crack center. The part of the crack volume that is free from liquid is filled with gas at a relatively low pressure, so that the elasticity of the gas can be neglected.

(3) The distance between the crack surfaces varies under a small varying stress $\sigma_{nn}$ directed normally to them; in the course of small oscillations of the crack, the tangential velocity of the liquid at the crack surfaces is zero because of the adhesion and no hysteresis of the wetting angle is observed.

To obtain the equation of state of a crack with a viscous liquid (i.e., the dependence $\sigma_{nn} = \sigma_{nn}(d, \dot{d})$, where $2d$ is the variation in the distance between the crack surfaces), we consider (as in [5–7]) a plane-parallel circular cavity of radius $R$ that is equivalent to a narrow elliptic crack [10] with the distance between the surfaces $D \ll R$. The equation of state of such a cavity without liquid has the form [6, 7]

$$\sigma_{nn} = Kd, \tag{1}$$

where $K = 3\pi E/8(1-\nu_0^2)R$ is the effective elastic coefficient of the cavity, $E$ and $\nu_0$ are Young's modulus and Poisson's ratio of the solid without cracks, $|d| < D$, and $|\sigma_{nn}| < \sigma_0 = \pi KD/2$.

Now, we assume that this cavity is partially filled with an incompressible viscous liquid of volume $b$, so that it connects the two surfaces of the cavity within a circle of radius $R_0$ (Fig. 1). (Generally speaking, the equilibrium states of cracks with a viscous liquid and with an ideal liquid are similar; they differ only when the liquids flow.) Because of the surface tension, the pressure in the liquid will differ from the pressure of the gas filling the rest of the cavity by the quantity [11–13]

$$\Delta P = 2\alpha\cos\vartheta/H \tag{2}$$

1063-7710/00/4606-0705$20.00 

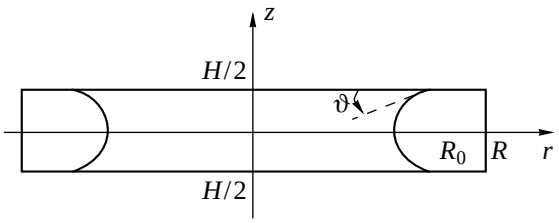


**Fig. 1.** Schematic diagram of a crack in the form of a plane-parallel narrow cavity partially filled with a liquid.

and the equilibrium (or static) state of the cavity will be determined by the following equation (the gas pressure is neglected):

$$\pi R^2 K d_0 + 2\alpha b\cos\vartheta/(D + 2d_0)^2 = 0,$$
$$\text{or } Kd_0 + 2\alpha\mu\cos\vartheta/H = 0, \quad (3)$$

where $\alpha$ is the surface tension coefficient of the liquid, $\vartheta$ is the static (or equilibrium) wetting angle, $\mu = b/\pi R^2 H = (R_0/R)^2$ is the volume (or surface) concentration of the liquid in the cavity, $2d_0$ is the equilibrium variation of the distance between the cavity surfaces due to the capillary pressure in the liquid, $H = D + 2d_0$ is the equilibrium distance between the cavity surfaces in the presence of the liquid in the cavity, and $H \ll R_0\cos\vartheta$.

From Eqs. (3), we obtain

$$2d_0 = -D(1 - [1 - 16\alpha b\cos\vartheta/\pi R^2 HKD^2]^{1/2})/2,$$
$$H = D(1 + [1 - 16\alpha\mu\cos\vartheta/KD^2]^{1/2})/2, \quad (4)$$

i.e., the presence of liquid in the cavity changes the initial distance $D$ between the cavity surfaces in such a way that, for a nonwetting liquid ($\pi/2 < \vartheta \geq \pi$), the cavity widens, and, for a wetting liquid ($\vartheta < \pi/2$), the cavity narrows. From these expressions, one can see that the equilibrium state of the cavity is possible when the condition $16\alpha\mu\cos\vartheta/KD^2 < 1$ is fulfilled. However, we note that, as the cavity narrows, the equilibrium distance between its surfaces cannot be less than $H^* = b/\pi R^2$. At $H = H^*$, the whole cavity will be filled with liquid ($\mu = 1$), and its further compression will be impossible; simultaneously, the nonlinearity of the crack will disappear. In this connection, in the following consideration we assume that the conditions $(16\alpha\mu\cos\vartheta/KD^2) < 1$, $H > H^*$, and $\mu < 1$ are valid.

For a narrow cavity ($H \ll a$, where $a = (2\alpha/\rho g)^{1/2}$ is the capillary constant, $\rho$ is the density of liquid, and $g$ is the acceleration of gravity), the profile of an unperturbed (i.e., static) meniscus is part of a circle of radius $R_m = H/2\cos\vartheta$ [11–13] and, in the cylindrical coordinates (Fig. 1), its shape will be determined by the expression

$$U_r(z, H, \vartheta) = R_0 + (H\tan\vartheta)/2 - [(H/2\cos\vartheta)^2 - z^2]^{1/2}, \quad (5)$$

where $\partial U_r(z = H/2, H, \vartheta)/\partial z = \cot\vartheta$.

## NONLINEAR DYNAMICAL EQUATION OF STATE FOR A CRACK

The fundamental difference in the nonlinear (i.e., dynamical) behavior of ideal and viscous liquids in a narrow crack lies in the fact that oscillations of an ideal liquid are accompanied by variations in its surface concentration ($R_0 \neq$ const) with the wetting angle $\vartheta$ being constant and the meniscus having the shape of part of a circle, whereas small oscillations of a viscous liquid are characterized by a constant surface concentration ($R_0 =$ const), a varying wetting angle, and a deviation of the meniscus shape from the circular one.

When a crack with a viscous liquid experiences a small varying stress $\sigma_{nn}$ (that corresponds to small oscillations of the meniscus), the distance $\tilde{H}$ between the crack surfaces will vary by a small quantity $2d \ll H$ ($\tilde{H} = H + 2d$), so that the equation

$$\dot{P}_z = \pi R^2\sigma_{nn} - \pi R^2 K(d + d_0) + 2\pi\int_0^{R_0} P(r, \tilde{H}, \dot{d})r\,dr \quad (6)$$

will be satisfied. Here, $P_z$ is the $z$ component of the momentum of the liquid enclosed in the layer $0 \leq z \leq \tilde{H}/2$; $P(r, \tilde{H}, \dot{d}) = P_1(\tilde{H}) + P_2(r, \tilde{H}, \dot{d})$, where $P_1(\tilde{H})$ and $P_2(r, \tilde{H}, \dot{d})$ are the capillary and viscous pressures in the liquid; and $\dot{d}$ is the rate of motion of the cavity surface. (The condition of smallness for the displacements $d$, which provides the absence of the liquid motion along the crack surfaces and, hence, the absence of the wetting angle hysteresis [13, 14], will be considered below.)

To determine the pressure $P(r, \tilde{H}, \dot{d})$, we solve the problem on the oscillations of a viscous liquid in a cavity when the distance $\tilde{H}$ between the cavity surfaces varies under a varying stress $\sigma_{nn}$. (The solution of a similar linear problem without taking into account the surface tension of the liquid can be found in [11].) In the cylindrical coordinates with the origin at the cavity center, the motion of the liquid is axially symmetric and, since the cavity is narrow, the motion is mainly radial and satisfies the conditions $V_z \ll V_r$ and $\partial V_r/\partial r \ll \partial V_r/\partial z$, where $V_z$ and $V_r$ are components of the liquid motion. Thus, at small Reynolds numbers ($\mathrm{Re} = \dot{d}H/\nu \ll 1$), the motion of the liquid in the cavity will be described by the linear equations of hydrodynamics [11]:

$$\partial V_r/\partial t = -(1/\rho)\partial P/\partial r + \nu\partial^2 V_r/\partial z^2 = 0, \quad (7)$$

$$(1/r)\partial(rV_r)/\partial r + \partial V_z/\partial z = 0 \quad (8)$$

with the nonlinear boundary conditions

$$V_r(z = \pm\tilde{H}/2) = 0, \tag{9}$$

$$V_z(z = \pm\tilde{H}/2) = \pm\dot{d}, \tag{10}$$

$$P(r = R_0, \tilde{H}, \dot{d}) = P_1(\tilde{H}), \tag{11}$$

where $\nu$ is the kinematic viscosity of the liquid.

For acoustic disturbances in the frequency range satisfying the condition $\omega \ll \omega^* = \nu/H^2$, the motion of the liquid in the cavity will be a steady one and the term $\dot{V}_r$ in Eq. (7) can be neglected [11]. For the same reason, we will neglect the inertial term $\dot{P}_z \sim \dot{V}_z$ in Eq. (6). (For narrow cracks, the frequency $\omega^*$ is sufficiently high. For example, for cracks with water ($\nu = 10^{-2}$ cm$^2$/s) at $H = 10^{-4}$ cm, we obtain $\omega^* \simeq 10^6$ Hz.) Then, the solution to Eqs. (7)–(11) has the form

$$V_r(z, r, \dot{d}) = \frac{6r\dot{d}}{\tilde{H}^3}(z^2 - \tilde{H}^2/4), \tag{12}$$

$$V_z(z, \dot{d}) = -\frac{4z\dot{d}}{\tilde{H}^3}(z^2 - 3\tilde{H}^2/4), \tag{13}$$

$$P(r, \tilde{H}, \dot{d}) = \frac{6\eta\dot{d}}{\tilde{H}^3}(r^2 - R_0^2) + P_1(\tilde{H}), \tag{14}$$

where $\eta = \nu\rho$ is the dynamic viscosity of the liquid. (When the surface tension is neglected ($P_1 = 0$), Eq. (14) coincides with the corresponding equation obtained in [11].) From Eq. (14), it follows that the viscous pressure in the liquid depends on the distance $\tilde{H}$ between the crack surfaces and the rate of change of this distance $\dot{d}$: $P_2(r, \tilde{H}, \dot{d}) \sim \eta\dot{d}/\tilde{H}^3$. This is the cause of the viscous nonlinearity of the crack.

To determine the capillary pressure $P_1(\tilde{H})$, we study the variations in the shape and area of the meniscus with varying the distance $\tilde{H}$ between the surfaces. As was mentioned, the oscillatory radial flow of the viscous liquid in the crack will lead to oscillations of the meniscus whose shape $\tilde{U}_r = \tilde{U}_r(z, \tilde{H}, \tilde{\vartheta})$ will be determined by the equation

$$\tilde{U}_r(z, \tilde{H}, \tilde{\vartheta}) = U_r(z, \tilde{H}, \vartheta) + \xi(z, r \simeq R_0, d). \tag{15}$$

Here, $\tilde{\vartheta}$ is the dynamical wetting angle; $U_r(z, \tilde{H}, \vartheta)$ is determined by Eq. (5) in which the constant quantity $H$ is replaced by the varying quantity $\tilde{H}$; and the perturbation of the meniscus shape $\xi(z, r \simeq R_0, d)$ is determined from the equation [11]

$$\partial\xi/\partial t + (V_r\partial\xi/\partial r + V_z\partial\xi/\partial z) = V_r(z, r \simeq R_0, \dot{d}). \tag{16}$$

In this case, as in the equilibrium state (5), the condition $\partial\tilde{U}_r(z = \tilde{H}/2, \tilde{H}, \tilde{\vartheta})/\partial z = \cot\tilde{\vartheta}$ will be fulfilled.

Solving Eq. (16) by the perturbation method, we determine the quantity $\xi$:

$$\begin{aligned}\xi(z, r \simeq R_0, d) &= 6R_0(d/H)((z/H)^2 - (1/4)) \\ &+ 6R_0(d/H)^2((z/H)^4 - 9(z/H)^2 + (1/16)) \\ &+ 20R_0(d/H)^3((z/H)^6 - (81/20)(z/H)^4 \\ &+ (33/16)(z/H)^2 - (1/64)).\end{aligned} \tag{17}$$

Differentiating Eq. (15) with respect to $z$ at $z = \tilde{H}/2$, we obtain an equation for the dynamical wetting angle $\tilde{\vartheta}$:

$$\cot\tilde{\vartheta} = \cot\vartheta + 6R_0d/H^2, \tag{18}$$

from which

$$\cos\tilde{\vartheta} = \cos\vartheta + (6R_0d/H^2)\sin^3\vartheta. \tag{19}$$

From this expression, it follows that, as the distance between the crack surfaces varies, the dynamical wetting angle $\tilde{\vartheta}$ behaves in different ways depending on the value of the static wetting angle $\vartheta$; namely, when the cavity widens ($d > 0$), for $0 < \vartheta < \pi/2$, the wetting angle $\tilde{\vartheta}$ decreases and, for $\pi/2 < \vartheta < \pi$, it increases, and vice versa; for $\vartheta = 0$ and $\vartheta = \pi$, the wetting angle $\tilde{\vartheta}$ remains constant, $\tilde{\vartheta} = \vartheta$; and at $\vartheta = \pi/2$, the wetting angle $\tilde{\vartheta}$ varies so that $\cos\tilde{\vartheta} > 0$ when the cavity widens and $\cos\tilde{\vartheta} < 0$ when it narrows. From Eq. (19), we obtain a limitation on the values of $d$ at which the liquid does not move along the crack surfaces and no hysteresis of the wetting angle is observed. Evidently, these conditions will be fulfilled when the dynamical wetting angle will satisfy the inequalities $\vartheta_r \le \tilde{\vartheta} \le \vartheta_a$ [13, 14] or (when $(6R_0|d|/H^2)\sin^3\vartheta \ll |\cos\vartheta|$)

$$\vartheta - \vartheta_a \le (6R_0d/H^2)\sin^2\vartheta \le \vartheta - \vartheta_r, \tag{20}$$

where $\vartheta_a$ and $\vartheta_r$ are the inflow and outflow wetting angles.

The hysteresis of the wetting angle depends on many factors (surface roughness, surface impurities, presence of surfactants in the liquid, etc.), and the difference between the angles $\vartheta_a$ and $\vartheta_r$ may exceed 10° [13, 14], so that, for liquids with the wetting angles $\vartheta \ll \pi/2$ and $\vartheta \simeq \pi$, inequalities (20) will be satisfied with a large safety margin in $d$. Using Eqs. (5), (15), and (17),

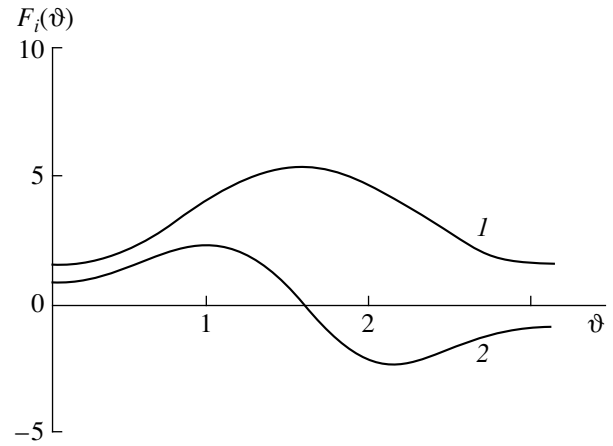


**Fig. 2.** Plots of the functions $F_i = F_i(\vartheta)$ ($i = 1, 2$).

we determine the area $S(\tilde{H})$ of the meniscus of the viscous liquid in the crack:

$$S(\tilde{H}) = 4\pi \int_0^{\tilde{H}/2} \tilde{U}_r(z, \tilde{H}, \tilde{\vartheta}) \times (1 + [\partial \tilde{U}_r(z, \tilde{H}, \tilde{\vartheta})/\partial z]^2)^{1/2} dz. \quad (21)$$

Performing some calculations (for $R_0 \gg H\tan\vartheta$, $R_0(\pi/2 - \vartheta) \gg H$, and $R_0\cos\vartheta \gg H$), from Eq. (21), correct to the third power of $d$, we obtain

$$S(\tilde{H}) = 2\pi R_0 H(\pi/2 - \vartheta)/\cos\vartheta + (4\pi R_0^2\cos\vartheta/H)d + (9\pi R_0^3/4H^3)F_1(\vartheta)d^2 - (216\pi R_0^4/35H^5)F_2(\vartheta)d^3, \quad (22)$$

where

$$F_1(\vartheta) = ((\pi/2 - \vartheta) + (\sin2\vartheta + \sin4\vartheta)/4 - (\sin6\vartheta)/12)/\cos^3\vartheta,$$

$$F_2(\vartheta) = \cos\vartheta(7 - 10\cos^2\vartheta + (35/9)\cos^4\vartheta).$$

The plots of the functions $F_i = F_i(\vartheta)$ ($i = 1, 2$) are presented in Fig. 2.

By the change in the meniscus area, we determine the capillary pressure in the liquid correct to the terms quadratic in $d$ [11]:

$$P_1(\tilde{H}) = -(\alpha/\pi R_0^2)\frac{\partial S(\tilde{H})}{\partial \tilde{H}} = -\alpha(2\cos\vartheta/H + (9R_0/4H^3)F_1(\vartheta)d - (324R_0^2/35H^5)F_2(\vartheta)d^2). \quad (23)$$

Finally, from Eqs. (3), (6), (14), and (23), we obtain the nonlinear (in the quadratic approximation in $d$) equation of state for a crack partially filled with a viscous liquid:

$$\sigma_{nn} = K_0 d - gd^2 + \beta\dot{d} - \gamma d\dot{d}, \quad (24)$$

where

$$K_0 = K + (9\alpha\mu R_0/4H^3)F_1(\vartheta) > 0,$$
$$g = (324\alpha\mu R_0^2/35H^5)F_2(\vartheta),$$
$$\beta = 3\mu\eta R_0^2/H^3, \quad \gamma = 18\mu\eta R_0^2/H^4. \quad (25)$$

The derived equation is nonlinear in the variation $d$ of the distance between the crack surfaces and in the rate of change of this distance $\dot{d}$. In this equation, the terms $K_0 d$ and $gd^2$ describe the linear and nonlinear components of the crack elasticity that is caused by the surface tension of the liquid and the terms $\beta\dot{d}$ and $\gamma d\dot{d}$ describe the linear dissipation and the dissipative nonlinearity related to the viscosity of liquid.

## DISCUSSION AND CONCLUSIONS

It is of interest to compare the equation of state (24) with the corresponding equation obtained in [6, 7] for a crack with an ideal liquid. With the notation used above, the latter equation will have the form of Eq. (24) in which the coefficients $K_0$ and $g$ are determined by the expressions

$$K_0 = K - 8\alpha\mu\cos\vartheta/H^2 \quad (K_0 > 0 \quad \text{at} \quad 18\alpha\mu\cos\vartheta/KD^2 < 1),$$
$$g = -24\alpha\mu\cos\vartheta/H^3, \quad (26)$$

and the coefficients $\beta$ and $\gamma$ are equal to zero.

From Eqs. (25) and (26), one can see that the equation of state for a crack with an ideal liquid cannot be derived from the equation of state for a crack with a viscous liquid by setting $\eta = 0$ in the latter (despite the fact that, in this case, the dissipative terms $\sim\eta\dot{d}$ vanish), because, for these two kinds of liquids, the boundary conditions at the crack surfaces are different. The difference in the boundary conditions leads to a difference in the behavior of the meniscus in the ideal and viscous liquids with varying distances between the crack surfaces and, hence, to differences in the linear and nonlinear elastic coefficients $K_0$ and $g$ of the crack. From Eqs. (25) and (26), it follows that the ratio between the values of the nonlinear elastic coefficient $g$ for cracks with a viscous and an ideal liquid is determined by the expression

$$G = -(27R_0^2/70H^2)F_2(\vartheta)/\cos\vartheta. \quad (27)$$

From this expression, it follows that, for wetting and nonwetting liquids when $R_0/H \gg 1$, the ratio $G$ can reach considerable values; in addition (in the quasi-

static case), the nonlinear parameter $\Gamma$ of a solid containing cracks with a viscous liquid will be determined by the expression

$$\Gamma = G\Gamma_0, \tag{28}$$

where $\Gamma_0$ is the nonlinear parameter of the same solid containing cracks with an ideal liquid [6, 7]. Calculations show that, for a solid characterized by an isotropic distribution of cracks partially filled with a viscous liquid and by the parameters $R = 5 \times 10^{-1}$ cm, $H = 1.6 \times 10^{-5}$ cm, $\mu_0 = 1/2$, $\nu_0 = 1/4$, $\alpha = 73$ g/s$^2$, $E = 5 \times 10^{11}$ g/cm s$^2$, $\vartheta = 0$, and the crack concentration $N_0 = 10^{-5}$ cm$^{-3}$, the nonlinear parameter is $\Gamma \simeq -2.5 \times 10^6$, which exceeds the molecular nonlinear parameter of homogeneous solids, liquids, and gases by more than five orders of magnitude.

Now, let us compare the capillary nonlinearity and the viscous nonlinearity of the crack, which are described by the second and fourth terms in Eq. (24). From Eqs. (25), it follows that, in the frequency range of acoustic disturbances

$$\omega < \omega_0 = |g/\gamma| = 18\alpha|F_2(\vartheta)|/35\eta H, \tag{29}$$

the capillary nonlinearity dominates over the viscous one.

The calculation shows that, for cracks with water ($\vartheta = 0$, $\alpha = 73$ g/s$^2$, and $\eta = 10^{-2}$ g/s cm) at $H = 10^{-4}$ cm, the frequency $\omega_0$ proves to be fairly high and is about $3.6 \times 10^7$ Hz.

Thus, the described mechanism of the acoustic nonlinearity of cracks partially filled with a viscous liquid is related to the nonlinear dependence of the capillary and viscous pressures in a liquid on the distance between the crack surfaces, and this mechanism can lead to a considerable increase in the acoustic nonlinearity of such cracks, as compared to cracks partially filled with an ideal liquid. We also note that the same mechanism of nonlinearity will manifest itself in other contact-type microinhomogeneous media containing a liquid and gas and, specifically, in water-saturated porous and granular media.

Equation (24) derived above will be used in the subsequent studies to derive the nonlinear equation of state for solids containing large numbers of cracks partially filled with viscous liquids.

## ACKNOWLEDGMENTS

This work was supported by the Russian Foundation for Basic Research, project nos. 98-05-64683 and 98-02-17686.

## REFERENCES

1. M. I. Isakovich, *General Acoustics* (Nauka, Moscow, 1973).
2. V. E. Nazarov, L. A. Ostrovsky, I. A. Soustova, and A. M. Sutin, Phys. Earth Planet. Inter. **50**, 65 (1988).
3. V. Yu. Zaĭtsev, Acoust. Lett. **19**, 171 (1996).
4. V. E. Gusev, W. Lauriks, and J. Thoen, J. Acoust. Soc. Am. **103**, 3216 (1998).
5. V. E. Nazarov and A. M. Sutin, J. Acoust. Soc. Am. **102**, 3349 (1997).
6. V. E. Nazarov, Acoust. Lett. **20**, 50 (1996).
7. V. E. Nazarov, Akust. Zh. **45**, 92 (1999) [Acoust. Phys. **45**, 82 (1999)].
8. A. Nur, Bull. Seismol. Soc. Am. **62**, 1217 (1972).
9. R. J. O'Connell and B. Budiansky, J. Geophys. Res. **79**, 5412 (1974).
10. I. N. Sneddon, *Fourier Transforms* (McGraw-Hill, New York, 1951; Inostrannaya Literatura, Moscow, 1955).
11. L. D. Landau and E. M. Lifshitz, *Course of Theoretical Physics*, Vol. 6: *Fluid Mechanics* (Nauka, Moscow, 1986; Pergamon, New York, 1987).
12. D. V. Sivukhin, *General Course of Physics: Thermodynamics and Molecular Physics* (Nauka, Moscow, 1979).
13. A. W. Adamson, *The Physical Chemistry of Surfaces* (Wiley, New York, 1982; Mir, Moscow, 1979).
14. P. G. de Gennes, Usp. Fiz. Nauk **151** (4), 619 (1987).

*Translated by E. Golyamina*

*Acoustical Physics, Vol. 46, No. 6, 2000, pp. 710–715. Translated from Akusticheskiĭ Zhurnal, Vol. 46, No. 6, 2000, pp. 809–815.*


# Acoustical Characteristics of a Multichannel Transmission Line

**V. V. Tyutekin**

*Andreev Acoustics Institute, Russian Academy of Sciences, ul. Shvernika 4, 117036 Russia*

*e-mail: bvp@akin.ru*

Received February 17, 2000

**Abstract**—The properties of an acoustic system called by the author "a multichannel transmission line" (MTL) are considered. Analytical expressions are derived for the following main acoustical characteristics of an MTL consisting of an arbitrary number $N$ of single lines: the input impedance, the resonance frequencies, the reflection and transmission factors for an MTL-insulator, and the reflection factor for an MTL-absorber. For these quantities, numerical calculations are performed, and their frequency dependences are presented for different parameters of the constituent lines in the cases $N = 2$ and 3. It is shown that the acoustical characteristics of MTL-insulators and MTL-absorbers have considerable advantages over the characteristics of similar systems designed on the basis of single lines. *© 2000 MAIK "Nauka/Interperiodica".*

The problem of sound and vibration absorption and insulation remains topical from both the theoretical and the practical points of view. In recent years, the progress in this field of acoustics has been characterized by the development of the so-called active methods [1–7]. However, the conventional methods of sound and vibration control are also undergoing further improvement and development (see, e.g., [8]).

An acoustic transmission line is a one-dimensional extended system whose transverse dimensions are small relative to the wavelength of the acoustic waves propagating in it. Examples of such lines are thin pipes with a liquid or without it, rods, thin narrow strips, etc. The theory that makes it possible to calculate the acoustical characteristics of such transmission lines (even with allowance for the dependence of their inertial and elastic parameters on the longitudinal coordinate) was developed many years ago [9, 10].

However, the solution of some practical problems may require the use of complex acoustic systems that provide high-quality acoustical characteristics. This paper studies one such system, which will be called "a multichannel transmission line" (MTL). This system makes it possible to transform and, specifically, to improve the acoustical characteristics typical of a conventional transmission line.

One of the possible models of such an MTL is shown in Fig. 1a. It consists of several parallel lines of equal lengths $l$. The left ends of the lines are connected with each other by a weightless, perfectly rigid plate, so that the particle velocities at these ends are equal for all lines. The same is true for the right ends. An example of such an MTL can be a multichannel exhaust muffler of an internal combustion engine [11].

Each of the single lines forming the model is characterized by a constant velocity and a wave impedance $z_j = \rho_j c_j S_j$, where $\rho_j$ and $S_j$ are the constant density and cross-sectional area, respectively; $1 \le i \le N$.

As the first acoustical characteristic to be calculated, we select the input impedance of the MTL. We assume that a harmonic force $F = F_0 \exp(-i\omega t)$, where $\omega$ is the circular frequency, is applied to the left end ($x = 0$) of the line (the factor $\exp(-i\omega t)$ will be omitted below).

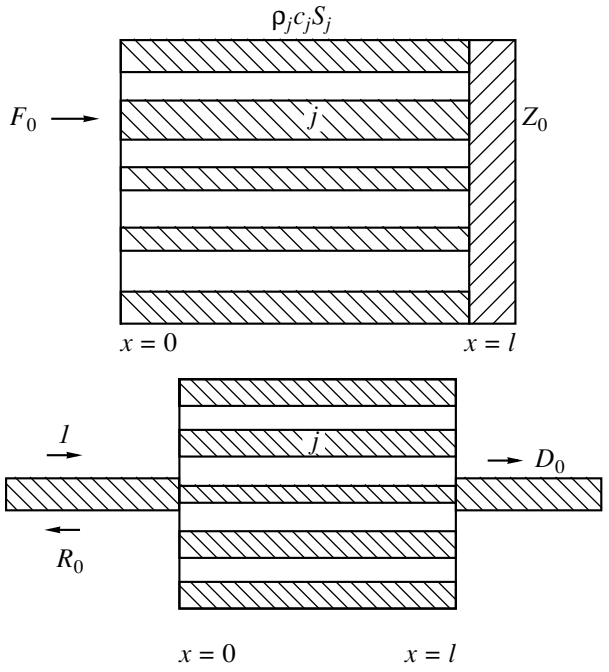


**Fig. 1.** Schematic diagram of a multichannel transmission line (MTL).

1063-7710/00/4606-0710$20.00 © 2000 MAIK "Nauka/Interperiodica"

The right end of the line ($x = l$) is assumed to be loaded by the impedance $Z_0$. We set the particle velocity for the $j$th line in the form

$$u_j(x) = A_j \cos k_j x + B_j \sin k_j x, \quad (1)$$

where $k_j = \omega/c_j$ is the wave number and $A_j$ and $B_j$ are unknown constants. The longitudinal force in the $j$th line will be determined by the expression

$$F_j = \frac{E_j S_j}{i\omega}\frac{du}{dx} = -iz_j(-A_j \sin k_j x + B_j \cos k_j x), \quad (2)$$

where $E_j = \rho_j c_j^2$ is the elastic modulus of the $j$th line.

Based on the model shown in Fig. 1, we can set the boundary conditions in the form

$$x = 0: \quad u_j = u(0), \quad \sum_{j=1}^{N} F_j = -F_0, \quad (3a)$$

$$x = l: \quad u_j = u(l), \quad \sum_{j=1}^{N} F_j = -Z_0 u(l). \quad (3b)$$

Here, $u(0)$ and $u(l)$ are the unknown particle velocities that are common for all lines.

The boundary conditions (3a) and (3b) lead to the following equations:

$$A_j = u(0), \quad (4a)$$

$$i\sum_{j=1}^{N} z_j B_j = -F_0, \quad (4b)$$

$$A_j \cos\varphi_j + B_j \sin\varphi_j = u(l), \quad (4c)$$

$$i\sum_{j=1}^{N} z_j(-A_j \sin\varphi_j + B_j \cos\varphi_j) = -Z_0 u(l), \quad (4d)$$

where $\varphi_j = k_j l$ is the phase shift in the $j$th line.

Substituting Eq. (4a) into Eqs. (4c) and (4d), we determine the quantities $B_j$ from Eq. (4c). Substituting these quantities into Eqs. (4b) and (4d), we obtain a system of two algebraic equations in two unknowns, $u(0)$ and $u(l)$:

$$Z_1 u(l) - Z_2 u(0) = -F_0, \quad (5a)$$

$$(Z_2 + Z_0)u(l) - Z_1 u(0) = 0. \quad (5b)$$

Here,

$$Z_1 = i\sum_{j=1}^{N} \frac{z_j}{\sin\varphi_j}, \quad Z_2 = i\sum_{j=1}^{N} z_j \cot\varphi_j. \quad (6)$$

We note that the quantity $Z_2$ is a sum of the impedances of individual lines loaded by an infinite load.

The solution to the system of Eqs. (5) has the form

$$u(0) = \frac{F_0}{2}, \quad u(l) = Wu(0),$$

where

$$Z = Z_2 - \frac{Z_1^2}{Z_2 + Z_0}, \quad W = \frac{Z_1}{Z_2 + Z_0}. \quad (7)$$

The quantity $Z$ is the input impedance of the system, and $W$ is the transfer coefficient. For the particle velocity in an individual line of arbitrary number $n$ (see Eq. (1)), the solution can be represented in the form

$$u_n(x) = \frac{F_0}{Z \sin k_n l}[\sin k_n(l - x) + W \sin k_n x].$$

One can easily verify that, at $N = 1$, expression (7) for $Z$ coincides with the known expression for the impedance of a single acoustic line loaded by the impedance $Z_0$ [10].

In the case of a series connection of multichannel lines, the total input impedance can be determined by the recurrence relation

$$Z^{(n)} = Z_2^{(n)} - \frac{(Z_1^{(n)})^2}{Z_2^{(n)} + Z^{(n-1)}}. \quad (8)$$

The resonance frequencies of the system are determined by the equation $Z = 0$, which, in the absence of the load (at $Z_0 = 0$), has the form

$$Z_2^2 - Z_1^2 = 0. \quad (9)$$

Taking into account the expressions for $Z_1$ and $Z_2$, Eq. (9) can be reduced to two independent equations

$$\sum_{j=1}^{N} z_j \tan\frac{\varphi_j}{2} = 0, \quad (10)$$

$$\sum_{j=1}^{N} z_j \cot\frac{\varphi_j}{2} = 0. \quad (11)$$

The antiresonance frequencies of an unloaded system are obtained from the condition $Z \longrightarrow \infty$:

$$\sum_{j=1}^{N} z_j \cot\varphi_j = 0. \quad (12)$$

Let us consider the examples for the cases $N = 2$ and 3. In the first case, we obtain the equations

$$\tan\frac{\varphi_1}{2} + x_2 \tan\frac{\varphi_2}{2} = 0, \quad (13)$$

$$\cot\frac{\varphi_1}{2} + x_2 \cot\frac{\varphi_2}{2} = 0, \quad (14)$$

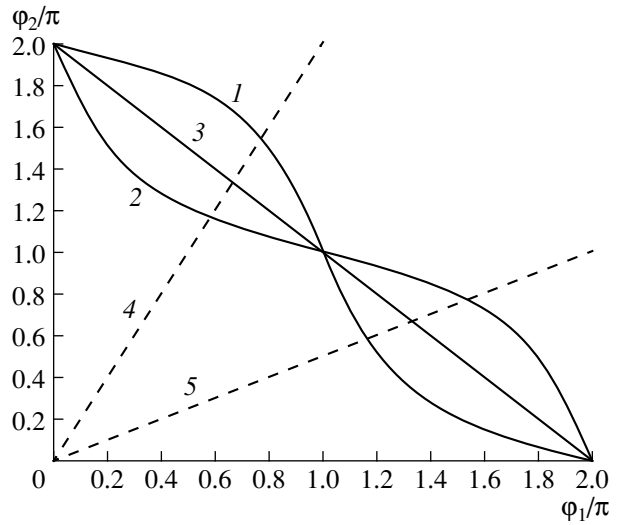


**Fig. 2.** Resonance frequencies of an MTL for $N = 2$.

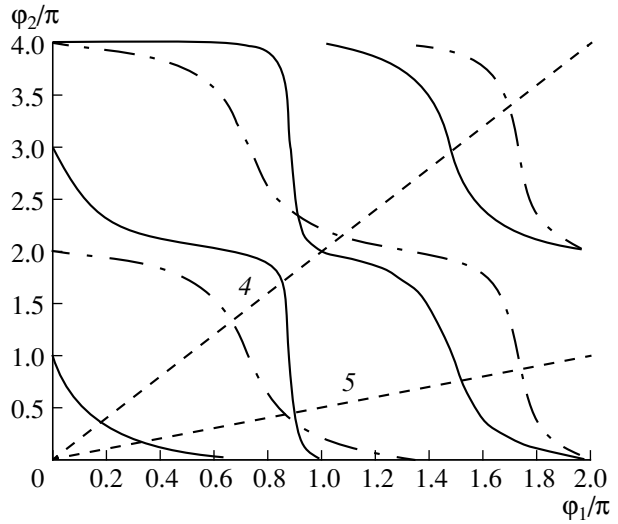


**Fig. 3.** Resonance frequencies of an MTL for $N = 3$: the solid curves correspond to Eq. (16) and the dot-and-dash curves correspond to Eq. (17).

where $x_2 = z_2/z_1$. One can readily see that Eqs. (13) and (14) for the resonance frequencies can be represented in the form

$$\cot\frac{\varphi_1}{2} + x_2^{-1}\cot\frac{\varphi_2}{2} = 0, \qquad (13')$$

$$\tan\frac{\varphi_1}{2} + x_2^{-1}\tan\frac{\varphi_2}{2} = 0. \qquad (14')$$

Hence, Eqs. (13) and (14) describe the same family of frequencies with the substitution of $x_2^{-1}$ for $x_2$. This family is shown in Fig. 2 in the form of the dependence $\varphi_2(\varphi_1)$ for $x_2 = 3$; the quantities $\varphi_1$ and $\varphi_2$ are presented in $\pi$ units. Curve *1* corresponds to Eqs. (13) and (13'), and curve *2* corresponds to Eqs. (14) and (14'). The straight line *3* corresponds to the case $x_2 = 1$. All these curves describe the functional relationships between $\varphi_1$ and $\varphi_2$. To determine the specific values of the resonance frequencies, it is necessary to set the ratio between the sound velocities in the acoustic lines: $a = c_1/c_2$. Then, the intersection of the straight line $\varphi_2 = a\varphi_1$ (Fig. 2) with the calculated curves will yield these frequencies. Figure 2 shows two such straight lines (the dashed ones) for $a = 2$ (curve *4*) and $a = 0.5$ (curve *5*); one can see that the system of two acoustic lines has two resonance frequencies (for each value of $a$).

The periodicity of the functions involved in Eqs. (13) and (14) leads to an infinite number of resonance frequencies:

$$\varphi_j = 2n\pi + \varphi_j, \qquad (15)$$

where $\varphi_j$ are the solutions to Eqs. (13) and (14).

It should be noted that the antiresonance frequencies will be lower than the resonance ones by a factor of two (as in the case of a single acoustic line), because Eqs. (11) and (12) differ only by the arguments.

For $N = 3$, Eqs. (10) and (11) can be written in the form

$$\tan\frac{\varphi_1}{2} + x_2\tan\frac{\varphi_2}{2} + x_3\tan\left(a_3\frac{\varphi_1}{2}\right) = 0, \qquad (16)$$

$$\cot\frac{\varphi_1}{2} + x_2\cot\frac{\varphi_2}{2} + x_3\cot\left(a_3\frac{\varphi_1}{2}\right) = 0. \qquad (17)$$

Here, $x_j = z_j/z_1$ and $a_3 = c_1/c_3$. As an example, Fig. 3 presents the solutions to Eqs. (16) and (17) for $x_2 = 1$, $x_3 = 3$, and $a_3 = 1.5$. The dashed lines correspond to the values $a = 0.5$ and 2. From this figure, one can see that the number of resonance frequencies is noticeably greater than in the previous case.

Now, let us consider acoustical characteristics of the MTL such as the sound and vibration insulation and the sound and vibration absorption. The model selected for the calculations is shown in Fig. 1b. The left and right ends of the MTL are connected with a single acoustic transmission line whose parameters will be labeled by $j = 0$. (Structurally, it may pass through the multichannel line by forming one of its channels.) A harmonic wave of unit amplitude

$$u_0 = \exp(ik_0x)$$

propagates along this line. This wave gives rise to a wave reflected from the system,

$$u_{01} = R\exp(-ik_0x),$$

and a wave transmitted through it,

$$u_{02} = D\exp(ik_0(x-l)),$$

where $R$ and $D$ are the reflection and transmission factors, respectively. In place of the system of Eqs. (4), one can easily obtain another system:

$$A_j = 1 + R,$$

$$i\sum_{j=1}^{N} z_j B_j = z_0(1-R),$$

$$A_j\cos\varphi_j + B_j\sin\varphi_j = D,$$

$$i\sum_{j=1}^{N} z_j(-A_j\sin\varphi_j + B_j\cos\varphi_j) = z_0 D$$

in the unknown quantities $A_j$, $B_j$, $R$, and $D$. This system can be reduced to a system of two equations

$$Z_1^0 D + (Z_2^0 + 1)R = Z_2^0 - 1,$$

$$(Z_2^0 + 1)D + Z_1^0 R = Z_1^0,$$

where $Z_{1,2}^0 = \dfrac{Z_{1,2}}{z_0}$. The latter system yields the expressions

$$R = \frac{Z_1^{02} - Z_2^{02} + 1}{Z_1^{02} - (Z_2^0 + 1)^2},$$

$$D = -\frac{2Z_1^0}{Z_1^{02} - (Z_2^0 + 1)^2}.$$

Recasting these expressions with the use of the substitutions

$$\Delta^+ = Z_1^0 + Z_2^0 = i\sum_{j=1}^{N} z_j^0 \cot\frac{\varphi_j}{2},$$

$$\Delta^- = Z_1^0 - Z_2^0 = i\sum_{j=1}^{N} z_j^0 \tan\frac{\varphi_j}{2},$$

where $z_j^0 = \dfrac{z_j}{z_0}$, we derive

$$R = \frac{\Delta^+\Delta^- + 1}{(\Delta^+ + 1)(\Delta^- - 1)},$$

$$D = -\frac{2Z_1^0}{(\Delta^+ + 1)(\Delta^- - 1)} = \frac{\Delta^+ + \Delta^-}{(\Delta^+ + 1)(\Delta^- - 1)}. \quad (18)$$

It can be easily verified that, at $N = 1$, Eqs. (18) pass into the corresponding expressions for a single acoustic transmission line [10]; in addition, in the general case, the energy flux conservation law is obeyed (in the absence of acoustic losses): $|R|^2 + |D|^2 = 1$.

If the lines forming the MTL are characterized by acoustic losses, which can be described by the complex wave numbers $\bar{k}_j = k_j(1 + i\alpha_j)$ and complex wave impedances $\bar{z}_j^0 = z_j^0/(1 + i\alpha_j)$, where $\alpha_j$ is the damping factor, the MTL can be used as an absorber positioned at the end of the initial acoustic transmission line ($j = 0$, $\alpha_0 = 0$). In this case, with the use of Eq. (7) at $Z_0 = 0$, the reflection from such an absorber can be characterized by the reflection factor

$$R = \frac{Z^0 - 1}{Z^0 + 1} = \frac{\Delta^+\Delta^- + Z_2^0}{\Delta^+\Delta^- - Z_2^0} = \frac{2\Delta^+\Delta^- + (\Delta^+ - \Delta^-)}{2\Delta^+\Delta^- - (\Delta^+ - \Delta^-)}. \quad (19)$$

Let us consider in more detail Eqs. (18) for the reflection and transmission factors; we will characterize these quantities by their magnitudes $R_0$ and $D_0$. It should be noted that the equalities $\Delta^+ = \Delta^- = 0$ coincide with Eqs. (10) and (11) and determine the resonance frequencies of the system. We also note that the quantities $\Delta^+$ and $\Delta^-$ may become infinite when at least one of their components becomes infinite. If we take these quantities as the "nodal" ones, the points of the total transparency ($R_0 = 0$, $D_0 = 1$) and total opacity ($R_0 = 1$, $D_0 = 0$) of the system can be represented by the table.

**Table**

| | $R = 1, D = 0$ | | | $R = 0, D = 1$ | |
|---|---|---|---|---|---|
| $\Delta^+$ | 0 | $\pm i\infty$ | $-\Delta^-$ | 0 | $\pm i\infty$ |
| $\Delta^-$ | 0 | $\pm i\infty$ | $-\Delta^+$ | $\pm i\infty$ | 0 |

It is essential that the indicated values of $R_0$ and $D_0$ are obtained only with a pair combination of the values of $\Delta^+$ and $\Delta^-$.

Let us illustrate these general results for an MTL consisting of two single lines with equal wave impedances $z_1^0 = z_2^0$. In this case, the resonance frequencies determined by Eqs. (13) and (14) coincide ($x_2 = 1$). (Specifically, this is illustrated by the straight line *3* in Fig. 2.) After some transformations, these equations can be represented in the form

$$\frac{\sin\dfrac{\varphi_1 + \varphi_2}{2}}{\cos\dfrac{\varphi_1}{2}\cos\dfrac{\varphi_2}{2}} = 0, \quad \frac{\sin\dfrac{\varphi_1 + \varphi_2}{2}}{\sin\dfrac{\varphi_1}{2}\sin\dfrac{\varphi_2}{2}} = 0, \quad (20)$$

which yields the relationship $\varphi_1 + \varphi_2 = 2\pi n$. Here, we can set $n = 1$ by virtue of the periodicity of the functions. If we assume that, as before, we have $\varphi_2 = a\varphi_1$ (where $a = c_1/c_2$), the resonance value of $\varphi_1$ will be determined by the expression

$$\varphi_1 = \frac{2\pi}{1 + a}. \quad (21)$$

At $a = 1$, the MTL turns into a single line and the value $\varphi_1 = \pi$ corresponds to the total transparency of the line. At $a \neq 1$, Eq. (21) yields the value of $\varphi_1$ corresponding

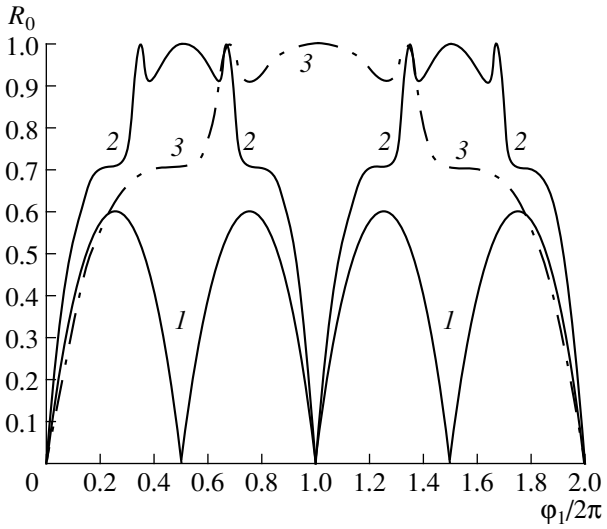


**Fig. 4.** Magnitude of the reflection factor of an MTL-insulator for different values of $a = c_1/c_2$: $a$ = (*1*) 1, (*2*) 2, and (*3*) 0.5. Other parameters are $a_1 = 1$ and $z_1^0 = z_2^0 = 1$.

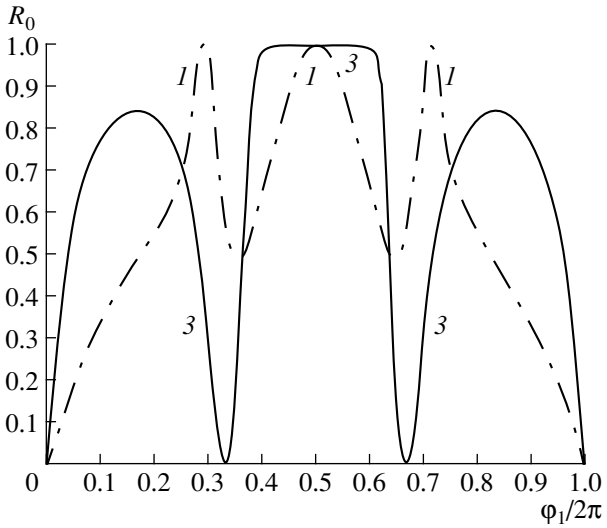


**Fig. 5.** Same as in Fig. 4, but for different values of the wave impedance: $z_2^0$ = (*1*) 0.5 and (*3*) 2. Other parameters are $a_1 = 1$, $z_1^0 = 1$, and $a = 2$.

to the total opacity of the line. Hence, at $a \approx 1$, the type of transparency for both a single line and an MTL changes to the opposite at practically the same frequency. If $a \gg 1$, the frequency corresponding to the total opacity can be made rather low.

Based on Eqs. (20), we obtain that the condition $\Delta^+ = \Delta^- = \infty$ leads to two independent systems of equations:

$$\varphi_1 = 2\pi, \quad \varphi_2 = \pi \quad \text{and} \quad \varphi_1 = \pi, \quad \varphi_2 = 2\pi.$$

Their solutions are $\varphi_1 = 2\pi$ at $a = 0.5$ and $\varphi_1 = \pi$ at $a = 2$. This means that, at the given values of $a$, the transparency frequencies for a single line become the opacity frequencies for the MTL.

The condition $\Delta^+ = -\Delta^-$ leads to one more solution:

$$\varphi_1 = \frac{\pi}{1 + a}, \tag{22}$$

which yields a frequency value two times less than that obtained from Eq. (21).

Thus, there exists a set of frequencies corresponding to the total opacity of the MTL.

Examples of calculations by Eqs. (18) and (19) are illustrated in Figs. 4–6. Figure 4 shows the quantity $R_0$ as the function of $\varphi_1/2\pi$ for the case $z_1^0 = 1$ and $a_1 = c_1/c_0 = 1$; i.e., the parameters of the line $j = 1$ coincide with the parameters of the initial line $j = 0$. (Since, in this example, the losses are assumed to be absent, the values of $D_0$ are not presented, because this quantity is uniquely related to $R_0$ through the conservation law.) The parameters of the line $j = 2$ are as follows: $z_0^2 = 1$ and $a = 1$ (curve *1*), 2 (curve *2*), and 0.5 (curve *3*). Curve *1* corresponds to a two-channel line that forms an extension of the initial line, but has a wave impedance that is twice as large. In this case, the reflection factor is known to reach its maximal values at the frequencies corresponding to odd numbers of wavelength quarters and to be zero for even numbers of wavelength quarters (i.e., for integral numbers of half-wavelengths). Curve *2* corresponds to the case when the odd number of wavelength quarters in the line $j = 2$ coincides with the odd number of half-wavelengths in the line $j = 1$, and, at these frequencies, the zero values of $R_0$ pass into the maximal ones. Thus, the bandwidth of frequencies corresponding to large values of $R_0$ considerably increases. For example, the values $R_0 > 0.7$ occur in a two-octave frequency band and the zero values are observed only for integral numbers of wavelengths. Curve *3* corresponds to the case with doubled intervals between the zero values, i.e., the intervals equal to even numbers of wavelengths. In this case, the values $R_0 > 0.7$ are also retained in a two-octave frequency band.

Figure 5 illustrates the effect of the wave impedance $z_2^0$ at $a = 2$ (the parameters of the line $j = 1$ are the same as before). Curve *1* corresponds to the value $z_2^0 = 0.5$, and curve *2* corresponds to $z_2^0 = 2$. Together with curve *2* from Fig. 4, they illustrate the effect of the wave impedance. Specifically, curve *3* shows that a large value of $z_2^0$ may lead to values of $R_0$ practically equal to unity in a wide frequency band (the ratio between the upper and lower frequencies is 1.5).

In designing wide-band sound and vibration absorbers on the basis of an MTL, it is necessary to take into account that the sum of the wave impedances $z_1^0 + z_2^0$ must be close to unity to provide a small value of $R_0$ at

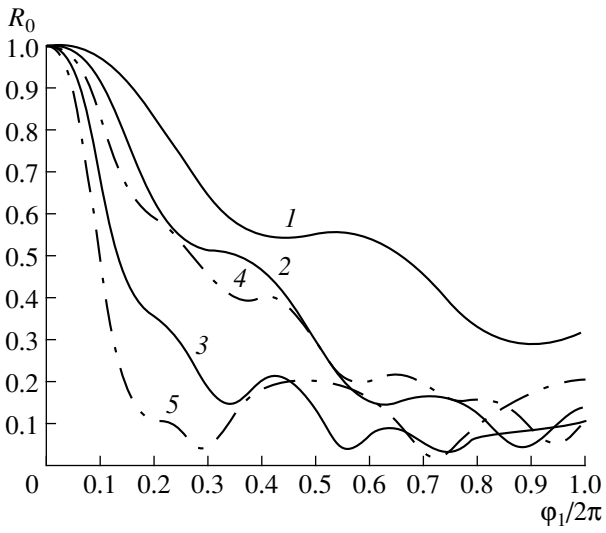


**Fig. 6.** Magnitude of the reflection factor of an MTL-absorber for different values of $a_2 = c_2/c_0$ and $\alpha_2$: $\alpha_2 = 0.2$ and $a_2 =$ (*1*) 1, (*2*) 0.5, and (*3*) 0.25; $a_2 = 0.25$ and $\alpha_2 =$ (*4*) 0.1 and (*5*) 0.4. Other parameters are $a_1 = 1$, $z_1^0 = z_2^0 = 0.5$, and $\alpha_1 = 0$.

high frequencies. Therefore, in the examples considered below, we take $z_1^0 = z_2^0 = 0.5$; in addition, as before, we take $a_1 = 1$ and $\alpha_1 = 0$. Figure 6 presents the frequency characteristics of $R_0$ for different damping factors $\alpha_2$ and different relative velocities $a_2$. One can see that the lower frequency of the frequency range corresponding to efficient absorption smoothly decreases with a decreasing velocity and with increasing damping factor in the line $j = 2$; simultaneously, the "stabilization" of the values of $R_0$ with varying frequency occurs much earlier.

The theoretical and computational results presented above show that, even on the basis of an MTL consisting of only two lines, it is possible to obtain MTL-insulators and MTL-absorbers that have much better acoustical characteristics than the corresponding acoustical systems constructed on the basis of single acoustic lines. From the results presented above, one can expect that, by varying the parameters of the line $j = 2$, as well as by increasing the total number of lines in the MTL, it is possible to achieve further improvement of the acoustical characteristics of the systems. Such problems are beyond the scope of this paper, but, in principle, they can be solved, specifically, with the use of the optimization techniques.

## ACKNOWLEDGMENT

I am grateful to Yu.I. Bobrovnitskiĭ for useful discussions.

## REFERENCES

1. V. V. Tyutekin, Akust. Zh. **43**, 238 (1997) [Acoust. Phys. **43**, 202 (1997)].
2. A. I. Boĭko and V. V. Tyutekin, Akust. Zh. **45**, 454 (1999) [Acoust. Phys. **45**, 402 (1999)].
3. J. Guo, J. Pan, and C. Bao, J. Acoust. Soc. Am. **101**, 1492 (1997).
4. Z. Wu, V. K. Varadan, and V. V. Varadan, J. Acoust. Soc. Am. **101**, 1502 (1997).
5. K. Wicker and E. Arens, Acust. Acta Acust., Suppl. 1 **85**, S47 (1999).
6. C. R. Fuller and P. E. Cambou, Acust. Acta Acust., Suppl. 1 **85**, S102 (1999).
7. E. V. Korotaev and V. V. Tyutekin, Akust. Zh. **46**, 84 (2000) [Acoust. Phys. **46**, 71 (2000)].
8. *Acoustics Handbook*, Ed. by M. J. Crocker (Wiley, New York, 1997).
9. L. M. Brekhovskikh, *Waves in Layered Media* (Nauka, Moscow, 1973; Academic, New York, 1980).
10. M. A. Isakovich, *General Acoustics* (Nauka, Moscow, 1973).
11. *Technical Encyclopedia* (Sov. Éntsiklopediya, Moscow, 1954).

*Translated by E. Golyamina*

*Acoustical Physics, Vol. 46, No. 6, 2000, pp. 716–727. Translated from Akusticheskiĭ Zhurnal, Vol. 46, No. 6, 2000, pp. 816–828.*


# Diffraction of a Sound Wave by the Open End of a Flanged Waveguide with Impedance Walls

**E. L. Shenderov**

*Morfizpribor Central Research Institute, Chkalovskiĭ pr. 46, St. Petersburg, 197376 Russia*

*e-mail: shend@peterlink.ru*

Received December 15, 1999

**Abstract**—Diffraction of a plane sound wave by the open end of an impedance-wall waveguide connected to an opening in an impedance screen is considered. The plane wave is incident on the waveguide from a free half-space. Two versions of the problem are considered: for a semi-infinite waveguide and for a finite-length waveguide with a specified bottom impedance; the impedances of the walls, screen, and waveguide bottom can be different. The finite-length waveguide can be treated as an open cavity in the impedance screen. For the cavity of zero length, the problem is reduced to the diffraction by an impedance insert in the impedance screen. The solution in the external region determines the scattered field; the solution in the internal region allows one to determine the directional pattern of an array of receivers located in the cavity. The problem is solved using the integral Helmholtz equation with a specially selected Green's function that provides the fulfillment of the boundary conditions. Formally, the problem is reduced to an infinite system of algebraic equations. The computational results obtained for bistatic and monostatic scattering patterns are presented. © *2000 MAIK "Nauka/Interperiodica".*

We consider the diffraction of a plane sound wave by the open end of an impedance-wall waveguide with a flange in the form of an impedance screen (see Fig. 1). We consider two versions of this problem: for a semi-infinite waveguide (Fig. 1a) and for a finite-length waveguide with a specified bottom impedance (Fig. 1b); the impedances of the walls, screen, and waveguide bottom can be different. The finite-length waveguide can be considered as an open cavity in the impedance screen. For the cavity of zero length, the problem is reduced to the diffraction by an impedance insert in the impedance screen. The solution in the external region determines the scattered field, and the solution in the internal region allows one to determine the directional pattern of an array of receivers located in the cavity. The solution of the formulated problem is of interest in

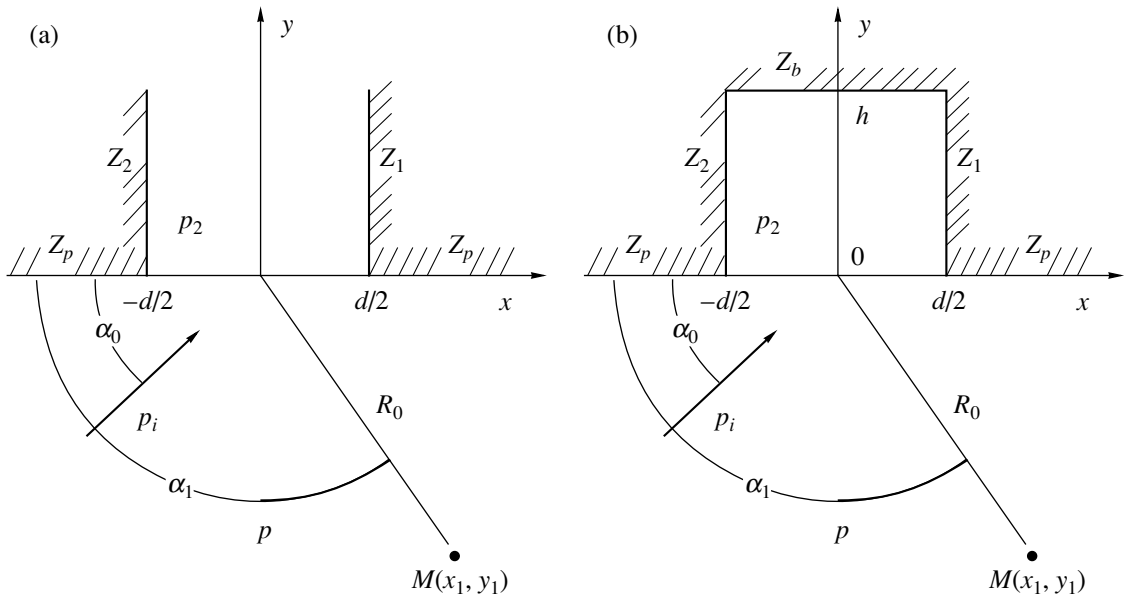


**Fig. 1.** Coordinate systems (a) for a semi-infinite waveguide with impedance walls and impedance flanges and (b) for a cavity with an impedance bottom in the impedance screen.

1063-7710/00/4606-0716$20.00 © 2000 MAIK "Nauka/Interperiodica"

many fields of acoustics. It provides the possibility of determining characteristics such as the sound scattering patterns of impedance pipes with impedance flanges, the sound energy penetrating into a waveguide whose inlet is insonified by sound waves, and the directional patterns of arrays of sound receivers located inside a waveguide or an open cavity.

Rawlins [1] considered the sound scattering by the open end of an unflanged waveguide with impedance walls by using the Wiener–Hopf method and obtained a solution in a closed, but rather cumbersome form. Shenderov [2] and Norris and Sheng [3] considered the scattering of sound waves by the open end of a waveguide with rigid walls and rigid flanges. Shenderov [4] presented the solution to the problem on the sound radiation from a waveguide with rigid flanges. Below, we consider a more complicated problem for a waveguide whose walls and flanges are impedance surfaces.

To obtain a solution for a plane incident wave, we first consider a linear source perpendicular to the $xy$ plane, and, then, we proceed to the case of the distance to the source tending to infinity to obtain the solution for the plane wave diffraction.

In the bottom halfspace, the sound field can be represented using the Helmholtz integral

$$p(\mathbf{r}_1, \mathbf{r}_0) = -ik\rho cQG(\mathbf{r}_1, \mathbf{r}_0) + \int_{-\infty}^{\infty}\left[p(\mathbf{r})\frac{\partial G(\mathbf{r}_1, \mathbf{r})}{\partial \boldsymbol{n}} - \frac{\partial p(\mathbf{r})}{\partial n}G(\mathbf{r}_1, \mathbf{r})\right]dx. \quad (1)$$

Here, $\mathbf{r}_0$ and $\mathbf{r}_1$ are the radius vectors of the source and the observation point $M(x_1, y_1)$, respectively; $\mathbf{r}$ is the radius vector of the point lying in the screen plane at $y = 0$; $Q$ is the productivity of the source; $G$ is the two-dimensional Green's function of the Helmholtz equation; $\rho c$ is the wave resistance of the medium; and $k = \omega/c$. The time dependence is assumed to have the form $\exp(-i\omega t)$. The differentiation is carried out along the normal directed inside the region under consideration, i.e., downwards, as shown in Fig. 1. The derivation of expression (1) is given in Appendix 1.

Note that the first term on the right-hand side of formula (1) corresponds not to the field of the source in the free space, but to the field obtained with the same Green's function as in the integrand.

At the screen surface, i.e., for $|x| > d/2$ and $y = 0$, the following boundary condition should be satisfied:

$$p|_{y=0} = \frac{Z_p}{ik\rho c}\frac{\partial p}{\partial y}\bigg|_{y=0} = -\frac{Z_p}{ik\rho c}\frac{\partial p}{\partial n}\bigg|_{y=0}, \quad (2)$$

where $Z_p$ is the impedance of the screen.

The sound pressure $p(\mathbf{r})$ involved in the integrand is unknown. When the observation point tends to the plane $y = 0$, expression (1) turns to an integral equation in $p(\mathbf{r})$. To carry out the integration over a finite-length interval, it is worthwhile to specify the Green's function so as to make the integral be equal to zero within the segments $|x| > d/2$. For this purpose, it is sufficient to chose the two-dimensional Green's function as the field of a linear source located perpendicularly to the plane of Fig. 1, in the presence of the impedance plane. This Green's function must satisfy the boundary condition coincident with that for the sound pressure in the halfspace, i.e., the condition

$$G|_{y=0} = \frac{Z_p}{ik\rho c}\frac{\partial G}{\partial y}\bigg|_{y=0} = -\frac{Z_p}{ik\rho c}\frac{\partial G}{\partial n}\bigg|_{y=0}. \quad (3)$$

We will construct this Green's function starting from the free-space Green's function in the form of an expansion in plane waves:

$$G_0(\mathbf{r}_0, \mathbf{r}_1) = \frac{i}{4}H_0^{(1)}(k|\mathbf{r}_0 - \mathbf{r}_1|) \quad (4a)$$

$$= \frac{i}{4\pi}\int_{-\infty}^{\infty}\exp[iku(x_1 - x_0) + ik\sqrt{1-u^2}|y_1 - y_0|]\frac{dx}{\sqrt{1-u^2}}.$$

With the substitution $x_1 - x_0 = R\sin\varphi$, $|y_1 - y_0| = R\cos\varphi$ and $u = \sin\theta$ (see Fig. 2), we obtain

$$G_0(\mathbf{r}_0, \mathbf{r}_1) = \frac{i}{4\pi}\int_\Gamma \exp(ikR\cos(\theta - \varphi))d\theta, \quad (4b)$$

where $\Gamma$ is the Sommerfeld contour $(-\pi/2 + i\infty, \pi/2 - i\infty)$ in the complex plane $\theta$. The substitution assumes that the point $(x_0, y_0)$ lies below the point $(x_1, y_1)$, i.e., $\varphi < \pi/2$. Every plane wave involved in the integrands of expressions (4a) and (4b) is reflected from the surface of the screen. The corresponding reflection coefficient has the form

$$A_p(\cos\theta) = \frac{w_p\cos\theta - 1}{w_p\cos\theta + 1}, \quad (5)$$

where $w_p = Z_p/\rho c$. The desired Green's function is obtained by combining the incident and reflected waves in the integrand:

$$G(\mathbf{r}_0, \mathbf{r}_1) = \frac{i}{4\pi}\int_\Gamma [\exp(ikR\cos(\theta - \varphi)) + A_p(\cos\theta)\exp(ikR'\cos(\theta - \varphi'))]d\theta, \quad (6)$$

where the second term in the integrand assumes that $\varphi' > \pi/2$, as is shown in Fig. 2. Going back to the initial variables, we obtain

$$G(\mathbf{r}_0, \mathbf{r}_1) = \frac{i}{4\pi}\int_{-\infty}^{\infty}\exp(iku(x_1 - x_0)) \times [\exp(ik\gamma(y_0 - y_1)) + A_p(\gamma)\exp(-ik\gamma(y_0 + y_1))]\frac{du}{\gamma}, \quad (7)$$

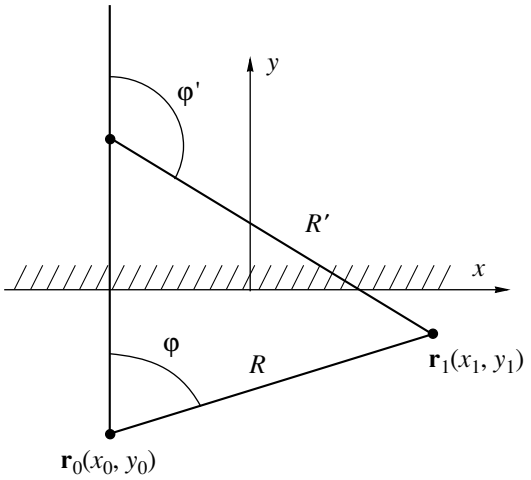


**Fig. 2.** For the definition of the Green's function.

where $\gamma = \sqrt{1-u^2}$ and

$$A_p(\sqrt{1-u^2}) = \frac{w_p\sqrt{1-u^2}-1}{w_p\sqrt{1-u^2}+1}. \quad (8)$$

We assume that a plane sound wave is incident on the system. Then, the first term on the right-hand side of expression (1) can be simplified. Since, in the case under study, we have $kR_0 \gg 1$, the integral (6) can be evaluated by the saddle-point method. In the case of the deformation of the integration contour, the latter can intersect the position of the pole of the function $A_p(\cos\theta)$; however, the residue at this pole can be omitted, because it determines the surface wave that exponentially decays with an increasing total distance $y_0 + y_1$. As a result, we obtain

$$G(\mathbf{r}_0, \mathbf{r}_1) \longrightarrow \frac{i}{4}\sqrt{\frac{2}{\pi kR_0}}\exp(ikR_0 - i\pi/4) \times \exp(ikx_1\sin\theta_0)[\exp(iky_1\cos\theta_0) + A_p(\cos\theta_0)\exp(-iky_1\cos\theta_0)]. \quad (9)$$

Note that this representation can be used only in the first term of the right-hand side of expression (1) but not in the integrand where both points $\mathbf{r}$ and $\mathbf{r}_1$ can simultaneously appear at the surface $y = 0$.

We normalize the first term on the right-hand side of expression (1) by the sound pressure in the incident wave at the origin of the coordinates, i.e., by

$$p_0 = -ik\rho cQ\frac{i}{4}\sqrt{\frac{2}{\pi kR_0}}\exp(ikR_0 - i\pi/4). \quad (10)$$

Then, this term can be represented in the form of the incident wave and the wave reflected from the infinite screen without opening:

$$p_0\exp(ikx_1\sin\theta_0)[\exp(iky_1\cos\theta_0) + A_p(\cos\theta_0)\exp(-iky_1\cos\theta_0)]. \quad (11)$$

In the integrand in expression (1), we use the exact Green's function (7) in which we replace the position of the source $\mathbf{r}_0$ by the position of the integration point $\mathbf{r}$. For this purpose, we replace $(x_0, y_0)$ by $(x, y)$, calculate the normal derivative (taking into account that $\partial G/\partial n = -\partial G/\partial y$), and then set $y = 0$.

We represent the integral as the sum of the integrals over the screen surface and the opening, i.e., in the form $\int_{|x|>d/2}(\ldots)\,dx + \int_{|x|<d/2}(\ldots)\,dx$. The boundary conditions (2) and (3) are satisfied at the screen surface. Substituting these conditions into the first integral, we obtain that this integral vanishes and only the integral over the opening remains in the solution. As a result, we obtain the sound field at the observation point $(x_1, y_1)$:

$$p(x_1, y_1) = p_i + p_r - p_s, \quad (12)$$

$$p_i = p_0\exp[ik(x_1\sin\theta_0 + y_1\cos\theta_0)], \quad (13)$$

$$p_r = p_0\exp[ik(x_1\sin\theta_0 - y_1\cos\theta_0)]A_p(\cos\theta_0), \quad (14)$$

$$p_s = \frac{-i}{4\pi}\int_{-\infty}^{\infty}\int_{-d/2}^{d/2}\exp[iku(x_1 - x) - i\gamma ky_1] \times\left[-p(x)ik\gamma(1 - A_p(\gamma)) + \frac{\partial p(x,y)}{\partial y}\bigg|_{y=0}(1 + A_p(\gamma))\right]\frac{du}{\gamma}dx. \quad (15)$$

Thus, we represented the sound field in the bottom halfspace in the form of the sum of the incident wave $p_i$, the wave reflected from the infinite impedance plane $p_r$, and the scattered field $p_s$. The distribution of the sound pressure and its normal derivative over the opening plane still remain unknown.

Now, we consider the field in the waveguide $p_2$. The boundary conditions at the waveguide walls and at its bottom can be written in the form

$$p_2 = \frac{w_1}{ik}\frac{\partial p_2}{\partial x}\bigg|_{x=d/2}, \quad p_2 = -\frac{w_2}{ik}\frac{\partial p_2}{\partial x}\bigg|_{x=-d/2}, \quad p_2 = \frac{w_b}{ik}\frac{\partial p_2}{\partial y}\bigg|_{y=h}, \quad (16)$$

where the following notation is used: $w_1 = Z_1/\rho c$, $w_2 = Z_2/\rho c$, $w_b = Z_b/\rho c$, $u_1 = w_1/(-ikd)$, and $u_2 = w_2/(-ikd)$. In the waveguide, the general solution to the Helmholtz

equation satisfying these boundary conditions is representable as the sum of normal waves [5]:

$$p_2 = \sum_{n=1}^{\infty} A_n \psi_n(x)[\exp(ik\gamma_n y) + qA_b(\gamma_n)\exp(-ik\gamma_n(y-2h))], \quad (17)$$

$$\psi_n(x) = u_2\beta_n\cos(x/d + \beta_n/2) + \sin(x/d + \beta_n/2), \quad (18)$$

where $A_n$ are the unknown coefficients; $\psi_n(x)$ are the eigenfunctions satisfying the two first boundary conditions (16); and

$$A_b(\gamma_n) = (w_b\gamma_n - 1)/(w_b\gamma_n + 1) \quad (19)$$

is the bottom reflection coefficient for the normal wave, i.e., the wave incident on the bottom at an incidence angle $\theta_n$ satisfying the condition $\cos\theta_n = \gamma_n$, where $\gamma_n = \sqrt{1-(\beta_n/kd)^2}$ and $\beta_n$ are the eigenvalues. In expression (17), we artificially introduced the parameter $q$ to obtain a unique expression for both the semi-infinite waveguide ($q = 0$) and the finite-length waveguide ($q = 1$). Indeed, for lossless media, the expression for the finite-length waveguide provides no way of obtaining an expression for the semi-infinite waveguide as a particular case corresponding to either $h = \infty$ or a zero reflection coefficient at the bottom. Note that, according to formula (19), one can chose $w_b$ so as to obtain a zero reflection coefficient for only one normal wave, but not for the whole set of normal waves. This situation is similar to that with the sound wave being reflected from an impedance plane; in this case, there is no way of simultaneously obtaining a zero reflection coefficient for all angles of incidence by the choice of some impedance value.

The eigenvalues $\beta_n$ are the roots of the equation [5]

$$F(\beta) = \exp(i\beta)(1+iu_1\beta)(1+iu_2) - \exp(-i\beta)(1-iu_1\beta)(1-iu_2) = 0. \quad (20)$$

The functions $\psi_n(x)$ satisfy the condition of orthogonality

$$\frac{1}{d}\int_{-d/2}^{d/2}\psi_m(x)\psi_n(x)dx = \begin{cases} 0 & \text{for } n \neq m \\ H_n & \text{for } n = m, \end{cases} \quad (21)$$

$$H_n = [1 + u_2 + \beta_n^2u_2^2 - u_2^2\cos(2\beta_n) + (\beta_n^2u_2^2 - 1)\sin(2\beta_n)/(2\beta_n)]/2. \quad (22)$$

Note that no sign of complex conjugation appears in the integrand of expression (21) despite the fact that the eigenfunctions can be complex. This result was first mentioned by Andreev [6] and, later, by Morse and Ingard [7].

Below, we will use the integrals that appear in the expansion of the plane wave in the eigenfunctions of the waveguide:

$$d_n(g) = \frac{1}{d}\int_{-d/2}^{d/2}\psi_n(x)\exp(ikxg)dx = \{[\exp(-ikdg/2) - \cos\beta_n\exp(ikdg/2)] \times (ikdg\beta_nu_2 - \beta_n) - \sin\beta_n\exp(ikdg/2) \times (\beta_n^2u_2 + ikdg)\}/((kdg)^2 - \beta_n^2). \quad (23)$$

For $kdg = \pm\beta_n$, the last term has an ambiguous point of type 0/0. In this case,

$$d_n(g) = \exp(\mp i\beta_n/2)[\exp(\pm i\beta_n)(u_2\beta_n \mp i)\sin\beta_n + \beta_n((u_2\beta_n \pm i))]/(2\beta_n).$$

Assume that the observation point $(x_1, y_1)$ tends to the plane $y_1 = 0$ within the opening. The continuity conditions

$$p = p_2, \quad \partial p/\partial y = \partial p_2/\partial y$$

must be satisfied on this segment. We substitute these conditions in the integrand involved in formulas (12)–(15), use representation (17), multiply both sides of the equation by $\psi_m(x)$, integrate over the opening, and take into account the orthogonality relationships (21). As a result, we obtain an infinite system of equations in the coefficients $A_n$:

$$A_n + \sum_{m=1}^{\infty} A_mU_{nm} = B_n, \quad n = 1, 2, 3\ldots, \quad (24a)$$

$$B_n = \frac{d_n(\cos\alpha_0)}{H_n(1+q_n)}[1 + A_p(\sin\alpha_0)], \quad (25)$$

$$U_{nm} = \frac{kd[\gamma_mw_p - 1 - q_m(\gamma_mw_p + 1)]}{2\pi H_n(1+q_n)}I_{mn}, \quad (26)$$

$$q_m = qA_b(\gamma_m)\exp(2ikh\gamma_m), \quad (27)$$

$$I_{mn} = \int_{-\infty}^{\infty}\frac{d_n(u)d_m(-u)}{w_p\sqrt{1-u^2}+1}du. \quad (28)$$

Note that, in deriving this system, we ensure the continuity of the field in the opening by equating the sound pressure involved in the left- and right-hand members of expression (1) and the series (17) determining the field in the waveguide. In doing so, we used the normal derivatives of the field only on the right-hand side of expression (1). Despite this fact, system of Eqs. (24a) ensures the continuity of not only the sound pressure, but of the normal derivative as well. The corresponding proof is given in Appendix 2.

The coefficients $U_{nm}$ decrease with increasing $n$ and increase with increasing $m$. As a result, the off-diagonal

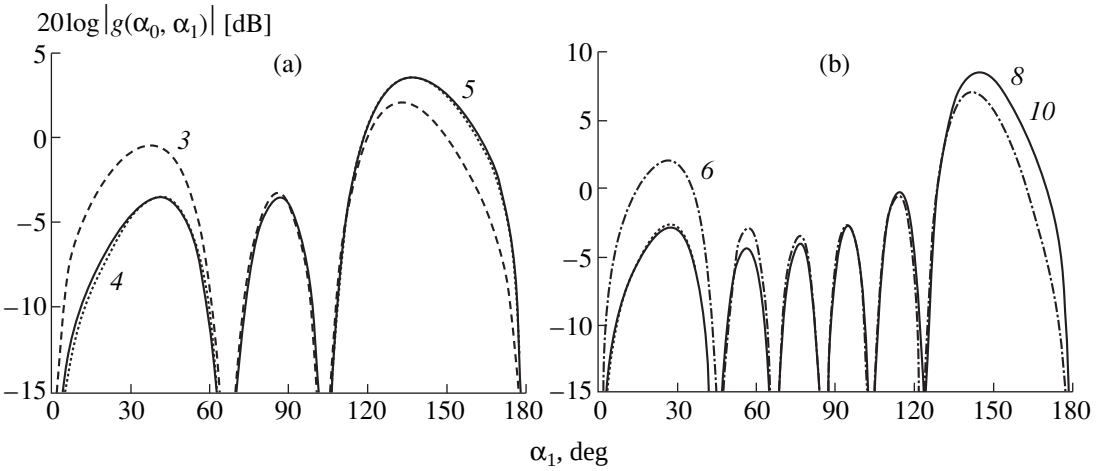


**Fig. 3.** Two-point scattering patterns for different numbers of terms retained in the series for $\alpha_0 = 30°$, $w_p = -i6.0$, and $w_1 = w_2 = -i100$; $k_d$ = (a) 10.0, (b) 20.0. The values of the parameter $n_{\max}$ are indicated near the curves.

terms can exceed the diagonal ones. To minimize this possibility, it is expedient to introduce the normalization $A'_n = A_n\sqrt{|H_n|}$. Then, system (24a) will take the form

$$A'_n + \sum_{m=1}^{\infty} A'_m U'_{nm} = B'_n, \quad n = 1, 2, 3, \ldots, \qquad (24b)$$

where $U'_{nm} = \sqrt{|H_n/H_m|}\,U_{nm}$ and $B'_n = B_n\sqrt{|H_n|}$.

Let us determine the far field of scattering. With this goal in mind, we substitute expansion (17) into expression (15) and use formula (23). After integrating over $x$, we obtain

$$p_s(x_1, y_1) = \frac{kd}{4\pi}\sum_{n=1}^{\infty} A_n \int_{-\infty}^{\infty} \exp(ikux_1 - i\gamma k y_1) d_n(-u) \times [-\gamma(1 - A_p(\gamma)) + \gamma_n(1 + A_p(\gamma))]\frac{du}{\gamma}.$$

Then, we change the variable $u = \sin\theta$ and introduce the polar coordinates $x_1 = R_0\sin\theta_1$, $y_1 = -R_0\cos\theta_1$ ($y_1 < 0$), and $\theta_1 = \alpha_1 - \pi/2$. As a result, we obtain the integral along the contour $\Gamma$

$$\int_{-\infty}^{-\infty} = \int_{\Gamma} \exp(ikR_0\cos(\theta - \theta_1)) d_n(-\sin\theta) \times [-\cos\theta(1 - A_p(\cos\theta)) + \gamma_n(1 + A_p(\cos\theta))]d\theta.$$

In the far zone, i.e., for $kR_0 \gg 1$, the saddle-point method is appropriate to evaluate the last integral. As the contour is deformed to the saddle-point contour, it can intersect the pole of the integrand at the point where the denominator in expression (5a) vanishes. The corresponding residue determines the surface wave that may be generated near the impedance plane. In the far field, this component disappears. As a result, we obtain the scattered field in the form

$$p_s \approx \sqrt{2/(\pi kR_0)}\exp(ikR_0 - i\pi/4) g(\alpha_0, \alpha_1), \qquad (29)$$

where $g(\alpha_0, \alpha_1)$ is the two-point (or bistatic) scattering pattern determined by the expressions

$$g(\alpha_0, \alpha_1) = \frac{kd}{2}\sum_{n=1}^{\infty} A_n d_n(\cos\alpha_1)\xi_n(\alpha_1), \qquad (30)$$

$$\xi_n(\alpha_1) = \sin\alpha_1 \frac{\gamma_n w_p - 1 - q_n(\gamma_n w_p + 1)}{w_p \sin\alpha_1 + 1}. \qquad (31)$$

We used the reduction method to solve the system of Eqs. (24b). The eigenvalues $\beta_n$ were calculated according to the procedure described in [5]. The computation of integrals $I_{mn}$ was the most time-consuming procedure. We used the symmetry property $I_{mn} = I_{nm}$ to decrease the computation time. The integral was reduced to a semi-infinite interval, which was further subdivided into the segments (0, 1) and (1, ∞). For symmetric waveguides, we additionally took into account that $I_{mn} = 0$ if $m$ and $n$ are of different evenness. The calculation error of the eigenvalues $\beta_n$ and integrals $I_{mn}$ was $10^{-5}$.

The computations were performed with a PC (66 MHz operating frequency). The computation time for the scattering pattern was between 2 and 3 s for a specified value of $kd$ within $kd < 5$. For $kd = 10$, this time was between 5 and 7 s and increased to 20–30 s for $kd = 20$.

Figure 3 shows the two-point scattering patterns calculated for different orders of system truncation $n_{\max}$. They show that the solution converges for $n_{\max} \cong E(kd/2)$, where $E$ is the integer part of the number. For small values of $kd$, we used at least four terms. For arbi-

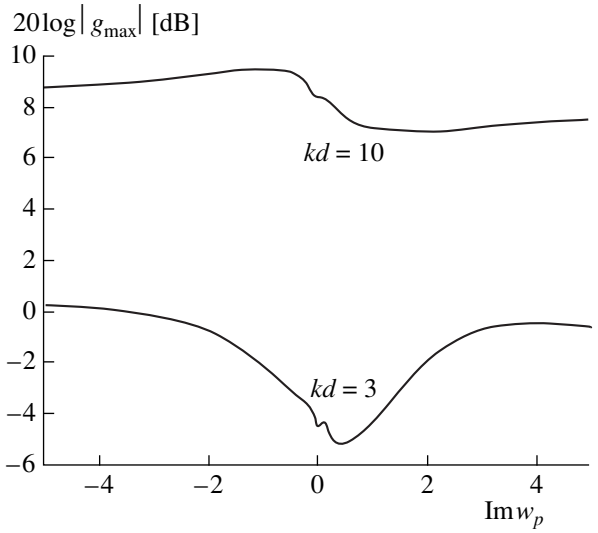


**Fig. 4.** Maxima of the two-point scattering patterns as functions of Im$w_p$ for Re$w_p$ = 0.05. $\alpha_0 = 30°$ and $w_1 = w_2 = -i5.0$.

trary values of $kd$, we used the expression $n_{max} = E(\sqrt{[(n_1 kd)^2 + 3kd + 16]})$, where $n_1 = 0.3–0.5$.

The computation time of integrals $I_{mn}$ essentially depends on $w_p$. For $w_p$ with a small real part and a positive imaginary part, the denominator may approach zero near certain $u$, which results in a narrow peak in the integrand. This situation corresponds to the generation of weakly decaying surface waves near the screen. In this case, the computation time can be somewhat longer.

Note that expressions (24)–(28) are inappropriate for a perfectly soft acoustic screen, i.e., for $w_p = 0$. In this case, both the left- and the right-hand sides of the system (24a) vanish simultaneously. The right-hand side vanishes because $A_p = -1$. To show that the left-hand side also vanishes, one should use expressions (A2.6) and (A2.7) of Appendix 2. These expressions show that the off-diagonal matrix terms vanish because $\delta_{mn} = 0$ for $m \neq n$, and the diagonal terms vanish because $I_{mn} = J_{mn} = 2\pi H_n/(kd)$, as follows from formula (A2.7) for $w_p = 0$ and $m = n$. Then, the diagonal coefficients $1 + U_{nn}$ also vanish. Despite this fact, the calculations appear quite efficient even for relatively small values of $w_p$, e.g., for $w_p = 0.05 + i0.05$. This is illustrated in Fig. 4, which shows the maxima of the two-point scattering patterns as functions of the imaginary part of the screen impedance for Re$w_p$ = 0.05. The small zigzags of this curve near the point Im$w_p$ = 0 are the consequence of increasing calculation errors for a screen whose properties approach those of a perfectly soft acoustic screen.

For openings of a small wave size (Fig. 5), the main lobe of the two-point scattering pattern is directed almost along the normal to the opening. The amplitude of the scattered wave essentially depends on the coefficient of sound reflection from the screen. For a perfectly absorbing acoustic screen (curves *5*), the amplitude of the scattered wave sharply decreases. The value $w_p = 1$ ensures a zero reflection coefficient only for waves incident on the screen along the normal. The corresponding deep gap is seen in the scattering patterns near $\alpha_1 = 90°$. For a given absolute value of the reflection coefficient, the curves for the screen with a normalized impedance $w_p > 1$ lie everywhere above the curves for the screen with a normalized impedance $w_p < 1$.

For openings of a large wave size (Fig. 6), the main lobe of the two-point scattering pattern is oriented approximately in the specular direction relative to the incident wave. In this case, the screens characterized by reflection coefficients that are equal in magnitude but

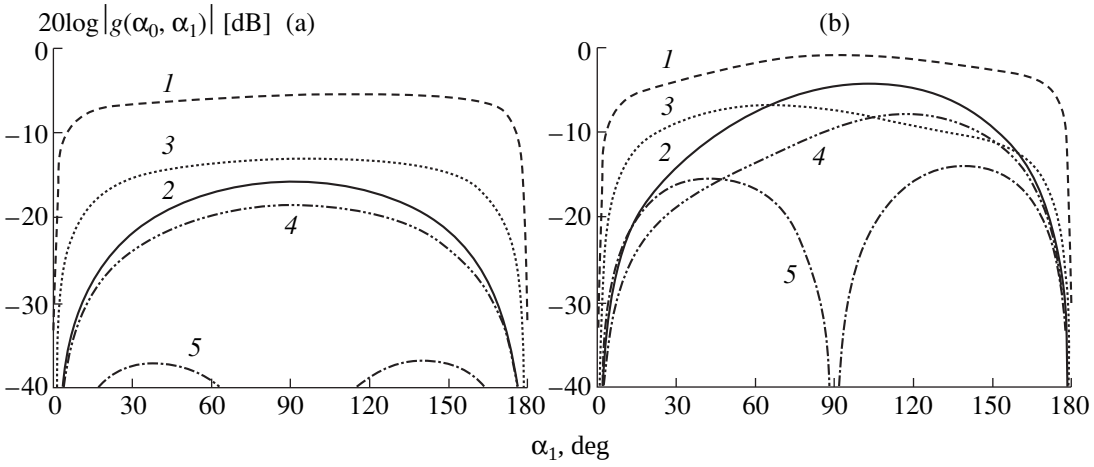


**Fig. 5.** Two-point scattering patterns for various sound reflection coefficients of the screen for $\alpha_0 = 30°$, $w_1 = w_2 = -i100.0$, and $kd$ = (a) 1.0 and (b) 3.0. Different curves correspond to the following parameters: (*1*) $w_p = 19.0$, $A_p = 0.9$; (*2*) $w_p = 0.0526$, $A_p = -0.9$; (*3*) $w_p = 3.0$, $A_p = 0.5$; (*4*) $w_p = 0.333$, $A_p = -0.5$; and (*5*) $w_p = 1.0$, $A_p = 0$. Here, $A_p$ is the reflection coefficient for the normal incidence, i.e., for $\alpha_0 = 90°$.

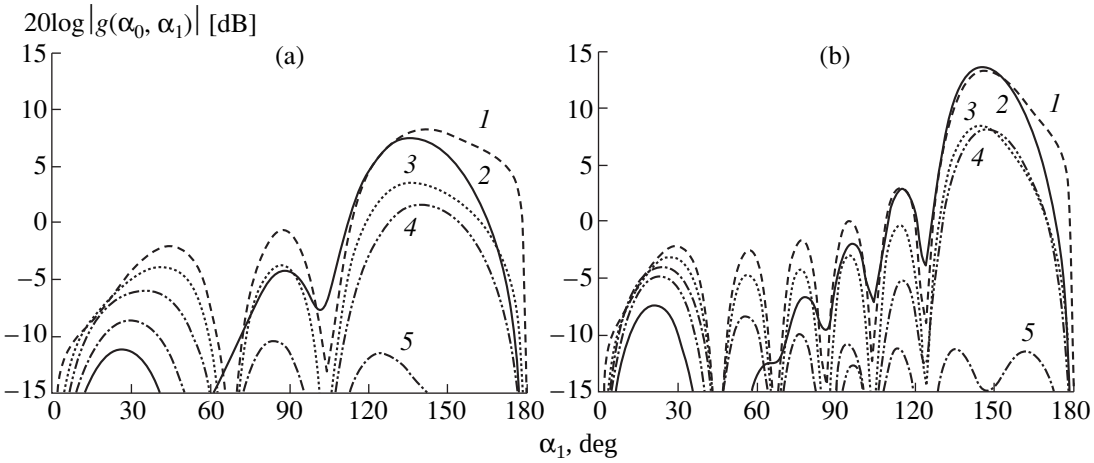


**Fig. 6.** Two-point scattering patterns for various sound reflection coefficients of the screen for $\alpha_0 = 30°$, $w_1 = w_2 = -i100.0$, and $kd$ = (a) 10.0 and (b) 20.0. The curves correspond to the following parameters: (*1*) $w_p = 38.0$, $A_p = 0.9$; (*2*) $w_p = 0.1052$, $A_p = -0.9$; (*3*) $w_p = 6.0$, $A_p = 0.5$; (*4*) $w_p = 0.666$, $A_p = -0.5$; and (*5*) $w_p = 2.0$, $A_p = 0$. Here, $A_p$ is the reflection coefficient for $\alpha_0 = 30°$.

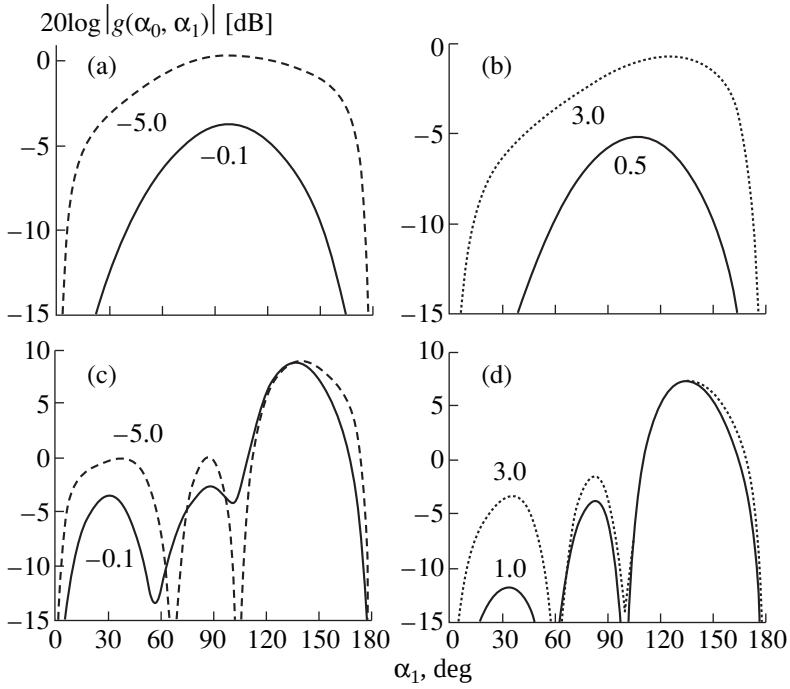


**Fig. 7.** Scattering patterns for different imaginary parts of the screen impedance for $\alpha_0 = 30°$, $w_1 = w_2 = -i5.0$, $\mathrm{Re}\, w_p = 0.05$, and $kd$ = (a, b) 3.0 and (c, d) 10.0. The values of $\mathrm{Im}\, w_p$ are shown near the curves.

different in sign produce the main lobes with almost equal maxima. Asymptotically, these maxima are given by the formula

$$g_{\max} \approx |A_p(\alpha_0)| \cos(\alpha_0) kd/2, \quad kd \gg 1. \qquad (32)$$

Figure 7 shows the two-point scattering patterns for several imaginary parts of the screen impedance under the condition that the real parts of these impedances are small. For $kd = 10$, the variations in the imaginary part of the impedance produce little effect and are seen only in regions far from the direction of the specular reflection.

Variations in the impedance of the waveguide walls (Fig. 8) have a profound effect on the scattered field for smaller $kd$ and little effect on the shape of the main lobe of the pattern for greater $kd$ (Figs. 8c, 8d).

Figure 9 shows the oscillating behavior of the amplitude of the backscattered wave as a function of

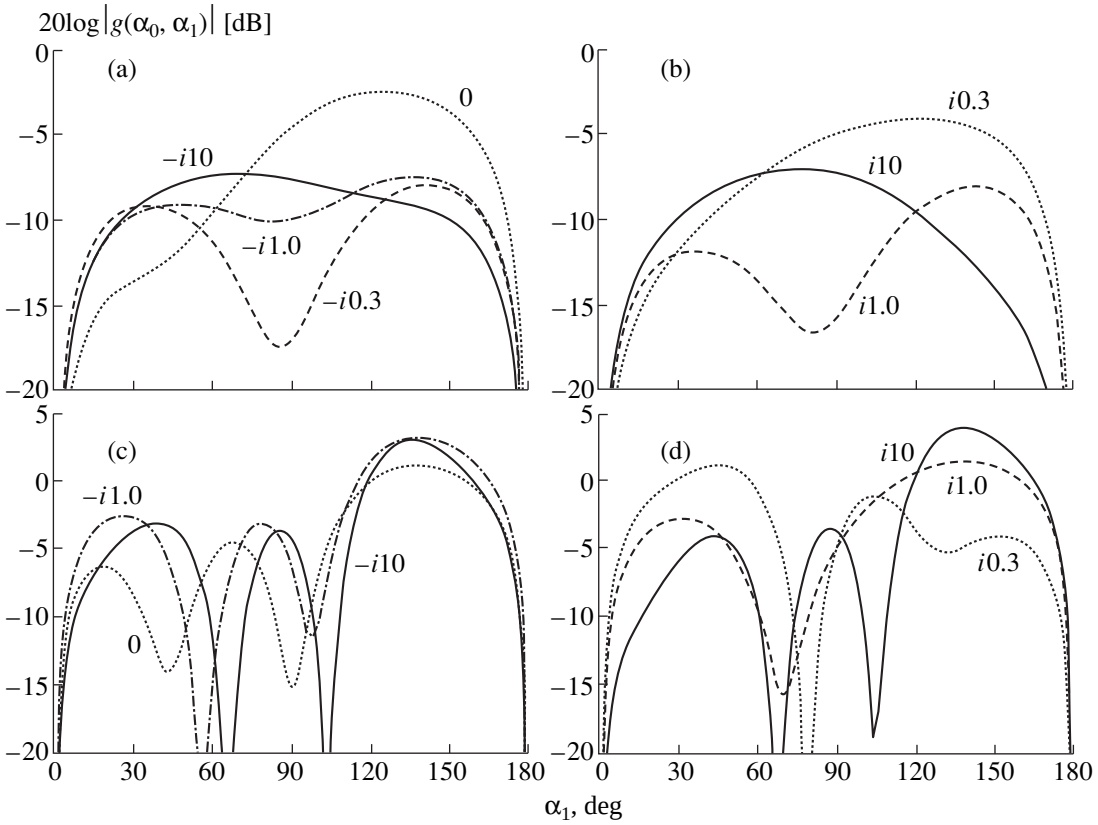


**Fig. 8.** Two-point scattering patterns for different impedances of the waveguide walls. A symmetric waveguide with $w_1 = w_2 = w$, $kd = 10.0$, $\alpha_0 = 30°$, and $w_p = 6.0$ ($A_p = 0.5$). The values of the impedance $w$ are shown near the curves.

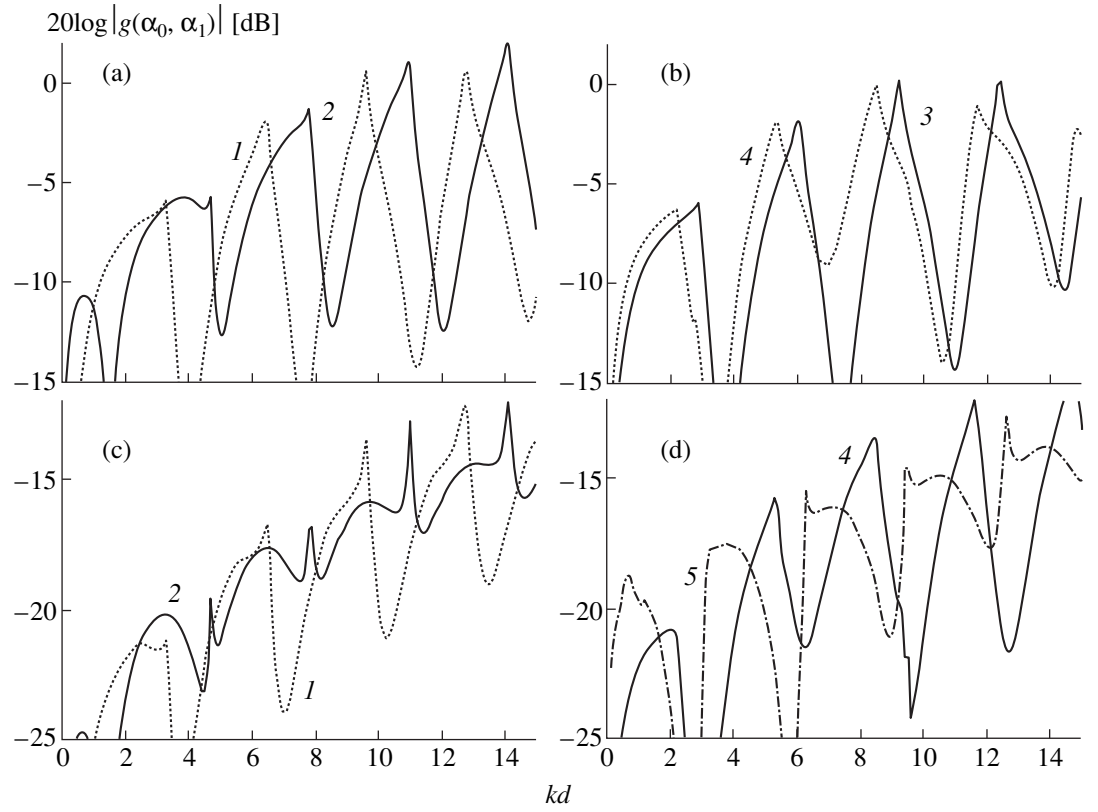


**Fig. 9.** Frequency characteristics of the backscattered wave amplitude (the form-function) for $\alpha_0$ = (a, b) 30° and (c, d) 5°; $w_p = 6.0$ and $w_1 = w_2 = w$. The impedance values are $w$ = (*1*) $-i10.0$, (*2*) $-i1.0$, (*3*) $0.1 + i10.0$, (*4*) $0.1 + i2.0$, and (*5*) 0.

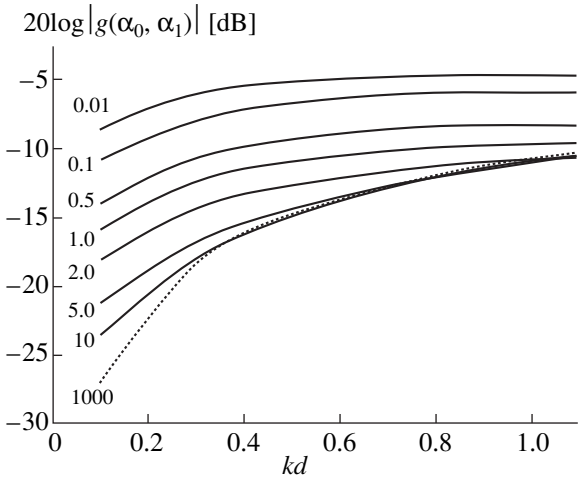


**Fig. 10.** Frequency characteristics of the backscattered wave amplitude (the form-function) for waveguides of a small wave width with various wall impedances; $\alpha_0 = \alpha_1 = 30°$ $w_p = 6.0$, and $\mathrm{Re}\,w = 0$. The values of $\mathrm{Im}\,w$ are shown near the curves.

the wave size of the opening (also called the form-function). For grazing angles of incidence, narrow peaks occur in the curves, as in the case of the similar curves (see [2]) for acoustically hard surfaces. To explain the behavior of these curves, we turn to the approximate expression (19) of paper [2]:

$$g(\alpha_0) = \frac{kd}{2}\frac{\sin(kd\cos\alpha_0)}{kd\cos\alpha_0},\quad kd \gg 1,\quad A(\alpha_0) = 1. \quad (33)$$

The minima of the directional pattern exist for $kd\cos\alpha_0 = \pi n$, $n = 1, 2, \ldots$, i.e., for $kd$ satisfying the condition $kd = \pi n/\cos\alpha_0$. In all our curves, the positions of the minima comply with this condition.

Narrow peaks can be explained by the variations in the number of oscillating modes propagating in the waveguide. The number of these modes is finite and depends on the wave width $kd$. The condition $kd = \pi m$ corresponds to the generation of the mode with the number $m$. In this case, the resonance conditions occur in the waveguide and the amplitude of the newly generated wave may appear very large. For a frequency exactly coincident with the resonance frequency, the oscillations occur strictly in the direction of the $x$-axis and the component of the oscillating particle velocity $v_y$ is equal to zero. For this reason, exactly at the resonance frequency, the newly generated mode does not affect the scattered field. However, for $kd$ slightly different from the resonance value, the amplitude of the mode with number $n$ remains large and the component

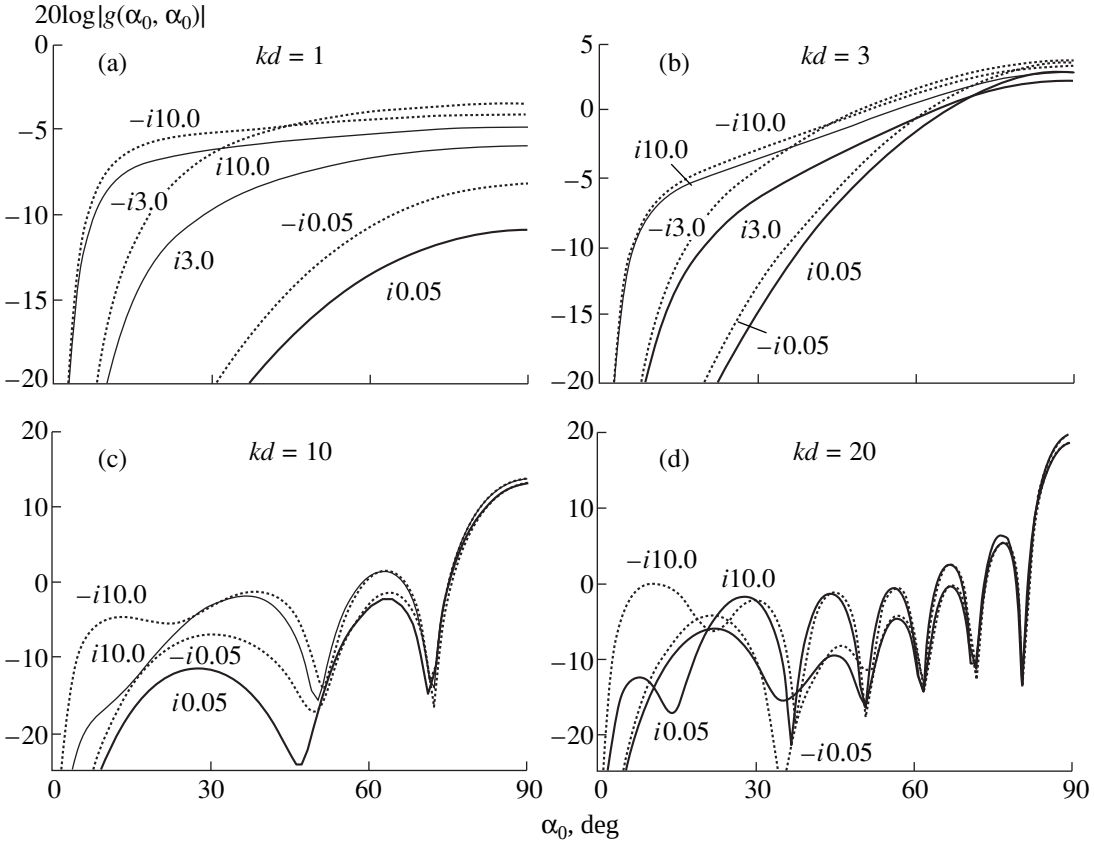


**Fig. 11.** Backscattered amplitude as a function of the angle of the sound wave incidence; $w = i10.0$ and $\mathrm{Re}\,w_p = 0.05$. The values of $\mathrm{Im}\,w_p$ are shown near the curves. The solid and dotted lines correspond to positive and negative values of $\mathrm{Im}\,w_p$, respectively.

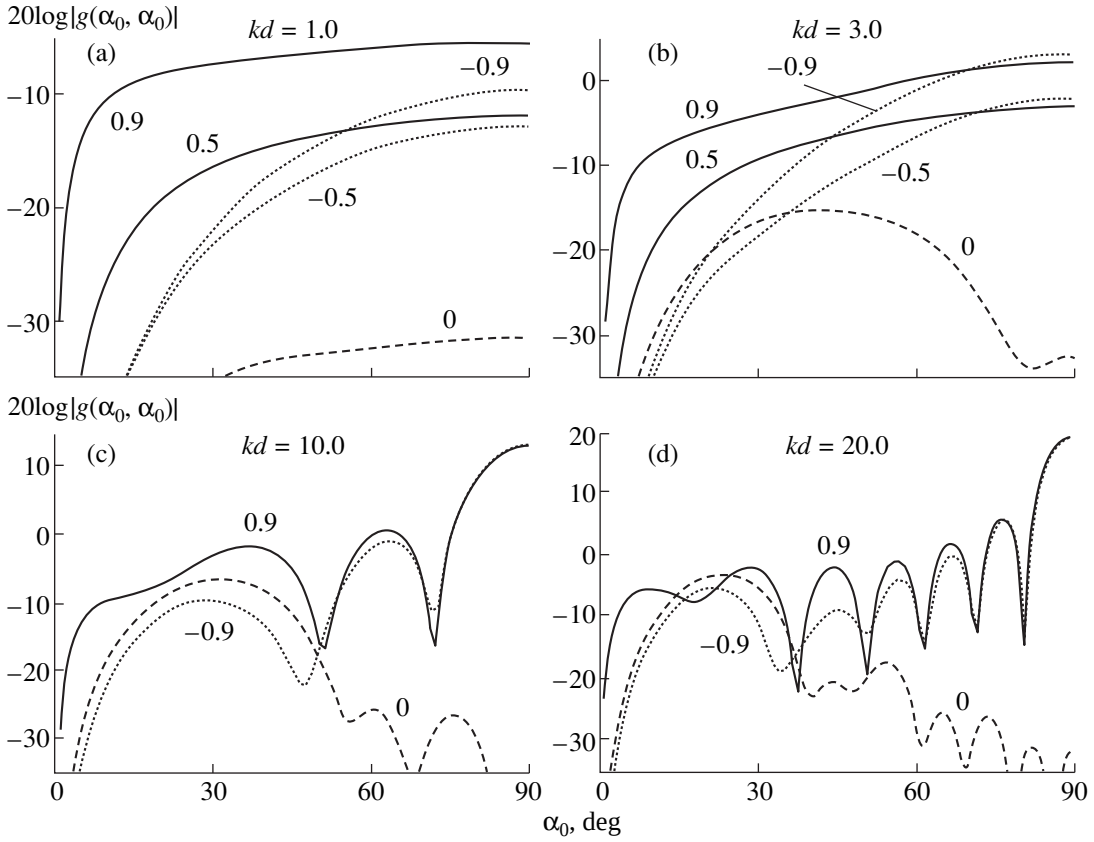


**Fig. 12.** Backscattered amplitude as a function of the angle of the sound wave incidence; $w_1 = w_2 = -i10.0$. The numbers near the curves are the values of the sound reflection coefficients for normal incidence.

of the particle velocity $v_y$ becomes nonzero. As a result, the scattered field increases sharply.

For waveguides of a smaller wave width (Fig. 10), the amplitude of the backscattered wave strongly depends on the impedance of the waveguide walls. The scattering intensity is much higher for waveguides with acoustically soft walls than for those with acoustically hard walls. With an increasing wave width, this difference decreases. In this respect, the situation is similar to the diffraction by any impedance obstacle.

Figure 11 shows the backscattered amplitude as a function of the angle of incidence. All graphs show pairs of curves corresponding to the screen impedances that differ in the sign of the imaginary part: positive for elastic screens and negative for inertial screens. For large wave widths (Figs. 11c, 11d), the backscattered amplitudes almost coincide for both types of screens, while, for small wave widths (Figs. 11a, 11b), the scattering amplitude for elastic screens appears to be noticeably less than for inertial screens. The explanation is that some portion of the energy is carried away with the surface wave generated in the elastic screens.

The backscattered amplitude essentially depends on the sound reflection coefficient of the screen. For $w_p = 1$ (which corresponds to the zero reflection coefficient for the case of normal incidence), the backscattering appears to be minimal (Fig. 12). Thus, a decrease in the reflection coefficient of the screen results in a decrease in not only the specular component of the wave, but also in the scattered component of the field. Note that, for an oblique incidence, the level of the scattered field strongly depends on the sign of the reflection coefficient. For example, a comparison of the curves calculated for $w_p = 19.0$ and $w_p = 0.0526$ (which, for the normal incidence, corresponds to the reflection coefficients 0.9 and –0.9, respectively) shows that, for a grazing incident wave, the level of the scattered wave in the second case is much lower than in the first case.

## ACKNOWLEDGMENTS

This work was supported by the Russian Foundation for Basic Research, project nos. 98-02-16017 and 00-02-17840.

## *APPENDIX 1*

## DERIVATION OF EQUATION (1)

Let a point sound source with a productivity $Q$ be located at a point $\mathbf{r}_0$ (see Fig. A1). It is necessary to determine the field that the source generates at a point $\mathbf{r}_1$ in the presence of a reflecting surface $S$. The sound

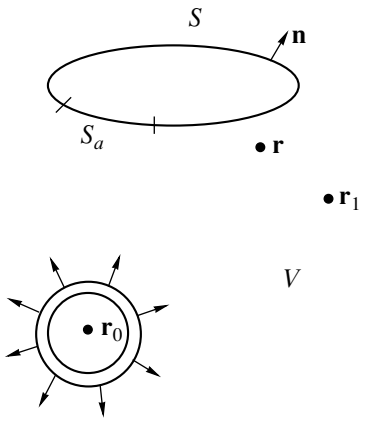


**Fig. A1.** For the derivation of equation (1).

field at an arbitrary point $\mathbf{r}$ is determined from the Helmholtz equation

$$\Delta p(\mathbf{r}, \mathbf{r}_0) + k^2 p(\mathbf{r}, \mathbf{r}_0) = -\delta(\mathbf{r} - \mathbf{r}_0)(-ik\rho cQ). \quad \text{(A1.1)}$$

We place an auxiliary point source at the point $\mathbf{r}_1$ and represent the field of this source in the form of the Green's function satisfying the equation

$$\Delta G(\mathbf{r}_1, \mathbf{r}) + k^2 G(\mathbf{r}_1, \mathbf{r}) = -\delta(\mathbf{r}_1 - \mathbf{r}). \quad \text{(A1.2)}$$

Then, we multiply Eq. (A1.1) by $G(\mathbf{r}_1, \mathbf{r}_0)$ and Eq. (A1.2) by $p(\mathbf{r}, \mathbf{r}_0)$, subtract the second equation from the first one, and integrate over the whole volume $V$ excluding the region bounded by the surface $S$. As a result, we obtain the relationship

$$\begin{aligned}\iiint_V (\Delta p(\mathbf{r}, \mathbf{r}_0) G(\mathbf{r}_1, \mathbf{r}) - p(\mathbf{r}, \mathbf{r}_0)\Delta G(\mathbf{r}_1, \mathbf{r}))dV_r \\ = ik\rho cQ \iiint_V \delta(\mathbf{r} - \mathbf{r}_0) G(\mathbf{r}_1, \mathbf{r}) dV_r \\ + \iiint_V \delta(\mathbf{r}_1 - \mathbf{r}) p(\mathbf{r}, \mathbf{r}_0) dV_r \\ = ik\rho cQG(\mathbf{r}_1, \mathbf{r}_0) + p(\mathbf{r}_1, \mathbf{r}_0).\end{aligned} \quad \text{(A1.3)}$$

Here, the index $r$ marking the elementary volume $dV_r$ (and the elementary area $dS_r$ below) means the integration with respect to the coordinates of the point $\mathbf{r}$. According to the Green's theorem, the volume integral can be transformed into the integral over the bounding surface. One can assume that the volume $V$ is bounded by the surface $S$ closed by a sphere of a large radius. The integral over this sphere decreases to zero with an increasing sphere radius due to the radiation condition. As a result, we obtain

$$\begin{aligned}p(\mathbf{r}_1, \mathbf{r}_0) = -ik\rho cQG(\mathbf{r}_1, \mathbf{r}_0) \\ + \iint_S \left( p(\mathbf{r}) \frac{\partial G(\mathbf{r}_1, \mathbf{r})}{\partial n} - \frac{\partial p(\mathbf{r})}{\partial n} G(\mathbf{r}_1, \mathbf{r}) \right) dS_r.\end{aligned} \quad \text{(A1.4)}$$

Here, we omitted one of the arguments of the function $p(\mathbf{r}, \mathbf{r}_0)$ in the integrand. For the two-dimensional case, this equation will hold, if we replace the surface integral by the line integral and use the two-dimensional Green's function. Assuming that the integration is performed along the $x$-axis, we obtain the desired expression (1).

Note that, until now, we did not require that the Green's function satisfy any boundary conditions at the surface. Consider now an inhomogeneous surface $S$ composed of two segments $S_a$ and $S–S_a$ with different properties. Let the sound pressure and the normal component of the particle velocity be related by the equation $p = Zv_n = Z/(i\omega\rho)\partial p/\partial n$ on the segment $S–S_a$. Let the Green's function satisfying the homogeneous boundary condition corresponding to the impedance of the segment $S–S_a$ be known (i.e., the function satisfying the condition $G = Z/(i\omega\rho)\partial G/\partial n$). We subdivide the integral over the surface $S$ into two integrals over the above segments and take into account the boundary conditions for the sound pressure and the Green's function in the second integral. Then, the integral over the segment $S–S_a$ vanishes, and only the integral over the segment $S_a$ (A1.4) will remain. We used this feature to reduce the integral with infinite limits to the integral over the opening.

## *APPENDIX 2*

## PROOF OF THE SOUND FIELD CONTINUITY IN THE OPENING

In deriving the system of Eqs. (24b), we assumed that the sound pressure is continuous over the opening and equated expressions (12) and (17). In so doing, we used the sound pressure and its normal derivative in the waveguide to substitute them into the integrand of formula (15). It turns out that this procedure automatically ensures the continuity of the normal component of the oscillating particle velocity rather than the sound pressure alone. To prove this statement, let us differentiate expressions (12)–(15) with respect to $y_1$ and expression (17) with respect to $y$ and equate them at the point $y_1 = y = 0$. Then, we use the orthogonality relationship (21) as we used it in the derivation of system (24b). As a result, we obtain the system of equations

$$A_n + \sum_{m=1}^{\infty} A_m V_{nm} = F_n, \quad n = 1, 2, 3\ldots, \quad \text{(A2.1)}$$

$$F_n = \frac{\sin\alpha_0 d_n(\cos\alpha_0)}{H_n(1 - q_n)}[1 - A_p(\sin\alpha_0)], \quad \text{(A2.2)}$$

$$V_{nm} = -\frac{kd[\gamma_m w_p - 1 - q_m(\gamma_m w_p + 1)]}{2\pi H_n(1 - q_n)} J_{mn}, \quad \text{(A2.3)}$$

$$J_{mn} = \int_{-\infty}^{\infty} \frac{d_n(u) d_m(-u)\sqrt{1 - u^2}}{w_p\sqrt{1 - u^2} + 1} du. \quad \text{(A2.4)}$$

We represent the last integral in the form $J_{mn} = (L_{mn} - I_{mn})/w_p$, where

$$L_{mn} = \int_{-\infty}^{\infty} d_m(-u)d_n(u)du \qquad \text{(A2.5)}$$

and $I_{mn}$ is determined by expression (28). Taking into account relationship (23), we can write

$$L_{mn} = \frac{1}{d^2}\int_{-d/2}^{d/2}\int_{-d/2}^{d/2} \psi_n(x)\psi_m(x') \times \int_{-\infty}^{\infty} \exp[ik(x-x')u]dudxdx'.$$

The integral with respect $u$ is proportional to the delta-function, namely to $(2\pi/k)\delta(x - x')$. Now, we can integrate over $x'$, which results in the integral coincident with that defined in the condition of orthogonality of eigenfunctions (21)

$$L_{mn} = \frac{2\pi}{kd^2}\int_{-d/2}^{d/2} \psi_n(x)\psi_m(x)dx = \frac{2\pi}{kd}H_n\delta_{nm}, \qquad \text{(A2.6)}$$

where $\delta_{nm}$ is the Kronecker delta, $\delta_{nm} = 1$ for $m = n$, and $\delta_{nm} = 0$ for $m \neq n$. As a result, we obtain

$$J_{mn} = [2\pi/(kd)H_n\delta_{nm} - I_{mn}]/w_p. \qquad \text{(A2.7)}$$

Substituting this expression into (A2.3) and rearranging relationships (A2.2)–(A2.4), we obtain a system of equations that coincides with system (24a)–(28). Thus, we obtain the same system of equations with any of the continuity conditions in the opening: the continuity of the sound pressure or the continuity of the normal component of the particle velocity.

## REFERENCES


1. A. D. Rawlins, Proc. R. Soc. London, Ser. A **361** (1704), 65 (1978).
2. E. L. Shenderov, Akust. Zh. **44**, 106 (1998) [Acoust. Phys. **44**, 88 (1998)].
3. A. N. Norris and I. C. Sheng, J. Sound Vibr. **195**, 85 (1989).
4. E. L. Shenderov, *Wave Problems of Hydroacoustics* (Sudostroenie, Leningrad, 1972).
5. E. L. Shenderov, Akust. Zh. **45**, 661 (1999) [Acoust. Phys. **45**, 589 (1999)].
6. N. N. Andreev, Izv. Akad. Nauk SSSR, Ser. Fiz., No. 5, 625 (1936).
7. Ph. M. Morse and K. U. Ingard, in *Handbuch der Physik* (Springer, Berlin, 1961), Vol. 11/1, pp. 1–128.


*Translated by A. Vinogradov*

*Acoustical Physics, Vol. 46, No. 6, 2000, pp. 728–733. From Akusticheskiĭ Zhurnal, Vol. 46, No. 6, 2000, pp. 829–834.*


# Sound Beams with Shockwave Pulses[1]

**B. O. Enflo**

*Department of Mechanics, Kungl. Tekniska Högskolan (Royal Institute of Technology), 10044 Stockholm*
*e-mail: benflo@mech.kth.se*

Received February 24, 1999

**Abstract**—The beam equation for a sound beam in a diffusive medium, called the Khokhlov–Zabolotskaya–Kuznetsov (KZK) equation, has a class of solutions, which are power series in the transverse variable with the terms given by a solution of a generalized Burgers' equation. A free parameter in this generalized Burgers' equation can be chosen so that the equation describes an N-wave which does not decay. If the beam source has the form of a spherical cap, then a beam with a preserved shock can be prepared. This is done by satisfying an inequality containing the spherical radius, the N-wave pulse duration, the N-wave pulse amplitude, and the sound velocity in the fluid. © *2000 MAIK "Nauka/Interperiodica".*

## INTRODUCTION

Most of the analytical work in nonlinear acoustics deals with sound waves in an infinite space. These waves are mathematically described by Burgers' equation (for plane waves) and by generalized Burgers' equations (for waves in other geometries). Accounts of analytical results achieved in this field are given, for example, by Rudenko and Soluyan [1], Crighton and Scott [2], and the present author [3, 4]. The generally adopted mathematical model of a limited beam is the Khokhlov–Zabolotskaya–Kuznetsov (KZK) equation [5, 6]. Formally it is obtained from Burgers' equation by deriving it with respect to time and by adding terms with second derivatives in the directions transverse to the beam propagation direction. Solutions of the KZK equation by numerical methods, mainly for periodic waveforms, have been published [7–10]. In addition, periodic waveforms short pulses, especially N-waves, are of both theoretical and practical interest. The solution method for the KZK equation developed in this paper is applied to N-waves, but it seems possible to apply it also to periodic waves, especially sawtooth waves.

In the present investigation it is shown that the KZK equation has a class of solutions that can be found by solving a generalized Burgers' equation. From the solution of this generalized Burgers' equation the coefficients are constructed of a series expansion in a transverse variable of a solution of the KZK equation. Such an expansion has been attempted for the KZ equation (the beam equation without dissipation) [11]. The solution found by Sionoid [12] for a case in which the KZK equation can be transformed into a generalized Burgers' equation is a special case among the solutions in the class presented in the present paper.

In order to obtain a solution of the KZK equation of the kind studied in this paper, special boundary conditions must be satisfied. An example of practical interest is given of boundary conditions giving solutions of the appropriate class. It is shown that an N-wave initiated on a concave spherical cap will retain its shock structure during its whole propagation if the cap curvature radius is appropriately adapted to the shock duration and the shock amplitude. In the present case the cap curvature radius is much greater than the cap aperture radius, so that shock decay may occur before focusing. The special type of solutions of the KZK equation presented in this paper may be of practical interest in designing an apparatus for creating shockwaves intended to have some effect on objects hit.

## THE BEAM EQUATION

The beam is assumed to be cylindrically symmetrical. The KZK equation will be considered in the normalized form (see, e.g., [10], Section 4.2):

$$\frac{\partial}{\partial\theta}\left(\frac{\partial V}{\partial X} - V\frac{\partial V}{\partial\theta} - \epsilon\frac{\partial^2 V}{\partial\theta^2}\right) = \frac{N}{4}\left(\frac{\partial^2 V}{\partial R^2} + \frac{1}{R}\frac{\partial V}{\partial R}\right). \quad (1)$$

Here the dimensionless variables are introduced according to the formulas

$$V = \frac{v}{v_0},\ \theta = \omega\tau,\ X - X_0 = \frac{\beta\omega v_0}{c_0^2}x,\ R = \frac{\rho}{a}, \quad (2)$$

where $v_0$ is a characteristic fluid velocity, $\omega^{-1}$ is a characteristic pulse duration and $a$ is the beam radius, all at the beam source, $x$ is a coordinate along the beam axis, $\rho = \sqrt{y^2 + z^2}$ is a transverse coordinate, $\tau = t - x/c_0$ with $c_0$ equal to the sound velocity of the undisturbed fluid, and $\beta = (\gamma + 1)/2$ with $\gamma$ equal to the ratio of heat capacities.

With $b$ equal to the effective viscosity of the medium and $\rho_0$ equal to the density of the undisturbed

[1] This article was submitted by the author in English.

fluid, the two dimensionless constants $\epsilon$ and $N$ are given as

$$\epsilon = \frac{b\omega}{2\beta c_0 v_0 \rho_0} = \frac{x_{sh}}{x_{abs}}, \tag{3}$$

$$N = \frac{2c_0^3}{\beta a^2 \omega^2 v_0} = \frac{x_{sh}}{x_{dif}}, \tag{4}$$

where the shock generation length $x_{sh}$, the absorption length $x_{abs}$, and the diffraction length $x_{dif}$ are given as

$$x_{sh} = \frac{c_0^2}{\beta\omega v_0}, \quad x_{abs} = \frac{2c_0^3\rho_0}{b\omega^2}, \quad x_{dif} = \frac{\omega a^2}{2c_0}. \tag{5}$$

No assumption is made about the magnitude of $N$. The parameter $\epsilon$, on the other hand, is assumed to be considerably less than unity.

## SERIES SOLUTION OF THE BEAM EQUATION

The KZK equation (1) has been solved numerically for different boundary conditions by many authors [7–9]. The analytical attempt [13] to expand the solution of (1) in powers of the transverse variable $R$ is rewritten

$$R^2 = \frac{N}{2} r^2. \tag{6}$$

The solution, studied by P.N. Sionoid [12], of the form

$$V(X, \theta, r^2) = V_0\left(X, \theta - \frac{r^2}{2X}\right), \tag{7}$$

where $V_0(X, \theta)$ fulfils the generalized Burgers' equation

$$V_{0X} + \frac{V_0}{X} - V_0 V_{0\theta} - \epsilon V_{0\theta\theta} = 0 \tag{8}$$

is an example of such an expansion, since $V_0(X, \theta - r^2/2X)$ can be expanded in a Taylor series

$$V_0\left(X, \theta - \frac{r^2}{2X}\right) = V_0(X, \theta) - \frac{r^2}{2X} V_{0\theta}(X, \theta) + \frac{1}{2}\frac{r^4}{4X^2} V_{0\theta\theta}(X, \theta) + \dots . \tag{9}$$

Now we will find a larger class than that given in Eq. (7) of solutions of the KZK equation (1). The new solutions are found from an expansion in $r^2$ with the coefficients given by a generalized Burgers' equation similar to Eq. (8). The sought generalization of (9) is

$$\begin{aligned} V(X, \theta, r^2) &= V_0(X, \theta) + k\frac{r^2}{2X} V_{0\theta}(X, \theta) \\ &+ \frac{1}{2!}\frac{k(k-1)}{2}\frac{r^4}{4X^2} V_{0\theta\theta}(X, \theta) \\ &+ \frac{1}{3!} k r^6 \left\{ \frac{(k-1)(k-2)}{3!}\frac{1}{8X^3} V_{0\theta\theta\theta}(X, \theta) \right. \\ &\left. - \frac{k+1}{3}\frac{1}{8X^2}(V_{0\theta} V_{0\theta\theta})_\theta \right\} \\ &+ \frac{1}{4!} k r^8 \left\{ \frac{(k-1)(k-2)(k-3)}{4!}\frac{1}{16X^4} V_{0\theta\theta\theta}(X, \theta) \right. \\ &+ \frac{k+1}{12}\frac{1}{16X^2}[-(V_{0\theta} V_{0\theta\theta})_{\theta\theta X} \\ &- (3k-5)\frac{1}{X}(V_{0\theta} V_{0\theta\theta})_{\theta\theta} \\ &\left. + (V_0(V_{0\theta} V_{0\theta\theta})_\theta)_{\theta\theta} + \epsilon(V_{0\theta} V_{0\theta\theta})_{\theta\theta\theta\theta}] \right\} + \dots . \end{aligned} \tag{10}$$

The expansion (10) is similar to the expansion given by Rudenko [11], in which the power series is in the variable $R = \rho/a$.

The generalized Burgers' equation satisfied by $V_0(X, \theta)$ is

$$V_{0X} - \frac{k}{X} V_0 - V_0 V_{0\theta} - \epsilon V_{0\theta\theta} = 0. \tag{11}$$

The number $k$ is arbitrary. Terms of the order $r^{2n+2}$ in the series (10) are calculated from terms of the order $r^{2n}$ using the fact that terms of the order $r^{2n+2}$ in $V_0$ at the right-hand side of Eq. (1) are compensated by terms of at most the order $r^{2n}$ in $V_0$ at the left-hand side of Eq. (1). The special case $k = -1$, leading to the expansion (9), is that treated by Sionoid [12].

For the special cases $k = -1$, $k = -1/2$, and $k = 0$, the generalized Burgers' equation (11) describes spherical, cylindrical, and plane waves, respectively [2]. It should be mentioned that Eq. (11) in this case has a formal meaning and has nothing to do with physical spherical, cylindrical, or plane waves. This means that the case $k < 0$, which does not occur for travelling waves in a homogeneous medium, is meaningful in this case, where the solving of the KZK equation can be reduced to solving a generalized Burgers' equation.

For $k \neq -1$ Eq. (11) will be transformed. Using the substitutions

$$W = -X^{-k} V_0; \quad \xi = \frac{1}{k+1} X^{k+1} \tag{12}$$

in Eq. (11), we obtain

$$W_\xi + W W_\theta - \epsilon\{(k+1)\xi\}^{-\frac{k}{k+1}} W_{\theta\theta} = 0. \tag{13}$$

For arbitrary $k \neq -1$ the wave equation (13) formally describes plane waves propagating in a medium with a variable viscosity.

Of special interest are cases with $k > 0$. In these cases the dissipative term in the wave equation (13) decreases as the distance traveled by the wave increases. This means that the decay of a shockwave is slower than for $k \leq 0$, in which case it is well known that the shockwave decays if the distance traveled is sufficiently long [2]. It is interesting to know how to prepare a beam with a shockwave that does not decay. This can be achieved by a solution of the form of Eq. (10) with a $k$ value greater than zero. Especially interesting is the case $k = 1$, because of the vanishing of the $r^4$ term in the series (10). This means that the first two terms of the series give a very good approximation of the solution in the center of the beam.

## A GENERALIZED BURGERS' EQUATION WITH A PRESERVED SHOCK SOLUTION

For $k = 1$ the following equation is obtained from Eq. (13):

$$W_\xi + WW_\theta - \frac{\epsilon}{\sqrt{2\xi}} W_{\theta\theta} = 0. \tag{14}$$

Generalized Burgers' equations of the type

$$W_\xi + WW_\theta - \epsilon G(\xi) W_{\theta\theta} = 0 \tag{15}$$

are treated by Crighton and Scott [2]. They show that the N-wave boundary condition

$$\begin{aligned} W(1, \theta) &= \theta, \quad |\theta| < 1, \\ W(1, \theta) &= 0, \quad |\theta| > 1 \end{aligned} \tag{16}$$

leads to the "outer" solution

$$\begin{aligned} W^{(e)}(\xi, \theta) &= \frac{\theta}{\xi} + o(\epsilon^n), \quad |\theta| < \sqrt{\xi}, \\ W^{(e)}(\xi, \theta) &= 0, \quad |\theta| > \sqrt{\xi}. \end{aligned} \tag{17}$$

An "inner" solution to (15) in the neighborhood of $\theta = \sqrt{\xi}$ is found by asymptotic matching [2]. For $G(\xi) = (2\xi)^{-1/2}$ this solution is

$$W^i(\xi, \theta^*) = \frac{1}{2\sqrt{\xi}} \left\{ 1 - \tanh \frac{\theta^* - \sqrt{2}\left(1 - \xi^{\frac{1}{2}}\right)}{2\sqrt{2}} \right\} + \epsilon W_1^i + \ldots, \tag{18}$$

where

$$\theta^* = \frac{\theta - \sqrt{\xi}}{\epsilon}. \tag{19}$$

The solution (18), (19) is valid until the second term in the asymptotic series (18) is of the same order of magnitude as the first one. This second term is calculated by Crighton and Scott [2]. From their result it can be seen that the term $\epsilon W_i^i$ in (18) is of the same order of magnitude as the first term for $\xi = O(\epsilon^{-2})$. In order to obtain a solution of Eq. (14) valid for $\xi = O(\epsilon^{-2})$, we make the new scaling

$$\xi_I = \epsilon^2 \xi. \tag{20}$$

The new scalings of $\theta$ and $W$ follow from Eqs. (14) and (20):

$$\theta_I = \epsilon\theta, \quad W_I = \epsilon^{-1} W. \tag{21}$$

The new generalized Burgers' equation is obtained from Eq. (14) and Eqs. (20), (21):

$$\frac{\partial W_I}{\partial \xi_I} + W_I \frac{\partial W_I}{\partial \theta_I} - \frac{\epsilon^2}{\sqrt{2\xi_I}} \frac{\partial^2 W_I}{\partial \xi_I^2} = 0. \tag{22}$$

It is easily seen from Eqs. (20), (21) that the outer solution of Eq. (22) is identical with the outer solution (17) of Eq. (14). The inner solution of Eq. (22) is written in the same variables as Eq. (18):

$$\epsilon W_I^i = \frac{1}{2\sqrt{\xi}} \left\{ 1 - \tanh \frac{\dfrac{\theta - \sqrt{\xi}}{\epsilon} - \sqrt{2}\left(1 - \epsilon\xi^{\frac{1}{2}}\right)}{2\sqrt{2}} \right\} + O(\epsilon^2). \tag{23}$$

From Eq. (23) we see that for $\sqrt{\xi} = O\left(\frac{1}{\epsilon}\right)$ we have still a shock solution whose discontinuity is $\xi^{-1/2}$. The shock center in the solution (18) is at

$$\theta = \theta_0 = \sqrt{\xi} + \epsilon\sqrt{2}(1 - \sqrt{\xi}), \quad \xi = O(1) \tag{24}$$

and the shock center in the solution (23) is at

$$\theta = \sqrt{\xi} + \epsilon\sqrt{2}(1 - \epsilon\sqrt{\xi}), \quad \xi = O(\epsilon^{-2}). \tag{25}$$

Because $\xi = O(\epsilon^{-2})$ in Eq. (25), it follows that the shock has not moved farther from the location $\theta = \sqrt{\xi}$ in Eq. (25) than it has already moved in Eq. (24). This is in contrast with the situation for plane waves in a homogeneous medium. In the latter case the distance of the shock center from the location $\theta = \xi$ increases to the same order of magnitude as the N-wave length $2\sqrt{\xi}$. From Eqs. (18) and (23) we also conclude that the coefficient $\epsilon/\sqrt{2\xi}$ of the second derivative term in Eq. (14) has exactly the necessary decreasing behavior with $\xi$ for giving the nongrowing shockwidth $2\sqrt{2}\epsilon$. In fact, the nonlinear term is important during the whole propagation of the wave. This can be seen if we investigate the consequences of neglecting it. Neglecting the non-

linear term in Eq. (14) gives a linear equation, whose "dipole" solution is

$$W = C\frac{\theta}{\xi^{\frac{3}{4}}}\exp\left(-\frac{\sqrt{2}\theta^2}{8\xi^{\frac{1}{2}}}\right), \tag{26}$$

where $C$ is a constant. However, the expression (26) put into Eq. (14) makes the nonlinear term greater than the two linear terms for great $\xi$ values. Thus neglecting of the nonlinear term in Eq. (14) is inconsistent for all $\xi$ values.

The solution (23) is no longer valid for $\xi = O(\epsilon^{-4})$, and a new rescaling is made similar to that made in Eqs. (20), (21). For every new rescaling, the small parameter ($\epsilon$, $\epsilon^2$, $\epsilon^4$, …) is squared and the shock amplitude decreases in the same way ($\epsilon$, $\epsilon^2$, $\epsilon^4$, …).

## A BOUNDARY CONDITION GIVING A PRESERVED N-WAVE SHOCK SOLUTION OF THE KZK EQUATION

Now it will be shown how a boundary condition for the KZK equation (1) should be prepared in order to give a preserved shock solution. This shock solution will be found by a solution of Eq. (14) used in the expansion (10) with an appropriate value of k. The original N-wave is generated on a spherical concave cap [13], whose surface has the equation

$$(x-d)^2 + y^2 + z^2 = d^2. \tag{27}$$

The cap surface is that part of this spherical surface which fulfils the inequality

$$y^2 + z^2 \le a^2. \tag{28}$$

Assuming that the spherical radius d of the cap is much greater its intersection radius,

$$d \gg a, \tag{29}$$

the cap equation is approximated:

$$x \approx \frac{y^2 + z^2}{2d}. \tag{30}$$

Following Ystad and Berntsen [9] we formulate a boundary condition on the plane $x = 0$ equivalent to the boundary condition on the curved cap surface. The phase $\omega t$ at the point $(x, y, z)$ on the curved surface corresponds to the phase

$$\omega t + \frac{\omega}{c_0}x = \omega t + \frac{\omega}{c_0}\frac{y^2 + z^2}{2d} \tag{31}$$

at the plane $x = 0$. We assume a boundary condition in which the wave phase is constant on the cap surface and the wave amplitude depends only on the distance from the beam axis. By using Eq. (31), the equivalent boundary condition at $x = 0$ thus becomes

$$\begin{aligned} v(x=0, \rho, t) &= v_0 g\left(\frac{\rho^2}{a^2}\right)F\left(\omega t + \frac{1}{2}\frac{\omega\rho^2}{c_0 d}\right), \quad \rho > a, \\ v(x=0, \rho, t) &= 0, \quad \rho > a, \end{aligned} \tag{32}$$

where $\rho = \sqrt{y^2 + z^2}$ is used. Putting

$$G(r^2) = g\left(\frac{\rho^2}{a^2}\right) = g\left(\frac{1}{2}Nr^2\right) \tag{33}$$

the boundary condition (32) is expressed by dimensionless variables for small $r^2$ using Eqs. (2) and (4)–(6):

$$\begin{aligned} V(X = X_0, r, \theta) &= G(r^2)F\left(\theta + \frac{1}{2}\frac{x_{sh}}{d}r^2\right) \\ &= \{G(0) + r^2 G'(0) + \ldots\} \\ &\times\left\{F(\theta) + \frac{1}{2}\frac{x_{sh}}{d}r^2 F'(\theta) + \ldots\right\} \\ &= G(0)F(\theta) + r^2\left\{G'(0)F(\theta) + \frac{1}{2}\frac{x_{sh}}{d}G(0)F'(\theta)\right\} \\ &+ \frac{r^4}{2}\left\{G''(0)F(\theta) + \frac{x_{sh}}{d}G'(0)F'(\theta)\right. \\ &\left. + \frac{x_{sh}^2}{4d^2}G(0)F''(\theta)\right\} + \ldots . \end{aligned} \tag{34}$$

From the boundary condition (34) a series solution of the form of Eq. (10) shall follow. Because the $\theta$ dependence of the N-wave is linear at the boundary according to Eq. (16), at the boundary $X = X_0$ the series solution (10) becomes

$$V(X = X_0, r, \theta) = V_0(X_0, \theta) + \frac{kr^2}{2X_0}V_{0\theta}(X_0, \theta). \tag{35}$$

Because of the vanishing of the higher $\theta$-derivative of $V_0$ only two terms remain in (35).

Comparing Eqs. (34) and (35) we find that $G(r^2)$ must be constant where it is not equal to zero. Otherwise the $r^4$ term in Eq. (34) does not vanish. Using the fact that $\xi = 1$ corresponds to $X + X_0$, we find from Eq. (12)

$$X_0 = (k+1)^{\frac{1}{k+1}}. \tag{36}$$

Because the absolute maximum of $W$ is 1 at the boundary $\xi = 1$, as is seen from Eqs. (16) and (17), then because of Eq. (12) we find that the maximum of $V_0$ at the boundary $X = X_0$ is $(k+1)^{\frac{k}{k+1}}$.

The phase-dependent function $F$ in the equivalent boundary condition (32) now has to be an N-wave:

$$F(\theta) = -\theta, \quad |\theta| < 1, \qquad F(\theta) = 0, \ |\theta| > 1, \tag{37}$$

which corresponds to the choice

$$G(r^2) = (k+1)^{\frac{k}{k+1}}, \quad r^2 < \frac{2}{N}, \qquad G(r^2) = 0, \quad r^2 > \frac{2}{N}. \tag{38}$$

Because the maximum of $V_0$ is $(k+1)^{\frac{k}{k+1}}$ and the absolute maximum of $F$ is 1, then Eq. (34) can be written

$$V(X = X_0, r, \theta) = (k+1)^{\frac{k}{k+1}} F\left(\theta + \frac{1}{2}\frac{x_{sh}}{d} r^2\right)$$

$$= (k+1)^{\frac{k}{k+1}} \left\{ F(\theta) + \frac{1}{2}\frac{x_{sh}}{d} r^2 F'(\theta) \right\}, \quad r^2 < \frac{2}{N}, \tag{39}$$

$$V(X = X_0, r, \theta) = 0, \quad r^2 > \frac{2}{N}.$$

A comparison between Eqs. (35) and (39) now gives

$$V_0 = (k+1)^{\frac{k}{k+1}} F(\theta), \tag{40}$$

$$\frac{x_{sh}}{d} = \frac{c_0^2}{\beta \omega v_0 d} = \frac{k}{X_0} = k(k+1)^{-\frac{1}{k+1}}. \tag{41}$$

In the first equality in Eq. (41), formula (5) is used. Putting

$$\omega = \frac{1}{T}, \tag{42}$$

where $2T$ is the duration of the original N-wave, and using Eqs. (2) and (4)–(6), the boundary condition expressed in Eq. (37) can be written by using physical variables, introducing the N-wave amplitude $u_0$

$$v(x = 0, \rho, t) = u_0 F\left(\frac{t}{T} + \frac{1}{2}\frac{\rho^2}{c_0 T d}\right), \quad \rho < a, \qquad v(x = 0, \rho, t) = 0, \quad \rho > a, \tag{43}$$

where

$$u_0 = (k+1)^{\frac{k}{k+1}} v_0. \tag{44}$$

In Eq. (43) the function $F$ is given by Eq. (37). Inserting Eq. (44) into Eq. (41), we find

$$d = \frac{(k+1)c_0^2 T}{k\beta u_0}. \tag{45}$$

The result (45) is the main result of this investigation. As follows from the previous section of this paper, the lowest $k$ value for which the shock width does not grow during the propagation of the N-wave is $k = 1$. The inequality which has to be fulfilled for an N-wave created on a spherical cap with radius $d$ of duration $2T$ and amplitude $u_0$ thus is

$$d \le \frac{2c_0^2 T}{\beta u_0}, \tag{46}$$

if the shock does not decay during the propagation of the wave.

## DISCUSSION

The appropriate boundary condition leading to a solution of the class given in Eq. (10) is found by putting $X = X_0$ in Eq. (10). Then a solution to the KZK equation can be found for all values of $(X, \theta, r^2)$ if the number $k$ and the function $V_0(X_0, \theta)$ are chosen. It is possible to give boundary conditions which cannot be satisfied by appropriate choices of $k$ and $V_0(X_0, \theta)$. It is interesting, however, that boundary conditions which imply a linear time dependence are easy to satisfy by Eq. (10) because of the vanishing of higher $\theta$-derivatives. At the same time, these boundary conditions must imply discontinuous jumps in the $\theta$-dependence and a discontinuous jump in the $r$-dependence in order to give a vanishing waveform for $\theta \longrightarrow \infty$ and for $r \longrightarrow \infty$. After the choice of $k$ and $V_0(X_0, \theta)$, the analytical method described in this paper gives $V_0(X_0, \theta)$. In order to give the vanishing $r^2$-dependence for great $r^2$ values, several terms in the series (10) must be calculated; the greater $r^2$, the more terms. The series is not uniformly convergent, so it cannot be approximated by a finite number of terms for all $r^2$. However, in the center of the beam, which means small $r^2$ values, the solution can always be approximated by a few terms in the series (10). The case $k = 1$ is especially interesting because of the vanishing of the third term in the series. This vanishing means that an approximation with only the two first terms in Eq. (10) has a wider range of validity than is otherwise expected. Since the case $k = 1$ is at the same time the theoretical limit case for the preservation of the shock structure, it would be interesting to make experiments with N-waves fulfilling relation (46) with an equal sign. In fact the main result of the paper is relation (46) together with the solution (10), (11) of the KZK equation. Further investigations of the KZK equation by analytical methods could deal with periodic sawtooth boundary conditions, which seem as easy to satisfy by the series (10) as N-wave boundary conditions. It is also desirable to represent the $r^2$-dependence of the solution in a better way by analytical methods.

## ACKNOWLEDGMENT

The author thanks Prof. O.V. Rudenko for making him aware of the problem studied and for his suggestion to attempt a series expansion in the transverse variable.

## REFERENCES

1. O. V. Rudenko and S. T. Soluyan, *Theoretical Foundations of Nonlinear Acoustics* (Nauka, Moscow, 1975; Plenum, New York, 1977).
2. D. G. Crighton and J. F. Scott, Philos. Trans. R. Soc. London, Ser. A **292**, 101 (1979).
3. B. O. Enflo, Radiofizika **36** (7), 665 (1993).
4. B. O. Enflo, Curr. Top. Acoust. Res. **1**, 601 (1994).
5. E. A. Zabolotskaya and R. V. Khokhlov, Akust. Zh. **15**, 40 (1969) [Sov. Phys. Acoust. **15**, 35 (1969)].
6. V. P. Kuznetsov, Akust. Zh. **16**, 548 (1970) [Sov. Phys. Acoust. **16**, 467 (1970)].
7. N. S. Bakhvalov, Ya. M. Zhileikin, and E. A. Zabolotskaya, *Nonlinear Theory of Sound Beams* (Nauka, Moscow, 1982; American Institute of Physics, New York, 1987).
8. J. Naze Tjøtta, S. Tjøtta, and E. H. Vefring, J. Acoust. Soc. Am. **89**, 1017 (1991).
9. B. Ystad and J. Berntsen, Acta Acust. **3** (4), 323 (1995).
10. K. Naugolnykh and L. Ostrovski, *Nonlinear Wave Processes in Acoustics* (Cambridge Univ. Press, Cambridge, 1998).
11. O. V. Rudenko, Usp. Fiz. Nauk **165** (9), 1011 (1995) [Phys. Usp. **38**, 965 (1995)].
12. P. N. Sionoid, in *Proceedings of the 13th ISNA on Advances in Nonlinear Acoustics, 1993*, p. 63.
13. B. O. Enflo, in *Proceedings of the EAA Symposium (Formerly 13th FASE Symposium), 1997*, p. 75.
14. M. F. Hamilton, in *Nonlinear Acoustics*, Ed. by M. F. Hamilton and D. T. Blackstock (Academic, San Diego, 1998), pp. 233–261.

*Acoustical Physics, Vol. 46, No. 6, 2000, pp. 734–736. Translated from Akusticheskiĭ Zhurnal, Vol. 46, No. 6, 2000, pp. 835–837.*


**SHORT COMMUNICATIONS**

# The Secondary Field of the Sum-Frequency Wave Caused by the Scattering of Interacting Acoustic Waves by a Stiff Cylinder

**I. B. Abbasov**

*Taganrog State Radio Engineering University, Nekrasovskiĭ per. 44, Taganrog, 347928 Russia*
*e-mail: ig@egf.tsure.ru*

Received December 30, 1999

The problems of sound scattering by cylindrical bodies were considered by Dubus *et al.* [1] and Klauson *et al.* [2], and the scattering of nonlinearly interacting plane acoustic waves by a cylinder was studied by Abbasov and Zagraĭ [3]. In the latter study, it was assumed that interacting plane waves are incident on an acoustically stiff cylinder normally to the $z$ axis. The cylinder is infinitely long, and its axis coincides with the $z$ axis of the cylindrical coordinate system. The wave scattering by the cylinder of radius $a$ gives rise to the propagation of scattered waves with cylindrical wave fronts in the surrounding medium. In a cylindrical layer enveloping the cylinder and bounded by the cylindrical surface of radius $d$, the incident plane waves interact with the scattered high-frequency cylindrical waves. Outside this layer, the nonlinear interaction gives rise to the propagation of waves belonging to the secondary wave field: the sum-frequency and difference-frequency waves and the second harmonics of the initial waves. We also assume that the initial waves die out outside the region where the nonlinear interaction takes place, i.e., the secondary field is formed exclusively by the initial waves interacting within the given region. The observation point is selected outside the interaction region. In the cited paper [3], we used the method of successive approximations [4] to obtain the solutions to the inhomogeneous wave equation for the difference-frequency waves in the first and second approximations.

In this paper, I consider the secondary field of the sum-frequency wave. Although the expressions for the difference-frequency and sum-frequency waves are similar, in the latter case, the scattering is geometric in nature ($ka \gg 1$), while the case of the difference-frequency wave corresponds to the Rayleigh ($ka \ll 1$) and the resonance ($ka \approx 1$) scattering. Hence, the scattering field of the sum-frequency wave should have some distinctive features.

In the second-order approximation, the solution for the sound pressure of the sum-frequency wave has a form similar to that for the difference-frequency wave and consists of four spatial components:

$$P_+^{(2)}(r, \varphi) = P_{+1}^{(2)}(r, \varphi) + P_{+2}^{(2)}(r, \varphi) + P_{+3}^{(2)}(r, \varphi) + P_{+4}^{(2)}(r, \varphi),$$

where the component $P_{+1}^{(2)}(r, \varphi)$ of the total sound pressure of the sum-frequency wave is formed by the interacting incident plane waves of frequencies $\omega_1$ and $\omega_2$, $P_{+2}^{(2)}(r, \varphi)$ and $P_{+3}^{(2)}(r, \varphi)$ are the combination components formed by the incident plane waves and the scattered cylindrical waves, and the term $P_{+4}^{(2)}(r, \varphi)$ represents the contribution of the interacting scattered cylindrical waves of frequencies $\omega_1$ and $\omega_2$.

To reveal the distinctive features of the acoustic field of the sum-frequency wave, we consider the final asymptotic expressions for the spatial components of the total sound pressure. The asymptotic expression for the first component $P_{+1}^{(2)}(r, \varphi)$ is analogous to Eq. (10) from our previous paper [3] with the substitution of the frequency $(\omega_1 + \omega_2)$ and the wave number $k_+$ for $\Omega$ and $k_-$.

Figure 1a shows the scattering diagram for the component $P_{+1}^{(2)}(r, \varphi)$ of the total sound pressure of the sum-frequency wave. This diagram has its main maxima in the forward and backward directions $\varphi = 0°$ and 180°. The shape of the diagram is determined by the behavior of the function $1/(\cos\varphi \pm 1)$, and the exponential factors manifest themselves in the lateral directions.

The asymptotic expressions for the second and third components of the total sound pressure of the sum-frequency wave, $P_{+2}^{(2)}(r, \varphi)$ and $P_{+3}^{(2)}(r, \varphi)$, are described by Eq. (13) from [3]. Analyzing the latter equation, one can see that the shape of the scattering diagrams of these components is determined by the function $1/\cos\varphi$. The corresponding scattering diagram is shown in Fig. 1b. The main maxima occur in the directions $\varphi = \pm 90°$ and 180°, and the field formed by the back-

1063-7710/00/4606-0734$20.00 

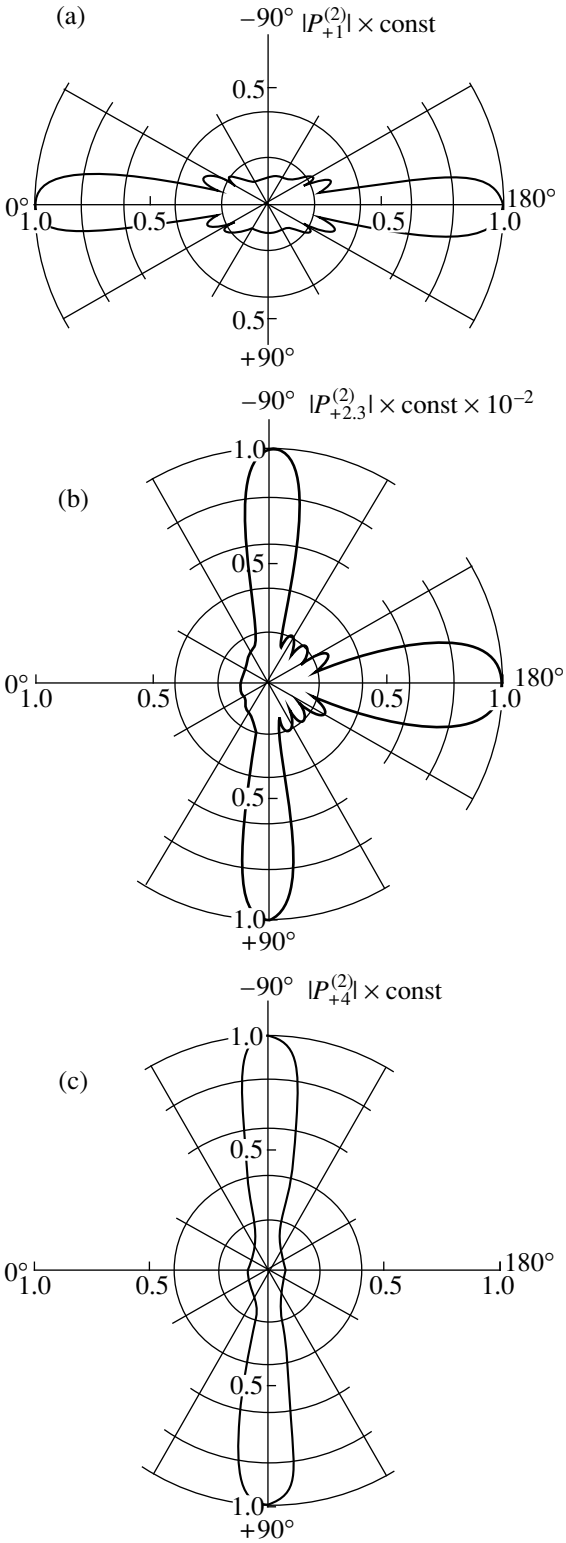


**Fig. 1.** Scattering diagrams of the spatial components (a) $P^{(2)}_{+1}(R, \varphi)$, (b) $P^{(2)}_{+2}(r, \varphi)$ and $P^{(2)}_{+3}(r, \varphi)$, and (c) $P^{(2)}_{+4}(r, \varphi)$ of the total sound pressure of the sum-frequency wave for $f_1$ = 976 kHz, $f_2$ = 1000 kHz, $F_+$ = 1976 kHz, $k_{1,2}a \approx 40$, $k_+a = 83$, $a$ = 0.01 m, and $d$ = 0.22 m.

ward scattering is characterized by a relatively insignificant level. Unlike the case of the difference-frequency wave, the scattering diagram for these components has a maximum in the forward direction.

The fourth component $P^{(2)}_{+4}(r, \varphi)$ of the total sound pressure of the sum-frequency wave is described by Eq. (14) from [3]. The corresponding scattering diagram is shown in Fig. 1c. The shape of the diagram is determined by the function $1/\cos^2\varphi$, which yields two main maxima in the lateral directions $\varphi = \pm 90°$.

Figure 2 presents the scattering diagrams for the total sound pressure of the sum-frequency wave $P^{(2)}_{+}(r, \varphi)$. From these diagrams, one can see that the main maxima occur in the directions $\varphi = 0°$, $\pm 90°$, and 180°, which correspond to the minimal phase differences between the initial high-frequency waves interacting in the cylindrical layer of the medium around the scatterer. An increase in the size of the cylindrical scatterer leads to insignificant changes in the scattering diagram, and an increase in the thickness of the cylindrical layer surrounding the scatterer leads to narrowing of the main maxima because of the increase in the reradiating volume. From the analysis of all spatial components, it follows that the incident plane waves form the scatter-

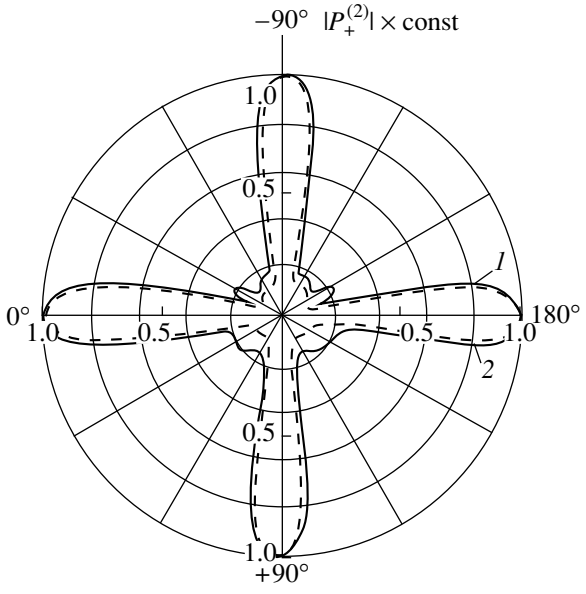


**Fig. 2.** Scattering diagram of the total sound pressure of the sum-frequency wave $P^{(2)}_{+}(r, \varphi)$ for $f_2$ = 1000 kHz; $a$ = 0.01 m; $k_{1,2}a \approx 40$; $f_1$ = (*1*) 976 and (*2*) 880 kHz; $F_+$ = (*1*) 1976 and (*2*) 1880 kHz; $k_+a$ = (*1*) 83 and (*2*) 79; and $d$ = (*1*, solid line) 0.22, (*1*, dashed line) 0.43, (*2*, solid line) 0.20, and (*2*, dashed line) 0.40 m.

ing field in the forward and backward directions and the scattered cylindrical waves form the lateral fields.

## ACKNOWLEDGMENT

I am grateful to N.P. Zagraĭ for supervising this study.

## REFERENCES

1. B. Dubus, A. Lavie, and N. D. Veksler, J. Acoust. Soc. Am. **102**, 3523 (1997).
2. A. Klauson, J. Metsaveer, N. Touraine, *et al.*, in *Proceedings of the 16th International Congress on Acoustics and 135th Meeting of the Acoustical Society of America "Sound Future: Global View of Acoustics of the 21st Century,"* Ed. by P. K. Kuhl and L. A. Crum (Acoustical Society of America, Woodbury, 1998), Prog. V. 1, pp. 575–576.
3. I. B. Abbasov and N. P. Zagraĭ, Akust. Zh. **45**, 590 (1999) [Acoust. Phys. **45**, 523 (1999)].
4. B. K. Novikov, O. V. Rudenko, and V. I. Timoshenko, *Nonlinear Underwater Acoustics* (Sudostroenie, Leningrad, 1981; Acoustical Society of America, New York, 1987).

*Translated by E. Golyamina*

*Acoustical Physics, Vol. 46, No. 6, 2000, pp. 737–739. Translated from Akusticheskiĭ Zhurnal, Vol. 46, No. 6, 2000, pp. 838–840.*


**SHORT COMMUNICATIONS**

# Formation of the Directional Pattern of a Parametric Array

**V. A. Voronin, T. N. Kutsenko, and S. P. Tarasov**

*Taganrog State Radio Engineering University, Nekrasovskiĭ pr. 44, Taganrog, 347928 Russia*

*e-mail: rector@trtu.rnd.su*

Received April 27, 1998

The characteristics of radiating parametric arrays are adequately described by the Khokhlov–Zabolotskaya–Kuznetsov (KZK) equation [1] derived from a nonlinear wave equation. The KZK equation takes into account the parameters of nonlinear interaction of waves and allows one to determine the acoustic field of the difference frequency at any point of space. In papers [2, 3] it is shown that the calculation of the transverse distributions of the field of a parametric array by the formulas derived from the KZK equation agrees well with the results of experimental studies in the chosen frequency band. Although the restrictions used in deriving the equation do not fundamentally affect the results, they somewhat narrow the range of validity of its solution.

Since the acoustic field of difference-frequency waves is formed by the structure of the acoustic field of pump waves, the directional pattern (DP) of a parametric array (PA) is determined by the directivity of the pump array and the length of the region of nonlinear interaction. The most intense generation of difference-frequency waves occurs in the near zone of the pump array. A reduction of the length of the interaction region noticeably affects the directional pattern by making it wider [1, 4]. For a sufficiently narrow directional pattern, i.e., for large wave dimensions of the pump array, a situation may arise when the length of the near zone is greater than the length of the zone of interaction, which usually is determined by the length of the zone of wave attenuation. The accuracy achieved in calculating the directional patterns of such parametric arrays by the existing methods is very low.

In this paper, on the basis of the analysis of nonlinear wave interaction and the antenna theory, we derive an expression for calculating the directional pattern of parametric radiators; we also present the results of calculations by different methods and perform the comparison of the computational results.

To determine the directional pattern of a radiating parametric array, we represent it as a three-dimensional array consisting of sources continuously distributed in the volume and formed at every point of the space as a result of the nonlinear interaction of pump waves. The volume occupied by the sources is determined by the volume of the pump wave interaction. The geometric form of the volume of interaction is sufficiently complex, but it can be described by the diffraction of pump waves and their attenuation.

From the point of view of antenna theory, the directional pattern of a three-dimensional array can be calculated by using the main theorems for the antenna directivity [5]. Thus, a three-dimensional array of secondary sources can be considered as a linear end-fire array, the length of which is limited by the decay of the pump waves due to their attenuation and diffraction [1, 4], with allowance for the increase in the cross section of the region of secondary sources due to the diffraction of pump waves along this linear array. We note that, near the pump transducer, the density of sources of secondary waves is maximal, because, with the distance from the transducer surface, the intensity of pump waves decreases as a result of both attenuation and diffraction.

Figure 1 shows the geometry of the arrangement of secondary sources in the volume of interaction. We consider the directional pattern of the parametric array in the $y$–$z$ plane. Assuming that the transducer is circular, we expect that the DP will be axially symmetric; therefore, in our calculations, a plane circular array will be replaced by an array in the form of a line segment, according to the shift theorem of the antenna theory [5].

The DP of an end-fire array limited by the attenuation in the far-field zone is given by the expression

$$R(\theta) = \frac{\int_0^{l_z} a(z) e^{-ikz(\cos(\theta)-1)} dz}{\int_0^{l_z} a(z) dz}, \qquad (1)$$

where $k = 2\pi/\lambda$ is the wave number of the pump waves; $\lambda = c/f_0$ is the wavelength of the pump waves; $f_0 = (f_1 + f_2)/2$; $l_z$ is the length of the end-fire array, which is equal to the length of the region of interaction of the pump waves $f_1$ and $f_2$; $l_z = 1/\alpha$; $\alpha$ is the coefficient of attenuation of the pump waves in the medium; $c$ is the velocity

1063-7710/00/4606-0737$20.00 

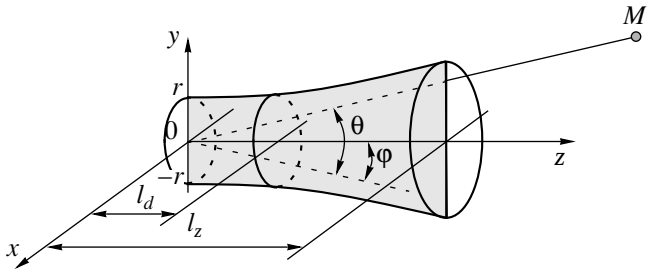


**Fig. 1.** Geometry of a three-dimensional parametric array.

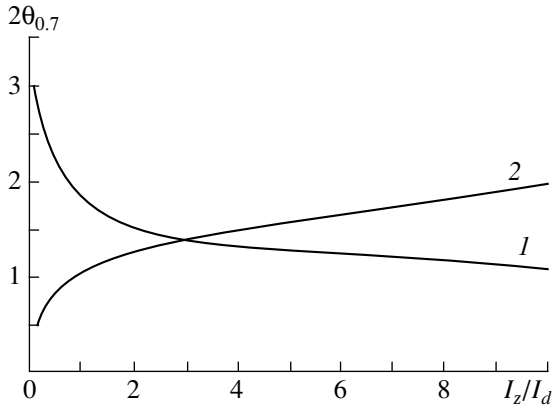


**Fig. 2.** Width of the directional pattern at 0.7 of its maximum as a function of the relative size of the interaction region for (*1*) the parametric array and (*2*) the pump array.

of wave propagation in the medium; and $a(z)$ is the amplitude distribution.

Using the multiplication theorem of the directivity theory, we obtain the expression for the DP of the array in the $y$–$z$ plane:

$$R(\theta) = \frac{\int_0^{l_z} a(z)e^{-ikz(\cos(\theta)-1)}dz \int_{-r(z)}^{r(z)} a(y)e^{-iKy\sin(\theta)}dy}{\int_0^{l_z}\int_{-r(z)}^{r(z)} a(y)a(z)dydz}, \quad (2)$$

where $K$ is the wave number of the difference-frequency wave and $r$ is the radius of the radiating array.

The second integral in Eq. (2) determines the contribution of the transverse aperture of the array to the formation of the DP. The limits of integration should change with the propagation of the pump waves, because $r(z)$ represents the radius of the pump wave beam at a distance $z$ from the surface of the pump transducer. This dimension changes due to the pump wave diffraction according to the law [1]

$$r_1(z) = r\sqrt{1+\left(\frac{z}{l_d}\right)^2},$$

where $l_d$ is the length of the pump wave diffraction zone.

The coefficients of the amplitude distribution, $a(z)$ and $a(y)$, can be determined as follows. The length of the region of interaction is determined by the wave attenuation. Thus, within the length of the attenuation zone $l_z$ determined by the coefficient of attenuation $\alpha$, the level of the generated difference-frequency wave decreases nearly by a factor of 9, and the process of the generation of these waves can be considered as terminated. Therefore, the amplitude distribution $a(z)$ can be defined as

$$a'(z) = e^{-\alpha z}.$$

On the other hand, the diffraction reduces the wave amplitude along the beam by the law

$$a''(z) = a_1\sqrt{1+\left(\frac{z}{l_d}\right)^2}.$$

Thus, assuming that the amplitude distribution across beam is uniform, we obtain the expression for calculating the DP in the form

$$R(\theta) = \left|\frac{\int_0^{l_z}\int_{-r_1(z)}^{r_1(z)} e^{-iKy\sin(\theta)}e^{-ikz(\cos(\theta)-1)-\alpha z}\sqrt{1+\left(\frac{z}{l_d}\right)^2}dydz}{\int_0^{l_z}\int_{-r_1(z)}^{r_1(z)} e^{-\alpha z}\sqrt{1+\left(\frac{z}{l_d}\right)^2}dydz}\right|. \quad (3)$$

Using Eq. (3), we calculate the change in the width of the directional pattern of the parametric array as a function of the ratio of the characteristic dimensions of the interaction region, $l_z/l_d$. Figure 2 shows the dependence of the width of the DP on $l_z/l_d$ calculated by Eq. (3) (curve *1*). Since, in many experimental investigations carried out by the authors, the width of the directional pattern of the pump array was close to the width of the directivity pattern of the parametric radiation, in the same figure we present curve *2*, which illustrates the dependence of the width of the DP of the pump array on the same parameters.

The analysis of these dependences shows that, for large ratios $l_z/l_d$, the width of the DP of the parametric array is determined only by the length of the region of interaction of the pump waves, $l_z$, and is close to the width of the directional pattern of the pump array.

For the values $l_z < l_d$, the DP of the parametric array broadens and it can become much wider than the directional pattern of the pump radiator.

Thus, when designing radiating parametric arrays with narrow directional patterns, it is necessary to keep in mind that the efforts to make a narrow DP through increasing the size of the pump transducer may lead to the situation when the length of the diffraction zone

exceeds the length of the attenuation zone, and the expected decrease in the width of the DP of the parametric array will not be achieved.

## ACKNOWLEDGMENTS

This work was supported by the Russian Foundation for Basic Research, project no. 96-02-16312.

## REFERENCES

1. B. K. Novikov, O. V. Rudenko, and V. I. Timoshenko, *Nonlinear Underwater Acoustics* (Sudostroenie, Leningrad, 1981; Acoustical Society of America, New York, 1987).
2. B. Ward, A. C. Baker, and V. F. Humphrey, J. Acoust. Soc. Am. **101**, 143 (1997).
3. B. Ward, A. C. Baker, and V. F. Humphrey, in *Proceedings of the 1st World Congress on Ultrasonics, Berlin, 1995*, pp. 965–968.
4. B. K. Novikov and V. I. Timoshenko, *Parametric Arrays in Underwater Detection and Ranging* (Sudostroenie, Leningrad, 1990).
5. M. D. Smaryshev and Yu. Yu. Dobrovol'skiĭ, *Hydroacoustic Arrays: Computation of Directional Properties of Hydroacoustic Arrays: A Handbook* (Sudostroenie, Leningrad, 1984).

*Translated by A. Svechnikov*

*Acoustical Physics, Vol. 46, No. 6, 2000, pp. 740–742. Translated from Akusticheskiĭ Zhurnal, Vol. 46, No. 6, 2000, pp. 841–843.*


**SHORT COMMUNICATIONS**

# Time Dependence of the Intensity of High-Frequency Surface Prereverberation of Sound in the Ocean

**Yu. P. Lysanov and V. M. Frolov**

*Andreev Acoustics Institute, Russian Academy of Sciences, ul. Shvernika 4, Moscow, 117036 Russia*

*e-mail: bvp@akin.ru*

Received March 9, 2000

In papers [1, 2], experimental data on sound prereverberation in the deep ocean are presented and a simple ray model of surface prereverberation is suggested. The kinematic characteristics, such as prereverberation times and their dependence on grazing angles and the number of ray reflections from the rough sea surface, were estimated. The calculated characteristics fit well the experimental data. However, the time dependence of the intensity of the surface prereverberation was not studied. Below, this problem is solved in the ray approximation; i.e., the reradiation of high-frequency sound incident on the rough ocean surface is considered as specular reflection from plane surface segments with different slope angles.

In the framework of the ray theory, a convenient measure of the surface prereverberation intensity (SPI) is the ratio of the intensity of scattered sound, which causes surface prereverberation, to the intensity of sound specularly reflected from a plane surface segment. In this paper, a simple method is suggested to estimate this quantity for the case of high-frequency sound prereverberation in a subsurface oceanic sound channel. The method is based on the idea that the grazing angles of sound waves scattered by the rough sea surface are statistically distributed, which is related to the statistical distribution of the slope angles of the surface waves. In a rather good approximation, we can assume that the slope angles of the wind waves are distributed according to the normal law and described by the one-dimensional Gaussian probability density

$$P(\delta) = \frac{1}{\sqrt{2\pi}\delta_0}\exp\left(-\frac{\delta^2}{2\delta_0^2}\right), \qquad (1)$$

where $\delta$ is the slope angle of wind waves and $\delta_0$ is the rms slope angle. The value $\delta_0$ (in radians) can be calculated from the frequency spectrum $S(\Omega)$ of isotropic wind waves:

$$\delta_0^2 \approx \frac{1}{g^2}\int_0^{\Omega_k}\Omega^4 S(\Omega)\,d\Omega,$$

where $\Omega_k$ is the cut-off frequency of the spectrum. For estimating $\delta_0$, we take the Pierson–Neumann frequency spectrum that is expressed by the formula

$$S(\Omega) = C\Omega^{-6}\exp\left[-2\left(\frac{g}{\Omega v}\right)^2\right],$$

where $C = 2.4$ m$^2$/s$^5$, $g = 9.81$ m/s$^2$, and $v$ is the wind speed in m/s. Then, for $\delta_0$, we obtain

$$\delta_0^2 \approx 1.6\times 10^{-3} v[1 - \Phi(\sqrt{6}\Omega_0/\Omega_k)], \qquad (2)$$

where $\Omega_0 = \sqrt{\frac{2}{3}}\frac{g}{v}$ is the frequency corresponding to the maximum of the spectrum and $\Phi(z) = \frac{2}{\sqrt{2\pi}}\int_0^z e^{-\frac{t^2}{2}}dt$ is the probability integral.

The maximum of the scattering pattern for high-frequency sound corresponds to the direction of the specular reflection, and, therefore, the greater the deviation of the grazing angle of a scattered wave is from the specular direction, the smaller the intensity of this wave is. Therefore, in the scattering process, the main role belongs to sloping surface waves with frequencies that are relatively close to that of the spectral maximum. For example, for a wind speed of 10 m/s, from formula (2), we obtain $\delta_0 = 0.87°$ for $\Omega_k = \Omega_0$ and $\delta_0 = 3.4°$ for $\Omega_k = 2\Omega_0$.

The method of the SPI calculation is demonstrated by an example of single reflection of sound from the rough sea surface in the surface oceanic channel in which the sound velocity varies with depth $z$ as $c = c_0(1 + az)$. Let a point sound source and a receiver be located near the surface at a distance $r$ from each other. In the case of a plane surface, a ray will be reflected from the surface at the distance $r/2$ from the source and arrive at the receiver. However, for a rough surface, it is easy to find other surface segments from which the reflection also contributes to the intensity of the received signal. The slope of these segments should be nonzero and be greater, the farther the segment from the specular point is.

1063-7710/00/4606-0740$20.00 

In a stratified medium, the sound intensity corresponding to a given ray is determined as follows (see, e.g., [3])

$$I = \frac{W\cos\chi_1}{4\pi r\sin\chi_2|\partial r/\partial\chi_1|},$$

where $W$ is the acoustic power generated by the source, $\chi_1$ and $\chi_2$ are the ray grazing angles at the source and at the point of reception, respectively, and $r$ is the horizontal distance between the source and the receiver.

Taking into account that the sound source is located near a statistically rough surface and the sound wave, after its refraction in the water layer, is reflected from a plane surface segment with the slope angle $\delta$, we obtain the following expression for the sound intensity propagating along the ray:

$$I = \frac{W\cos\chi_1 P(\delta)}{2\pi r\sin\chi_2|\partial r/\partial\chi_1|}.$$

Here, $P(\delta)$ is the probability density of the rough surface slopes, $r = r_1 + r_2 = 2(\tan\chi_1 + \tan\chi_2)/a$, and $r_1$ and $r_2$ are the ray cycle lengths before and after reflection from the surface. The grazing angle of a ray reflected from an inclined surface segment is $\chi_2 = \chi_1 + 2\delta$.

For a ray reflected from a segment with zero slope, the sound intensity is

$$I = \frac{W\cos\chi_0 P(0)}{2\pi r\sin\chi_0|\partial r/\partial\chi_0|},$$

where $\chi_0$ is the ray grazing angle at the source and the receiver.

Now, the relative intensity of the prereverberation signal can be calculated by the formula

$$\frac{I}{I_0} = \frac{P(\delta)}{P(0)}\frac{\cos\chi_1\tan\chi_0}{\sin\chi_2}\left|\frac{\partial r/\partial\chi_0}{\partial r/\partial\chi_1}\right|. \quad (3)$$

The relation between the grazing angles $\chi_1$, $\chi_2$, and the slope angle $\delta$ of the surface segment can be found by using two equalities: $\chi_2 - \chi_1 = 2\delta$ and $2(\tan\chi_1 + \tan\chi_2) = ar$. Using the smallness of these angles, we obtain the approximate values $\chi_1 \approx \chi_0 - \delta$ and $\chi_2 \approx \chi_0 + \delta$. Expanding all factors on the right-hand side of formula (3), except for $P(\delta)$, in powers of $\delta$ and $\chi_0$ and retaining only the first-order terms, we arrive at the expression

$$\frac{I}{I_0} = \frac{P(\delta)}{P(0)}\left(1 - \frac{\delta}{\chi_0}\right) = \exp\left(-\frac{\delta^2}{2\delta_0^2}\right)\left(1 - \frac{\delta}{\chi_0}\right). \quad (4)$$

Note that this result can also be obtained if, instead of the probability density of slopes of the rough sea surface in formula (3), we use the scattering coefficient calculated in a high-frequency approximation, this coefficient also being determined only by the statistics of the slopes.

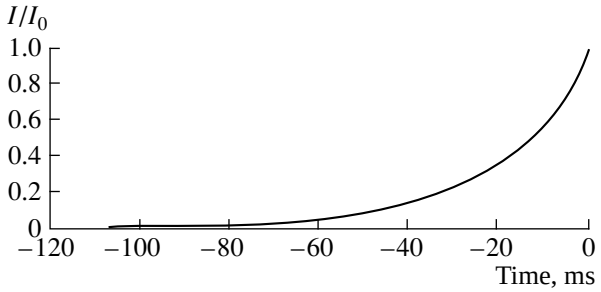


Time dependence of the relative intensity of a high-frequency prereverberation (the instant $t = 0$ corresponds to the signal arrival along the specular ray).

The prereverberation time, i.e., the difference in the propagation times of a signal over specular and prereverberation rays, is determined by the formula from [4], which in our case takes the form

$$\Delta t = r\delta^2/2c_0. \quad (5)$$

Thus, the parameter $\delta$ relates the time to the prereverberation intensity; i.e., the time dependence of the relative intensity of the prereverberation is determined by formula (4), where $\delta = \sqrt{\dfrac{2c_0\Delta t}{r}}$.

The limiting angle of the slope of a surface segment, which restricts the prereverberation time, is the angle $\delta_m$ corresponding to the grazing angle $\chi_2 = \chi_m \approx \sqrt{2aH}$. The segments with slope angles $\delta > \delta_m$ reflect the rays so that the latter suffer reflection from the bottom. In calculating the SPI, these rays can be neglected because of their strong attenuation in the bottom.

We calculate now the dependence of the SPI on the prereverberation time for the following values of the parameters: $c_0 = 1.45$ km/s, $a = 1.1 \times 10^{-2}$ 1/km, $H = 5$ km, $r = 100$ km, and $\delta_0 = 1°$. In this case, the maximal grazing angle is $\chi_m = 18.6°$, which corresponds to the maximal slope angle $\delta_m = 3.3°$; the corresponding maximal prereverberation time is $\Delta t_m = 115$ ms. The figure shows the dependence of the ratio $I/I_0$ calculated by formulas (4) and (5) on the parameter $\Delta t$. The comparison between this plot and the experimental dependence of the sound pressure on the prereverberation time [1] allows one to explain the increase in the intensity of the prereverberation signal.

The simple ray method suggested here for calculating the intensity distribution over the scattered rays can find applications not only for the case of surface prereverberation, but for other problems where the sound scattering from a rough sea surface is involved.

## ACKNOWLEDGMENTS

We are grateful to E.A. Kopyl for useful discussions. This work was supported by the Russian Foundation for Basic Research, project no. 98-05-64302.

## REFERENCES

1. N. V. Studenichnik, in *Proceedings of the IX All-Union Acoustical Conference* (AKIN, Moscow, 1977), Sect. D, p. 45.
2. L. M. Brekhovskikh, Yu. P. Lysanov, and N. V. Studenichnik, Dokl. Akad. Nauk SSSR **239** (1), 211 (1978).
3. L. M. Brekhovskikh and O. F. Godin, *Acoustics of Layered Media II: Point Sources and Bounded Beams* (Springer, Berlin, 1999).
4. V. S. Gostev and R. F. Shvachko, in *Ocean Acoustics: Proceedings of the School–Seminar of Academician L. M. Brekhovskikh* (GEOS, Moscow, 1998), pp. 62–66.

*Translated by Yu. Lysanov*

*Acoustical Physics, Vol. 46, No. 6, 2000, pp. 743–745. Translated from Akusticheskiĭ Zhurnal, Vol. 46, No. 6, 2000, pp. 844–846.*


**SHORT COMMUNICATIONS**

# Vibrations of a Thin Bounded Plate Excited by Modulated Laser Radiation

**M. L. Lyamshev**

*Wave Research Center, General Physics Institute, Russian Academy of Sciences, ul. Vavilova 38, Moscow, 117942 Russia*

*e-mail: lyamshev@kapella.gpi.ru*

Received June 29, 2000

Vibrations of a thin bounded plate excited by harmonically modulated laser radiation may be relevant to remote laser optoacoustic diagnostics of materials, especially under the conditions when conventional contact methods of acoustic diagnostics are inapplicable (e.g., at high temperatures or in an aggressive environment). Investigations of the mechanisms of the interaction between laser radiation and a substance are also frequently conducted using target samples in the form of bounded plates. The characteristic features of their vibrations can provide useful information on the physical processes in the plates [1, 2].

Let a laser beam harmonically modulated in intensity be incident vertically upon the surface of a thin bounded plate. We consider flexural oscillations of the thin plate. For the plate displacements $w(r)$, we can write the equation [3]

$$\left(g\Delta^2 + m_s\frac{\partial^2}{\partial t^2}\right)w(r) = F(r). \quad (1)$$

In the case of harmonic oscillations, the equation takes on the form

$$(\Delta^2 - k^4)w(r) = \frac{F(r)}{g}, \quad (2)$$

where

$$\Delta = \partial^2/\partial x^2 + \partial^2/\partial y^2 + \partial^2/\partial t^2, r(x, y),$$

$$g = \frac{Eh^3}{3(1-\nu^2)},$$

$g$ is the flexural rigidity, $m_s = \rho h$ is the plate mass per unit area, $F(r)$ is the function characterizing the external dynamic force due to the effect of laser radiation incident on the plate, $k^4 = [3\omega^2\rho(1 - \nu^2)]/Eh^2$, $\omega$ is the circular frequency of modulation of the laser radiation intensity, $\rho$ is the density, $\nu$ is Poisson's ratio, $E$ is Young's modulus, and $h$ is the plate thickness.

We write the solution to Eq. (2) in the form

$$w(r) = \int_s F(r_0)G(r_0/r)ds(r_0), \quad (3)$$

where $G(r_0/r)$ is the Green's function that represents the solution to the equation

$$(\Delta^2 - k^4)G(r_0/r) = -\delta(r_0 - r) \quad (4)$$

and obeys the boundary conditions or the conditions of fixation at the plate edge.

Using a standard procedure for solving Eq. (4), we obtain [4]

$$G(r_0/r) = \sum_{m,n}\frac{\Psi_{mn}(r_0)\Psi_{mn}(r)}{k_{mn}^4 - k^4}, \quad (5)$$

where $\Psi_{mn}(r)$ are the normalized eigenfunctions of plate vibrations, which satisfy the equation

$$(\Delta^2 - k_{mn}^4)\Psi_{mn}(r) = 0, \quad (6)$$

the boundary conditions, and the normalization conditions

$$\int_S \Psi_{mn}(r)\Psi_{kl}(r)ds(r) = \delta_{mnkl},$$

where $\delta_{mnkl}$ is the Kronecker delta.

Let us write an expression for the function $F(r)$ characterizing the external force acting on the plate. We consider the thermoelastic (thermooptical) mechanism of the laser excitation of plate vibrations.

We assume that the plate is opaque to laser radiation, and the latter is absorbed in a thin surface layer whose thickness is much less than the plate thickness. In this case, for $F(r)$, we obtain the expression [5]

$$F(r) = -\frac{E\alpha\mu m}{C_p}J_0 f(r)\exp(-i\omega t), \quad (7)$$

where $J_0$ is the intensity; $f(r)$ is the function characterizing the distribution of the laser radiation intensity over the plate surface; $\alpha$ is the coefficient of cubic thermal expansion; $C_p$ is the specific heat of the plate material; $\mu$ is the absorption coefficient characterizing the absorption of laser radiation in the plate material; $m$ is the modulation coefficient characterizing the intensity

1063-7710/00/4606-0743$20.00 

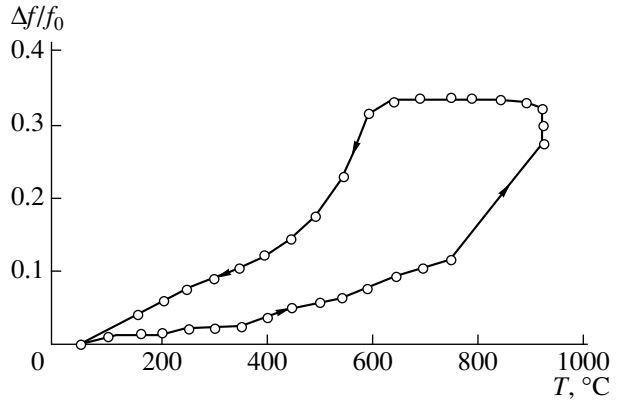


**Fig. 1.** Temperature dependence of the normalized fundamental resonance frequency $\Delta f/f_0$ of a silicon oxide ceramic plate [2].

modulation laser radiation, $0 \le m \le 1$; and $\exp(-i\omega t)$ is the time factor, which is omitted everywhere in our calculations.

In most cases, the samples used for laser optoacoustic diagnostics and for studying the interaction of laser radiation with a substance have the form of rectangular or circular plates, and the distribution of the radiation intensity in the laser beam has a Gaussian form [1, 2].

Let us consider vibrations of a circular plate. We can write down the following expression for the intensity of laser radiation:

$$f(r) = \exp\left(-\frac{r^2}{a_0^2}\right), \tag{8}$$

where $a_0$ is the radius of the laser beam.

Only axially symmetric vibrations are excited in the plate. Let us first assume that the plate edges are fixed, though, in the experiment, they may be free or fixed with a joint (supported). The selection of the boundary conditions does not restrict the generality of our consideration and conclusions. The normalized eigenfunctions for the vibrations of a fixed circular plate in the case of axially symmetric vibrations have the form [4]

$$\Psi_n(r) = \frac{1}{a\sqrt{\pi\Lambda_n}}\left[J_0\left(\frac{\pi\beta_n r}{a}\right) - \frac{J_0(\pi\beta_n)}{I(\pi\beta_n)} I\left(\frac{\pi\beta_n r}{a}\right)\right], \tag{9}$$

where $\Lambda_n = 2\{[J_0(\pi\beta_n)]^2 + [J_0'(\pi\beta_n)]^2\}$, $J_0'(u) = \frac{\partial}{\partial u} J_0(u)$, $\beta_1 = 1.015$, $\beta_2 = 2.007$, $\beta_3 = 3.000$, and $\beta_n \longrightarrow n$ when $n \longrightarrow \infty$.

Using Eqs. (3) and (5)–(9), we obtain an expression for the plate displacements:

$$w(r) = \frac{3(1-\nu^2)\alpha\mu m}{\pi a^2 h^3 \rho C_p} J_0$$

$$\times \sum_{n=1}^{\infty} \frac{\left[J_0\left(\frac{\pi\beta_n r}{a}\right) - \frac{J_0(\pi\beta_n)}{I_0(\pi\beta_n)} I_0\left(\frac{\pi\beta_n r}{a}\right)\right]}{\Lambda_n(k_n^4 - k^4)} \tag{10}$$

$$\times \int_0^{2\pi} d\varphi \int_0^a \left[J_0\left(\frac{\pi\beta_n r_0}{a}\right) - \frac{J_0(\pi\beta_n r_0)}{I\left(\frac{\pi\beta_n r_0}{a}\right)} I\left(\frac{\pi\beta_n r}{a}\right)\right] r_0 dr_0.$$

Performing the integration, we obtain

$$w(r) = \frac{3(1-\nu^2)\alpha\mu m a_0^2}{a^2 h^3 \rho C_p} J_0 \sum_{n=1}^{\infty} \frac{1}{\Lambda_n(k_n^4 - k^4)}$$

$$\times \left[\exp\left(\frac{-\pi^2\beta_n^2 a_0^2}{4a^2}\right) - \frac{J_0(\pi\beta_n)}{I_0(\pi\beta_n)} \exp\left(\frac{\pi^2\beta_n^2 a_0^2}{4a^2}\right)\right] \tag{11}$$

$$\times \left[J_0\left(\frac{\pi\beta_n r}{a}\right) - \frac{J_0(\pi\beta_n)}{I_0(\pi\rho_n)} I_0\left(\frac{\pi\beta_n r}{a}\right)\right].$$

Now, let us consider Eq. (11). First of all, one can see that, when the modulation frequency of laser radiation $\omega$ coincides with some frequency of natural oscillations of the plate $\omega_n$, the resonance of oscillations is observed and the plate performs intense vibrations corresponding to the resonance of a normal mode. Indeed, the condition for the resonance follows from the equality $k^4 - k_n^4 = (k^2 + k_n^2)(k^2 - k_n^2) = 0$. From the condition $k^2 - k_n^2 = 0$, it follows that $\omega = \omega_n$, where, for $\omega_n$, the following expression corresponding to the functions $\Psi_n(r)$ is valid [see Eq. (9)] [4]:

$$\omega_n = \frac{\pi h}{2a^2}\sqrt{\frac{E\beta_n^2}{3\rho(1-\nu^2)}}. \tag{12}$$

Now let us turn our attention to the possibility of using the results obtained above for, e.g., remote laser optoacoustic diagnostics of materials.

Figure 1 demonstrates the experimental temperature dependence of the fundamental eigenfrequency of vibrations of a circular ceramic plate [2]. The experiments were conducted using a remote laser excitation and sensing for the plate oscillations. If we assume that the parameters of the plate $h$, $a$, and $\rho$ do not depend on temperature in the experimental conditions, then, the given dependence characterizes the temperature variations of the Young's modulus of the ceramic plate [see Eq. (12)]. The hysteresis of the temperature dependence of the eigenfrequency of plate vibrations attracts one's attention. Such a hysteresis can be explained if we take into consideration the specific features of the internal structure of ceramic materials. Ceramics are often considered as consisting of a matrix (host material) and strengthening particles, i.e., grains of some

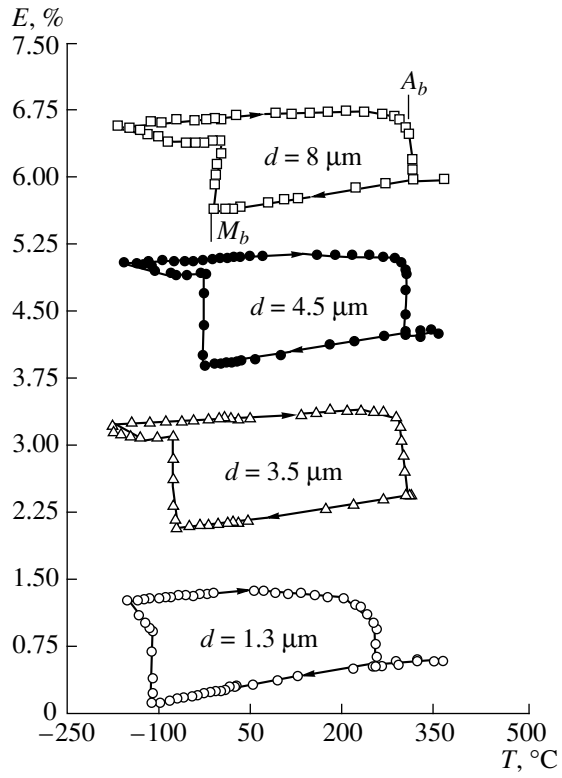


**Fig. 2.** Temperature dependence of the thermal expansion ε (in percent) of the Ce–TZP ceramics. The parameter is the size of strengthening grains *d*. The arrows indicate the direction of the temperature cycle [7].

other material [6, 7]. As the temperature changes, internal thermal strains arise in the ceramics:

$$\varepsilon_{\pm}^{T} = (\alpha_m - \alpha_f)\Delta T, \tag{13}$$

where $\alpha_m$ and $\alpha_f$ are the coefficients of thermal expansion of the materials of the matrix and the grains and $\Delta T$ is the temperature variation. Internal strains are accompanied by internal stresses, which leads to changes in the material rigidity, i.e., in Young's modulus.

The temperature dependence of the thermal expansion of Ce–TZP ceramics is shown in Fig. 2 as an illustration. The parameter is the size of grains *d* [7]. According to Hannin and Swain [7], the temperature hysteresis of thermal expansion is connected with the concentration of local stresses at the boundary of grains (particles) in the matrix (in ceramics) under the effect of temperature.

Measurements of the amplitude of plate vibrations at resonance frequencies and the shift of the eigenfrequency of vibrations can also provide an opportunity to estimate the value and the temperature variations of the Gruneisen parameter $\Gamma(T)$ of the plate material:

$$\Gamma(T) = \frac{\alpha c^2(T)}{C_p}, \tag{14}$$

where $C^2(T) = E(T)/\rho$.

## ACKNOWLEDGMENTS

This work was supported by the Russian Foundation for Basic Research, project no. 99-02-16334, and by INTAS, project no. 97-31680.

## REFERENCES

1. M. Tyunina and S. Leppävuori, J. Appl. Phys. **87**, 8132 (2000).
2. G. Busse, M. L. Lyamshev, and J. Stanullo, Akust. Zh. **42**, 35 (1996) [Acoust. Phys. **42**, 28 (1996)].
3. P. M. Morse, *Vibration and Sound* (McGraw-Hill, New York, 1936, 1st ed.; GITTL, Moscow, 1949).
4. P. M. Morse and K. U. Ingard, *Theoretical Acoustics* (McGraw-Hill, New York, 1968).
5. L. M. Lyamshev, *Thermooptic Laser Excitation of Sound* (Nauka, Moscow, 1989).
6. D. S. Kupperman, Annu. Rev. Mater. Sci. **24**, 265 (1994).
7. R. H. J. Hannin and M. V. Swain, Annu. Rev. Mater. Sci. **24**, 359 (1994).

*Translated by M. Lyamshev*

*Acoustical Physics, Vol. 46, No. 6, 2000, pp. 746–748. Translated from Akusticheskiĭ Zhurnal, Vol. 46, No. 6, 2000, pp. 847–849.*


**SHORT COMMUNICATIONS**

# Radiation Power in the Case of the Parametric Phase Conjugation of Ultrasound in a Magnet

**V. L. Preobrazhenskiĭ**

*Wave Research Center, General Physics Institute, Russian Academy of Sciences, ul. Vavilova 38, Moscow, 117942 Russia*

*e-mail: preobr@orc.ru*

Received November 4, 1999

The interest in the problem of phase conjugation of ultrasound has noticeably increased in the last few years, which is caused by the recent progress in the experimental techniques used for the generation of phase-conjugate acoustic beams [1–3]. Multichannel electronic systems of time inversion on the basis of matrix electroacoustic transducers [1] and distributed parametric systems of phase conjugation on the basis of piezoelectric and magnetoacoustic ceramics [2, 3] have acquired practical importance. One of the advantages of magnetoacoustic systems of phase conjugation is the practical opportunity to realize the overthreshold conditions of giant amplification of a conjugate ultrasonic wave [4]. A parametric amplifier of sound in the overthreshold mode of operation is a source of coherent stimulated radiation of phase-conjugate phonon pairs.

High quality of reproduction of the wave field of quasi-plane and focused beams in solids and liquids, compensation of phase distortions of waves, self-focusing of conjugate beams to regular and random objects, and other effects typical of phase conjugation have been demonstrated in numerous experiments on the overthreshold phase conjugation [2, 5].

The giant amplification facilitates the development of nonlinear phenomena in the process of the propagation of conjugate waves, including the formation of shock wave fronts [6]. Conjugate acoustic beams of high intensity may find application in high-intensity ultrasonic technologies, engineering, and medicine. In this connection, the analysis of the factors determining the fundamentally attainable intensity levels in the case of the parametric phase conjugation is of interest. Many researchers studied the contributions of various nonlinear mechanisms to the limitation of amplitude in overthreshold amplification of a phase-conjugate wave [7, 8]. Comparison of the theoretical and experimental results on the amplification dynamics in magnetic ceramics [7] provided an opportunity to single out the inverse effect of the generated waves on pumping (the so-called pumping depletion) as the main mechanism.

The propose of this study is the calculation of the limiting radiation power in the case of the acoustic phase conjugation in a system consisting of an electromagnetic pumping source and a parametrically active magnetic medium. The relation between the limiting output acoustic power and the main parameters of the active medium, the pumping source, and their electromagnetic matching circuits is determined.

Let us consider a magnetoacoustically-active medium with the matrix of elasticity moduli $C_{ik;\,lm}(H)$ depending on the magnetic field strength $H$. The parametric interaction of acoustic waves is accompanied by nonlinear oscillations of magnetization in the medium, which are described by the expression

$$m = -\frac{1}{2\mu_0}(\partial/\partial H)C_{ik;\,lm}(H)u_{ik}u_{lm}, \qquad (1)$$

where $u_{ik}$ is the elastic deformation tensor and $\mu_0$ is the magnetic permeability of a vacuum. Without essential limitation of generality, we consider the interaction of a pair of quasi-plane waves of finite aperture with the amplitudes $A$ and $B$ and frequency $\omega_k$ propagating toward each other. In this case, the quasi-homogeneous part of the magnetization oscillations with the pumping frequency $2\omega_k$ is described by the next relationship following from expression (1):

$$m = -2i\rho\nu(\partial\nu/\partial H)k^2AB\exp(2i\omega_k t) + \text{c.c.}, \qquad (2)$$

where $\nu$ is the wave velocity, $\rho$ is the density of the medium, and $k$ is the wave number.

In conformity with the common experimental conditions of parallel pumping [4, 5], we assume that the active medium is placed into an inductance coil with the axis $x$ parallel to the bias field. The amplitude of the alternating voltage of frequency $2\omega_k$ induced by sound in the coil can be represented with the help of expression (2) in the form

$$U = 2i\omega_k L(1 - iQ^{-1})J_p + (4W/l)\omega_k\rho\nu(\partial\nu/\partial H)k^2\int dVAB, \qquad (3)$$

1063-7710/00/4606-0746$20.00 

where $L$, $Q$, $W$, $l$, and $V$ are the inductance, quality factor, number of coils, length, and volume of the coil, respectively, and $J_p$ is the pumping current in the coil in the presence of parametrically coupled waves.

If the parameters of the pumping source are preset (i.e., in the case of a fixed rated voltage $U_0$ and a complex internal resistance $Z_0$), the current $J_p$ and the voltage $U$ vary as the functions of the level of the intensity of the amplified waves. Using equality (3), the law of the pumping current variation can be represented in the form

$$J_p = J_p^0 - (1/SW\mu_0\mu)\rho(\partial\nu^2/\partial H)k^2\zeta\int dVAB, \quad (4)$$

where $\mu$ is the magnetic permeability of the medium and $\zeta$ is the parameter of matching of the pumping source with the active element. The latter quantity is equal to

$$\zeta = 2\omega_k L(Z_0 + Z_2)/\Delta, \quad (5)$$

where

$$\Delta = (2i\omega_k L + Z_1)(Z_0 + Z_2) + Z_0 Z_2 \quad (6)$$

and $Z_1$ and $Z_2$ are the impedances of the series (with respect to the coil) and parallel branches of the matching circuit, respectively. In the case of a negligibly small inverse effect of the generated sound on pumping (in particular, at the initial stage of the amplification process), the rated current $J_p^0$ in the coil is equal to

$$J_p^0 = U_0 Z_2/\Delta. \quad (7)$$

The slowly varying amplitudes of the parametrically coupled waves are described by a known set of equations [9]

$$\begin{aligned}(\partial/\partial t + \nu\partial/\partial x)A &= h_p B^*,\\ (\partial/\partial t - \nu\partial/\partial x)B^* &= h_p^* A,\end{aligned} \quad (8)$$

where $h_p$ is the pumping parameter proportional to the current in the coil:

$$h_p = \omega_k \frac{W}{l}\left(\frac{1}{\nu}\frac{\partial\nu}{\partial H}\right)J_p. \quad (9)$$

In the process of the amplification, the pumping current decreases from its rated value $|J_p^0|$ down to the critical value $J_c$ corresponding to the threshold of absolute parametric instability. In this case, the magnitude of the pumping parameter becomes equal to $|h_p| = \nu\pi/2l$ and the amplitudes of waves attain their stationary level. The output acoustic power $P_a$ radiated by a conjugate wave in the stationary mode and the integral in expression (4) are connected by a relationship following from system (8) (at $\partial/\partial t = 0$):

$$P_a = 4\rho\nu k^2 h_p^* \int dVAB. \quad (10)$$

Using equalities (4), (9), and (10), it is possible to express the radiation power through the characteristic values of the pumping current

$$P_a = (2\omega_k L/\zeta)(J_p^0 J_p^* - |J_p|^2). \quad (11)$$

The phase shift between the rated and stationary currents that occurs in the process of the sound amplitude growth is determined by the phase $\varphi$ of the complex parameter of matching $\zeta$. Taking into account the condition of a steady state $|J_p| = J_c$, it is possible to represent the output power in the final form

$$\begin{aligned}P_a &= (2\omega_k L/|\zeta|)\\ &\times J_c[(|J_p^0|^2 - J_c^2\sin^2\varphi)^{1/2} - J_c\cos\varphi].\end{aligned} \quad (12)$$

Expression (12) relates the output power radiated by a conjugate wave to the electric parameters of the pumping circuit and to the properties of the active medium. In addition, according to expression (9), the sensitivity of the sound velocity to variations in the magnetic field strength determines the critical current $J_c$ and the complex magnetic permeability determines the inductance and the quality factor of the pumping coil.

The parameter of electric matching affects both the dynamics of the parametric amplification and the attainable level of the acoustic power.

For definiteness, we consider a pumping source with an active internal resistance ($Z_0 = R_0$) connected with the pumping coil through a capacitive matching circuit ($Z_{1,2} = -i/2\omega_k C_{1,2}$). It is possible to demonstrate that the optimal detuning of the series $LC_1$-link with respect to the resonance at the frequency $2\omega_k$ corresponds to the maximal current $J_p^0 = U_0\zeta/2\omega_k\eta$, where $\eta = 1 + (2R_0\omega_k C_2)^2$, and, in this case, the matching parameter turns out to be real ($\varphi = 0$): $\zeta^1 = Q^{-1} + R_0/2\omega_k L\eta$. The phase of the pumping current at a real $\zeta$ does not change in the process of amplification, and the parametric interaction renormalizes the current amplitude only. The output power in the case under consideration is equal to

$$P_a = (R_0\eta^{-1} + 2\omega_k L Q^{-1})J_c(|J_p^0| - J_c), \quad (13)$$

where

$$|J_p^0| = |U_0|/(R_0\eta^{-1} + 2\omega_k L Q^{-1})\eta^{1/2}. \quad (14)$$

It follows from expression (13) that, in the case of fixed parameters of the pumping source and matching circuits, the maximal power is radiated at the optimal parametric coupling corresponding to the supercritical conditions $\beta \equiv |J_p^0|/J_c = 2$. The quantity $P_a^{\max}$ is expressed by the formula

$$P_a^{\max} = P_e R_0/2(R_0 + 2\omega_k L\eta Q^{-1}), \quad (15)$$

where $P_e = U_0^2/2R_0$ is the electric power, which can be given out by this source in a matched resistive load.

Thus, under the optimal conditions, the power of radiation into a conjugate wave does not exceed $0.5P_e$ and tends to this limiting value in the case of a high enough quality of the pumping circuit $Q \gg 2\omega_k L\eta/R_0$.

Expression (13) allows us to estimate the radiated power from the data of electric measurements. For example, in the case of typical values of the parameters ($|J_p^0| = 20$ A, $R_0 = 3\ \Omega$, $2\omega_k L = 120\ \Omega$, $Q = 100$, $\beta = 2$, and $\eta \cong 1$), it constitutes $P_a \cong 360$ W, which agrees well with the experimental data on the intensity of radiation into a solid medium [4]. If a phase-conjugate wave is radiated into a liquid [6], the measured intensity is considerably lower because of the reflection loss at the magnet–liquid interface. An additional factor reducing the output power can be the competition of the signal and noise modes within the range of parametric amplification [7]. This factor manifests itself most strongly in the case of relatively low levels of the wave intensity at the active medium input, which is typical of the experiments on phase conjugation of sound in liquids.

In closing, we note that the results obtained above by calculating the radiation power in the case of the parametric phase conjugation in a magnet demonstrate a potentially high efficiency of the ultrasonic wave conversion in the overthreshold mode of amplification. With the attainable levels of the pumping power and the optimal matching of the generator with the active medium, the intensity of the phase-conjugate waves can reach tens of watts per square centimeter, which is of interest from the point of view of various applications in technology and medicine.

## ACKNOWLEDGMENTS

This work was supported by the Russian Foundation for Basic Research, project no. 98-02-16761.

## REFERENCES

1. M. Fink, IEEE Trans. Ultrason. Ferroelectr. Freq. Control **39**, 555 (1992); Phys. Today **50**, 34 (1997).
2. A. P. Brysev, L. M. Krutyanskiĭ, and V. L. Preobrazhenskiĭ, Usp. Fiz. Nauk **168**, 877 (1998) [Phys. Usp. **41**, 793 (1998)].
3. M. Ohno and K. Takagi, Appl. Phys. Lett. **69**, 3483 (1996).
4. A. P. Brysev, F. V. Bunkin, D. V. Vlasov, *et al.*, Akust. Zh. **34**, 986 (1988) [Sov. Phys. Acoust. **34**, 567 (1988)].
5. A. P. Brysev, F. V. Bunkin, L. M. Krutyanskiĭ, and A. D. Stakhovskiĭ, Izv. Akad. Nauk, Ser. Fiz. **60**, 117 (1996).
6. A. P. Brysev, F. V. Bunkin, M. F. Hamilton, *et al.*, Akust. Zh. **44**, 738 (1998) [Acoust. Phys. **44**, 641 (1998)].
7. V. L. Preobrazhensky, Jpn. J. Appl. Phys., Part 1 **32**, 2247 (1993).
8. V. N. Strel'tsov, BRAS Physics, Suppl. Phys. Vibr. **61**, 228 (1997).
9. R. B. Thompson and C. F. Quate, J. Appl. Phys. **42**, 907 (1971).

*Translated by M. Lyamshev*

*Acoustical Physics, Vol. 46, No. 6, 2000, pp. 749–758. Translated from Akusticheskiĭ Zhurnal, Vol. 46, No. 6, 2000, pp. 850–860.*


**HISTORY OF RUSSIAN SCIENCE**

# Comprehensive Studies of Sound Fields in the Kuril-Kamchatka Region of the Northwestern Pacific

**N. V. Studenichnik**

*Andreev Acoustics Institute, Russian Academy of Sciences, ul. Shvernika 4, Moscow, 117036 Russia*

*e-mail: bvp@akin.ru*

Received December 6, 1999

**Abstract**—The technique, experimental conditions, and main results of comprehensive studies of sound fields in the northwestern region of the Pacific Ocean are presented. The experiments are carried out on paths up to 2100 km in length. The power–frequency, space–time, and correlation characteristics of the sound fields are studied in sonic and infrasonic frequency bands for long- and extra-long-range propagation with the use of cw and explosion-generated sound signals. Effects of the bottom relief and the spatial distribution of the speed of sound on the frequency characteristics of the sound field are investigated. The role of front zones in the formation of sound fields received at the coastal shelf and in the open ocean is revealed. The loss coefficients are estimated. The space–time stability of the sound field components is studied, and the possibility is shown for the coherent components to be conserved and resolved in frequency at distances up to 2100 km. The phase velocities of these components are determined. The total broadening of the frequency spectra is considered. The correlation characteristics of the total field are obtained for horizontally separated receivers in sonic and infrasonic frequency bands. © *2000 MAIK "Nauka/Interperiodica".*

In accordance with the main tasks of fundamental studies of the World Ocean, in 1980, Andreev Acoustics Institute of the Russian Academy of Sciences (RAS), jointly with the Institute of Applied Physics of RAS and the Navy Hydrographic Service of the USSR, carried out comprehensive studies of the acoustic-oceanographic characteristics in the northwestern region of the Pacific Ocean. The Morfizpribor Central Research Institute, the Kiev Research and Development Bureau, the Pacific Institute of Oceanology of the Far-East Scientific Center of the RAS, the General Physics Institute of the RAS, and other organizations and teams also participated in these works. The studies were performed in summertime, near the southern end of the Kamchatka peninsula, on paths up to 2100 km long. The author of this paper, as the principal investigator of these studies, developed the working program. He determined the content of the ship-borne equipment and the set of instruments used in the studies, the locations for the main receiving and transmitting systems along with their operational modes, and the sequence of individual stages of the complex program.

The program of the studies implied that experimental data should cover a wide scope of key parameters of the sound fields in sonic and infrasonic frequency bands, for long and extra-long ranges of sound propagation along paths with a complex bottom relief, in intricate acoustic-hydrographic environments.

## IMPLEMENTATION OF THE EXPERIMENTS

Because of the variety of hydrophysical processes and spatial distributions of oceanographic parameters, the northwestern Pacific seems to be one of the most complex regions of the ocean. This complexity is primarily caused by the existence of hydrological fronts that are generated by the interaction of the subtropical waters of Kuroshio and the subarctic waters of the cold Oyashio current. With these phenomena accompanied by an equally complex bottom relief, the studies were planned to be performed for a broad band of sonic and infrasonic frequencies, with large separations of the sources and receivers in distance and depth. The program was intended to collect information on the sound field structure and its decay laws, the coefficients of spatial attenuation, the bottom reflectivity, the time-frequency stability of the field components, and the correlation functions of the total field. Studies of the effect of the front zones on the power–frequency field characteristics were considered as highly urgent. Studies of hydrological and hydrographic parameters of the near-Kamchatka region were included in a separate subprogram. The acoustic experiments were carried out for the frequency band 5 Hz to 3 kHz with the use of explosions as the sound sources and at frequencies of 100, 230, 380, and 1000 Hz with cw sources that were highly stable in frequency. The monochromatic transmitting systems and explosive sound sources were car-

1063-7710/00/4606-0749$20.00 

ried by the *Baikal* research vessel. The signals were received by various receiving systems that were spatially separated by up to 10–25 km, mainly in the shelf zone of the region. In addition, the cw signals were received in an open ocean, in the vicinity of the front zones, 1200–1400 km offshore. Seven research vessels of the Navy Hydrographic Service of the Far-East region participated in the studies, along with the coastal receiving stations, all reception points having a common communication system. Managing the experiments, performing the basic measurements, coordinating the modes of operation of transmitters and receivers located both in open ocean and in the shelf zone—these were the tasks performed by the author of this paper from the coastal control station in accordance with the unified program.

Some results of these studies were reported at scientific seminars and sessions of the Russian Acoustical Society and can be found in several publications (e.g., [1]).

## EXPERIMENTAL CONDITIONS

The acoustic experiments were accompanied by detailed hydrologic and geologic measurements in the region. From June 16 to September 4, two quasi-synchronous hydrological surveys were carried out. These measurements followed the specially developed scheme of the stations. A fragment of this scheme is presented in Fig. 1. As straight-line segments, the acoustic paths are also shown on the map. The first path is oriented along the arc of the big circle at 120° (path 1), the second one at 150° (path 2). The stations were located at arc and radial sections, 50 to 1500 km in length. The path lengths reached 2100 km. The range of azimuth angles was 80°.

Hydrological measurements were carried out before, simultaneously with, and after the acoustic experiments. Points of the measurements were separated by about 20 nautical miles at the sections that were 50 nm apart from each other. In the regions with high vertical gradients and on the propagation paths, these separations were 5–10 miles. As a result, the frontal zones were located and characterized prior to the acoustic experiments. In parallel, the sea floor was surveyed in the entire region and along the propagation paths. At several points, geologic parameters of the upper sediment layer were measured, and the available data were generalized in view of the measured parameters. In the hydrological measurements, four research vessels took part: *Bashkiriya, Nevel'skoĭ, F. Litke,* and *Taĭga*. The vessels operated mostly independently, according to individual subprograms. A number of self-contained deep-water buoys were arranged in the region for long-term operation. At separate points, measurements taken over several days and multiset measurements were carried out. The buoy stations and multiset ones are shown by triangles and rectangles on the map with indications of the observation duration (in days). In total, 15 sections were made that covered 233 points of hydrological measurements. At each point, the measurements were carried out twice, with an interval of 1.5–2 months. The data on the hydrological-acoustical characterization of the region, along with the results of full data processing to yield the hydrological, physical, and partially chemical parameters of the waters, are summarized in 18 separate volumes. This work was done by the Hydrographic Service of the Far-East Region.

For the Kamchatka coastal region, a characteristic feature of the thermal structure of waters is the presence of cold waters (with temperatures lower than 1°C) at depths of 50–100 m and waters with positive temperatures (up to 3–4°C) at depths of 300–400 m. The temperature monotonically decreases with depth and reaches +1.5°C near the bottom, at the depth of 5000 m. Four main fronts can be distinguished in the region:

Kamchatka front, the Oyashio Current (50–150 km offshore);

Oyashio front, the Oyashio Countercurrent (800–850 km);

North Polar front (1200–1300 km);

Kuroshio front (1400 km along path 2 and 2000–2100 km along path 1).

The three former fronts weakly affect the main properties of the profile of the speed of sound. These fronts are associated with waters of the polar and moderate latitudes. Here, at ranges up to 2000 km along path 1 and up to 1380 km along path 2, the axis of the sound channel lies at depths from 80 to 150 m. The most significant changes occur on path 2 at the deep-water Kuroshio front. Here, the depth of the channel axis sharply increases from 100–150 to 1000 m as the distance changes by less than 10 km. The axis value of the speed of sound increases up to 1480 m/s, which is higher than near the coast (1450 m/s) by 25–30 m/s. At the depths of 50–100 m, the difference in the sound speeds reaches 50 m/s or more. Figure 2 shows the most typical speed of sound profiles along path 2 and the isospeed curves at ranges up to 1500 km, including the front zone (1400 km), for the upper layers of the channel. In Fig. 2b, characters 1–40 indicate the numbers of the hydrological stations on the path; crosses display the positions of the channel axis. In Fig. 2a, a significant inversion is pronounced in the regular range dependence of the speed of sound profiles. Thus, at distances of 850–1265 km and depths of 100–1000 m, the speed of sound exhibits only a weak depth dependence and varies from 1473 to 1477 m/s, with a minimum at 400–500 m (curve *3*). At the same time, at distances of 1290–1375 km, the minimal speed of sound decreases by 8–10 m/s, and a channel is formed with a sharp minimum of 1468 m/s at the depths 100–200 m. The speed

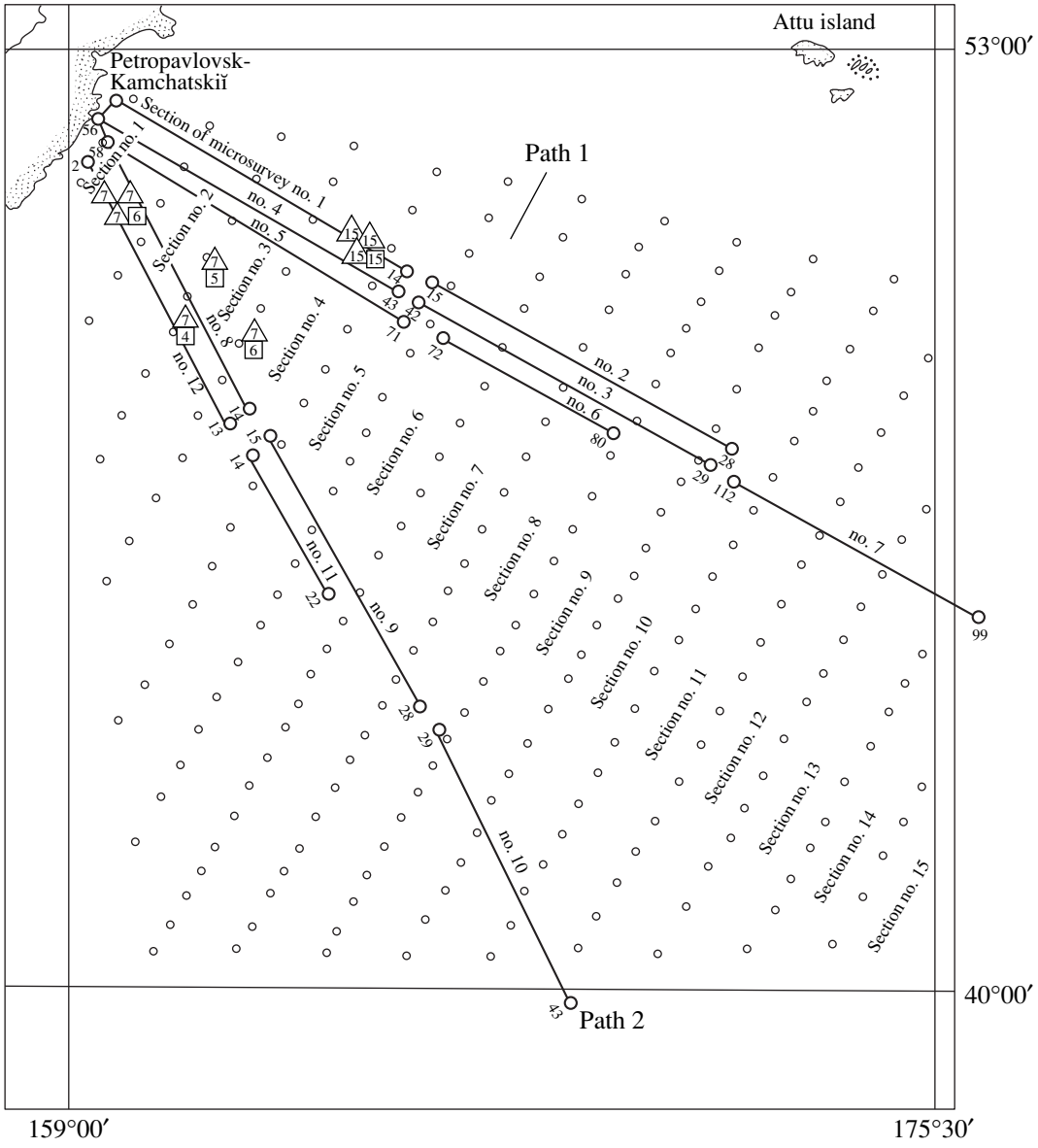


**Fig. 1.** Region of experimentation, propagation paths, and layout of the hydrophysical stations. Circles show the positions of the hydrological stations. Portions of solid lines show the sections of oceanographic surveys, triangles show the triple self-contained buoy systems, and squares represent multiset hydrological stations. Numbers in and near triangles and squares indicate the observation durations (in days).

of sound profile acquires parameters that are close to those of the coastal zone (curves *1*, *2*). At the other side of the front zone, the speed profiles become similar to those of tropical latitudes. The inversion-type changes in the speed of sound field can be also observed in other regions [2].

The acoustic experiments themselves were carried out from July 17 to August 15, with a fully developed underwater sound channel. Two paths were selected that were most typical for the region (Fig. 1). The first one was oriented at 120°, perpendicularly to the isobaths. It passed mainly through the cold polar waters, and the path parameters weakly changed with distance up to 2000 km. At distances of 800–1000 km, the path crossed the Emperor Mounts. The second path oriented at 150° exhibited more pronounced changes in the profiles of the speed of sound and a sharp frontal zone at the distance 1400 m (Fig. 2). Starting from 150 km, the ocean depth was within 5000–5500 m along the path. Along path 1, the front zone and the beginning of a tropical-like environment were observed at the distances of 2000–2100 km. There were favorable meteorological conditions during the experimenta-

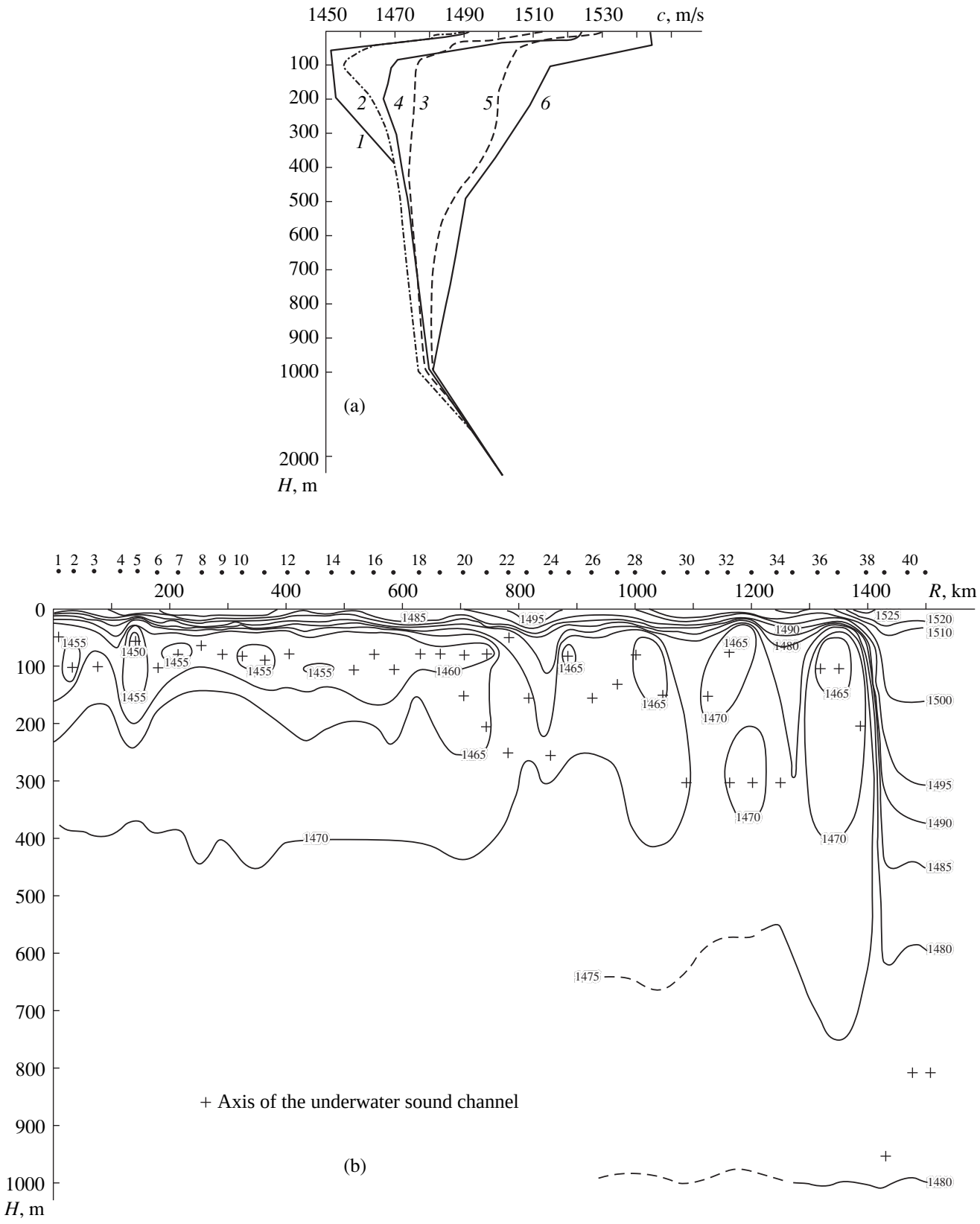


**Fig 2.** (a) Selected profiles of the speed of sound on path 2 at the distances (*1*) 100, (*2*) 850, (*3*) 1380, (*4*) 1412, (*5*) 2000, and (*6*) 3000 km and (b) the field of the speed of sound up to the Kuroshio front zone for upper layers of the waveguide; the field is represented by the isospeed curves.

tion: the wind speed was not higher than 10–12 m/s, the sea state was Beaufort 3–4.

## RECEIVING AND TRANSMITTING SYSTEMS: EXPERIMENTAL TECHNIQUE

In the experiments with the cw sound signals, the transmitters were continuously towed and all the frequencies were emitted simultaneously by different transducers. The four transmitters were mounted on a single frame, which was deployed from the vessel's stern. A depth-measuring device was also mounted on the frame. With the towing speed of 5–6 k, the transmission depth varied from 60 to 70 m. On both paths, the distances of towing reached 300 km, with short stops at the distances 50, 100, 200, and 300 km for performing other experiments. At longer ranges, the cw transmission was carried out on separate parts of the paths, 50–150 km in length, at the distances 400–450, 600–650, 900–1000, 1200–1250, 1330–1500, 1500–1600, 1800–1850, and 1950–2100 km. Quartz-stabilized oscillators were used to feed the power amplifiers, along with associated manipulating devices. The devices allowed one to choose different power levels and types of the signal, with a given ratio of its duration to the repetition rate. A transmission mode was chosen that was close to a continuous one: the signal duration was 480 s, the pause duration was 20 s. All four transmitters were controlled from a single controller that continuously monitored the transmission mode and depth. A reference hydrophone was mounted on the frame for calibrating the whole circuit. Thus, the power of each transmitter could be measured and maintained at the desired level. The aforementioned technique was common for both paths. With the cw signals, the measurements were carried out at linear tacks, when the transmitting vessel went offshore, towards the open ocean; the explosive charges were dropped from the vessel at reverse tacks. The explosions were performed at the vessel's speeds of 10–12 k, in the form of series. Each series consisted of six explosions. The explosions were separated by an interval of 3 min. The depths of explosions were 50, 100, and 300 m. The mass of the charge was about 200 g, the detonators were of the KZM type. In total, 600 explosions were performed on both paths. With the explosions, the length of path 2 was 1600 km.

For signal reception and recording, different devices were used for the frequency band at hand. The depths of the shelf-positioned receivers were 100 to 200 m, depending of their distance from the coast; they were separated by 10–25 km in space. The low-frequency (from several hertz) radio-acoustic buoys were bottom-moored (100 m), with the frontal separations up to 15 km. Their signals were recorded by the *Astronom* receiving vessel. The vertical receiving array (with the hydrophone depths 20, 40, 60, 80, and 100 m) was deployed from the *Antares* research vessel. Both receiving vessels were anchored at a distance of 15 km from each other. Only cw signals were received in the open ocean, near the front zones. For this purpose, drifting vessels were used: *Taĭga* on path 1 and *F. Litke* on path 2. They were positioned 1200–1400 km offshore, at points with 5000–5600-m sea depths. At these points, the signals were received at depths of 80–100 m when the transmitting vessel approached the receiving ones from the shelf, passed them (at the distances 400–450 m), and moved away from them up to the end points of the paths. The signals were recorded with the use of multichannel magnetic tape-recorders and level recorders. The distances between the sources and receivers were determined by means of satellite navigation systems and monitored by measuring the propagation times of the sound signals.

## MAIN RESULTS OF THE STUDIES

The cw-signal studies of the sound field structure showed that, for weakly changing hydrological properties of the path, the decay law is practically monotone, with a pronounced exponential dependence that is associated with the frequency. However different rates of the decay were observed at different parts of the paths. Thus, at the distances of 200 to 280 km on path 2, the level decay was 1–2 dB at the frequency of 380 Hz, while it reached 10–12 dB as the distance changed from 280 to 400 km. Parts of the paths were found where, for a distance change of 20 km, a nearly monotone (with the same interference maximums and minimums) increase in the level was observed up to 10–12 dB relative to its initial value. With the use of the narrow-band analysis, a consistent reception of the 1000-Hz signals took place up to the distance 1200 km, with the 8–10-dB excess over the noise level. At 1000 Hz, the total loss in the signal level, including absorption in water, losses at the boundaries (rough ocean surface, shallow-water shelf zone), and inhomogeneities of the channel, was 30–32 dB/Mm on path 1 and 40–45 dB/Mm on path 2. At the frequencies 100, 230, and 380 Hz, the signals were reliably received up to 2100 km on both paths, with a signal-to-noise ratio of 10–20 dB (for path 1). At these frequencies, the losses in the front zone are 10–12 dB (for the distances of 2000–2100 km of path 1). The additional losses, i.e., those measured relative to the cylindrical decay law and the predicted absorption as given by the formula $\alpha = 0.036 f^{3/2}$ dB/km, are 3–7 dB/Mm for a 2000-km path. On path 2, at the front zone, the decay and total losses of the 100-, 230-, and 380-Hz signals are close to those on path 1. Some differences can be found only in the envelope structures and local level variations. These differences seem to be caused by the unlikeness of the bottom reliefs on the two paths, especially on the continental slope and the coastal shelf. On path 1, the length of the shelf zone (up to the depths 250–300 m) was 3–4 km, while it

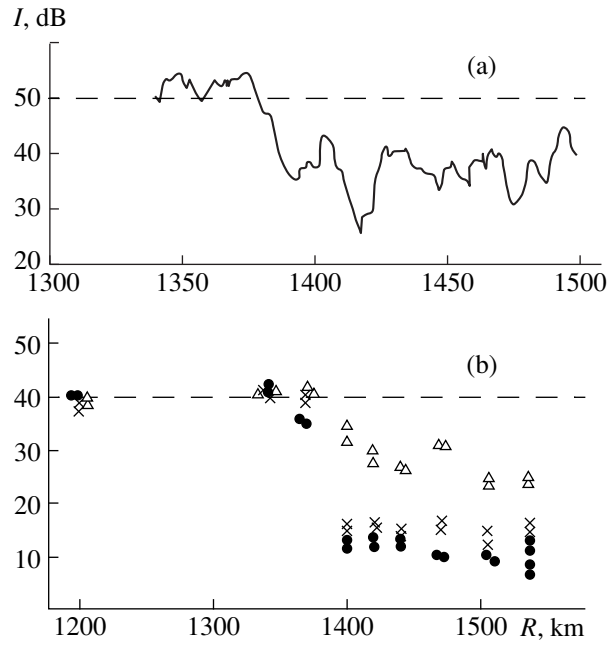


**Fig. 3.** Experimental sound field levels for (a) cw and (b) explosive signals on path 2 in the vicinity of the front zone; reception in the coastal wedge; distances 1200–1600 km. Depth of the cw source 70 m and frequency 100 Hz. Explosion depths: (dots) 50, (crosses) 100, and (triangles) 300 m. Frequency: 250 Hz, 1/3-octave band. Reception depth in both experiments: 200 m.

increased up to 10–12 km on path 2. The steepness of the continental slope was 10° to 17° on the paths.

Naturally, the most pronounced differences in the decay laws occur at the front zone. At the frequencies 100, 230, and 380 Hz, the passage over the front zone is followed by a level decrease of 12–16 dB, which is weakly dependent on the frequency. Figure 3a shows a fragment of the signal level record obtained at the frequency 100 Hz when the sound source was crossing the front zone. This signal was received at the shelf zone. The plots present the signal levels averaged over 480 s. The points are connected by a continuous curve. At the frequencies 230 and 380 Hz, the decay laws and the mean losses associated with front crossing are similar. For higher frequencies, a more complex shape of the level envelopes can be observed, though without any pronounced frequency dependence. For the sake of comparison, Fig. 3b presents the changes in the sound field level at the front zone, which were obtained with the explosive sound sources. The depths of explosions were 50, 100, and 300 m. The reception was carried out within the 1/3-octave frequency band around 250 Hz. A strong dependence of the level decay on the source depth can be noticed: up to 20 dB. Just as on path 1, the 1000-Hz signals were not detected on the noise background near the front zone at the distances 1350–1400 km, although the signal-to-noise ratio was 10–12 dB at the distances 1000–1200 km on both paths.

The front-zone losses can be associated both with variations profiles of the speed of sound at the source and receiver depths and with changes in the "energy capacity" of the sound channel behind the front zone. Here, the energy capacity means the angular width of the sound beam captured by the waveguide at high frequencies of the spectrum. Generally, the channel capacity is frequency dependent: as the frequency decreases, it decreases down to zero at the critical frequency of the refraction components of the entire waveguide. In this case, at each frequency, the energy capacity of the channel is determined by the angular aperture of the sound beam that is bounded by the boundary ray and the ray determined by the dispersion relation at the given frequency. For the region at hand, the difference in the speeds of sound at the channel axis reaches 23–30 m/s. At the same time, the ocean depth remains constant, as well as the near-bottom speed of sound. In ray-theory terms, these phenomena lead to a decrease in the channel capacity by +10°–11° and, as a consequence, to a decrease in the integral level of the sound field, because a large part of the water rays changes into bottom-surface-reflected ones, the latter rays suffering high losses in the bottom sediments.

Another important feature of the sound field propagating along the paths should be mentioned. It is concerned with the changes in the envelope of the signal amplitude in the course of propagation. The experimental records exhibited a regular nature of the changes in the amplitude envelopes, which are frequency dependent at the distances up to 1500–2100 km. This regularity indicates a high stability of the phase fronts and coherent components of the sound field in the observed field structures at the long ranges studied. At the distances up to 2000 km, the spatial interference period (with the modulation depth up to 30 dB) was on average equal to 100–150 m at the frequency 1000 Hz and 350–600, 400–1000, and 500–1000 m at the frequencies 400, 230, and 100 Hz, respectively. Note that, if the phases of the field components were lost, the regularity of the frequency dependences of the spatial interference periods would be violated and the envelopes of the total signals would exhibit the characteristics of a statistically homogeneous field with a chaotic amplitude distribution.

Figure 4 shows the calculated sound field structure and the level decay as a function of range on path 2, for the low-frequency portion of the spectrum. A computer code developed by Avilov [3, 4] on the basis of the wide-angle parabolic equation was used. Here, the distances are one to 2200 km, the frequency equals 16 Hz, and the source depth is 70 m. The reception at the coastal shelf, at a depth of 200 m, is implied. The shelf zone is 12 km long. The following environment characteristics are specified for the computations: 40 profiles of the speed of sound along the path; the measured bottom relief and the known parameters of the sediments

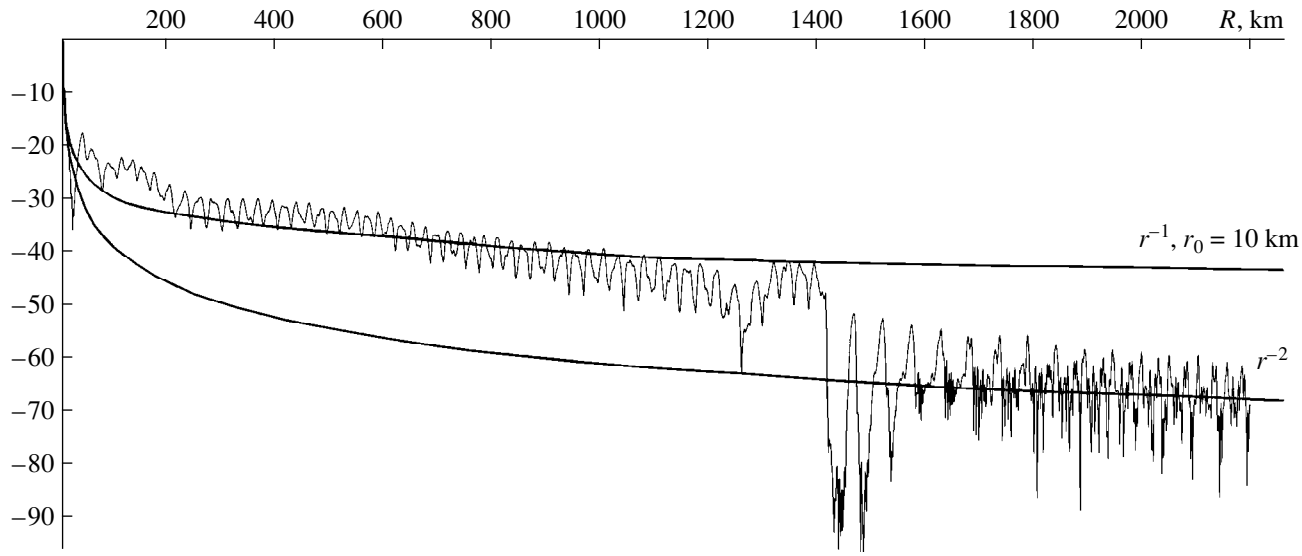


**Fig. 4.** Calculated sound field levels for the monochromatic source; reception in the coastal wedge. Computations in view of the bottom relief, changing sound speed profiles (40 measured profiles are used), and geological properties of the sea floor. Source depth: 70 m. Receiver depth: 200 m. Frequency: 16 Hz. Front zone distance: 1400 m. (*1*) Spherical decay law; (*2*) cylindrical decay law; transition distance: $r_0$ = 10 km.

in view of the losses; and the halfspace model for the sea floor. Curve *1* represents the spherical spread, and curve *2* corresponds to the cylindrical one, with the transition distance $r_0$ = 10 km. The obtained results show that, even at this low frequency, the front zone significantly influences the power characteristics of the sound field. In addition, according to the decay law, the computational model agrees well with the observed dependence of the sound level on the changes in the profile of the speed of sound along the path.

Figure 5 illustrates the studies of the sound field structure in the vicinity of the open-ocean front zone. These data are obtained for the transmitting vessel passing from the area of total insonification to the zone-structured one. The receiving vessel was positioned 1340 km offshore, at a distance of 60 km from the front zone. After passing the receivers (with the minimum distance 450 m), the transmitting vessel went along the initial course toward the front zone, and then, after crossing it, toward the end point of the path. The figure presents the sound field decays at the frequencies 100, 230, 380, and 1000 Hz, for the distances 0.5 to 200 km. The dotted curve at the top indicates the sound field levels calculated in the ray approximation. In the computations, the bottom was assumed to be fully absorptive. According to the data obtained at all frequencies, starting from 10–15 km up to the front zone and at longer ranges up to 200 km, the level decay is closer to the spherical law (with a positive anomaly of 8–18 dB) than to the cylindrical one, the latter being expected in the case of a homogeneous sound channel along the path. The experimental values of the level, along with its range dependence, agree well with the computations. The positive propagation anomaly reaches 12–18 dB in the convergence zones. As a result of two- and threefold reflections from the bottom and surface in the second and third shadow zones, the sound field decays more rapidly than the spherical curve and changes from –(2–7) to –25 dB. A strong frequency dependence of the bottom reflection coefficient can be noticed. The highest losses are observed at the frequency 1000 Hz. According to the calculations, if the effective bottom and surface reflection coefficients are close to 0.8–0.9 at 100 Hz, they will decrease down to 0.25–0.38 at 1000 Hz. As follows from the absolute values of the level and the trend of the general decay, the anomaly in the secondary zones is close to that corresponding to the totally insonified fraction of the path and the sound level follows the spherical law with a constant positive anomaly.

As we mentioned above, the studies with the explosive sound sources were carried out at the reverse tacks on both paths, when the transmitting vessel went ashore from an open ocean. The signals were received by all coastal systems at distances from 2100 km on path 1 and from 1600 km on path 2. In the case of a broadband reception at 2100 km, the signal level exceeded the noise one by 10–20 dB. With a narrow-band analysis at individual frequencies, the signal-to-noise ratio reached 25–30 dB. At the distance 2100 km, the change from 50 to 300 m in the explosion depths leads to an increase of 5 dB in the broadband signal level. The total duration of the signals is 10 s. At the front zone on path 2, the broadband level decay ranges from 5–10 to 15–20 dB for the explosion depths of 50 to 300 m. As measured in the 1/3-octave band, the maximum level difference in the front zone is 12–35 dB, which is somewhat higher

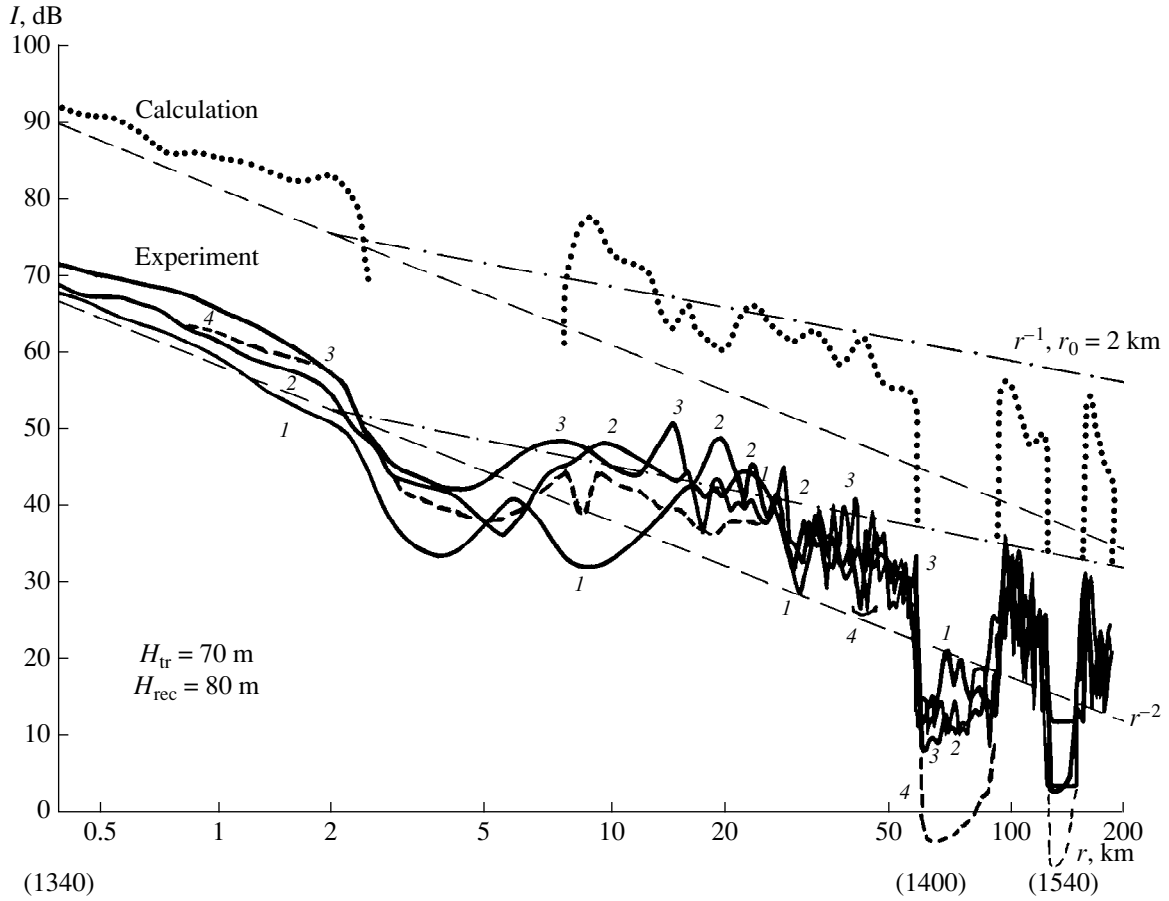


**Fig. 5.** Range decays of the sound field level near the open-ocean front zone on path 2, at distances of 1340–1500 km. The data are obtained for the transmitting system moving away from the receiver. The transmission depth is 70 m, and the reception depth is 80 m. Frequencies: (*1*) 100, (*2*) 230, (*3*) 380, and (*4*) 1000 Hz. The upper plot shows the values computed with the ray code for a perfectly absorbing bottom. The dashed lines correspond to the spherical decay law, and the dash-and-dot lines, to the cylindrical decay law; the transition distance is $r_0$ = 2 km.

than with the cw transmission. This effect is well pronounced in Fig. 3.

To finish with analyzing the power characteristics of the sound field, it is worth mentioning that, in experimentation with explosions (and with the use of a bottom-moored low-frequency antenna array), there were permanently observed (and recorded by the level recorders and infrasonic magnetic tape-recorders) rather intense low-frequency signals from underground earthquakes.

In these studies, the studies of the spatial and temporal stability of the sound fields were carried out with the use of a highly stabilized transmission from a moving source. For the first time, data were obtained on the frequency splitting of the field components in the presence of continuous signals, at extra-long ranges in a spatially inhomogeneous waveguide. The signals used in these studies were those recorded at distances of 1000–2100 km, with the frequencies 230 and 380 Hz and durations 300 and 1050 s, the latter values corresponding to path intervals of 750 and 2625 m. The frequency resolutions of the analysis were 0.003 and 0.00095 Hz. Figure 6 shows an example of the frequency splitting in the field components. These data were obtained at the distance of 1000 km at the frequency 380 Hz. The abscissa of the plot is the frequency band $\Delta f$ (the scale is linear). On the ordinate axis, the amplitudes of the components (quartets) are presented for the received signal (relative units, linear scale). The frequency resolution is 0.00095 Hz. (It is worth mentioning that, to split the quartets themselves with the experiment layout at hand, the resolution must be higher by an order of magnitude.) The total spread of the frequency spectrum (for the split components) is 50 mHz at this frequency and 30 mHz at the frequency 230 Hz–30 mHz. These values weakly change as the distance increases up to 2100 km. The record contains up to 8–9 well resolved maximums corresponding to individual groups (quartets) of the arrivals with phase velocities changing within 1460–1540 m/s. It is impossible to split the near-axis quartets, because they have lost their coherence and have low relative time delays.

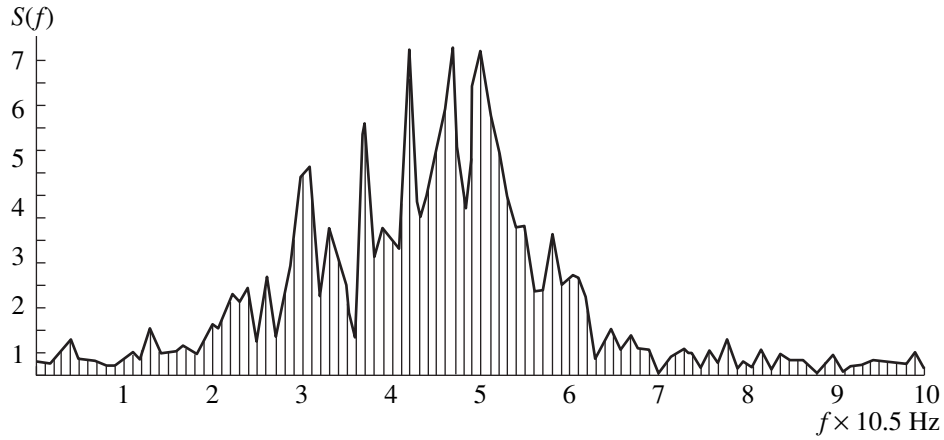


**Fig. 6.** Frequency spectrum of the cw signal from a moving source. Speed: 2.5 m/s; range: 1000 km; frequency: 380 Hz. The total scale of $\Delta f$ is 0.095 Hz. The vertical lines are separated by 0.00095 Hz.

With these experimental conditions and depths of the source and receiver, within the limited band of the characteristic angles, an analysis band of $\Delta f = 0.00095$ Hz is sufficient for the field components to be reliably split at all studied distances. With the analysis band $\Delta f = 0.003$ Hz, the detection of individual components becomes much more difficult. The obtained results confirm the high efficiency of the method used and, above all, the high space–time stability of the phase properties of the sound field and the conservation of the coherence of the field components (for a certain band of the characteristic angles) at the frequencies at hand (in summertime conditions), even in a waveguide that is inhomogeneous along the path.

To study the frequency and space–time stability of the sound field for the total signal, the correlation characteristics of the explosive, cw, and noise signals were calculated with the signal reception within the coastal wedge. Here, the signals used were received by individual receivers spaced by several dozen meters to 10–15 km in the horizontal plane. The ranges up to 1000 km were studied. The frequencies used were 20–1000 Hz. The obtained correlation coefficients vary from 0.35 to 0.96 for different frequencies, distances, and signal types.

To explain the experimental data theoretically (on the formation of the sound fields at sonic and infrasonic frequency bands at the coastal shelf, the continental slope, and in an open ocean with varying hydrological and geological parameters along the path), different waveguide models were used that were closest to the actual propagation conditions, along with different mathematical methods and computer software. These are the wave computer code by Avilov [3, 4] for inhomogeneous waveguides (based on the method of the wide-angle parabolic equation); the wave computer code by Polyanskiĭ [5] (the method of parabolic equation correction); the wave codes by Vagin and Mal'tsev [6], Kudryashov [7], and Shilin (the normal mode method) for stratified waveguides; and the codes by Buldyrev and Yavor [8, 9] (the asymptotic approximation for the normal mode method). Also used were different modifications of ray codes (by Vagin, Shilin, and others) that are applicable to stratified and inhomogeneous waveguides and allow for the bottom relief, changes in the hydrological and geological parameters of the path, and surface waves.

The comprehensive studies of the sound fields, which were carried out in the northwestern region of the Pacific Ocean in 1980, contributed to our knowledge of the field structure in sonic and infrasonic frequency bands on paths of up to 2100 km in length. The influence of front zones on the frequency characteristics of the sound field was studied. Additional losses associated with the inhomogeneities of the waveguide were estimated for very long paths. Space–time and space–frequency stabilities were investigated for the field components and correlation characteristics of the total signal. A large body of data was collected on the hydrophysical properties of the region that is complicated but interesting from the scientific point of view and important for practical applications.

## ACKNOWLEDGMENTS

I am grateful to V.I. Mazepov, F.I. Kryazhev, and Yu.I. Tuzhilkin for assistance in organizing the expeditionary studies; to Yu.M. Sukharevskiĭ and L.M. Lyamshev for useful discussions and assistance in implementing the experimental results into practical-purpose developments; to A.D. Silaev, S.I. Dvornikov, Yu.N. Morgunov, A.P. Maryshev, V.A. Petnikov, I.P. Shkol'nikov, L.N. Shcherbak, and other participants of the expeditions for the assistance in the experiments and the experimental data processing.

This work was supported by Russian Foundation for Basic Research, project no. 99-02-18359.

## REFERENCES

1. N. V. Studenichnik, in *Ocean Acoustics: Proceedings of the Academician L.M. Brekhovskikh Workshop* (GEOS, Moscow, 1998), pp. 330–335.
2. J. H. Churchill and T. J. Berger, J. Geophys. Res. **103** (C13), 30605 (1998).
3. K. V. Avilov, in *Waves and Diffraction-85: Proceedings of the All-Union Symposium on Diffraction and Propagation of Waves* (Tbilis. Gos. Univ., Tbilisi, 1985), Vol. 2.
4. K. V. Avilov, Akust. Zh. **41**, 5 (1995) [Acoust. Phys. **41**, 1 (1995)].
5. É. A. Polyanskiĭ, *Method for Correcting the Solution of the Parabolic Equation in a Planar Inhomogeneous Waveguide* (Nauka, Moscow, 1985).
6. A. V. Vagin and N. E. Mal'tsev, Vopr. Sudostr., Ser. Akust., No. 9, 61 (1977).
7. V. M. Kudryashov, Akust. Zh. **22**, 724 (1976) [Sov. Phys. Acoust. **22**, 406 (1976)].
8. V. S. Buldyrev and M. I. Yavor, Akust. Zh. **28**, 601 (1982) [Sov. Phys. Acoust. **28**, 356 (1982)].
9. M. I. Yavor, Vopr. Sudostr., Ser. Akust., No. 18, 17 (1984).

*Translated by E. Kopyl*

*Acoustical Physics, Vol. 46, No. 6, 2000, pp. 759–761. Translated from Akusticheskiĭ Zhurnal, Vol. 46, No. 6, 2000, pp. 861–864.*


**INFORMATION**

# VIII Brekhovskikh Workshop on Ocean Acoustics

May 29–31, 2000, the VIII Brekhovskikh Workshop on Ocean Acoustics was held. The workshop was combined with the X Session of the Russian Acoustical Society. The participants of the event were acousticians from Moscow, Nizhni Novgorod, Taganrog, Voronezh, Vladivostok, and Georgia. More than 50 papers were presented. The Workshop program covered nearly all topics of present-day ocean acoustics. The papers can be schematically broken up into five groups: sound propagation in the ocean (theory and experiment), acoustic tomography and ocean monitoring, underwater sound scattering and reflection, generalization of the experimental data over the World Ocean, and techniques and instruments for full-scale studies in the ocean. In a brief review, we cannot consider all papers presented at the workshop and, therefore, we mention only some representatives of each group.

**1. Sound propagation in the ocean.** The papers on Arctic acoustics are a matter of interest. Underwater acoustic studies in the Arctic Ocean were initiated by the Acoustics Institute during the existence of the USSR, and these studies were rather comprehensive. Later, they were continued at the General Physics Institute and the Institute of Oceanology of the Russian Academy of Sciences. The underwater sound fields were studied experimentally and theoretically for both deep- and shallow-water arctic regions and for different frequencies. The mode structure of the sound field, its space–time variability in depth and range, and sound scattering and attenuation caused by the interaction with the ice cover were investigated. The experimental data on underwater ambient noise were obtained, and the sound fields on long paths (up to 2600 km) were modeled. The results of these works were highly appreciated by the international scientific community. Two factors are most important for sound propagation in the Arctic Ocean: the ice cover and the monotone increase in the sound speed as a function of depth, both factors complicating the sound field structure. In the paper presented by V.M. Kudryashov and F.I. Kryazhev, on the basis of computer modeling, the spatial variability of the coherence parameter of the sound field due to sound scattering by the rough undersurface of the ice cover was analyzed for both uniform and irregular arctic waveguides. The effect of the ice cover was also considered by V.D. Krupin who reported on the dependence of the propagation anomaly on the ice cover thickness for tonal sound signals in shallow-water arctic regions for the frequency band 0.1–1.0 kHz.

The ocean sound field is influenced by large-scale disturbances in the medium parameters. The effects of intense internal waves on the sound field were considered by A.N. Serebryanyĭ and A.I. Belov. In this paper, the influence of the internal solitons on sound propagation is numerically modeled for a shallow-water path. The paper also presents a brief review of intense internal waves in a shelf region. In the calculations, the authors used the data on the soliton-like internal waves, which were obtained in the coastal region of the Pacific Ocean, near the Kamchatka peninsula. The soliton-like internal waves give rise to a specific structure of the sound speed field in the ocean. In the paper by B.G. Katsnel'son and S.A. Pereselkin, with the use of the model known as "horizontal rays and vertical modes," the formation of dynamical horizontal sound channels is established for a shallow sea where solitons exist. Because of these channels, time-periodic focusing and defocusing occur for the rays that propagate at small angles to the front of internal waves. A.N. Rutenko reported on the experimental and theoretical studies that reveal the effect of short-period internal waves on the interference and mode structures of the sound field on a fixed path in the shelf zone of the Sea of Japan, for both winter and autumn water stratifications. A strong effect of the internal waves on the frequency interference structure of the sound field and on the energy distribution between the lower seven modes is revealed. In the paper by L.V. Bondar', L.N. Bugaev, and A.N. Rutenko, the data of in-sea experiments are presented on the changes in the low-frequency sound field, which are caused by the surface tide and tide-associated disturbances in the water bulk in the shelf zone. The measurements were carried out on fixed paths up to 260 km in length, oriented both along and across isobaths. The experimentalists managed to distinguish between the effects of internal and surface tides.

A number of papers were devoted to new theoretical methods for calculating the ocean sound fields. K.V. Avilov developed pseudo-differential parabolic equations to describe the propagation of seismoacoustic waves in a two-dimensionally inhomogeneous ocean with a rigid bottom and presented numerical solutions for these equations. The algorithm for calculating the total sound field for the waves propagating both forward and backwards was presented. The problem of the lateral wave excitation by a parametric sound source in a shallow sea was studied by S.A. Egorychev, D.A. Zakharov, V.V. Kurin, L.M. Kustov, and N.V. Pronchatov-Rubtsov.

Several researchers reported on in-sea measurements of various characteristics of the underwater sound field: the mode content and the dispersion characteristics in shallow- and deep-water oceanic waveguides on paths of different lengths (V.A. Lazarev, A.D. Sokolov, and G.A. Sharonov); the cross-correlation of pulsed

1063-7710/00/4606-0759$20.00 

broadband signals with a linear frequency modulation in the second shadow zone in the Central Atlantic (K.I. Malyshev); the angular structure of the sound field in the deep ocean (V.A. Baranov); and the spatial and temporal variability in the coastal wedge (A.V. Kulakov).

An important problem of underwater acoustics is the analysis and interpretation of the experimental data. R.A. Vadov proposed a computer method to separate two signals that are close in their arrival times when the signals propagate to a distant receiver over paths that differ by a single contact with the caustic. The method proved to be highly efficient in analyzing the experimental data obtained earlier.

**2. Acoustic tomography of the ocean and ocean monitoring.** In recent years, studies of the acoustic tomography of the ocean and ocean monitoring were carried out very actively in many countries, including Russia. The well-known work by Munk and Wunsh (1979) was the starting point. Various ray and mode tomography techniques were proposed. In the paper presented by A.N. Gavrilov at the joint session of the Workshop and the Russian Acoustical Society, the state of the art and future prospects for acoustic ocean thermometry were analyzed. Already accomplished, current, and future experiments on acoustic tomography in the Pacific, Arctic, Indian, and Atlantic Oceans were considered. V.V. Goncharov developed a new approach to the acoustic tomography of currents, which is based on matching the unreciprocity of the sound field. By numerical simulations, the possibility for linearizing the proposed procedure is demonstrated, this approach significantly accelerating the calculations. The effect of an inaccuracy in the *a priori* data on the reconstruction of the mean temperature of the water layer is analyzed in the paper by A.L. Virovlyanskiĭ, A.Yu. Kazarov, L.Ya. Lyubavin, and A.A. Stromkov. It is shown that, by omitting a number of the empirical orthogonal functions, which are used to parametrize the inhomogeneities, one comes to significant errors. In a number of papers, specific tomography problems were considered. D.L. Aleĭnik, V.V. Goncharov, and Yu.A. Chepurin presented the data on the dynamical acoustic tomography of the interthermocline lens observed in 1994 in the studies carried out on the scientific research vessel *Akademik Sergeĭ Vavilov* in the North Sea. Owing to the detailed hydrological measurements and the large number of acoustic stations, the differential tomography was implemented in well-established environment. The reconstruction results agree well with the measured parameters of the lens. The paper by E.F. Orlov was focused on studying the hydrophysical parameters of oceanic waveguides by observing the interference structure of the low-frequency sound fields of broadband sources. A.V. Furduev presented two new methods for acoustically monitoring the medium variability. In the pulse-difference method, the difference of two time–power sequences of a multiray signal indicates the changes in the medium along the propagation path. In the regenerative method, the monitored medium serves as part of the measuring device, namely, the feedback loop in the self-sustained oscillator, whose frequency deviation carries information on the medium variability. Both methods were tested to demonstrate their high sensitivity.

**3. Underwater sound scattering.** For decades, underwater sound scattering has been the subject of numerous theoretical and experimental studies. To date, the physical mechanisms of this phenomenon are well established, and the intensity levels of scattering are reliably estimated for different oceanic environments. Theoretical and computer models were developed that relate the acoustic effects to the associated medium parameters: the spectrum of surface waves, the structure and relief of the sea floor, and the characteristics of volume inhomogeneities of a hydrophysical and biological nature.

These models allow one to use the experimentally recorded scattered signals for solving the inverse problems, i.e., for estimating the medium parameters from these signals. Evidently, the reliability and accuracy of solving the inverse problems is higher, if the associated models are tested in an independent way, simultaneously or in advance. In this connection, the paper by A.I. Belov should be mentioned: the author proposes to determine the physical properties of the bottom sediments in a shallow sea by measuring the bottom reflection coefficient. The results are compared with the data obtained by calculation in another way, namely, from independently measured values of the sediment density and porosity. The same subject is touched upon in the paper by V.N. Fokin and M.S. Fokina. By theoretically analyzing the frequency dependences of the reflection coefficient and losses caused by sound reflection from the shallow-sea bottom, the authors propose a technique for estimating the physical parameters of the bottom represented by a sediment layer and an underlying elastic halfspace. The same authors developed a theory of resonant sound reflection from an elastic layer overlying an elastic halfspace.

D.E. Leĭkin theoretically treated the feasibility of detecting the coherently scattered waves in the ocean with random inhomogeneities of the refraction index. It was shown that such waves can be detected for the direction of their forward propagation, even if there is no *a priori* information on the parameters of the inhomogeneities. This allows one to use the coherently scattered waves for measuring the time trend of the mean temperature on the propagation path. New experimental data on volume sound scattering in ocean waters (the Pacific Ocean, subtropical regions) were presented by A.V. Akulichev, V.A. Bulanov, and P.N. Popov. The data analysis showed that, at frequencies of several hundreds of hertz, the frequency dependence of the volume scattering coefficient in the subsurface water layer can be explained by the fractal structure of the scattering inhomogeneities.

In addition to solving the inverse problems, the models of underwater sound scattering allow one to

interpret and quantitatively estimate complex physical phenomena, such as ocean reverberation and prereverberation. In the paper by E.A. Kopyl and Yu.P. Lysanov, some parameters were theoretically estimated and numerically computed for prereverberation caused by scattering of low-frequency sound by the rough ocean surface. The amplification effect was established for volume sound scattering in the presence of caustics in the subsurface water layer (V.S. Gostev and R.F. Shvachko). O.P. Galkin, R.Yu. Popov, Yu.V. Semenov, and E.V. Simakina presented experimental data on reverberation in the Pacific Ocean, near the continental slope of the Kamchatka peninsula. An interesting explanation was proposed for the broadened spectra of the bottom reverberation, which were observed with a fixed sound source and receiver; the degree of coherence was estimated for the reverberation signals.

**4. Generalization of the in-sea experimental data over the World Ocean.** The small number of new experiments on underwater sound scattering, as well as on other subjects of ocean acoustics, is governed by the sharp decrease in the number of scientific ocean expeditions carried out in Russia in recent years. This seems to stimulate many works on the generalization and classification of archive experimental data collected earlier and concerned with different branches of ocean acoustics, which, for some reason, were not published before.

As a first step in this direction, computer databases are usually created in order to collect, store, and subsequently use various experimental data that are in the possession of many researchers. A solution to this problem was proposed by L.F. Bondar', B.A. Kosyrev, and T.V. Saltanova who reported on developing a database that covers a wide variety of underwater acoustic applications with the use of modern software. These researchers are now filling the database. Computer databases are also being developed for specific branches of underwater acoustics. For example, N.N. Galybin, L.L. Tarasov, and V.Ya. Tolkachev in their paper considered the structure of a database intended for the experimental information on acoustics of the deep scattering layers (DSL) in the ocean; they also presented some results on using the information already stored. The data are reported on the regional classification of the Atlantic Ocean in values of the total column strength, which is the main acoustic parameter of DSL. The classification is based on the statistical processing of a large body of experimental data and covers the frequency band 3–20 kHz. With the use of this database, new information was obtained on the depth structure of DSL for different ocean regions, and on the effects of some hydrological inhomogeneities on the DSL structure (I.B. Andreeva, N.N. Galybin, and L.L. Tarasov). Another paper devoted to the analysis of a large body of experimental data was that presented by R.A. Vadov. This paper considered sound absorption and attenuation in ocean regions that differ in their hydrological properties. For the analysis, a special-purpose database developed by the author was used. The paper presented by A.V. Furduev stands somewhat apart from those mentioned above. In this paper, a generalized description is given for the phenomena that cause fluctuations of underwater ambient noise in different frequency bands of the fluctuations, from 0.001 Hz to several hertz. These phenomena include the variations in the meteorological environment and in the propagation conditions within the noise-forming ocean region.

**5. Techniques and instruments for in-sea measurements.** A number of papers described the use of parametric acoustic devices in full-scale experiments in the ocean. In this connection, we should mention the review by V.A. Voronin, S.P. Tarasov, and V.I. Timoshenko. The authors work in the organization that is the most advanced in Russia in the development of such instruments. This paper described the features of the devices as applied to studies of random inhomogeneities in the ocean water column and in the bottom structure. Methods were proposed for developing parametric antenna arrays, and information on the already designed parametric sonars was presented. Examples of using these devices in oceanic scientific experiments aimed at studying the fine structure of waters, fish shoals, upper layers of the sea floor, etc., were described. In addition to this review, a number of papers were presented on particular problems of improving the performance and characteristics of various parametric devices (e.g., papers by I.B. Starchenko and S.A. Borisov).

In several papers, acquisition and processing systems were described for various hydrophysical data such as the parameters of currents, the sound speed, and the electrical conductivity of water and its other characteristics. In particular, to monitor the position of biological objects within a shallow-sea coastal area, S.A. Bakhirev, L.F. Bondar', and V.B. Ignat'ev proposed the development of a system that consists of underwater parametric arrays and a number of self-contained acoustic and hydrophysical sensors that transmit radio signals to a coastal radar.

Several papers analyze the performance of acoustic devices that are to be applied to remote acoustic studies of the sea-floor structure (e.g., the paper by I.B. Zheleznyĭ, D.B. Ostrovskiĭ, and S.A. Smirnov) or acoustic properties of the bottom (A.V. Nosov and G.A. Postnov).

The papers presented at each of the first six workshops (1980–1990) were published by the NAUKA publishing house and were edited by Academician Brekhovskikh: Ocean Acoustics: State of the Art (1982); Problems of Ocean Acoustics (1984); Acoustic Waves in the Ocean (1987); Acoustics of the Oceanic Medium (1989); Acoustics in the Ocean (1992); and Oceanic Acoustics (1993). Proceedings of the VII (1998) and VIII (2000) workshops were published by the GEOS publishing company (Moscow).

**I. B. Andreeva and Yu. P. Lysanov**

*Translated by E. Kopyl*